

Electronic Thesis and Dissertation Repository

12-10-2010 12:00 AM

Nickel-based Catalysts for Gasification of Glucose in Supercritical Water

Muhammad Badrul Islam Chowdhury, *The University of Western Ontario*

Supervisor: Professor Paul A. Charpentier, *The University of Western Ontario*

A thesis submitted in partial fulfillment of the requirements for the Doctor of Philosophy degree in Chemical and Biochemical Engineering

© Muhammad Badrul Islam Chowdhury 2010

Follow this and additional works at: <https://ir.lib.uwo.ca/etd>

 Part of the [Catalysis and Reaction Engineering Commons](#)

Recommended Citation

Chowdhury, Muhammad Badrul Islam, "Nickel-based Catalysts for Gasification of Glucose in Supercritical Water" (2010). *Electronic Thesis and Dissertation Repository*. 48.

<https://ir.lib.uwo.ca/etd/48>

This Dissertation/Thesis is brought to you for free and open access by Scholarship@Western. It has been accepted for inclusion in Electronic Thesis and Dissertation Repository by an authorized administrator of Scholarship@Western. For more information, please contact wlsadmin@uwo.ca.

Nickel-based Catalysts for Gasification of Glucose in Supercritical Water.

(Thesis format: Integrated)

by

Muhammad Badrul Islam Chowdhury

Graduate Program
in
Engineering Science
Department of Chemical and Biochemical Engineering

A thesis submitted in partial fulfillment
of the requirements for the degree of
Doctor of Philosophy

School of Graduate and Postdoctoral Studies
The University of Western Ontario
London, Ontario, Canada

© Muhammad Chowdhury 2010

Certificate of Examination

Supervisor

Prof. Paul A. Charpentier

Supervisory Committee

Prof. Hugo De Lasa

Prof. Ajay K. Ray

Examiners

Prof. Charles Xu

Prof. Andy Sun

Prof. Modhumita B. Ray

Prof. Lars Rehmann

The thesis by

Muhammad Badrul Islam Chowdhury

Entitled:

Ni-based Catalysts for Gasification of Glucose in Supercritical Water

is accepted in partial fulfillment of the
requirements for the degree of
Doctor of Philosophy

Date _____

Chair of Thesis Examination Board

Abstract and Keywords

Gasification of waste biomass to form hydrogen, H₂, is a promising new source of green energy; while providing the additional benefit of treating challenging and hazardous waste streams that pollute the environment. Gasification of biomass in supercritical water (SCW) offers an attractive alternative to avoid the energy intensive drying process. In this approach, biomass is hydrolyzed by water into smaller molecules in the presence of a suitable catalyst. This study was aimed at developing an alumina supported nickel based non-noble metal catalyst suitable for biomass gasification in SCW. A lack of detailed characterization on fresh and spent catalysts in SCW has held back progress in this field and is critical due to the highly unusual properties of SCW at high pressure and temperature compared to ambient water. Typically hydrogen rich gaseous product from gasification of biomass in SCW requires temperatures higher than 700 °C, while low temperature processes (300-500 °C) produce methane rich gases. Use of suitable catalysts can lower the activation energy of the reaction, and hydrogen rich gaseous products can be achieved at low temperatures thus lower the operating cost. Use of suitable catalysts also can reduce the formation of chars and tars formed during the gasification process in SCW. Moreover, non-noble catalysts could be beneficial in terms of availability and cost. A kinetic study of SCW gasification is still under development due to the numerous intermediate and final products and complex reaction pathways.

In this research, supercritical water gasification (SCWG) and partial oxidation (SCWPO) of a model biomass compound was studied to produce hydrogen rich syngas at lower temperatures (400-500 °C). In this respect non-noble nickel catalysts were synthesized,

evaluated and characterized (fresh and spent) to study the catalyst role in SCWG. The catalysts studied were synthesized via incipient wetness impregnation of metal salts on synthesized θ -alumina nanofibers and commercial gamma alumina (converted to theta) pellets (3mm average diameter) as catalyst supports. To synthesize nano structured catalyst supports (alumina nanofibers); a one-pot sol-gel route in $scCO_2$ was adopted without using any hazardous organic solvents, surfactants or other additives for the first time. Aerogel nano catalysts were also directly synthesized via a sol-gel technique using isopropanol as solvent and supercritical carbon dioxide ($scCO_2$) as the drying agent.

In this research, it was found that introduction of oxidant after gasification is beneficial in terms of gaseous products and reducing the chemical oxygen demand (COD) in the liquid effluents. Another finding is that nickel (Ni) loading on alumina above 11 wt% consumed carbon dioxide with a simultaneous increase in methane attributed to hydrogen consumption by the methanation reaction. However, lanthanum (La) modified Ni/ θ - Al_2O_3 enhanced production of hydrogen by retarding the methanation reaction and promoting the water gas shift (WGS) reaction. In addition, adsorption of CO_2 , one of the main products, by La was attributed to shifting the reaction equilibrium to the products and thus contributed to enhance hydrogen production.

Nano catalysts showed higher activity towards hydrogen production, carbon gasification efficiency and total organic carbon (TOC) destruction in the liquid effluent compared to coarser heterogeneous catalysts. However, hydrogen production using aerogel catalysts where metals were loaded directly through sol-gel reaction was found comparatively less than nanofiber catalysts where metals were impregnated on the nano support. This phenomenon was attributed to the formation of Ni-La-Al-O nano structure complex by

direct addition of metals during sol-gel reaction. Unlike impregnated catalysts, incorporation of La to the main structure of the sol-gel derived catalysts could not contribute to enhance the WGS reaction.

The fresh and spent catalysts were characterized using different physicochemical techniques which revealed that the catalysts were active in SCW even though the metallic sites of nickel agglomerated when exposed to SCW conditions, oxidized and reacted with the support alumina. It was found that lanthanum retards the formation of graphitic coke, and adsorbed carbon dioxide during supercritical water gasification.

To our knowledge, hydrogen yield, total organic carbon destruction and gasification efficiency were significantly higher using La modified Ni/ θ -Al₂O₃ nano catalyst fibers than that of any other reported results of SCWG of any biomass compound at moderate temperatures (~500 °C) and pressures (~28 MPa). However, exposing the nanofiber catalysts to the SCW environment led to disintegration of the fibrous structure.

A global kinetic model for TOC destruction in supercritical water was developed using non-linear regression, which convincingly fit with the experimental results.

Key Words: Catalysis, Hydrogen production, TOC destruction, Supercritical water, Supercritical Carbon dioxide, Nanomaterials, Characterization of heterogeneous catalysts, Kinetics of TOC destruction.

Co-Authorship

Title: Supercritical water gasification and partial oxidation of glucose: Effect of Ni/Al₂O₃ catalysts on gaseous products and chemical oxygen demand destruction (Chapter 3).

Authors: Muhammad B.I. Chowdhury, Emhemmed A. Youssef , George Nakhla and Paul A. Charpentier.

The catalysts development, experimental works were conducted by Muhammad B.I. Chowdhury under the guidance of advisor Dr. Paul A. Charpentier. The experimental setup was implemented by Emhemmed A. Youssef and Muhammad B.I. Chowdhury. The liquid analysis was conducted by Emhemmed A. Youssef under supervision of Dr. George Nakhla. The draft of this manuscript was written by Muhammad B.I. Chowdhury and Emhemmed A. Youssef. Modifications were carried out under close supervision of George Nakhla and Paul A. Charpentier. The final version of this article was published by the journal of International Journal of Hydrogen Energy 35 (10), 5034-5042, 2010.

Title: Production of Hydrogen-rich gas through supercritical water gasification of glucose using La-modified Ni/Al₂O₃ catalysts (Chapter 4)

Authors: Muhammad B.I. Chowdhury and Paul A. Charpentier.

La modified Ni based heterogeneous catalysts (including nano catalysts) were developed and evaluated for supercritical water gasification by Muhammad B.I. Chowdhury. The drafts of this manuscript written by Muhammad B.I. Chowdhury and modifications were carried out under close supervision of advisor Dr. Paul A. Charpentier. The final version of this article was submitted to the journal Industrial Engineering and Chemistry Research.

Title: Characterization of nickel based catalysts used in supercritical water gasification of glucose. (Chapter 5)

Authors: Muhammad B.I. Chowdhury, Mohammad Mozahar Hossain, and Paul A. Charpentier.

Fresh and spent catalysts were characterized for determination of catalyst role in supercritical water gasification by Muhammad B.I. Chowdhury under close supervision of advisor Dr. Paul A. Charpentier. Dr. Mohammad Hossain actively helped in characterization and trouble shooting of characterization equipments. The draft of this manuscript was written by Muhammad B.I. Chowdhury and modifications were carried out by Dr. Mohammad M. Hossain and Dr. Paul A. Charpentier. The final version of this article was submitted to the journal Applied Catalysis A: General.

Title: Development of kinetic model for TOC destruction from supercritical water gasification of glucose. (Chapter 6)

Authors: Muhammad B.I. Chowdhury, Mohammad Mozahar Hossain, and Paul A. Charpentier.

A global kinetic model for TOC destruction in supercritical water was developed by Muhammad B.I. Chowdhury. Dr. Mohammad Hossain actively helped in MATLAB program development for non-linear regression of the model. The draft of this manuscript was written by Muhammad B.I. Chowdhury and modifications were carried out under close supervision of advisor Dr. Paul A. Charpentier. The final version of this article was submitted to the journal Industrial Engineering and Chemistry Research.

Title: One-Pot Procedure to Synthesize High Surface Area Alumina Nanofibers Using Supercritical Carbon Dioxide. (Chapter 7)

Authors: Muhammad B.I. Chowdhury, Ruhong Sui, Rahima. A. Lucky, and Paul A. Charpentier.

Alumina nanofibers as a catalyst support were synthesized in supercritical carbon dioxide without using any extra water, organic solvent, surfactant, chelating agent, or other additives by Muhammad B.I. Chowdhury under the guidance of advisor Dr. Paul A. Charpentier. Dr. Ruhong Sui was involved in XPS analysis and the schematic diagram alumina nanofiber structure. Dr. Rahima Lucky helped in experimental work and trouble shooting. The draft of this manuscript was written by Muhammad B.I. Chowdhury and modifications were carried out by Dr. Ruhong Sui and advisor Dr. Paul A. Charpentier.

The final version of this article was published by the journal the journal *Langmuir* 26 (4), 2707–2713, 2010.

Dedication

To my parents:

Muhammad Abu Bakkar Siddique Chowdhury
&
Mostaq Firun Nesa Chowdhury

Acknowledgements

First and foremost, I would like to express my heartfelt gratitude to my beloved deceased father Muhammad Abubakkar Siddique Chowdhury and mother Mostaq Firun Nesa Chowdhury for their cares and sacrifices for me throughout their whole life. I would like to thank my wife Sabiha, and daughter Manha. Throughout all my endeavors, their love, support, guidance and endless patience have been truly inspirational.

I would like to express my deepest gratefulness to my supervisor Professor Paul A. Charpentier for his continuous support, encouragements and guidance throughout this endeavor. His meticulous supervision not only ensured the successful fulfillment of this study but also brought great improvement of my comprehension skills, which I will enjoy for ever.

I would like to express my sincere gratitude to Professor Hugo De Lasa for his kind help and constructive advices during my research and permitting me to use his laboratory equipments. I gratefully acknowledge Professor Ajay Ray for his helpful guidance, discussion and encouragements.

I would like to acknowledge Dr. Mozahar Hossain for TPR, TPO, Chemisorption analysis, Dr. Pastor for TOC analysis, Dr. Richard Gardiner for TEM, Dr. Todd Simpson for SEM and Ms Kim Law for XRD, Mr. Gribbons for TGA analysis, Mr. Celeb for FTIR analysis.

I have been indebted to Dr. Ruohong Sui, Dr. Rahima Lucky, my former colleagues of the research group, for sharing their scientific and technical knowledge and experiences on initiating my research.

I would like to thank Canadian Foundation for Innovation and the Petro-Canada Young Innovator Award (P.A.C.) for financial support of the research.

Finally, I am grateful to my friends, brothers, sisters and parents-in-law, whose encouragements and supports have become my motivation to do and finish this work.

Table of Contents

Certificate of Examination	ii
Abstract and Keywords	iii
Co-Authorship	vi
Dedication	ix
Acknowledgements.....	x
Table of Contents	xi
List of Tables.....	xvii
List of Figures	xviii
Chapter 1	1
General Introduction.....	1
1.1 Background and Motivation.....	1
1.2. Selection of Technology	2
1.3. Selection of Catalysts	6
1.4. Synthesizing nano catalysts.....	8
1.5. Selection of Model Compound	9
1.6. Objectives.....	9
Chapter 2	12
Literature Review.....	12
2.1 Introduction	12
2.2 Supercritical water	13
2.3 Economic feasibility and current status.....	17

2.4 Thermodynamics and Chemistry.....	19
2.5 Kinetics	29
2.6 Challenges.....	32
2.7 Effects of process parameters	33
2.7.1 Effects of temperature	34
2.7.2 Effects of reaction pressure	39
2.7.3 Effects of residence time.....	40
2.7.4 Effects of solution concentration.....	41
2.8 Catalysis as a solution.....	42
2.8.1. Homogeneous catalysts.....	44
2.8.2. Heterogeneous catalysts.....	45
Chapter 3	49
Supercritical water gasification and partial oxidation of glucose: Effect of Ni/Al ₂ O ₃ catalysts on gaseous products and chemical oxygen demand (COD) destruction.....	49
3.1 Introduction	49
3.2. Materials and methods.....	52
3.2.1. Materials	52
3.2.2 Catalyst preparation.....	52
3.2.3 SCWG Apparatus.....	54
3.2.4 Experimental procedures.....	55
3.2.5 Gas & liquid analysis.....	57

3.2.6 Yield calculations	57
3.3 Results and discussions.....	58
3.3.1 Effect of oxygen to carbon molar ratio (MR) on gas and liquid products	58
3.3.2 Effect of temperature on gas and liquid product distribution	61
3.3.3 Effect of the commercial catalyst on gas and liquid product distribution.....	63
3.3.4 Effect of the synthesized catalyst loading on gas and liquid product distribution.....	66
3.4 Conclusions	68
Chapter 4	70
Production of hydrogen-rich gas through supercritical water gasification of glucose using La-modified Ni/Al ₂ O ₃ catalysts	70
4.1 Introduction	70
4.2 Experimental	76
4.2.1 Catalysts Synthesis	76
4.2.1.1 Incipient impregnation.....	76
4.2.1.2 Sol-gel technique	78
4.2.2 Catalyst Activity Tests in Supercritical Water	79
4.2.3 Products Analysis	80
4.3 Results and Discussion.....	81
4.3.1 BET Surface area, Pore size, Pore volume.....	81

4.3.2 Catalysts evaluation	83
4.3.2.1 Effects of types of catalysts	83
4.3.2.2 Effects of catalyst size	89
4.3.2.3 Effects of Oxidant	92
4.3.2.4 Effect of Residence Time and Temperature	94
4.3.2.5 Effect of Feed Concentration.....	97
4.3.2.6 Effects of TOC destruction on gaseous yield.....	99
4.3.3 Mechanistic Elucidation and Reaction Mechanism.....	100
4.4 Conclusions	103
Chapter 5	105
Characterization of fresh and spent Ni based catalysts used for supercritical water gasification.	105
5.1 Introduction	105
5.2 Experimental	108
5.2.1 Characterization Techniques	108
5.3 Results and Discussion.....	113
5.3.1 BET Surface area, Pore size, Pore volume.....	113
5.3.2 Temperature Programmed Reduction	115
5.3.3 H ₂ Pulse Chemisorption	122
5.3.4 Temperature Programmed Desorption	124
5.3.5 TGA Analysis	125
5.3.6 Raman Spectroscopy Analysis.....	128

5.3.7 XRD Analysis	129
5.3.8 Temperature Programmed Oxidation of Spent Catalysts.....	133
5.3.9 TEM analysis	134
5.3.10 Reaction mechanism	136
5.4 Conclusions	139
Chapter 6	141
Development of kinetic model for TOC destruction from supercritical water gasification of glucose.....	141
6.1 Introduction	141
6.2 Experimental method.....	146
6.3 Results and Discussion.....	148
6.3.1 Effect of Reaction Time and Temperature.....	148
6.3.2 Effect of Concentration	150
6.4 Reaction Kinetics of TOC destruction.....	151
6.4.1 Model one	152
6.4.2 Model two	156
6.5 Conclusions	159
Chapter 7	160
One-pot procedure to synthesis of high surface area alumina nanofibers in supercritical carbon dioxide	160
7.1 Introduction	160
7.2 Experimental	163

7.2.1 Materials	163
7.2.2 Preparation of Al ₂ O ₃	163
7.2.3 Characterization	164
7.3 Results and discussion	166
7.3.1 Synthesis of Nanofibers	166
7.3.1.1 Effects of Calcination on Nanostructure	173
7.3.1.2 Mechanism of Nanofiber Formation.....	180
7.4 Conclusions	184
Chapter 8	186
Conclusions and Recommendations.....	186
8.1 Conclusions	186
8.2 Recommendations.....	188
Bibliography.....	191
Appendices	212
Appendix A1: American Chemical Society’s Policy on reprinting published material in Theses and Dissertations.....	212
Appendix A2: Elsevier Policy on reprinting published material.....	215
Appendix A3: Matlab Program for non-linear regression of global kinetic model for TOC destruction.....	216
Curriculum Vitae	220

List of Tables

Table 1.1: Moisture content in several common biomass wastes.....	2
Table 1.2: A comparison of energy conversion efficiency of different options for biomass conversions	3
Table 2.1 Properties of Ambient Water, Steam, and Supercritical Water.	16
Table 2.2 Division of hydrothermal reaction by temperature of reaction	34
Table 2.3: Summary of the catalysts used in SCWG.....	46
Table 3.1. Physical properties of the synthesized catalysts.....	54
Table 3.2: Liquid effluent characteristics at 500 °C with commercial Ni/silica- alumina (63wt% Ni).....	66
Table 4.1. Physical properties of the synthesized catalysts.....	81
Table 5.1: Physiochemical properties of catalysts:	113
Table 5.2: Hydrogen chemisorption results for reduced catalysts.....	122
Table 7.1: Physiochemical properties of the synthesized alumina nanostructures at different conditions.....	167

List of Figures

Figure 2.1: Schematic phase diagram of water.	14
Figure 2.2: Density, static dielectric constant and ion dissociation constant (K_w) of water at 30 MPa as a function of temperature.....	15
Figure 2.3: Supercritical water gasification of glucose at $P= 28.0$ MPa and feed concentration of 0.6 M glucose.....	25
Figure 2.4: Effect of temperature on glucose gasification in SCW	26
Figure 2.5: Effect of pressure on glucose gasification in SCW.....	27
Figure 2.6: Effect of concentration on glucose gasification in SCW.....	28
Figure 2.7: Simplified reaction scheme of liquefaction and/or gasification of biomass model compound.	29
Figure 2.8: Effect of reactor temperature on 0.6 M glucose in supercritical water at 28 MPa and 30 s reactor residence time	36
Figure 3.1: Schematic diagram of the SCWO batch unit.	55
Figure 3.2: Oxygen to carbon molar ratio (MR) effect on gas yield in the non- catalytic partial oxidation at 400 °C.	59
Figure 3.3: Liquid effluent characteristics in the non-catalytic partial oxidation at 400 °C.....	60
Figure 3.4: Temperature effect on gas yield in the non-catalytic partial oxidation.....	61
Figure 3.5: Liquid effluent characteristics in the non-catalytic partial oxidation.....	62

Figure 3.6: Effect of commercial catalyst on gas yield at 500 °C.....	63
Figure 3.7: Effect of nickel loading on gas yield at 500 °C.....	67
Figure 3.7: Effect of nickel loading on liquid effluent at 500 °C.....	68
Figure 4.1: Block diagram of catalyst synthesis.....	78
Figure 4.2: Effect of Ni loading on theta alumina pellets.	84
Figure 4.3: Effect of Ni, La ₂ O ₃ and Ni-La ₂ O ₃ on theta alumina pellets	85
Figure 4.4: Effect of Ni, La ₂ O ₃ and Ni-La ₂ O ₃ on carbon gasification efficiency and TOC destruction.....	88
Figure 4.5: Effect of catalysts (Ni-La ₂ O ₃ /Al ₂ O ₃) size on gaseous products.	89
Figure 4.6: Effect of catalysts (Ni-La ₂ O ₃ /Al ₂ O ₃) size on TOC conversion and CGE	91
Figure 4.7: Effect of oxidant on gaseous products.	93
Figure 4.8: Effect of oxidant on TOC conversion and CGE.....	94
Figure 4.9: Effect of time and temperature on gaseous products..	95
Figure 4.10: Effect of time and temperature on TOC conversion and CGE... ..	96
Figure 4.11: Effect of time and temperature on gaseous products and TOC conversion and CGE.....	97
Figure 4.12: Effect of feed concentration on gaseous products and TOC conversion and CGE.....	98
Figure 4.13: Effect of TOC destruction on gaseous products..	99
Figure 5.1: TPR profile of fresh catalyst.	116
Figure 5.2: TPR profile of spent catalysts.....	118

Figure 5.3: TPR profile of fresh nano catalysts.	119
Figure 5.4: TPR profile of spent nano catalysts.....	120
Figure 5.5: Metal percent reduction.....	121
Figure 5.6: Temperature programmed desorption profile.....	125
Figure 5.7: TGA Analysis of fresh and spent catalysts.	127
Figure 5.8: Raman spectra of the coke of spent catalysts.	129
Figure 5.9: XRD patterns of fresh and spent catalysts	130
Figure 5.10: Reaction time effect on XRD patterns.....	131
Figure 5.11: XRD patterns of fresh and spent nano catalysts	132
Figure 5.12: Temperature programmed oxidation profile spent catalysts...	133
Figure 5.13: TEM images of fresh and spent catalysts	135
Figure 6.1: Effect of time and temperature on TOC conversion and CGE... 149	
Figure 6.2: Effect of extended time on TOC conversion and CGE.	149
Figure 6.3: Effect of feed concentration on TOC conversion and CGE.	150
Figure 6.4: Plot $-\ln([TOC]/[TOC]_0)$ against residence time for TOC decomposition in SCWG.	153
Figure 6.5: Assumed first order Arrhenious plot for TOC decomposition in SCWG	154
Figure 6.6: Comparison of the TOC conversion between experimental data and predicted values by model one.	155
Figure 6.7: Comparison of the TOC conversion between experimental data and predicted values by model two	159

Figure 7.1: Experimental supercritical carbon dioxide set up.	163
Figure 7.2: SEM and TEM images of nanoscale alumina particles with varying synthesis temperatures.....	169
Figure 7.3: N ₂ adsorption/desorption isotherms and pore-size distributions of nanostructured alumina	170
Figure 7.4: SEM images of nanoscale alumina particles at varying synthesis conditions in scCO ₂ at 80 °C.....	172
Figure 7.5: SEM images of calcined (600 °C) nanoscale alumina particles at varying synthesis conditions in scCO ₂ at 80 °C.....	173
Figure 7.6: SEM and TEM images of alumina nanofibers calcined at varying temperatures	174
Figure 7.7: Calcination effect on N ₂ adsorption/desorption isotherms and pore-size distributions of alumina nanofibers..	175
Figure 7.8: TGA-DTA analysis of alumina nanofibers.....	176
Figure 7.9: FTIR analysis of as prepared and calcined samples.....	178
Figure 7.10: XRD analysis of as prepared and calcined samples.	179
Figure 7.11: XPS Analysis of as prepared alumina nanofiber.	181
Figure 7.12: Schematic diagram of the structure of the linear macromolecule with a repeating unit of Al(OH)(CH ₃ CO ₂) ₂	182

Chapter 1

General Introduction

1.1 Background and Motivation

Disposal of hazardous agricultural and industrial organic biomass waste generated from feedlots and food processing operations has received worldwide concern in light of environmental and health concerns with diminishing land resources. The major sources of biomass are agriculture and forest biomass, forestry residues, food processing residues, industrial wastes, municipal sewage and household garbage. As one example, direct application of livestock manure for soil amendment causes contamination of surface and groundwater, and emission of methane gas and nitrous oxide, two potent greenhouse gases. In Ontario, Canada, the recent promulgation of the Nutrient Management Act, jointly by OMAFRA and the Ontario Ministry of Environment (MOE) has led to a limited availability of land for disposal of municipal and agricultural wastes. This not only results in higher disposal costs but also may seriously hamper industrial growth.

Agricultural waste contains up to 95% water¹ whereas municipal waste contains approximately 80% water and 20% dry solid², 75% of this solid is organic matter². Conversion of such waste streams to valuable fuels and chemicals using conventional techniques such as pyrolysis or catalytic gasification would be energy intensive and costly due the excessive drying costs. Society's need for new sources of green energy, while treating challenging and hazardous waste streams that are polluting the environment has resulted in the opportunity for new technologies to emerge.

1.2. Selection of Technology

A major problem of biomass is high moisture content (Table 1.1), which is generally more than that from solid fossil fuels. As well, sewage may have moisture contents exceeding 90 wt%³. Direct combustion would require drying of the biomass that would drastically lower the net energy production.

Table 1.1: Moisture content in several common biomass wastes.⁴

Biomass type	Moisture (% wet basis)
Wheat straw	8-20
Sawdust	25-55
RDF pellet	25-35
Wood bark	30-60
Corn stalk	40-60
Rice straw	50-80
Food waste	70
Cattle manure	88
Water hyacinth	95.3

As shown in Table 1.2, at above 31% moisture content, the energy conversion efficiency of supercritical water gasification is always higher than that of thermal gasification, pyrolysis, liquefaction, and anaerobic digestion⁵.

Table 1.2: A comparison of energy conversion efficiency of different options for biomass conversions (Data from Yoshida et al.⁵).

Moisture content in feed	5%	31%	55%	75%
Biomass conversion processes	Energy conversion efficiency (%)			
Thermal gasification	61	55	47	27
Pyrolysis	57	53	45	27
Liquefaction	39	37	36	34
Anaerobic digestion	31	31	31	31
Supercritical water gasification	55	55	55	55

Gasification of biomass in supercritical water offers an attractive alternative to avoid the energy intensive drying process, particularly when the water content is above 30%⁶. Supercritical water gasification (SWG) and supercritical water partial oxidation (SWPO), potentially offers a solution, producing syn gas; especially methane or hydrogen rich gases depending on the operation conditions and catalysts. This state of the art technology is expected to be a significant breakthrough in waste-to-energy power generation. This process exhibits unparalleled environmental compliance capabilities, without the need for a pollution-abatement system.

Compared to other biomass thermochemical reforming processes, supercritical water reforming has a high gasification efficiency and operates at a lower temperature⁷. The main advantages are: since the solvent is water, the thermal efficiency is not affected by biomass humidity; a hydrogen rich gas can be produced by driving the water gas-shift reaction ($\text{CO} + \text{H}_2\text{O} \rightarrow \text{CO}_2 + \text{H}_2$); reaction proceeds in a homogeneous medium

inhibiting tar formation; the product is compressed to about 30 MPa, avoiding additional work for compression of gases and the hydrogen flammability is drastically reduced by water. Supercritical water (SCW) possesses physical properties that are very different from those of liquid water under ambient conditions. The dielectric constant of SCW is much less than that of ambient water (80 at room temperature to 2.5 at 450 °C at 30 MPa⁸) with the hydrogen bonding being much weaker. Therefore, SCW behaves like an organic solvent and is completely miscible with organic materials. Thus with SCW it is possible to conduct reactions with organic compounds in a single fluid phase which would otherwise occur in a multiphase system under conventional conditions. The high diffusivity of SCW (diffusion coefficient is about 100 times higher than ambient water⁹) can significantly enhance mass transfer. SCW can reduce coke formation on the catalyst as it is a good solvent for the intermediate coke precursors¹⁰. Hence, gasification of biomass in SCW has many advantages including high gasification efficiency and a high yield of hydrogen⁷.

However, many major difficulties exist, although formation of char and tar are much less than that of conventional processes, still plugging and formation of chars and tars during biomass gasification is a major concern. Chars come from non-converted biomass, while tars are unwanted reaction products. Chars are linked to the conversion yields of the process while tars are usually formed by the pyrolysis of organic molecules. Char and tar can be minimized by partial oxidation to enhance the gasification process and the resulting yield of hydrogen¹¹. Although the formation of char and tar are much lower than conventional processes, the complete removal of chars and tars has not yet been reported. Catalysts have the advantage of helping on both the conversion yield and solving the

plugging problem caused by the presence of char and tars. That is one of the reasons why it has been considered by several researchers.

For hydrogen rich gas production by gasification of biomass, high activation energy i.e. high temperatures¹² (above 600 °C) are required. To sustain high temperature processes, a supply of external energy is needed. This is one of the major shortcomings of the high temperature process. In order to moderate the condition (reducing reaction temperature) of SCWG, and to reduce investment and equipment cost, one available means is to reduce the activation energy by adding a suitable hydrothermal catalyst.

On the other hand, Peterson et al.¹² concluded that obtaining the thermodynamic equilibrium gas composition below 600 °C is not possible. Therefore, for low temperature processes reduction of activation energy with the use of catalysts becomes vital. However, lower temperatures are also more suitable for the production of methane¹². Methane, which is one of the main products of SCW gasification, is very stable in SCW and is not converted into any smaller molecules¹³. The production of methane could be high in the intermediate temperature range of 374-500°C¹². Temperature also affects the tar yield (in the liquid effluent) during SCWG. At low temperatures (<600°C), yellowish and a thin layer of a dark brown, oil-like tar has been observed in the liquid effluent^{3, 14}. However, clear water was observed at 650°C^{3, 14}. In addition, some organic intermediates may form solid coke (char), which is not a thermodynamically stable product, and has a low reactivity at low temperatures (<600°C)¹². The gasification step must be very fast to avoid the formation of polymeric materials and eventually char.

Therefore the use of suitable catalysts is required to reduce the methanation reaction while breaking the tars and retarding the formation of char at lower temperatures.

1.3. Selection of Catalysts

As a solution for SCWG, catalysts must both decrease the amount of formed tars and chars and increase the proportion of hydrogen in the synthesized gas. Homogeneous materials like alkali catalysts are readily miscible with water and have been found very effective for biomass gasification. Lu et al.⁷ used K_2CO_3 for biomass gasification in SCW and found the H_2 yield two times higher than that without catalyst under the same conditions. Watanabe et al.¹⁵ studied the effect of both base (NaOH) and metal (ZrO_2) catalysts on the gasification of lignin in SCW. NaOH proved 2-5 times more effective than ZrO_2 for hydrogen production. However, alkali catalysts recovery, re-use and corrosion problems are still the main concerns with these types of catalysts¹⁶.

In this regard, Hao et al.¹⁷ compared the performance of five types of metal catalysts: 5 wt% Ru on activated carbon, 5 wt% Pd on activated carbon, CeO_2 particles, nano- CeO_2 and nano- $(CeZr)_xO_2$ during the gasification of cellulose at 500 °C at 27 MPa. The Ruthenium based catalyst gave the best performance with the highest yield of hydrogen and methane, while the others had a similar level of performance. For SCWG of glucose, Byrd et al.¹⁸ evaluated the Ru/Al_2O_3 at 700 °C and found a high a yield of H_2 with low CO and CH_4 , while Osada et al.¹⁹ found CH_4 rich gas at 400 °C.

Although Ru shows very good activity for gasification, Ru catalysts can be poisoned by even a trace amount of S²⁰. Pt group noble metals are also prone to the methanation reactions of carbon oxides (equation 1.1 and 1.2) in the presence of hydrogen, which

increases with an increase of temperature²¹. Noble metals are mainly used for preferential methanation of carbon monoxide^{21,22}. Typical methanation reactions can be written as:



Furthermore, the relatively high price of noble metals makes these catalysts less attractive if suitable low cost heterogeneous catalysts can be utilized, particularly for low cost energy production processes.

Nickel is a commonly used catalyst for SCW gasification with Furusawa et al.²³ finding that carbon and hydrogen yields increased from 8.3% and 14.1% to 22.7% and 46.2% respectively when 0.05 g of 20 wt% Ni/MgO catalyst was added at 400 °C. The reduced nickel catalyst was found to enhance the gasification under SCW conditions. A nickel catalyst is also known to be favorable for cracking tar molecules and promoting the WGS reaction²⁴. Savage and Resende²⁵ reported that nickel and copper provided higher gas yields compared to Ru and Rh. When compared to the available alternative catalysts, nickel displays several favorable attributes including high activity and low cost.

Lanthanum (La) may increase a catalyst stability as well as enhance the water gas shift reaction like cerium (Ce)²⁶. La and Ce have very similar chemical properties with respect to cation charge, ionic radii, and the stability of organic and inorganic complexes²⁷. Kim previously found that cerium acts as a promoter of the WGS reaction while investigating the removal of CO with non-noble metal oxide²⁶. The stability of Ni/La₂O₃ was observed in methane reforming with CO₂²⁸. It was previously shown to remain active and stable even after 150h of conventional steam reforming of ethanol²⁹. That study also showed that complete ethanol conversion was achieved with contact times higher than ca. 0.1g s

cm⁻³ and was highly selective (ca. 95%) towards hydrogen²⁹. In this regard, Ni on La₂O₃/Al₂O₃ may be a favorable catalyst for supercritical water gasification. La₂O₃ also might be active and stable in SCW, while also having a high melting point (2315°C).

Thus, the use of catalysts seems to be one of the key points for gasification in supercritical water, both towards lowering the amount of residual chars and tars while increasing the proportion of hydrogen in the synthesized gas.

However, the catalyst role in SCWG is still poorly understood due to the unusual properties of SCW and a lack of detailed characterization of fresh and spent catalysts. The published literatures mostly reported the catalyst's activity by product evaluation in SCWG/SCWO. A recent review of catalytic hydrogen production from biomass in SCW by Guo et al.³⁰ showed activity tests of noble and non-noble catalysts and a possible mechanism of Ru and acid-base catalysts activity for hydrogen production. This review also lacks details on catalyst characterization which are required to evaluate the effectiveness of each catalyst and also to provide specifications for future products.

1.4. Synthesizing nano catalysts

Conventional catalysts have low surface areas per unit volume which limits the contact area between the reactants and the metallic surface of the catalysts. Nano catalysts with high surface areas and aspect ratios can help to eliminate this challenge. Supercritical carbon dioxide (ScCO₂) can be used as a green solvent to synthesize nano materials³¹⁻³⁴. In this research, ScCO₂ is adopted to synthesize nano structured catalyst supports without using any hazardous organic solvents, surfactants or other additives. The nano support was then used for impregnation of catalyst development for SCWG. Another approach

for nano catalyst synthesis was direct addition of active metals to the support during sol-gel reaction using isopropanol as solvent and ScCO_2 as drying agent. In this approach, metal oxide aerogel was synthesized.

1.5. Selection of Model Compound

Using a model compound for a feedstock provides several advantages including making it easier to understand the basic chemical pathways occurring during conversion in an unusual reaction medium such as supercritical water.

Biomass is typically composed of cellulose, hemicellulose, lignin, and other organic and inorganic components. Cellulose is known as one of the most unmanageable components for dissolving in hot water³⁵. The complete conversion of cellulose to glucose and its oligomers can be achieved at temperatures as high as 400 °C in supercritical water conditions³⁶. Therefore glucose ($\text{C}_6\text{H}_{12}\text{O}_6$) serves as a model compound for the more complex sludge and cellulosic wastes for gasification in supercritical water.

1.6. Objectives

The main purpose of this research is to provide a quantitative mechanistic understanding of the destruction of wet organic matters so that no other apparatus is necessary for the further treatment of liquid effluent while producing hydrogen-rich gas at comparatively low temperatures using non-noble catalysts. This understanding is vital for the practical application of organic waste treatment, energy recovery from waste, and a cost analysis of the supercritical water gasification process. Another goal of this research is to gain a detailed structural picture of the catalysts used in SCW and thus to develop a better

understanding of the function of the catalysts and to provide guidance in synthesizing new and improved catalysts. From the engineering perspective, development of a global kinetic model can guide the reactor design for real life application which has not yet been developed.

The objectives of this research can be divided as follows:

- Production of hydrogen rich gas from a model compound of waste biomass.
- Destruction of total organic compounds (TOCs) in the liquid effluent so no subsequent treatment is necessary.
- Synthesis of non-noble heterogeneous catalysts (Ni based catalysts).
- Synthesis of high surface area nano catalysts without using environmentally hazardous solvents, additives or surfactants.
- Evaluation of the impact of the synthesized catalysts in a 600 ml reactor constructed by Autoclave Engineers by Hastelloy C-276.
- Gaining the structural picture of the synthesized fresh and spent catalysts for SCWG by using different physical and chemical characterization techniques including TPR, TPO, TPD, chemisorptions, Raman, SEM, TEM, FTIR, TGA, BET and XRD analysis.
- Development of a global kinetic model which could be a fundamental tool for the potential industrial reactor design.

Other than the objectives mentioned above, the following objectives are also considered to have been achieved:

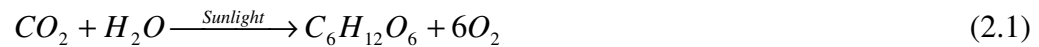
- Retardation of the methanation reaction at comparatively lower temperatures and thus improving hydrogen selectivity.
- Adsorption of CO₂, one of the main gaseous products of supercritical water gasification, to shift the equilibrium towards product while increasing the desired product selectivity.
- Increasing the water gas shift reaction to maximize hydrogen production.
- Avoiding the formation of intermediate polymeric materials that eventually leads to the formation of char or coke.

Chapter 2

Literature Review

2.1 Introduction

Biomass is the organic material coming from plants which contains stored energy from the sun through photosynthesis.



The chemical energy in plants gets passed onto animals and people through the food chain. This chemical energy also gets passed onto agricultural and industrial wastes, municipal sewage and household garbage. One of the better means of utilization of biomass resources involves converting the biomass waste into fuel gases. There are several potential options to convert solid biomass into gases as follows:

- Thermal gasification
- Pyrolysis
- Anaerobic digestion
- Supercritical water gasification (SCWG)

The total energy conversion efficiency is reduced as the moisture content of the biomass feed increases, except for anaerobic digestion and supercritical water gasification processes (Chapter 1, Table 1.2). This is primarily due to the increasing amount of energy consumed in drying the feedstock. In supercritical water gasification, water does not have to be removed as it serves as both the solvent and as a hydrogen donor. Thus the drying

problem can be avoided using SCWG. Similar to SCWG, the conversion efficiency of an anaerobic digestion route (31%) is insensitive to the moisture content in biomass, but its efficiency is well below that of SCWG. Above moisture contents of $\approx 31\%$, the conversion efficiency of supercritical water gasification is always higher than that of other processes⁵ (Chapter 1, Table 1.2).

Under supercritical water conditions, waste feed is quickly and efficiently converted to hydrogen, carbon oxides, water and salts with negligible production of NO_x , or SO_x . Supercritical water oxidation (SCWO) is well known to have the ability to treat hazardous and toxic chemicals such as chemical warfare agents³⁷.

2.2 Supercritical water

A supercritical fluid is defined as a substance at a temperature and pressure above its critical point. Figure 2.1 shows the phase diagram of water. The critical point specifies the conditions at which a phase boundary ceases to exist. Along the equilibrium line, as temperature and pressure increase, the liquid density decreases and vapor density increases until the two reach the critical point. Above that point, the fluid becomes a single supercritical phase with properties in between those of a gas and a liquid. Water above its critical point ($T_c = 374^\circ\text{C}$, $P_c = 22\text{MPa}$)³⁸ has physical properties such as density, dielectric constant, dissociation constant, and viscosity that undergo dramatic changes.

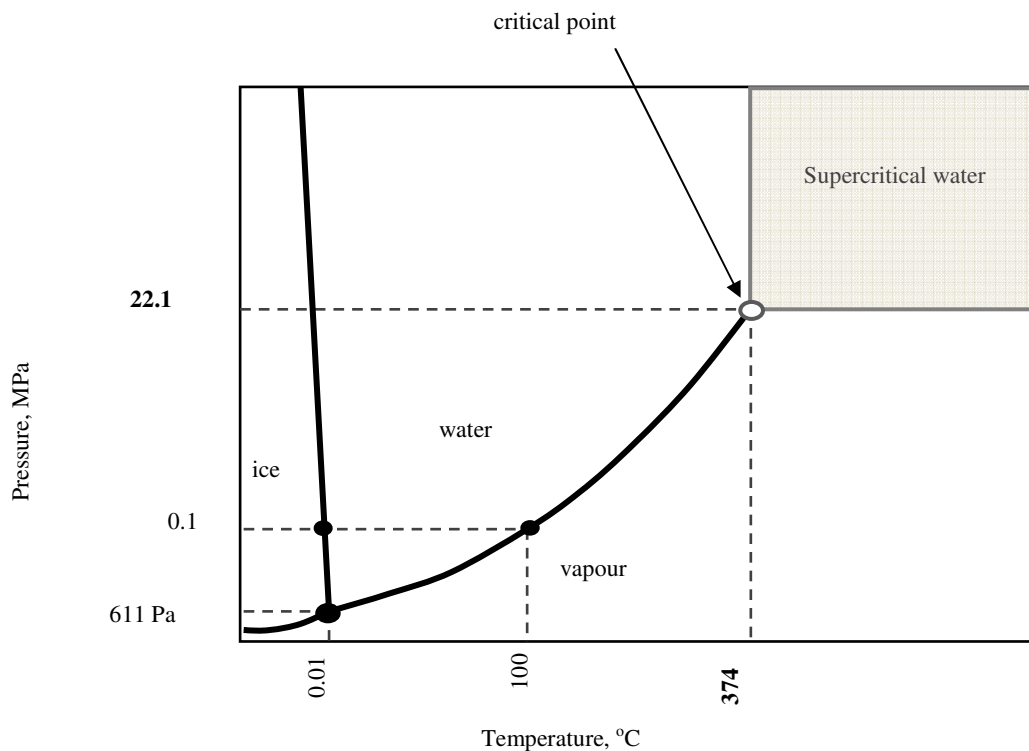


Figure 2.1: Schematic phase diagram of water.

Figure 2.2 illustrates the change in density, dielectric constant, and dissociation constant as a function of temperature at a constant pressure of 30 MPa. The density of supercritical water is about one-tenth that of ambient water. This very low density allows greater spacing between water molecules and much less effective hydrogen bonding. As a result, SCW has very little capacity to shield ions. The dielectric constant decreases from 80 at room temperature to 2.5 at 450 °C and 1.2 at 650 °C. This range of dielectric constants is similar to the values of typical nonpolar hydrocarbon solvents such as hexane 1.88, benzene 2.3, toluene 2.38, and chloroform 4.81. Again as seen in Figure 2.2, at 30 MPa the ionic dissociation constant (K_w) first increases from 10^{-14} to 10^{-11} just below 350 °C and then decreases by five orders of magnitude or more above 500 °C. The ion product, or self-ionization constant, is defined as the product of the concentrations of the acidic

and basic forms of water, $K_w = [\text{H}_3\text{O}^+][\text{OH}^-]$, in units of $\text{mol}^2 \text{kg}^{-2}$. With a low dielectric constant and low ionic dissociation constant, ionic species, namely inorganic salts, are practically insoluble in supercritical water. Additionally, SCW has a high diffusivity and low viscosity³⁹.

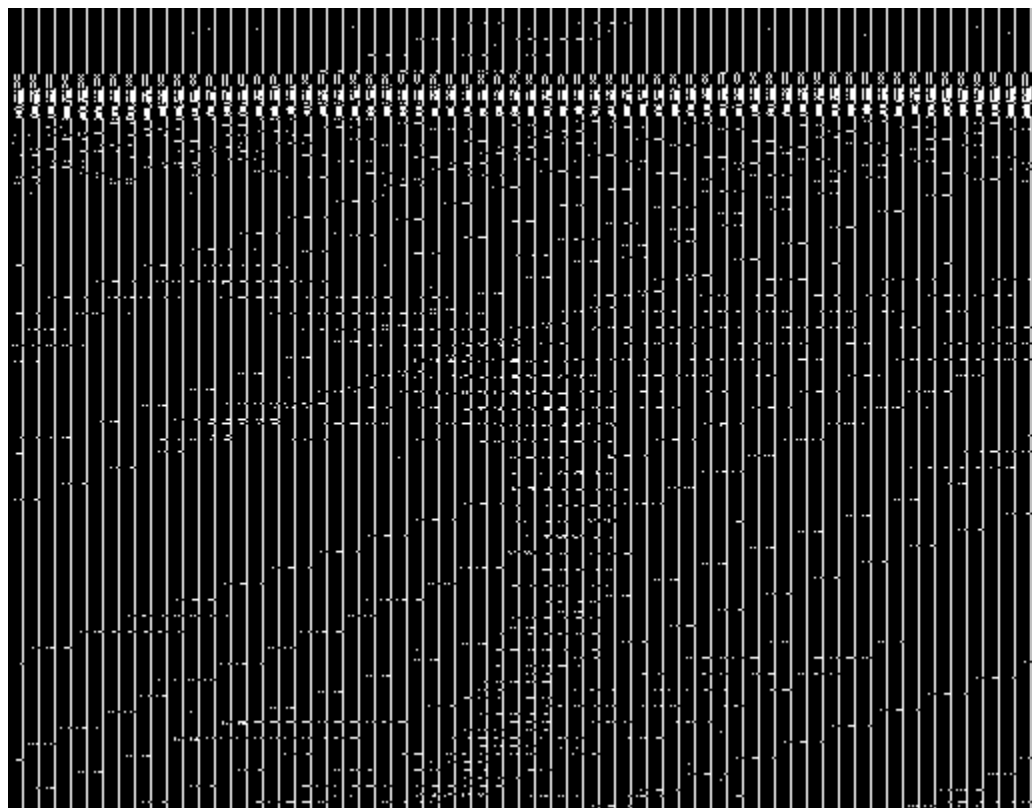


Figure 2.2: Density³⁸, static dielectric constant⁸ and ion dissociation constant (K_w)⁴⁰ of water at 30 MPa as a function of temperature.

One important property of SCW is that there exists almost no mass transfer limitation. Generally any catalytic reactions are mass-transfer limited due to the high reaction rates, low diffusion rates, and poor fluid flow characteristics. Table 2.1 compares the water properties for ambient water, supercritical water and superheated steam⁹. A highly effective diffusion coefficient of supercritical water (about 100 times higher than ambient

water) diminishes the chance of a mass-transfer gradient developing in a catalyst internal surface area⁹. The low density and viscosity of SCW enhances the particle Reynolds number and effective diffusion coefficient. A catalyst particle Reynolds number ($N_{Rep} = ud_p\rho/\mu$) is defined as the ratio of inertial forces to viscous forces along the particle. Dautzenberg⁴¹ suggested that a particle Reynolds number of 10 would prevent external mass-transfer limitations. The particle Reynolds number criterion is easily met for both SCW and superheated steam scenarios. Similarly, the degree of internal or pore diffusion limitation is often represented by the Thiele modulus, ϕ . Values much lower than unity indicates that pore-diffusion limitations do not exist in the catalyst.

Table 2.1 Properties of Ambient Water, Steam, and Supercritical Water⁹.

Fluid	Ambient water	Supercritical water	Superheated steam
Typical Conditions			
Temp. (°C)	25	450	450
Pressure (psia)	14.7	4000	200
Properties and Parameters			
Dielectric constant	78	1.8	1.0
Hydrocarbon solubility (mg/L)	variable	∞	variable
Oxygen solubility (mg/L)	8	∞	∞
Density, ρ (g/cm ³)	0.998	0.128	0.00419
Viscosity, μ (cp)	0.89	0.0298	2.65×10^{-5}
Particle Reynolds no. Rep	18.5	553	622
Effective diffusion coeff. D_e (cm ² /s)	7.74×10^{-6}	7.67×10^{-4}	1.79×10^{-3}
Thiele modulus, ϕ	2.82	0.0284	0.0122

The overall result of these properties is that supercritical water acts as a non-polar dense gas that has solvation properties similar to those of low polarity organic solvents. Hence, hydrocarbons and gases (e.g O₂, N₂, CO₂ etc.) are highly soluble and usually completely miscible under typical SCWG operating conditions. The lower solubility of ions and lower activities of H⁺ and OH⁻ cause reactions to proceed via free radical pathways rather than ionic pathways. Due to higher diffusion constants and lower viscosities, mass transfer limitations are much lower than those from liquid water. Even pore diffusion limitations in catalysts can be avoided using supercritical water.

2.3 Economic feasibility and current status

The supercritical water gasification process is still in the early stages of development. Experimental research based on bench scale reactors are presently being examined at several universities and research centers. Yoshida et al.⁵ compared the efficiency and carbon dioxide emissions among various biomass conversion methods to determine the energy flow from biomass resources to electricity, automobile fuels and heat. The supercritical water gasification combined cycle was found to be the most efficient option for biomasses having high moisture content. Matsumara⁴² evaluated biomass gasification in supercritical water from the point of view of energy, environmental and economic aspects. He assumed the system is energetically independent, and no environmentally harmful material should be released and that carbon dioxide should be removed from the product gas. For supercritical water gasification he found the energy efficiency to be 64.8%, the cost of product gas 3.05 yen/MJ (0.0342CAD/MJ) which is 1.86 times higher than city gas in Tokyo (1.64 yen/MJ), CO₂ payback time is 4.19 years. This study found that supercritical water gasification is a practical process for decreasing carbon dioxide

emissions, and is more advantageous compared to biomethanation. Gasafi et al.⁴³ conducted an economic analysis of sewage sludge gasification in supercritical water for hydrogen generation using the total revenue requirement (TRR) method. The calculated cost of hydrogen production and the revenues obtained from the disposal of sewage sludge for the TRR were determined. They found that in the case of 211€ t⁻¹_{dry matter} (\$270 t⁻¹_{dry matter}) from sewage sludge disposal, that hydrogen production costs are similar to those from natural gas reforming. If average revenues are assumed to be obtained from sewage sludge disposal 245€ t⁻¹_{dry matter} (\$314 t⁻¹_{dry matter}), the costs of hydrogen production is 2.3€ GJ⁻¹ (\$2.95GJ⁻¹). They found that the production costs of hydrogen as a secondary fuel are closely coupled with the fuel costs (primary energy costs) in conventional processes. The primary energy costs increase the medium and long term production, whereas gasification of sewage sludge costs play only a minor role. Moreover, the sewage sludge disposal is associated with negative costs (revenues). Consequently, the sewage sludge gasification in supercritical water is a cost effective process. Concentrated carbon dioxide evolved from the supercritical water gasification can be further used, such as in the beverage industry.

Commercial application of SCWG has not yet occurred. The pilot plant VERENA is one of the largest SCWG units in operation with a capacity of 100kg/h⁴⁴. This experimental facility using agricultural matter as feedstock has an operating capacity to 35MPa and 700 °C, while the usual operating condition is 28MPa and 660 °C⁴⁴. To improve efficiency of SCWG, studies on the effect of operating parameters, reaction kinetics and thermodynamic analysis are required.

2.4 Thermodynamics and Chemistry

Thermodynamic analysis of biomass gasification can provide a theoretical basis for the design, optimization and operation of a system where the energy efficiency is important⁴⁵. A system is in equilibrium when there is no tendency in thermal, mechanical, chemical and phase changes within the system. These conditions are met only when there is no heat transfer from one location to another, no unbalance of forces between parts of the system, or no chemical reaction or any transfer of mass between the various phases in the system.

The equilibrium composition and thermodynamic limits of gasification of biomass in supercritical water can be predicted using equilibrium models. For process design, evaluation and improvement, an equilibrium model can serve as a guide. Generally two approaches are adopted for equilibrium modeling:

1. Stoichiometric
2. Non-stoichiometric.

A clearly defined reaction mechanism including information on the reaction rates of all chemical reactions and species involved is required for the stoichiometric approach. Within the given residence time, the chemical reactions are not sufficiently fast to reach equilibrium in most gasification processes⁴⁶. Moreover, the stoichiometric approach gives the limiting conditions for a known gasification reaction rather than the true composition of the product gas.

On the other hand, the non-stoichiometric method requires information only on the reaction temperature, pressure and an elemental composition of the feedstock, which may

be available directly from the ultimate analysis of the feed. The non-stoichiometric approach is suitable for reactions whose mechanism is complex or less clear, for example hydrogen production from biomass gasification in SCW.

Both chemical equilibrium and phase equilibrium problems have to be solved for in the design of a SCW gasifier. Minimization of the Gibbs free energy can be one of the most effective means to solve these problems. This is based on the principle that at an equilibrium state, the total Gibbs free energy of a system is minimized subject to molar balance constraints.

This approach has been successfully used for conventional thermal gasification in air i.e. oxygen⁴⁷. The situation is different using supercritical water gasification than with conventional gasification. This is because in the equation of state for the mixture, the fugacity of each species is a relatively complex function of pressure, temperature and mixture composition. Thus, it is beyond the scope of most commercial software packages for equilibrium calculation⁴⁸. The non-stoichiometric equilibrium based on Gibbs free energy minimization approaches used by researchers for supercritical water gasification is described as follows.

Based on Gibbs free energy minimization, Lu et al.⁴⁵ and Tang and Kitagawa⁴⁸ performed chemical equilibrium analysis for the production of hydrogen from biomass gasification in SCW. Yan et al.⁴⁹ also used a non-stoichiometric approach to predict the performance of hydrogen production in SCW based on Gibbs free energy minimization.

Let us consider a system of fixed mass with uniform temperature and pressure. In the absence of kinetic and potential energy, the energy balance is:

$$dU = dQ - dW \quad (2.2)$$

$$dU = dQ - PdV \quad (2.3)$$

For irreversible processes:

$$dS \geq \frac{dQ}{T} \quad (2.4)$$

$$dQ \leq T dS \quad (2.5)$$

Eliminating dQ between equations (2.3 and 2.5):

$$TdS - dU - PdV \geq 0 \quad (2.6)$$

We know,

$$G = H - TS \quad (2.7)$$

$$H = U + PV \quad (2.8)$$

The Gibbs function can be written as follows:

$$G = U + PV - TS \quad (2.9)$$

Differentiating both sides of equation (2.9) gives:

$$dG = dU + PdV + VdP - TdS - SdT \quad (2.10)$$

$$dG - VdP + SdT = - (TdS - dU - PdV) \quad (2.11)$$

From equation 2.9 and 2.11, we get

$$dG - VdP + SdT \leq 0 \quad (2.12)$$

For a system with constant temperature and pressure, we get

$$dG \leq 0 \quad (2.13)$$

Equation 2.13 indicates that the Gibbs energy of a system always gets very small during an irreversible process. This brings the system close to equilibrium which reaches equilibrium at minimum Gibbs energy.

At equilibrium, the total Gibbs free energy must be minimized. Therefore,

$$dG = 0 \quad (2.14)$$

The equation of element conservation also should be satisfied at equilibrium:

$$\sum_{i=1}^N a_{ki} n_i = b_k^0, \quad k = 1, 2, 3, \dots, M \quad (2.15)$$

where a_{ki} = molar number of element k in compound i , and b^0 = total molar number of element in the initial reactant.

The Gibbs free energy of a system involving several species, i with number of moles, n_i in the mixture is:

$$G = \sum_i^{i=K} n_i \mu_i \quad (2.16)$$

If at unity pressure, the reference state is set, the chemical potential for species i can be calculated as

$$\mu_i = \mu_i^0 + RT \ln f_i \quad (2.17)$$

At a certain temperature and pressure, the number of moles of each species in the system can be calculated by optimization, until the calculation reaches the minimum Gibbs free energy.

The fugacity coefficient of component i , ϕ_i , can be expressed as:

$$\ln \phi_i = \int_V^{\infty} \left[\frac{1}{RT} \left(\frac{\partial P}{\partial n_i} \right)_{T,V,n_{j \neq i}} - \frac{1}{V} \right] dV - \ln Z \quad (2.18)$$

The fugacity can be calculated from the relation as follows:

$$\phi_i = \frac{f_i}{P} \quad (2.19)$$

An equation of state is needed to evaluate the integral equation 2.18. The ideal gas law equation of state can be misleading providing erroneous results, as at high pressure the mixture is non-ideal. Due to non-idealities, different researchers have used the following equations of state to solve the above problem.

1. Van der Waals equation of state
2. Peng-Robinson (PR) equation of state
3. Statistical association fluid theory (SAFT) equation of state
4. Soave-Redlich-Kwong (SRK) equation of state
5. Duan's equation of state

Antal in 1978 predicted complete gasification with hydrogen rich gas product by steam reforming of cellulose in a high excess of water above 600 °C⁵⁰. Glucose is considered as the model compound of biomass for thermodynamic analysis to make the stoichiometry easier. Complete conversions of glucose to H₂ or CH₄ are the limiting steps of the reaction.

Formation of hydrogen



Formation of methane



The strong variation of reaction enthalpies of H₂ and CH₄ formation is attributed to the gas composition variation as a function of temperature. Equation 2.20 is endothermic while equation 2.21 is slightly endothermic⁴⁵. From equation 2.20, it is seen that water is not only the solvent but is also a reactant with hydrogen in the water being released by the gasification reaction. According to Le Chatelier's principle, for an endothermic reaction increased temperature favours more product formation. Thus the formation of H₂ predominates over that of CH₄ at high temperatures (equation 2.20 is a stronger endothermic reaction than equation 2.21). The pressure dependence of the gas yields is far less pronounced. With increasing pressure, the yield of H₂ decreases, whereas that of CH₄ increases. In accordance with Le Chatelier's principle, an increase in pressure due to decreasing volume causes the reaction to shift to the side with fewer moles of gases. Thus CH₄ is preferred at higher pressures. As shown in equations (2.20) and (2.21), the formation of H₂ needs more water than the formation of CH₄. Hence, a higher concentration of biomass, which means a lower concentration of water, should support CH₄ formation.

Voll et al.⁵¹ and Tang and Kitagawa⁴⁸ (Figure 2.3) provided a thermodynamic analysis of supercritical water gasification of glucose at temperatures above 500 °C. Their analysis by minimizing the Gibbs free energy considered the following chemical species: glucose

and H₂O as reactants, and H₂, CO, CO₂, CH₄, C₂H₆, C₃H₈, C₂H₄, and C₃H₆ as products of the reaction. Voll et al.⁵¹ found the molar fraction (mol of product per mol of feed) of glucose, C₃H₈, C₂H₄, C₃H₆ and solid carbon equal to zero whereas C₂H₆ was less than 10⁻⁵ ppm. They observed that an increase in the temperature increased the molar fraction of hydrogen and carbon monoxide while it decreased the molar fraction of carbon dioxide and methane. They attributed this result to the higher temperatures favoring the methane reforming reaction.

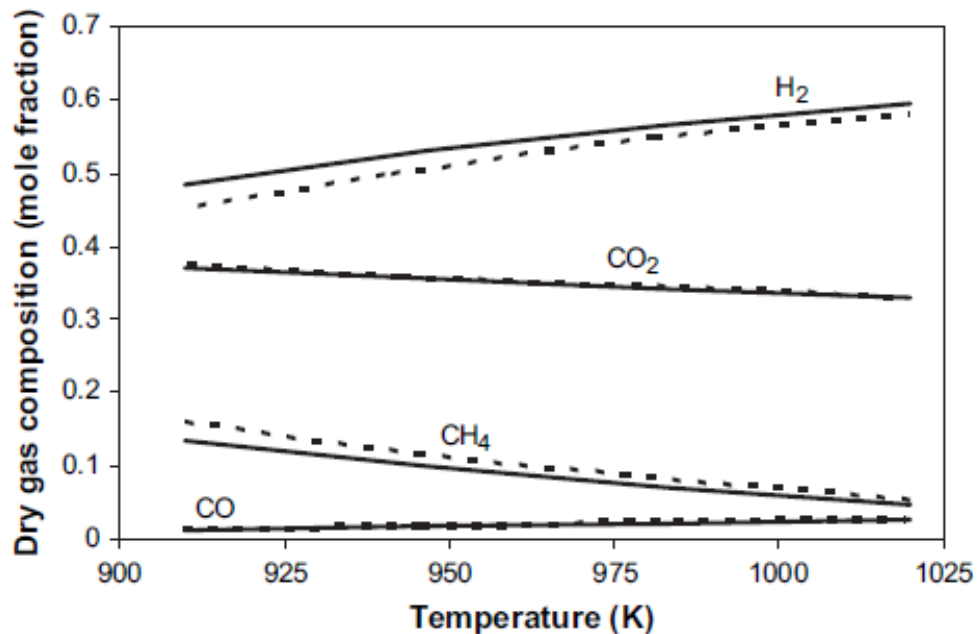
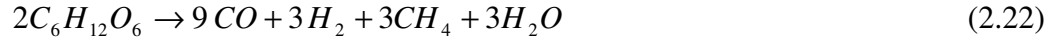


Figure 2.3: Supercritical water gasification of glucose at $P = 28.0$ MPa and feed concentration of 0.6 M glucose. Dashed line: Solid line: Voll et al.⁵¹, Tang and Kitagawa⁴⁸.

Tang and Kitagawa showed by calculation that at low temperatures, glucose gasification does not consume water but forms water⁴⁸. They assumed the following reaction for glucose decomposition at lower temperatures:



The authors predicted methane reforming and water gas shift reaction at higher temperatures as follows:



Yan et al.⁴⁹ developed a non-stoichiometric thermodynamic model based on minimum free energy to predict the performance of hydrogen production from biomass in SCW.

Figure 2.4 illustrates the influence of temperature on gaseous products of glucose gasification in SCW.

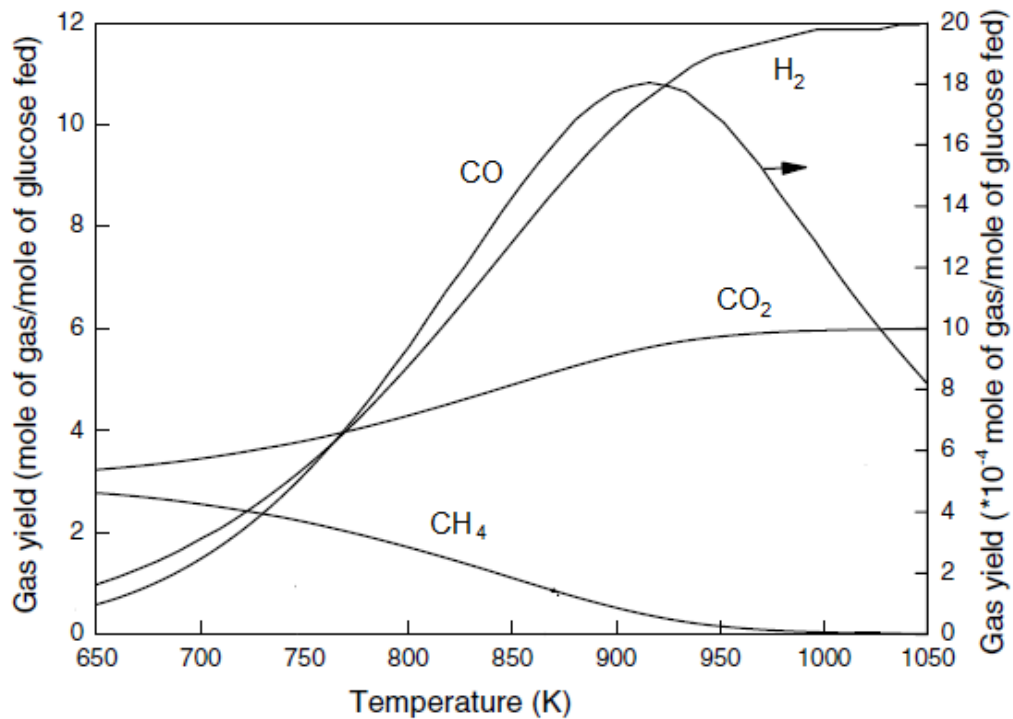


Figure 2.4: Effect of temperature on glucose gasification in SCW⁴⁹ (Feed concentration 0.6 M; $P = 28.0$ MPa).

The hydrogen and carbon dioxide yields increase as the temperature increases, while the methane yield decreases. The carbon monoxide yields increase at first and then decrease as the temperature increases, and it is much lower than that of the other species.

Figure 2.5 illustrates the effect of pressure on the gaseous products of glucose gasification in SCW.

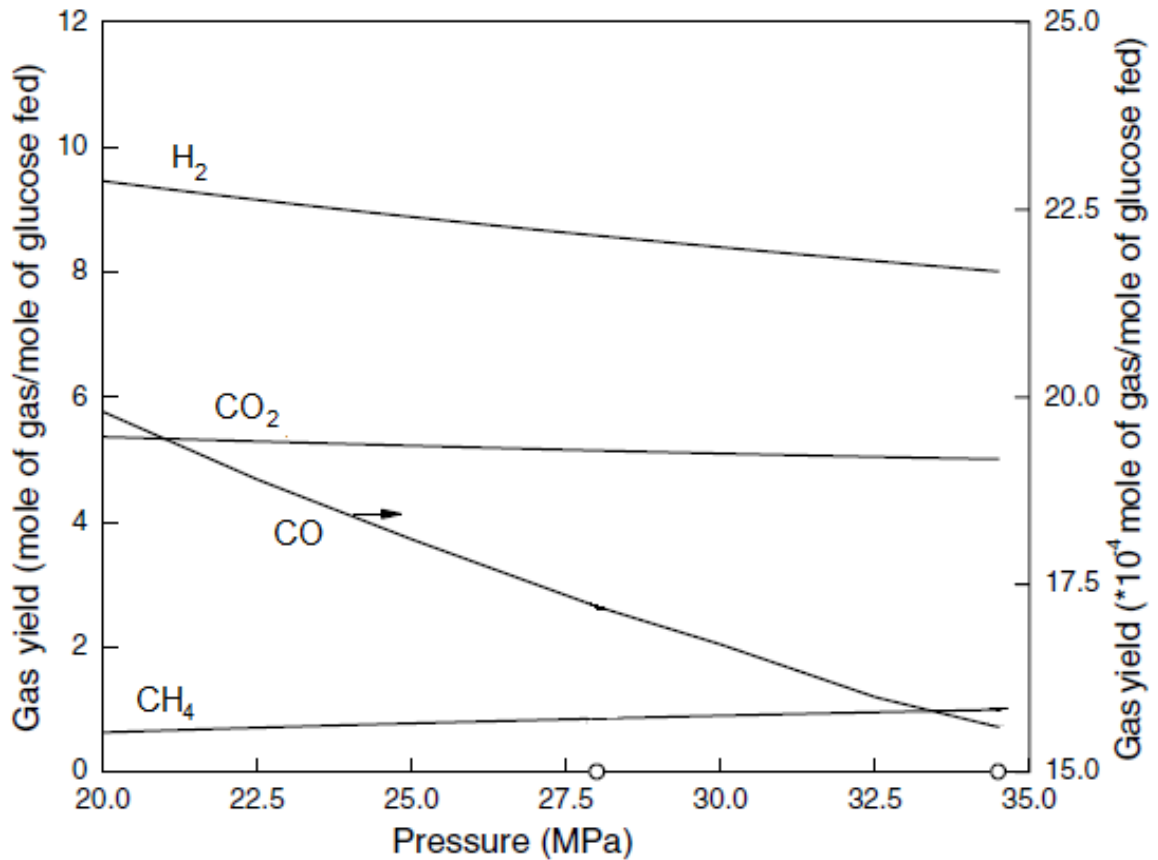


Figure 2.5: Effect of pressure on glucose gasification in SCW⁴⁹ (Feed concentration 0.6 M; T = 873 K).

In each case, methane is in competition with hydrogen formation. The hydrogen yield slightly decreases while the methane yield slightly increases as the pressure increases. Carbon dioxide remains almost constant. The carbon monoxide yield is much lower than

that of the other gases. Therefore, pressure from 20 MPa to 35 MPa, has no great effect on the glucose gasification.

Figure 2.6 illustrates the effect of concentration on gaseous products of glucose gasification in SCW. The hydrogen yield drops by 81%, and the methane yield increases by a factor of 20 as the glucose concentration increases from 0.1 to 1.0 M. A decrease of 29% in the carbon dioxide yield and a small increase in the carbon monoxide yield were also predicted.

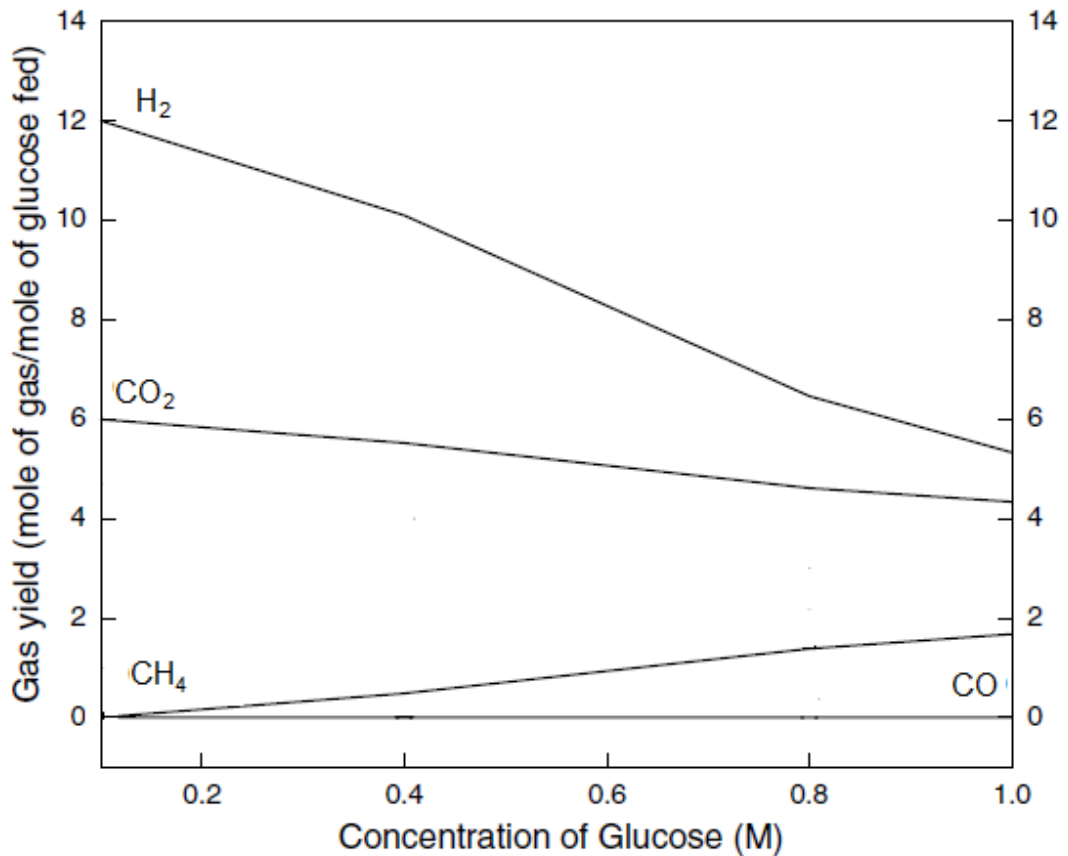


Figure 2.6: Effect of concentration on glucose gasification in SCW⁴⁹ ($P = 28.0$ MPa; $T=873$ K).

From the above thermodynamic analysis it is seen that high temperature, low pressure and low concentration is favourable for high hydrogen yield. Catalysts can minimize the activation energy and thus promote the yield of hydrogen at lower temperatures.

2.5 Kinetics

A kinetic analysis of the decomposition rate in SCWG is important to design the reactor system for the potential industrial implementation. Kruse and Gawlik studied the sub and supercritical conversion of biomass and concluded that the following simplified reaction pathways of liquefaction and/or gasification for the biomass (Figure 2.7)⁵² are occurring.

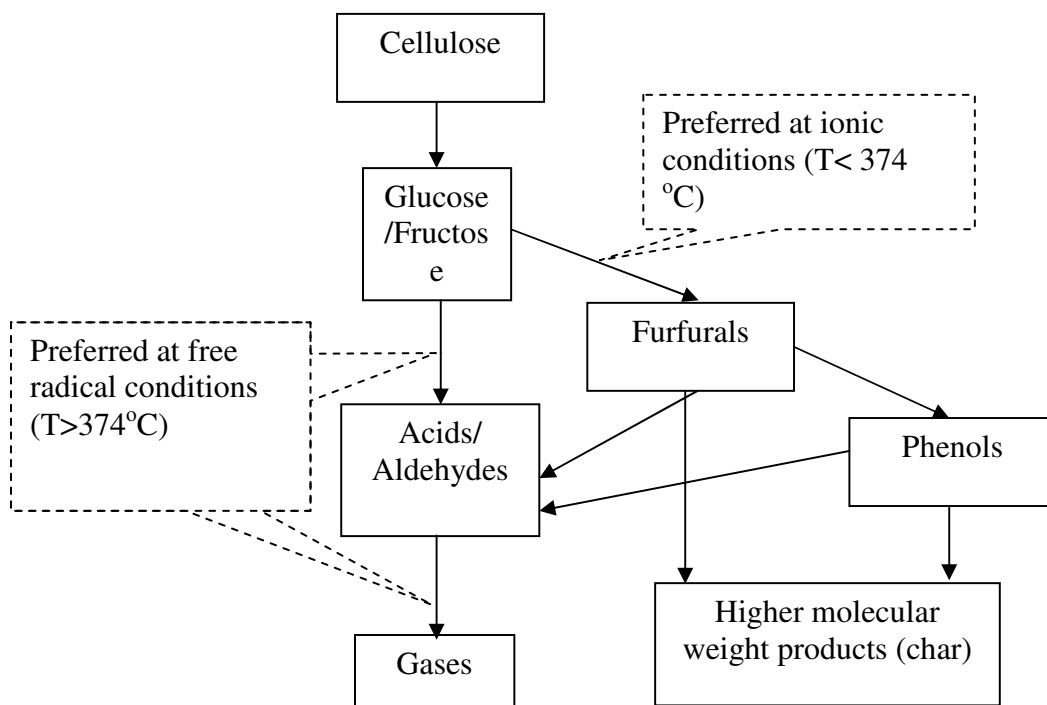
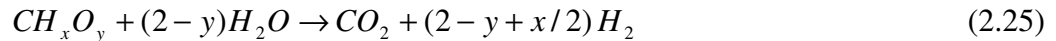


Figure 2.7: Simplified reaction scheme of liquefaction and/or gasification of biomass model compound⁵².

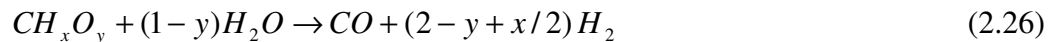
They showed two parallel paths of conversion; the left path is through a free radical reaction process which is preferred at supercritical conditions while the right path is through ionic reactions, preferred at subcritical conditions. From the properties of SCW as discussed before, it may be concluded that the intermediate decomposition products are dissolved in SCW as a result of its high solvent power for organic compounds. This allows faster reaction rates while minimizing the formation of tar or char⁵².

The overall biomass gasification reaction in supercritical water for the production of hydrogen is represented as follows¹:



where x and y are the elemental molar ratios of H/C and O/C in biomass, respectively. In addition to gasification, three major competing reactions occur during the gasification of biomass in supercritical water¹ as follows:

Steam reforming:



Water gas shift reaction:



Methanation reaction:



As the primary objective of biomass gasification in supercritical water gasification is hydrogen production, reaction (2.28) and (2.29) must be restrained while CO reacting

with water to form CO₂ and H₂ is desired in reaction (2.27). Other than the products mentioned above, other intermediate products (i.e. char and tar) are also formed during SCW gasification.

The detailed kinetics of biomass gasification, even using the model compound glucose is still unavailable due to multi-component intermediate reactants and products involved in this complex reaction mechanism. More than thirty components in the liquid product stream were detected during gasification of glucose in SCW^{53, 54}. Kabyemela et al. studied glucose and fructose decomposition in sub and supercritical water at residence times to 2 sec in a tubular reactor, finding first order reaction kinetics. The main products of glucose decomposition reported were fructose, erythrose, glycolaldehyde, dihydroxyacetone, glyceraldehyde, 1,6-anhydroglucose, and pyruvaldehyde. The reactions involved were three types, namely isomerization, bond cleavage, and dehydration. On the other hand, Lee et al.¹³ studied the conversion of glucose without catalysts in a tubular reactor at 480-750° C, 28 MPa, 10-50 sec. They found that below 600 °C the hydrogen yield increases with increased residence time when gasifying glucose in supercritical water. They did not study the liquid phase in detail, rather performed a kinetic analysis of COD (chemical oxygen demand) destruction assuming pseudo first order reaction during the gasification of glucose in supercritical water. Their kinetic investigation leads to the following first order reaction rates:

Glucose as a function of its concentration, C_g:

$$-r_g = 10^{3.09 \pm 0.26} \exp\left(-67.6 \pm \frac{3.9}{RT}\right) C_g \quad (2.30)$$

The COD as a function of the corresponding concentration C_c:

$$-r_c = 10^{2.95 \pm 0.23} \exp\left(-71.0 \pm \frac{3.9}{RT}\right) C_c \quad (2.31)$$

Jesus et al.⁵⁵ developed a model for corn silage using a mathematical approximation based on zero-order kinetics as follows:

$$Y = 10^2 \exp\left(\frac{47.9[KJ]}{RT[K]}\right) \tau(\text{min}^{-1}) + 10^{-2.8} \exp(6.1 \times 10^{-3} T[K]) \quad (2.32)$$

Jin et al.⁵⁶ studied the TOC (Total organic carbon) kinetics of oxidation of food wastes. They found a fast reaction rate at an early stage of reaction (within 50 seconds) and slow reactions afterwards.

2.6 Challenges

Although the SCWG process seems to be very efficient for hydrogen production, some physical limitations and/or technical difficulties have been encountered. Due to the severe process conditions (typically: T = 600 °C, P = 300 bar and a corrosive environment), experimental investigations on SCWG is expensive and time consuming. Chars from non-converted biomass and tars from unwanted reaction products are two major challenges in SCWG. Chars are linked to the conversion yields of the process, while tars are usually formed by pyrolysis of organic molecules. Because of sedimentation, these char and tars plug continuous reactors after several hours of running, while also limiting the amount of hydrogen production. Although SCWG can lower the amount of chars and tars compared to low pressure processes, this drawback has to be carefully considered because of the rather small volume of laboratory reactors and tubing. Antal et al.¹⁶ produced less than a few percent of such residual compounds in SCWG, whereas Corella

and his coworkers⁵⁷ observed 10-20% chars and 4% tars in atmospheric pressure steam gasification.

Three major limitations considering the material of reactor construction should be considered; i.e. corrosion, pressure resistance and hydrogen aging. Antal et al.¹⁶ showed that the inner walls of nickel alloy reactors were strongly corroded by the reaction. Only specific geometries and specific materials can be used due to the high pressures and temperatures used in SCWG. As an example, it is impossible to build whole titanium reactors with high corrosion resistance by comparison to classical stainless steels, due to the low allowable stress (pressure resistance) of titanium. The contact of metallic materials with hydrogen gas is well known for weakening the strength (pressure resistance) of the used materials. Combined with the high pressure constraint, hydrogen aging can limit the duration of use of reactors and tubing. In this research a 600ml Hastelloy C-276 reactor was utilized to withstand these difficulties while preventing plugging from chars and tars.

Separation of hydrogen from the other formed gases, especially carbon dioxide, is another relevant problem. Matsumura et al.⁵⁸ proposed to mix the formed gas and sub-critical water, which dissolves most of the carbon dioxide.

2.7 Effects of process parameters

Despite the above mentioned challenges, experiments conducted by various research groups have revealed that the influence of process conditions (temperature, pressure, residence time, concentration of the organics, catalysis) can control the yields and selectivity of the desirable gas products.

2.7.1 Effects of temperature

Perhaps the reaction temperature is the single most important parameter that influences the performance of SCW gasification. As discussed earlier in the thermodynamic and kinetics analysis sections (Figure 2.4), it was seen that with increased temperature, production of hydrogen yield was increased and the gasification efficiency and destruction of COD was also increased (Figure 2.8). In the absence of a catalyst, temperature has a significant effect on the specific yield of gasification¹. Peterson et al.¹² divided the gasification process in pressurized water into three groups depending on the primary products of gasification.

In the high temperature range (500-800°C) the gasification efficiency in SCW is high due to the high reactivity of biomass⁵⁹. For these high temperatures, catalysts may not be required as hydrogen rich gas is produced.

Table 2.2 Division of hydrothermal reaction by temperature of reaction¹²

Temperature range	Catalyst	Product yield
High temperature (>500°C)	No catalyst*	Hydrogen rich gas
Medium temperature (T_c to 500°C)	With/without catalysts	Methane rich gas
Low temperature (< T_c)	With catalysts	Other gases from smaller organic molecules

* catalysts may be used if needed, T_c – critical temperature

One major shortcoming of the high temperature process is that thermodynamically high temperature processes are less efficient than low temperature ones. To sustain the process, external energy may be needed. In this respect, low temperature (300-600°C) processes are more efficient, but the unaided gasification in this temperature range may

be difficult to achieve. Hence, the use of a catalyst becomes essential for low temperature processes. In addition, a lower temperature is more suitable for methane production.

The gaseous products from SCWG depend on the chemical reactions involved and their rate. The product gas composition would be governed by the chemical equilibrium of the reactions involved. The kinetic rate of any Arrhenius type equation increases with temperature^{55, 60}. Equations (2.30, 2.31 & 2.32), developed for SCW gasification also predict that the reaction rate constant increases with temperature. Therefore, the overall gasification yield increases with temperatures and also with time.

As shown in Figure 2.8 by Lee et al.¹³ for glucose gasification at 28MPa, the hydrogen and carbon dioxide yield increases with temperature. Carbon monoxide increases with temperature at low temperature, but after reaching a maximum it drops rapidly. Figure 2.8 also shows that the carbon, hydrogen, and oxygen conversion gasification efficiencies increase with the reaction temperature. The gasification efficiencies are defined as the percentage of the total moles of C, H or O atom in gaseous products per moles of C, H or O atom of glucose feed. At 700°C, the carbon gasification efficiency reaches 100% attributing complete conversion of glucose to product gas. Interestingly, the hydrogen gasification efficiency is higher than 100% due to the contribution of the supercritical water to the hydrogen in the product gas. This helps confirm the role of SCW that serves as both a hydrogen source as well as a solvent for glucose gasification.

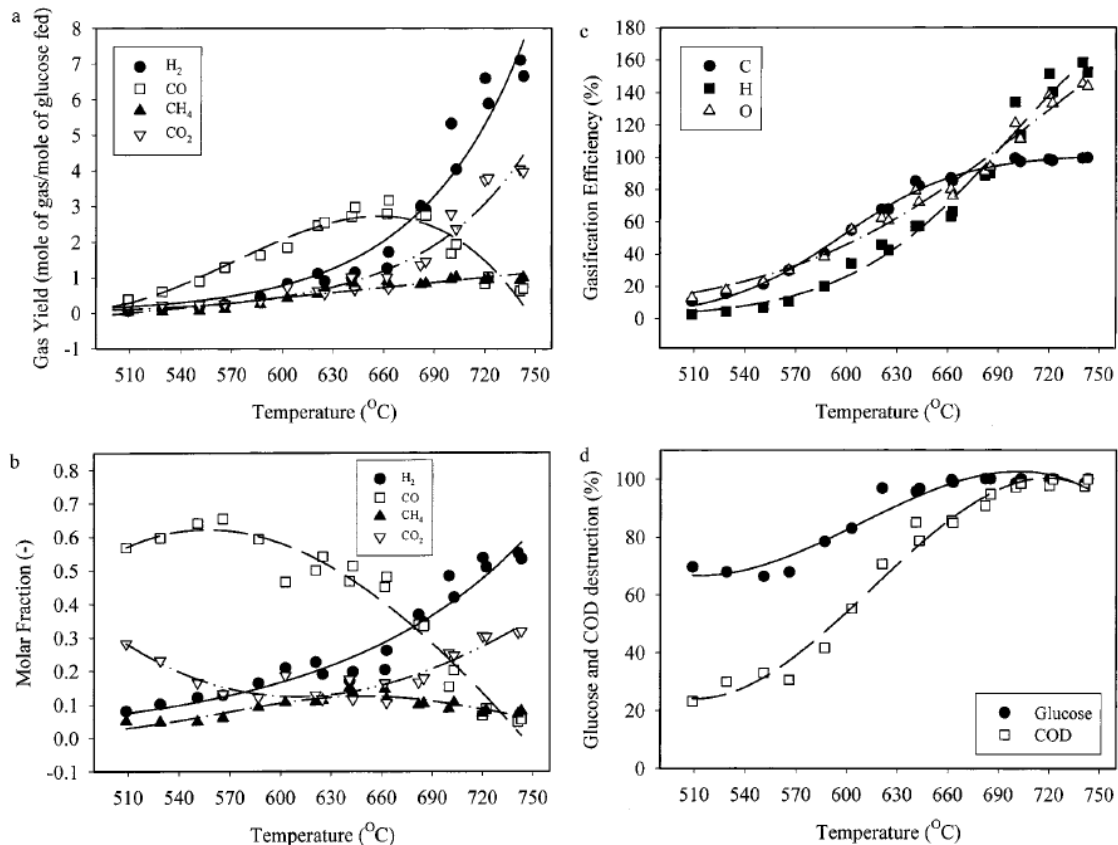


Figure 2.8: Effect of reactor temperature on 0.6 M glucose in supercritical water at 28 MPa and 30 s reactor residence time: (a) gas yields, (b) molar fractions of gaseous products, (c) gasification efficiencies, (d) glucose and COD conversion¹³.

Hao et al.¹⁴ noticed a very large effect of temperature at 25 MPa. A 167% increase in the carbon conversion efficiency (CE), and more than 300% increase in the gasification efficiency (GE) was observed with a 30% increase in reaction temperature (500 to 650°C). They also noticed that the hydrogen production increased by 46% and the CO was reduced by 74%. Whereas Lee et al.'s¹³ results showed that both hydrogen and CO increase with temperature but beyond 660°C, the CO yield dropped below that of H₂.

Lee et al.¹³ inferred that a significant fraction of the glucose is converted to carbon monoxide and remains stable between temperatures 510-660°C. Above 660°C, carbon

monoxide undergoes the water gas shift reaction and other intermediate products are also converted to hydrogen. According to most researchers^{13, 53, 61, 62}, glucose is first broken down into several water-soluble intermediates before being converted to final gaseous products. To explain the effect of temperature for glucose conversion in SCW Lee et al.¹³ proposed the following mechanism:

Biomass \rightarrow water-soluble intermediate \rightarrow gases (mostly CO)



CO later undergoes the water gas shift reaction forming additional hydrogen.



Lee et al.¹³ summarized that the rate of CO formation is faster than that of the water gas shift reaction at low temperatures. However, at higher temperatures the WGS reaction is very fast which results in an increase in hydrogen and a net reduction in CO. They found that above 650 °C, CO production was reduced due to the water-gas shift reaction (Figure 2.8). Some of the intermediate products also undergo reaction that produces hydrogen and carbon dioxide.



From reactions (2.34) and (2.35) it is evident that with a rise in temperature, the carbon dioxide and hydrogen yields increase.

Holgate et al.⁵³ conducted supercritical water gasification in a tubular reactor in the temperature range 425-600 °C at 24.6 MPa with 5.1-9.9 s reaction times. In contrast to the calculated chemical equilibrium, at 550 °C the production of CO was about two mol

per mol glucose feed. About the same yield of CO₂ and H₂ was observed. However, at 600 °C they found the CO content was minimal and about 10 mol H₂ and 6 mol CO₂ were formed per mol of glucose.

On the other hand, the results from Kersten et al.⁶³ from the University of Twente are different from Holgate et al. Kersten et al. investigated the gasification of glycerol, glucose, and pinewood in supercritical water in quartz capillary reactors with internal diameters of 1mm. Over 700 experiments were conducted in the temperature range 400-800 °C, at 5-45 MPa, and 1-20wt% organic feedstock concentration. Below 650 °C, very low carbon conversion to gases was observed being a strong function of the temperature. Focusing on the results with glucose, an interesting finding was that CO was the main gas product at 600 °C. The yields of hydrogen and CO₂ increased with temperature, with CO still being the main product at 650 and 700 °C. At 800 °C, H₂ and CO₂ strongly increased with a corresponding decrease of CO caused by the water-gas shift reaction. Complete conversion of glucose was achieved at much diluted solution (1wt %) at 650 °C or above.

Methane, which is another important product of SCW gasification, could be high in the intermediate temperature range of 374-500°C (Table 2.2). Methane is very stable in SCW, and is not converted into any smaller molecules¹³. From Figure 2.4 and 2.5 it was shown that with an increase in temperature methane production decreases. But Lee et al.¹³ found an increase in methane formation with an increase in temperature (Figure 2.8).

Tar yield (in the liquid effluent) is also affected by the temperature during SCWG. At low temperatures ($T < T_c$), the tar yield is high with low gas production⁵⁹. A yellowish and thin layer of a dark brown, oil-like tar was observed in the liquid effluent at low temperatures

(<600°C)^{3, 14}. But at 650°C, clear water was observed^{3, 14}. Lee et al.¹³ observed the liquid product was almost red at 510°C, while it varied to dark brown, orange, yellow as the temperature increased up to 600°C. They found the liquid product clear at 680°C.

Total organic compound (TOC) analysis is used to measure the liquid effluent (tar) quantitatively. Chemical oxygen demand (COD), an alternative to TOC in the liquid effluent, was used by Lee et al.¹³ The decomposition of glucose and destruction of COD highly increased and thereby reached 100% conversion at higher temperatures (>700°C). At low temperatures (~600°C) Lu et al.⁷ also observed yellowish liquid (tar) while gasifying sawdust in SCW. They found that the amount of TOC in the liquid at 650°C is much lower than TOC at 600°C.

In summary, it can be concluded that the effect of temperature is significant particularly in the temperature range of 500-700°C¹² and the total gas yield increases with an increase in temperature while TOC in the liquid product decreases. The yield of hydrogen, and carbon dioxide is higher at high temperatures¹².

2.7.2 Effects of reaction pressure

Conducting over 200 experiments Kersten et al.⁶³ found the pressure dependence range of 13.8 to 41.8 MPa on reaction products is insignificant. Hao et al.¹⁴ observed no great effect of pressure on gasification efficiency and the fraction of gas product from 25MPa to 30 MPa at temperatures of 500 and 650 °C.

On the other hand, Lu et al.⁷ found a 7% increase in the hydrogen yield for a 65% increase in pressure, although the unconverted TOC increased with pressure. Gasification

efficiency (GE) and carbon conversion efficiency (CE) are not monotonic functions of pressure. Over a wider range of pressure, GE and CE seem to be independent of pressure.

2.7.3 Effects of residence time

Residence time has an important effect on the conversion of biomass, especially at the beginning of the reaction. However, this time depends on many factors including reaction temperature, biomass type and the reactor vessel type.

Jesus et al.⁶⁰ correlated results from the gasification of corn silage, with time at 700 °C and 25 MPa. A linear relationship between carbon conversion and residence time was developed.

$$Y_C = K\tau = 0.11\tau (R^2=1) \quad (2.36)$$

Hao et al.¹⁴ studied the effect of residence time from 0.5 to 3.8 min on SCW gasification of 0.4 M glucose at 650°C and 25 MPa. GE increased from 93.6% to 117.6% and CE increased from 77.5% to 98.7% with increasing residence time from 1.7 to 3.7 minutes. In their experiments, a minimum of 3.6 minutes resident time was needed for reasonable gasification efficiency.

Lee et al.¹³ examined the effect of residence time for 0.6 M glucose gasified in SCW at 28 MPa, 600 °C and 700°C. At 700 °C the yields of all the gases remained almost constant except at the shortest residence time, 10.4 s. However H₂ and CH₄ yields increased with residence time at the lower temperature, 600°C. A slight decreasing tendency of CO was observed with increasing residence time.

Lu et al.⁷ found the yields of H₂, CO₂ and CH₄ increased with residence time. They gasified wood sawdust in SCW at 25 MPa, 650°C within the range of 9 to 46 second. The gasification efficiency (GE) and carbon conversion efficiency (CE) increased while the unconverted TOC in the liquid effluent decreased with increasing residence time. These data suggest that longer residence times were favorable for biomass gasification.

2.7.4 Effects of solution concentration

Solid biomass and water are the main components of the feedstock for SCWG. The solid concentration in the feedstock could be a major design issue for the commercial application of SCWG.

Gasification of glucose as a model biomass in SCW, Matsumura et al.⁵⁹ found that the yields of H₂, CH₄ and CO₂ decrease while CO increases with an increase in glucose concentration in the feedstock. Hao et al.¹⁴ showed that the percentages of H₂ and CO₂ in the total product gas increases with increasing glucose concentration in the range of 0.1 M to 0.9 M, but that CO and CH₄ fractions were reduced while the GE decreased. Kersten et al.⁶³ found that at 700 °C and 30 MPa, H₂ and CO₂ decreased with initial glucose concentration from 1 to 7wt% while CO and CH₄ remained almost constant. Nearly complete gasification was achieved with the lowest concentration at 650 °C or above.

The experiments with real biomass gasification in SCW^{1, 7} also showed that both gasification efficiency (GE) and carbon conversion efficiency (CE) decreased with an increase in feed concentration. The yields of H₂, CH₄ and CO₂ also decreased with feed concentration, while the yield of CO increased.

2.8 Catalysis as a solution

Without catalysts, high activation energy is needed for the various discussed reactions to increase the selectivity of hydrogen production. From the earlier discussion (section 2.6.1) it is seen that high temperatures (600 °C and above) are favourable for the production of hydrogen rich product gas while moderate temperatures (~ 500 °C) favour the production of methane in SCW gasification (Table 2.2). Since catalysts lower the activation energy, hydrogen rich gas production is possible at lower temperatures. The biggest obstacle to the development of this technology is the high costs of equipment and operation. Therefore, research on the catalytic supercritical water gasification is gaining significant attention.

As a solution, catalysts must increase the rate of a desired chemical reaction (activity) and guide the product distribution towards those desired (selectivity). Therefore, a catalyst may still be useful in the case of unfavourable thermodynamics, if reaching the chemical equilibrium is not the goal¹².

For SCWG, catalysts should not only decrease the amount of tars and chars formed, but also increase the proportion of hydrogen in the synthesized gas. Since the chemical equilibrium composition is not influenced by the catalyst, increasing the rate of a gasification reaction with a catalyst is only useful if the thermodynamics are favourable. The primary objective of biomass gasification at moderate temperatures (~ 500 °C) is to produce either a gas with a medium calorific value (*i.e.*, methane-rich) or to produce hydrogen¹². At temperatures below 500 °C, catalytic effects from the reactor wall is

insignificant¹². As summarized by Peterson et al.¹², obtaining the thermodynamic equilibrium gas composition below 600 °C is not possible due to the following reasons:

1. Glucose decomposed in SCW to reactive intermediates such as 5-HMF can form polymeric materials of very low reactivity.

2. Formation of methane by decarboxylation of acetic acid or by decarbonylation of acetaldehyde may occur. A secondary methane formation by the hydrogenation of CO and/or CO₂ can also happen.

3. Although not a thermodynamically stable product, some organic intermediates may form solid coke (char), which has a very low reactivity at these temperatures.

The complete conversion of the biomass feed by catalysis depends on the catalyst's ability to gasify reactive intermediates that are rapidly formed from the feed molecules by hydrolysis and dehydration. To avoid the formation of polymeric materials and eventually char, the gasification step must be very fast. Two competing reaction pathways can be followed by these reactive intermediates; firstly formation of gaseous products (CO, CO₂, H₂), and secondly formation of oils and finally char⁶⁴.

A good catalyst must rupture the C–C bond very fast and at the same time dissociate H₂O into H⁺ and OH⁻ radicals on the catalyst surface. Adsorbed C_xH_yO_z fragments can then combine with these radicals and release CO and CO₂. The adsorbed hydrogen atoms from the cleaved C_xH_yO_z fragments and from water splitting combine to form H₂. A good gasification catalyst must exhibit these minimum mechanistic features. Additional features include fast equilibration of the water–gas shift reaction, and the hydrogenation of CO and CO₂ to CH₄ and H₂O. Depending on the selected catalyst, either a hydrogen-rich or a methane-rich gas is produced by the SCW gasification process.

2.8.1. Homogeneous catalysts

Alkali metal catalysts (Na_2CO_3 , KHCO_3 , K_2CO_3 , NaOH , etc) for SCWG of biomass mainly improve the water-gas shift reaction. SCWG of pyrocatechol by Kruse et al.⁶⁵ reported that increasing the content of KOH from 0 to 5%, the production of H_2 and CO_2 increased while the CO yield was smallest. This phenomenon was attributed to the catalytic effect on the water-gas shift reaction in the process by adding KOH . They reported similar activity on the gas-phase composition when compared with LiOH but to a smaller extent. Garcia Jarana et al.⁶⁶ reported that the water-gas shift reaction is accelerated by adding KOH while conducting SCWG of industrial organic waste using KOH . The water gas shift reaction was described as follows:



Conducting SCWG experiments on *n*-hexadecane and lignin with NaOH (400 °C, 30 Mpa) Watanabe et al.¹⁵ reported that the addition of NaOH makes the output of H_2 four times higher than that of being without NaOH . They found the production of coke is also effectively inhibited. Kersten et al.⁶³ reported that adding Na^+ or K^+ cations as an assistant to Ru/TiO_2 catalyst for SCWG can promote the water-gas shift reaction, although the carbon conversion rate was not affected. Using K_2CO_3 and Trona ($\text{NaHCO}_3 \cdot \text{Na}_2\text{CO}_3 \cdot 2\text{H}_2\text{O}$) as catalysts by Yanik et al.⁶⁷ it was found that the H_2 yield increased significantly for the SCWG of lignocellulosic materials (cotton stalk and corncob) and tannery waste. Sinag et al.⁶⁸ gasified glucose in SCW using 0.5wt% K_2CO_3 . At 1°C/min and 3°C/min heating rates, the hydrogen yield was higher with K_2CO_3 than that with Raney nickel. The K_2CO_3 catalyzed water-gas shift reaction on H_2 production can be explained through the formation of HCOO^-K^+ :



Reaction of formate ($HCOO^-K^+$) with water forms hydrogen.



Formation of CO_2 and K_2CO_3 completes the catalytic cycle



From the above discussion it is clear that alkali catalysts are important to achieve high hydrogen yield, but may cause corrosion, plugging or fouling^{16, 68}. The recovery and reuse of homogeneous catalysts is also difficult.

2.8.2. Heterogeneous catalysts

Heterogeneous catalysts have the advantages of high selectivity, recyclability, and environment-friendliness over homogeneous catalysts. Metals give a high level of carbon conversion to gas at a relatively low temperature⁵⁹.

Due to the relatively low cost of nickel catalyst and its wide application in many petrochemical industries, many researchers have introduced it into supercritical water gasification reaction systems to gain a better understanding of its hydrothermal activity and stability. Other researchers use metals like Ru, Rh, Pt, Pd, Cr, W; although Pt, Pd, Cr, W have shown low activity⁶⁹. Savage and Resende²⁵ reported that nickel and copper provided higher gas yields. They summarized the effect of metals on SCWG as shown in Table 2.3.

Table 2.3: Summary of the catalysts used in SCWG²⁵

Catalyst	Reactions promoted	Comments
Nickel	Tar cracking, water gas shift, methanation, hydrogenation	Increases gas yields substantially
Raney nickel	Same as Ni	Provides colorless aqueous phase
Ruthenium	Actively breaks C–C bonds	Maintains activity for long time
Rhodium	Effective to decompose benzene rings	High activity for decomposition

Stable supports for these active metals includes ZrO_2 (monoclinic), $\alpha-Al_2O_3$, TiO_2 (rutile), and carbon¹². With many kinds of real compounds (lignin, cellulose, etc) for gasification in supercritical water, Ni catalysts have shown high activity. However, due to the adsorption of intermediate products on the catalyst surface from the process, the catalyst deactivates⁷⁰. Although Elliott⁶⁹ reported that only reduced nickel possesses catalytic activity, Savage and Resende²⁵ found that exposure of nickel wires to supercritical water did not reduce the activity of H_2 production. Therefore the deactivation may be due to the formation of coke or adsorption of intermediate products on the catalyst surface.

Furusawa et al.²³ gasified lignin in SCW using a Ni/MgO catalyst. They found that with an increase of the Ni metal surface area, carbon gasification increased. The best catalytic performance observed used a 10 wt% Ni/MgO (600 °C) under the reaction conditions tested. Minowa et al.⁷¹ showed the importance of Ni catalyst on the steam reforming and methanation reactions. Sinag et al.⁶⁸ investigated Raney nickel for degradation of

glucose in SCW at 500 °C, 30 MPa and found both the intermediate phenols and furfurals were reduced and the gas yield increased in the presence of catalysts.

Byrd et al.¹⁸ evaluated the Ru/Al₂O₃ catalyst for SCWG of glucose at high temperature (700 °C). They reported high yields of H₂ with low CO and CH₄ yield at high temperature and low glucose concentration. In the subsequent investigation of gasification of glycerol in SCW⁷², the high activity of Ru/Al₂O₃ for C–C bond scission was shown. The catalytic mechanism can be explained as: hydroxyl groups containing oxygenated compounds adsorb to the catalytic Ru surface predominantly through one or more oxygen atoms. On the catalyst surface, the reactant undergoes dehydrogenation first, followed by subsequent cleavage of C–C or C–O bonds. Cleavage of C–C bonds leads to the water-gas shift reaction and possible methanation reaction to form synthesis gas. Cleavage of C–O bonds gives organic acids and alcohols.

High H₂ selectivity using a Ru catalyst was shown by Osada et al.¹⁹ at low temperature (400 °C) for SCWG of lignin and glucose. When catalyzed at the low temperatures, the intermediate compound formaldehyde was decomposed to CH₄, CO₂ and H₂ rapidly. However, without a catalyst, formaldehyde was converted to methanol and CO₂. A wide range of heterogeneous catalysts for SCWG was investigated by Sato et al.⁷³ They found that the activity order is: Ru/γ-Al₂O₃ > Ru/C > Rh/C > Pt/γ-Al₂O₃, Pd/C and Pd/γ-Al₂O₃.

Although Ru shows very good activity, even a trace amount of S can cause Ru catalyst poisoning²⁰. This trace amount of S can exist in Ru/C catalysts in the form of sulphur and sulphate ions²⁰. Sulphur most likely blocks the sites necessary for C-C bond scission and for methanation.

ZrO₂ was investigated by Watanabe et al.^{15, 74} for the SCWG of glucose and lignin. They reported that ZrO₂ not only reduced CH₄ production but also increased the H₂ yield, although the catalytic effect was less than NaOH. Activated carbon such as spruce wood charcoal, macadamia shell charcoal, coal activated carbon and coconut shell can also be used for catalytic SCWG of organic feedstocks. Matsumura and co-workers³ showed that activated carbon not only increased carbon gasification efficiency, but also improved the water-gas shift and methanation reactions. However, deactivation on carbon gasification occurred after 4 h and water-gas shift reaction occurred after 2 h. Antal et al.¹⁶ reported that steam reforming of biomass laden gel over a carbon catalyst can produce a gas composed of hydrogen, carbon dioxide, methane, carbon monoxide, and traces of ethane.

Comparing with the noble metals, Ni is very inexpensive; therefore it is more suited for large-scale hydrogen production by biomass gasification. Ni has shown higher activity and performance than alkali catalysts, and activated carbon. Ni provides higher gas yield than Ru and Rh²⁵. Moreover, if Ni is doped with other metals like cerium or lanthanum, the stability and reactivity can be potentially enhanced.

Chapter 3

Supercritical water gasification and partial oxidation of glucose: Effect of Ni/Al₂O₃ catalysts on gaseous products and chemical oxygen demand (COD) destruction

In this chapter, gasification and partial oxidation of glucose was conducted with and without catalysts at various temperatures in supercritical water. Part of this chapter is reproduced from the published article by the author: Effect of nickel loading on hydrogen production and chemical oxygen demand (COD) destruction from glucose oxidation and gasification in supercritical water⁷⁵ with permission from International Journal of Hydrogen Energy 35 (10), 5034-5042, 2010; Copyright [2009] Elsevier Ltd.

3.1 Introduction

With increasing public awareness about the growing environmental impacts and depletion of fossil fuels, hydrogen production from biomass is considered an effective solution towards green energy production. The CO₂ produced from gasification is balanced by photosynthesis through biomass growth providing a carbon neutral approach. However, the water content of biomass is generally high, in the range of 90% or above. Thermochemical conversion processes require prior drying which consumes a large amount of energy. Supercritical water gasification (SCWG) can be a promising alternative to the pyrolysis of wet biomass or incineration of aqueous organic waste

streams. Supercritical water oxidation (SCWO) is an emerging technology to treat hazardous wastewater streams^{37, 76}. SCWG is also used in producing green gases such as hydrogen¹¹. Supercritical water (SCW) can dissolve most organic substances and gases and has low viscosity and excellent mass transfer ability⁸. Above the critical conditions of water (374 °C, 22.13 MPa) all organic compounds are present in a single dense fluid phase, minimizing mass-transfer resistance and facilitating rapid reaction rates. In the last decades, there have been a number of studies carried out on the gasification of wet biomass^{3, 61 7, 16, 23} and aqueous organic wastes^{66, 77, 78} in supercritical water. Enhancement of biomass conversion through oxidation in supercritical water^{53, 79} or partial oxidation^{11, 15, 80} has also been studied. The gaseous product composition from supercritical water gasification of glucose significantly depends on the reactant concentration⁶¹ and temperature^{3, 13, 53}.

Catalysts play an important role in hydrogen production from biomass gasification in supercritical water by increasing the hydrogen yield, reducing tar and char formation, and affecting the matter gasification efficiencies. Watanabe and co-workers¹⁵ studied the effect of various catalysts on the gasification of biomass model compounds in a batch reactor at a temperature range of 400–440 °C and observed that the yield of H₂ from *n*-C₁₆ and lignin with zirconia was twice that without a catalyst at the same conditions. The H₂ yield with NaOH was 4 times higher than that without catalyst. However, Yu and Antal⁶¹ reported that 95% or higher gasification efficiency in supercritical water requires a reaction temperature above 600 °C. Courson et al.²⁴ and Wang et al.⁸¹ reported that nickel catalysts cracked tar and enhanced the water–gas shift, methanation, and hydrogenation reactions. From an economic and energy efficiency point of view, high

gasification efficiency at low temperatures with higher hydrogen yields is favorable. Nickel has a high melting point of 1453 °C and is a readily available inexpensive metal widely used in the petrochemical industries, making it a reasonable choice for examination of supercritical water gasification and oxidation. Homogeneous catalysts such as KOH and NaOH, which can easily dissolve in SCWG to produce hydrogen-rich gas, can cause corrosion of the reactor wall^{16, 67}. Minowa et al.⁷¹ reported that reduced nickel catalyst enhanced the gasification of cellulose and the water gas shift reaction in hot compressed water. From an economic perspective, lower temperature gasification that coincides with maximum hydrogen and methane rich fuels is favorable¹¹. These findings motivated us to study nickel as a catalyst to obtain hydrogen-rich gas from the gasification of biomass and partial oxidation of ungasified products (char and tar) in supercritical water.

In this study, we demonstrate a new approach of introducing hydrogen peroxide as an oxygen source after 15 min of reaction time for glucose gasification in supercritical water at relatively low temperatures i.e. 400–500 °C. Hydrogen peroxide can help to decompose intermediate products that are not gasified during supercritical water gasification (SWG) in the first 15 min of the reaction time. The yield of hydrogen is expected to increase via CO formation by partial oxidation of the intermediate products as well as char and tar formed prior to H₂O₂ injection. In this work, different loadings of nickel on theta(θ) alumina catalysts were synthesized via an impregnation method²² and were subsequently tested for supercritical water gasification (SCWG) and supercritical water partial oxidation (SWPO) at a temperature range 400, 450, and 500 °C to investigate catalysis of hydrogen production.

3.2. Materials and methods

3.2.1. Materials

Nickel nitrate hexahydrate ($\text{NiNO}_3 \cdot 6\text{H}_2\text{O}$), reduced commercial nickel on silica alumina and glucose were obtained from Sigma–Aldrich (Oakville, Ontario, Canada). Hydrogen peroxide aqueous solution (50% H_2O_2 solution) was obtained from EMD Chemicals Inc (Gibbstown, NJ, U.S.A). De-ionized water was obtained from a compact ultrapure water system (EASY pure LF, Mandel Scientific co, model BDI-D7381). For catalyst preparation, $\gamma\text{-Al}_2\text{O}_3$ pellets with 3 mm average particle diameter, 198 m^2/gm BET surface area and pore volume of 0.421 cm^3/gm received from Aldrich (Mississauga, Canada).

3.2.2 Catalyst preparation

$\theta\text{-Al}_2\text{O}_3$ pellets were used as catalyst supports for catalyst synthesis. Because it was found to be stable in SCW. On the other hand $\gamma\text{-Al}_2\text{O}_3$ was found to be dissolved in SCW. It may be due the defects in crystalline structure of $\gamma\text{-Al}_2\text{O}_3$ ⁸². $\theta\text{-Al}_2\text{O}_3$ has monoclinic symmetry in catalyst structure⁸². In addition, converting $\gamma\text{-Al}_2\text{O}_3$ to $\theta\text{-Al}_2\text{O}_3$ pore size increased which allows better impregnation of active metals, and penetration of bulky intermediate products formed by SCWG. Calcining $\gamma\text{-Al}_2\text{O}_3$ to 1050 °C at a rate of 10 °C per min converts $\gamma\text{-Al}_2\text{O}_3$ to $\theta\text{-Al}_2\text{O}_3$. Catalyst synthesis by the incipient impregnation method was described elsewhere²². For a typical synthesis, the required metal salt solution was prepared in a volume of pure water corresponding to 130 vol% of pore volume of alumina (0.248 cm^3/gm , measured by Micromeritics ASAP 2010) used for catalyst support. The required amount of nickel is calculated from the nickel present in

$\text{NiNO}_3 \cdot 6\text{H}_2\text{O}$. For example, preparing one gram 18wt% Ni on alumina catalyst requires 0.18 gram nickel that can be obtained from 0.89 gram $\text{NiNO}_3 \cdot 6\text{H}_2\text{O}$. All alumina was dipped into the solution at once for uniform metal dispersion. The catalysts were then placed in a beaker which was then placed in another closed beaker of 10 vol% $\text{NH}_3\text{-H}_2\text{O}$ solution for ammonia vapor treatment for 10 min at 60 °C inside the oven. Any metal salt on the catalyst support was converted to ammonium salt by ammoniacal treatment which increases the activity and Ni dispersion⁸³. Ammoniacal treatment converts the metal salt anion to ammonium salt. The $\text{NH}_3\text{-H}_2\text{O}$ vapor treated catalysts were then taken out from the closed beaker and heated from 60 to 120 °C at rate of 1°C, then to 250 °C at a rate of 1.5 °C. In this step most of the ammonium salts attached to the catalysts are removed by sublimation. Hydrogen reduction and thermal treatment at 600 °C for 2 h was performed afterwards, in a stream of 10 vol% H_2 diluted with N_2 with a rate of 6 L/h from room temperature to 600 °C at 3 °C/min.

The reduced catalysts were weighed to measure the actual loading of nickel by the difference between support alumina and nickel loaded catalyst. In our synthesis the actual loading was slightly less than the calculated loading. For instance, the calculated 8 wt% nickel on alumina was actually approximately 7.5 wt% nickel on alumina, calculated 12 wt% loading was found 11 wt% and 20 wt% loading was 18 wt%. Due to diffusion limitations, impregnation was repeated more than once in order to achieve high nickel loadings. For example, while the 7.5 wt% nickel on $\theta\text{-Al}_2\text{O}_3$ was loaded in one step using incipient impregnation, the 18 wt% nickel was synthesized in three steps wherein the reduced 7.5 wt% nickel/alumina was further impregnated to approximately 14 wt% nickel/alumina and then to 18 wt% nickel/alumina. The BET (Brunauer-Emmett-Teller)

surface area, pore size distribution, and pore volume were determined from nitrogen adsorption- and desorption isotherm data obtained at $-193\text{ }^{\circ}\text{C}$ in a constant-volume adsorption apparatus (Micromeritics ASAP 2010) using 99.995% pure N_2 gas obtained from Praxair (Oakville, Canada). The prepared samples were degassed at $150\text{ }^{\circ}\text{C}$ for 5 hour before measurements. Table 3.1 portrays the summery of surface area, pore size and pore volume of gamma (γ) and theta (θ) alumina and synthesized catalysts.

Table 3.1. Physical properties of the synthesized catalysts.

Sample	BET surface area (m^2/g)	Average pore size (nm)	Micropore volume (cm^3/g)
γ -alumina	198	8.5	0.42
θ -alumina	57	17.4	0.25
7.5 wt% Ni/ θ -alumina	51	14.0	0.18
11 wt% Ni/ θ -alumina	49	15.8	0.19
18 wt% Ni/ θ -alumina	46	10.2	0.12
63 wt% Ni/silica–alumina commercial catalyst (powder)	190	7.54	0.27

3.2.3 SCWG Apparatus

Figure 3.1 portrays a schematic diagram of the experimental SCWG setup. Experiments were performed in the main reactor body which was obtained from Autoclave Engineers, Erie, Penna, U.S.A. The reactor was constructed of Hastelloy C-276 with a capacity of 600 ml. The batch reactor allows for sampling of gas and liquid samples throughout the experiments. The reactor was heated with a 1.5 kW electrical furnace that surrounded its main body supplied by the same manufacturer.

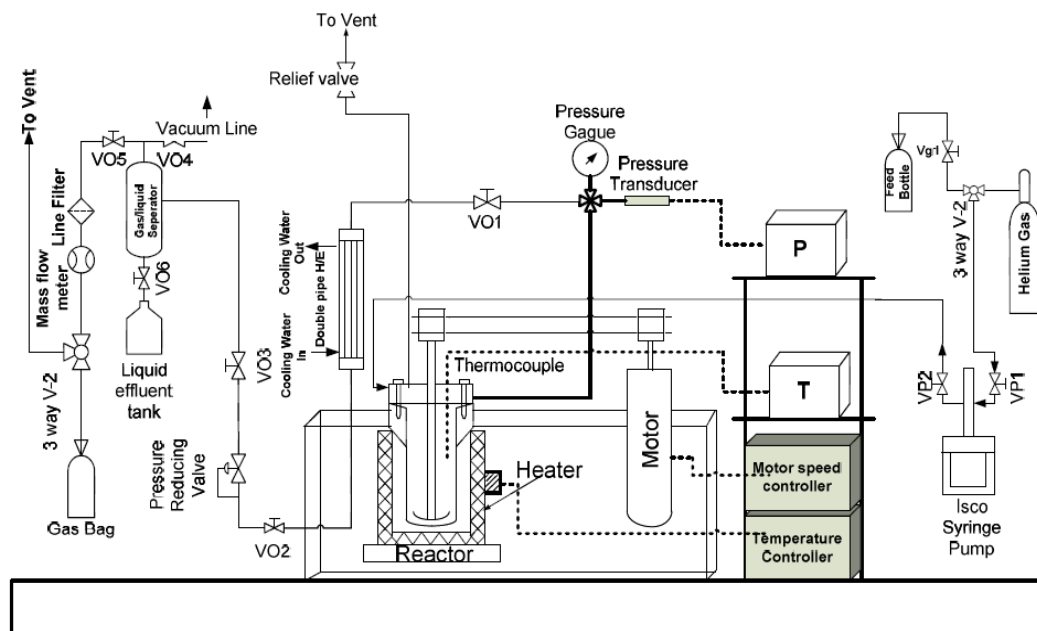


Figure 3.1: Schematic diagram of the SCWO batch unit.

3.2.4 Experimental procedures

The experimental procedure consists of several steps started by opening and washing the reactor body thoroughly with distilled water to remove any residue from previous experiments. The catalyst and 70 ml of de-ionized water were added to the reactor, after which it was closed and purged with helium gas at a constant pressure of 0.2 MPa for 20 min to drive away any air and oxygen present in the system. After purging with helium, the outlet valve (VO1) was closed and the pressure in the reactor increased to 0.7 MPa to prevent water evaporation during the heating phase. The reactor was then heated to the desired temperature, and the pressure was increased accordingly to about 22.8 MPa. After reaching the desired temperature, the reactor was left for 5 min to stabilize. Subsequently, the feed was injected into the reactor by employing a syringe pump (Model 100 DX, Lincoln NE, USA). As soon as the feed injection was complete,

the reaction time (t) was started. Injection of feed solution increased the pressure to about 28MPa. After 15 min of reaction time, a known amount of hydrogen peroxide was injected into the reactor using the syringe pump. After 30 min, the valve (VO1) was opened to allow for effluent gases to pass through the condenser (double pipe H/E), where it was cooled and then depressurized using a high pressure reducing regulator (KHP series Solon, OH, USA). The cooled depressurized effluent passed to a gas liquid separator from which the gases left the separator to pass through an in-line filter to remove any moisture prior to the OMEGA mass flow meter (FMA 1700/1800 series 0–2 L/min, Laval (Quebec), Canada). The mass flow meter was equipped with a totalizer that utilizes a K-factor to relate the mass flow rate of an actual gas to nitrogen, the calibrated reference gas. The actual gas flow rate was calculated by determining the average K-factor for the produced gas by means of the mole fraction of each gas in the stream, as shown by equation (3.1).

$$Avg K_{factor} = \frac{1}{K_{ref} \sum y_i K_{factor(i)}} \quad (3.1)$$

where K_{ref} is the K-factor for the reference gas, and y_i is the mole fraction of the individual components. The actual gas flow rate was calculated by (3.2)

$$Q_{total} = Avg K_{factor} \times Q_{ref} \quad (3.2)$$

where Q_{total} is the mass flow rate of the actual gas and Q_{ref} is the mass flow rate of the reference gas. After passing through the mass flow meter, the product gases were collected in 3L Tedlar gas sampling bags for subsequent analysis.

3.2.5 Gas & liquid analysis

The gaseous products were analyzed by a gas chromatograph (Shimadzu, GC-2014) equipped with a thermal conductivity detector (TCD) and 120/80 D Hayesep stainless steel 3.18 mm ID, 6.2 m nickel packed column (Grace Davidson, City and State). Helium was used as the carrier gas. The gas chromatograph was calibrated using a standard gas mixture of known composition. The analysis was performed manually using 1 ml SGE gas tight syringe (Model number 008100, Reno, NV USA) by collecting the sample from the gas bag. The injection of sample gas into the GC was repeated and the results were averaged to minimize analytical error. The liquid effluent was analyzed for chemical oxygen demand (COD), and pH. Total chemical oxygen demand (TCOD) was measured using HACH methods and test kits (HACH Odyssey DR/2500). pH was measured using an OAKTON portable pH meter (Model WD-35615-22).

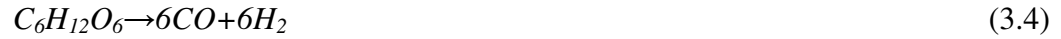
3.2.6 Yield calculations

Calculation of product gas yield and carbon gasification efficiency (CGE) was performed using the procedure of Yu and Antal⁶¹. The aforementioned authors calculated the CGE as mol carbon in gas per mol carbon in feed and measured gas yields as mol of gas species produced per mol of glucose in the feed. The maximum theoretical hydrogen that can be produced from glucose ($C_6H_{12}O_6$) is 12 mol H_2 in accordance with equation (3.3) following the method proposed by Cortright et al.⁸⁴ 6 moles of H_2 is generated directly (Equation 3.4) and another 6 moles of H_2 is formed through the water–gas shift reaction (Equation 3.5).



Equation (3.3) may follow reactions as follows⁸⁴:

Thermal decomposition,



The water–gas shift reaction,



However, carbon oxides may undergo methanation reactions in the presence of hydrogen depicted by Equations (3.6) and (3.7).

Methanation reaction



COD destruction efficiency was selected as a parameter to track the liquid effluent quality and to optimize, together with the maximum hydrogen yield for the gasification and partial oxidation of glucose in supercritical water. The COD destruction efficiency was defined as:

$$COD_{destruction} = \frac{COD_{initial} - COD_{final}}{COD_{initial}} \times 100 \quad (3.9)$$

3.3 Results and discussions

3.3.1 Effect of oxygen to carbon molar ratio (MR) on gas and liquid products

A series of non-catalytic experiments were conducted at 400 °C at different oxygen to carbon molar ratios (MR) to maximize the hydrogen yield in the product gas (Figure 3.2). The maximum yield of hydrogen (0.32 mol/mol feed) and CO (1.13 mol/mol feed) was

observed at a MR of 0.8. Lee et al. observed only 0.08 mol H₂ / mol glucose feed at 480° C while gasifying glucose in supercritical water without oxidant¹³. Introducing hydrogen peroxide at 15 minutes of reaction time, partially oxidized the ungasified intermediate products to CO rich gases; CO later undergoes the water gas shift reaction to produce more hydrogen and carbon dioxide (Equation 3.5). However, hydrogen production decreased while CO₂ increased significantly when the MR was increased to 0.9. This phenomenon can be attributed to the availability of oxygen which converts CO to CO₂ by direct oxidation instead of through the water gas shift reaction. The optimized MR of 0.8 was selected as a base line for the higher examined temperatures of 450 and 500 °C. The production of methane slightly decreased with an increase of MR as shown in Figure 3.2.

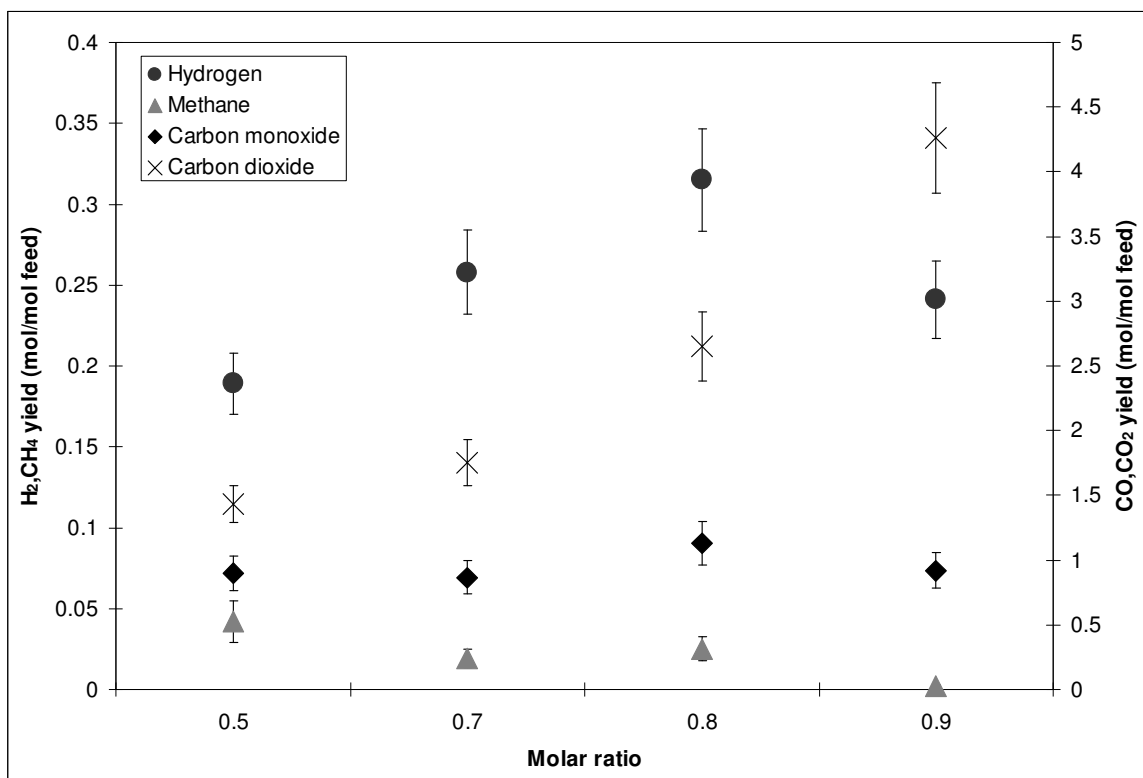


Figure 3.2: Oxygen to carbon molar ratio (MR) effect on gas yield in the non-catalytic partial oxidation at 400 °C.

Figure 3.3 exhibits the liquid effluent characteristic results which show that the COD reduction and carbon gasification efficiency were increased with an increase in MR. The higher the COD reduction, the higher the purity of the liquid effluent. The low COD reduction efficiency with low MR of 0.5 can be explained by the lack of oxidant to oxidize ungasified intermediate products. Increasing the MR to 0.9 gave a 97% COD reduction efficiency. The highest carbon gasification efficiency (86%) was achieved at a MR 0.9. Without using any oxidant, Lee et al. found only 38.6% COD destruction while carbon gasification efficiency was only 16.5% at 480 °C while gasifying 0.6M glucose in supercritical water¹³. The liquid effluent is acidic due to formation of organic acids, mainly acetic acid⁵⁴. The pH was slightly increased with increasing of the MR.

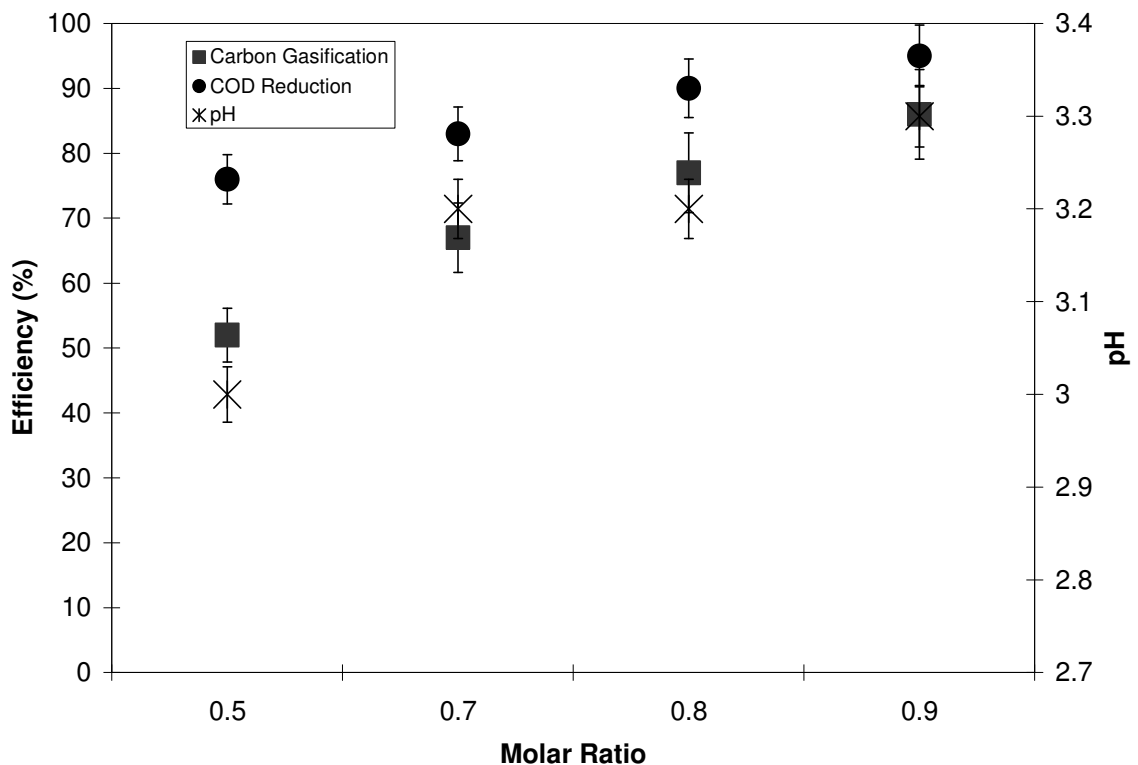


Figure 3.3: Liquid effluent characteristics in the non-catalytic partial oxidation at 400 °C.

3.3.2 Effect of temperature on gas and liquid product distribution

The effect of reaction temperature on the gas yield without use of a catalyst is depicted in Figure 3.4. By increasing the temperature from 400 to 500 °C, the hydrogen yield increased from 0.24 to 0.61 mol/mol glucose feed, which is attributed to the higher conversion at higher temperatures⁸⁵. The CO₂ and CH₄ yield also increased whereas CO remains relatively constant; similar to the results of Holgate and Tester⁵³.

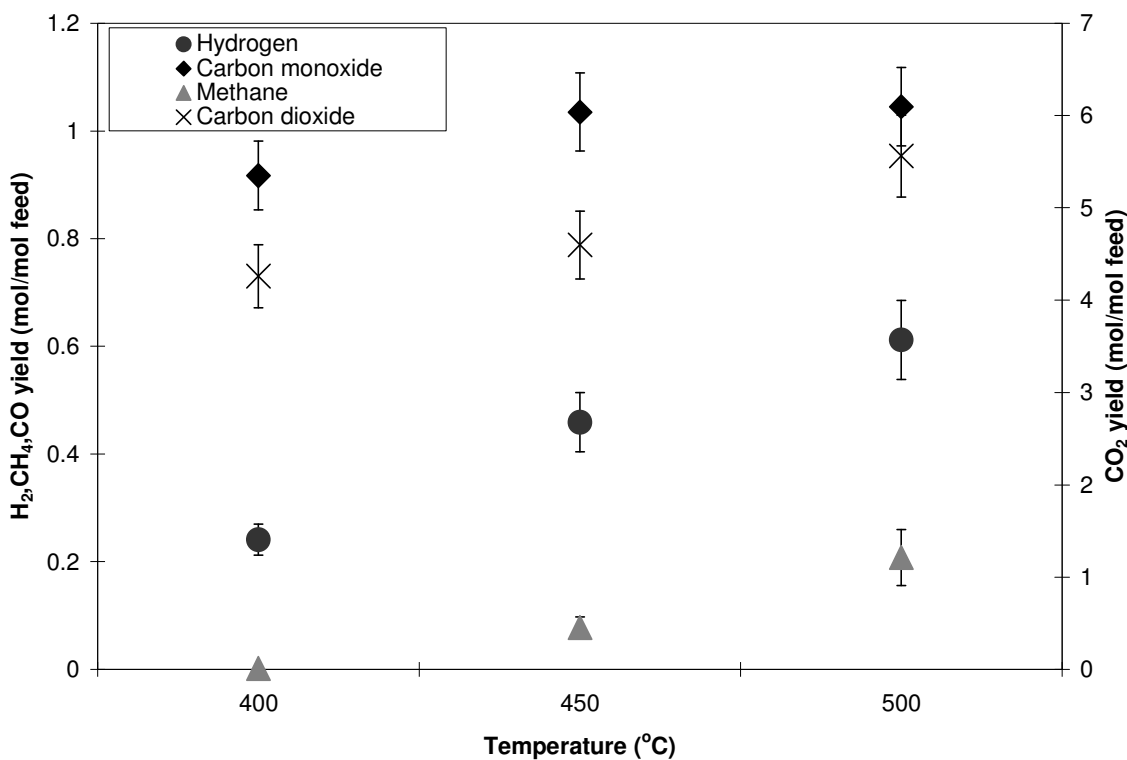


Figure 3.4: Temperature effect on gas yield in the non-catalytic partial oxidation where MR: 0.8.

Figure 3.5 shows the liquid effluent results. COD destruction was found over 90% due to the use of H₂O₂ oxidant. Lee et al. found much less COD destruction (38.6%) at 480 °C without using oxidant while gasifying 0.6M glucose in supercritical water¹³. They

increased the reaction temperature for higher COD destruction. At 600 °C and 750 °C they observed 86.7% and 99.8% COD reduction respectively. The main aim of tracking the COD is to understand the amount of carbeneous products (tar) remaining in the liquid. Similarly, the carbon gasification efficiency was increased with an increase in temperature. Without oxidant Lee et al. found 16.5% carbon gasification efficiency at 480 °C, while it reached 99.7 % at 750 °C¹³. It was seen that pH remained relatively unaffected by the reaction temperature. Accordingly, a temperature of 500 °C and MR of 0.8 were selected as the baseline for the following catalytic experiments.

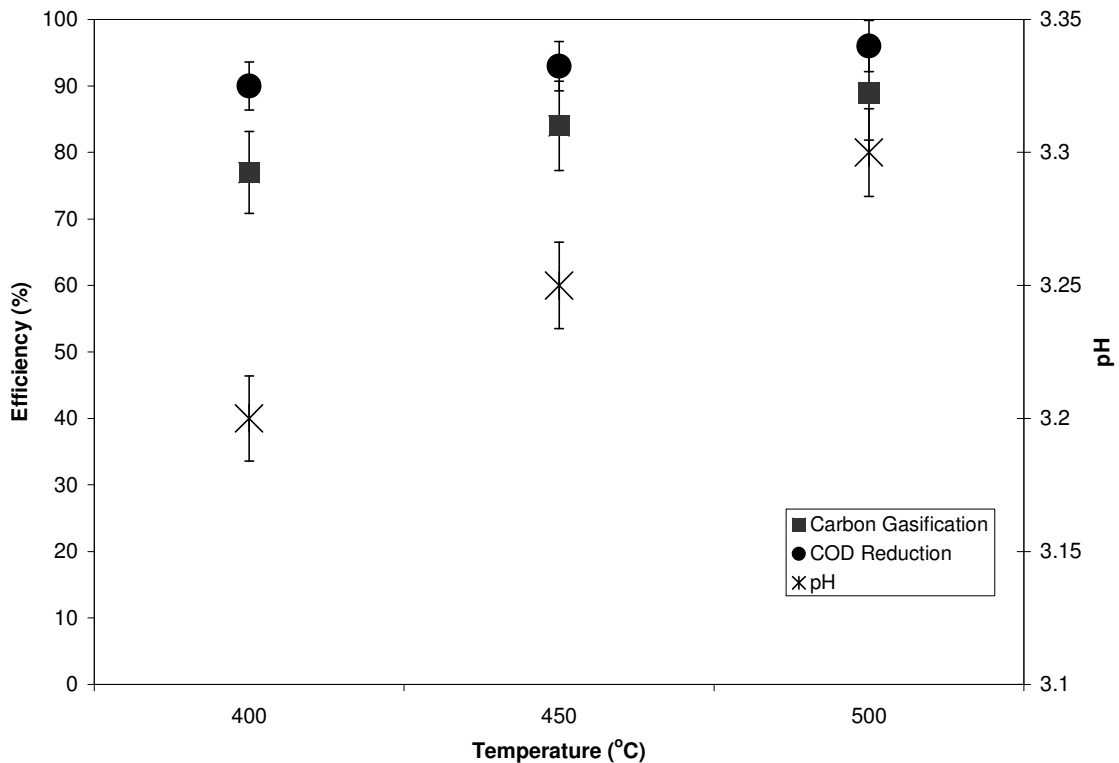


Figure 3.5: Liquid effluent characteristics in the non-catalytic partial oxidation where MR: 0.8.

3.3.3 Effect of the commercial catalyst on gas and liquid product distribution

To examine the effect on gaseous and liquid products, a commercial powder catalyst (i.e. 63wt% Ni on silica-alumina) was evaluated with and without oxidant. Figure 3.6 portrays the gas yield for these experiments.

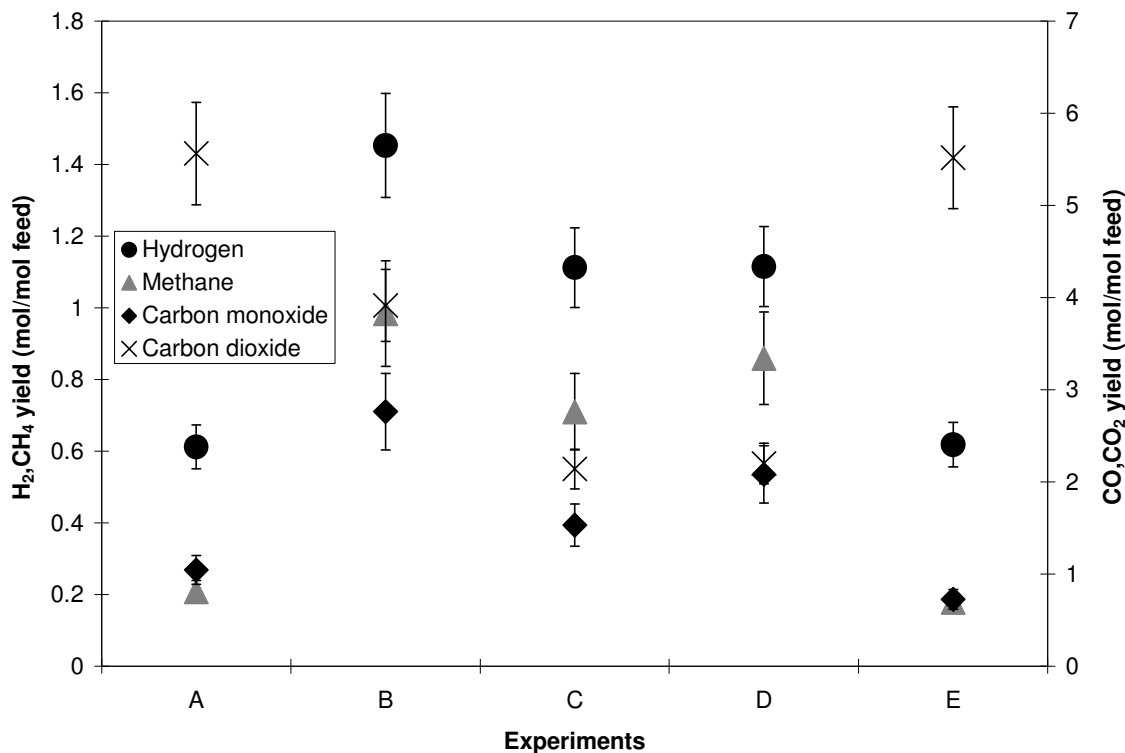


Figure 3.6: Effect of commercial catalyst on gas yield at 500 °C; where A: non-catalytic, MR=0.8; B: catalyst amount 1.0 gm, MR= 0.8; C: catalyst amount 1.0 gm, MR= 0; D: catalyst amount 0.5g, MR= 0; E: catalyst amount 1g, MR= 0.8. H₂O₂ injected after 15 min gasification reaction except experiment E in which H₂O₂ was injected prior to the feed.

In experiment A and B, H₂O₂ (oxidant) was introduced at 15 minutes reaction time while experiment A and B are non-catalytic and catalytic gasification of glucose respectively. Upon introducing the catalyst, the hydrogen yield was enhanced by 2.5 times (0.6

mol/mol feed to 1.5 mol/mol feed). The observed higher amount of CO is attributed to the cracking of intermediate products by the catalyst. Tar was cracked by Ni catalysts to produce gaseous products; especially CO^{24, 81}. Carbon monoxide may undergo the water gas shift reaction catalyzed by Ni to produce more hydrogen. Some of the carbon oxides may undergo methanation reaction catalyzed by Ni. As seen, the CO₂ yield is decreased while CH₄ formation increased by introducing catalyst (comparing experiment A and B). By examining equations 3.3 and 3.5, the CO₂ amount should be increased with increased H₂. This result can be explained as the high loading of Ni (63 wt%) enhanced the methanation reaction of CO₂ (Equation 3.7) which reduced the amount of CO₂, increasing the amount of CH₄ and consuming H₂; otherwise the H₂ yield would be much higher. Experiment C shows the catalytic gasification on the product yield without using any oxidant (H₂O₂). There is a significant difference in the product distribution between gasification and gasification followed by partial oxidation (experiments B and C), showing that the product yield decreased drastically without oxidant. This result confirms that H₂O₂ helps to increase the gasification of unconverted carbon species (tar and char).

Comparing the gasification results without oxidant, using 1 gm and 0.5 gm catalyst (experiment C and D) shows that the amount of catalysts had little influence on the H₂ fraction in the gaseous products. Experiment E was conducted to understand the effect of oxygen on products if H₂O₂ was introduced prior to the feed (i.e. before gasification). Hydrogen and other gaseous yields (experiment E) were found almost the same as without using any catalyst (experiment A), which is attributed to the potential inhibition of catalyst activity by oxidation of the metallic sites of Ni on the catalyst surface.

Hydrogen production was found much higher if the oxidant was introduced after gasification (i.e. at 15 minutes reaction time).

This finding validates our new approach of injecting the hydrogen peroxide (H_2O_2) after gasification reaction for 15 minutes (that is, the feed was injected first and after 15 min, the oxidant was injected). By using this procedure, catalyst inhibition can be mitigated and potentially more hydrogen could be obtained by oxidizing the intermediate products.

The liquid effluent characteristics are reported in Table 3.2. Experiment B shows the highest yield of all types of gaseous products examined corresponding with higher COD destruction. Upon introducing the catalyst, the COD destruction increased to 95%. This result confirms that Ni catalysts have a strong effect on cracking tars and chars. Again without oxidant (experiments C and D), the observed COD destruction is much lower. At a MR of 0.8 (experiment B) the COD reduction efficiency increased from 78% (experiment C without oxidant) to 95%. This result indicates that the presence of oxygen enhances the gasification process, which is confirmed by the higher yield of gases in experiment B compared to C. Industrially, oxygen or air could be used instead of H_2O_2 to lower the operating cost.

Table 3.2: Liquid effluent characteristics at 500 °C with commercial Ni/silica-alumina (63wt% Ni).

Experiments	MR	p ^H	Carbon gasification efficiency (%)	COD reduction efficiency (%)
A	0.8	3.3	87	91
B	0.8	3.2	107	95
C	0	3.2	90	78
D	0	3.2	82	78
E	0.8	3.3	109	82

A: non-catalytic, MR=0.8; B: catalyst amount 0.5g, MR= 0.8; C: catalyst amount 0.5g, MR= 0; D: catalyst amount 1g, MR= 0; E: catalyst amount 1g, MR= 0.8. (H₂O₂ injected after 15 min gasification reaction except experiment B in which H₂O₂ was injected before the feed).

3.3.4 Effect of the synthesized catalyst loading on gas and liquid product distribution

From the previous section it was seen that the excess loading of Ni increase methanation reaction, there we synthesized our own catalysts to evaluate the effect of Ni loading. Figure 3.7 portrays the effect of nickel loading on the gaseous product distribution using the synthesized metallic Ni on θ -alumina catalyst. The maximum yield of hydrogen, which coincided with the maximum COD reduction efficiency, was observed at 11 wt% loading. The trend of hydrogen yield was similar to that reported for gasification of lignin using Ni/MgO⁸⁶ where the H₂ yield increased from 1.9 to 11% by increasing the amount of nickel deposited on MgO from 5 to 15 wt% Ni/MgO. However, as the amount of deposited nickel increased to 20 wt%, the H₂ yield decreased to 9.3%. It was also noted that by increasing the Ni loading to 18 wt%, a significant decrease in CO₂ was found along with an equivalent increase in methane (Figure 3.7). This is possibly due to CO₂

reacting with hydrogen to form methane which could have consumed some of the hydrogen and eventually decreased its yield (Equation 3.7). The lower available surface area with increased loading (Table 3.1: physical properties of the synthesized catalysts) may have enhanced the methanation reaction.

To investigate the effect of metal size on hydrogen yield, the 11 wt% Ni/ θ alumina catalyst pellet was crushed to a mesh size of 0.2-0.5 mm. As shown in Figure 3.6 (11wt%Ni*), the hydrogen yield increased from 1.06 to 1.18 mol/mole glucose.

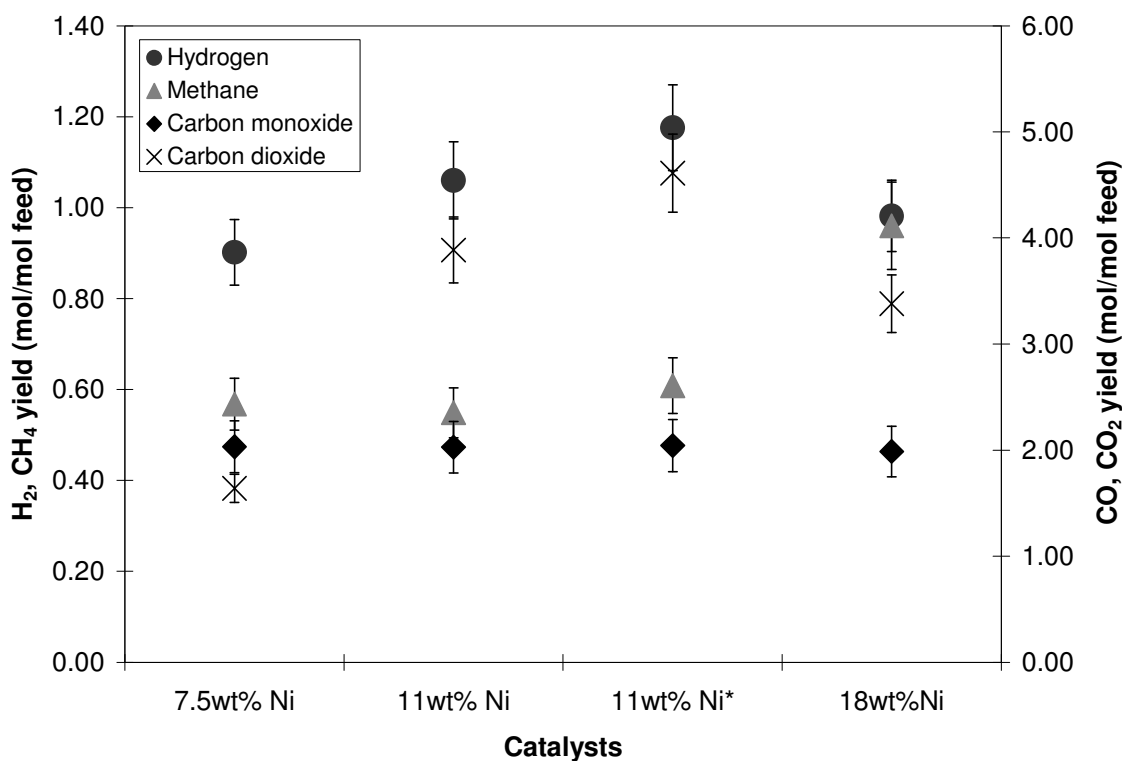
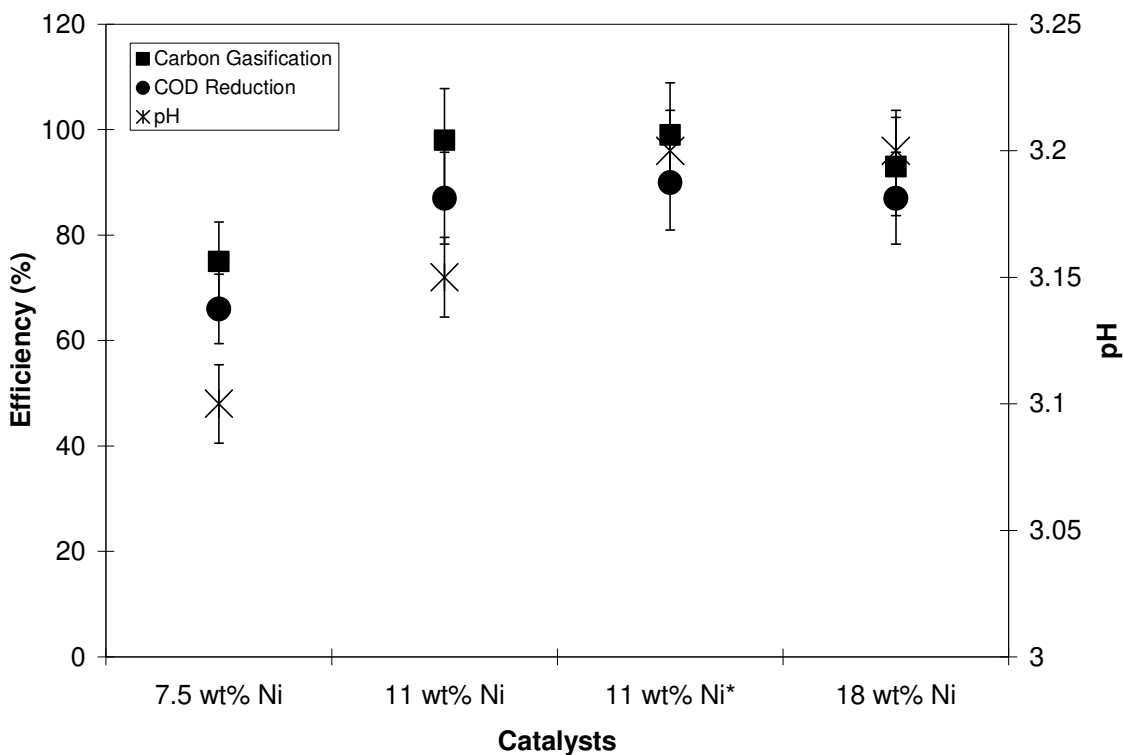


Figure 3.7: Effect of nickel loading on gas yield at 500 °C, where MR: 0.8. *crushed catalyst.

The COD reduction was found slightly increased from 87% (uncrushed catalysts) to 90% (crushed catalysts). This result can be explained as crushing of the catalyst helps open

any blocked active metallic pore walls that were blocked during metal salt impregnation on the support surface during synthesis. The liquid effluent remained acidic with the pH remaining relatively constant.



**Figure 3.7: Effect of nickel loading on liquid effluent at 500 °C and MR 0.8.
*Crushed catalyst.**

3.4 Conclusions

Using a new approach in which gasification is followed by partial oxidation, the production of hydrogen was enhanced compared to only gasification or partial oxidation of glucose in supercritical water. The presence of oxygen after gasification for 15 minutes enhanced the decomposition of the intermediate products to form gaseous products. The gaseous products were composed mainly of carbon dioxide (CO₂), carbon monoxide

(CO), hydrogen (H₂), and methane (CH₄). Nickel catalysts were found to facilitate cracking of the tar and char intermediates. The hydrogen gas yield and destruction COD increased with an increase in temperature. For partial oxidation, the optimum oxygen to carbon molar ratio (MR) was found at 0.8. Among the different metallic Ni loadings (7.5, 11, 18 wt%) on θ -Al₂O₃, 11 wt% was found optimum in terms of hydrogen yield. Increasing the metallic loading from 11wt% to 18wt% decreased the hydrogen yield along with increasing the methane formation by methanation of carbon dioxide. Hydrogen production was found sensitive to the catalyst size as crushed catalysts enhanced the hydrogen yield and COD destruction. Commercial Ni/silica–alumina catalyst (0.1 mm average diameter) enhanced the yield of H₂ by 0.3 mol/mol glucose due to the higher active metal surface area (four times) compared to the synthesized catalysts (3.0 mm average diameter). However, with an excess loading of nickel (63wt%), the methanation reaction of carbon dioxide was enhanced. The COD destruction efficiency reached as high as 97%; i.e. almost clear liquid effluent was formed which could be disposed to lake or sand without further treatment. The relatively low hydrogen yield (maximum 1.5 mol/mol glucose) obtained was due to limitations in reactor temperature i.e. 500 °C.

Chapter 4

Production of hydrogen-rich gas through supercritical water gasification of glucose using La-modified Ni/Al₂O₃ catalysts

In this chapter, synthesized Ni/Al₂O₃ catalyst was modified through La adsorption. Commercial alumina pellets, synthesized alumina nanofibers were taken as the catalyst support for incipient impregnation while a sol-gel process were adopted for synthesizing the Ni-La-Al-O nano-structure as catalyst. Evaluation of fresh and spent catalysts was conducted. La adsorption of the Ni/Al₂O₃ catalyst was found to increase the activity and production of hydrogen rich gaseous yield and reduce methanation reactions. Nano catalysts were found to be very active towards the production of hydrogen. This chapter is mostly a reproduction from the article by the author submitted to Industrial Engineering & Chemistry Research⁸⁷: Production of hydrogen-rich gas in Supercritical Water from Glucose using La-modified Ni/Al₂O₃ catalysts.

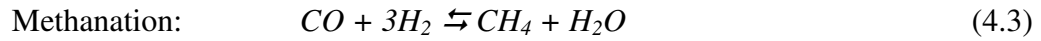
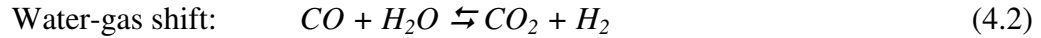
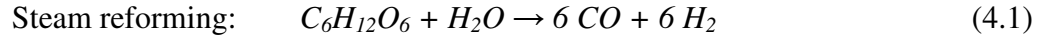
4.1 Introduction

Hydrogen (H₂) is considered as one of the most promising potential clean energy sources for sustainable development and has a high energy density by weight⁸⁸. One of the most promising renewable sources for hydrogen generation is from the gasification of waste biomass. Gasification of waste biomass allows destroying hazardous organic matters into

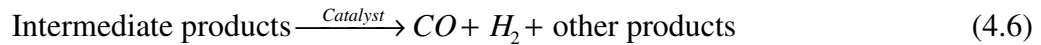
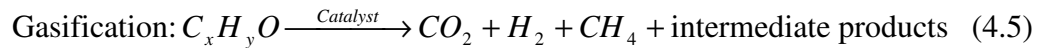
light gases, such as H₂, CH₄, CO₂ and CO⁸⁹. Hydrogen can be used in fuel cells for power generation while the syngas (H₂+CO) can be used for producing chemicals and liquid fuels. Syngas is also used for cleaner combustion technology, as well as direct feeding for next generation high efficiency internal combustion engines⁹⁰.

In recent years, low quality biomasses such as agricultural and municipal waste have received significant attention to produce syngas via the gasification process. However, a large amount of energy is lost for drying these wet feedstocks, which significantly decreases the overall thermal efficiency of a gasifier^{69, 89}. In addition, formation of char and tar from the biomass during gasification decreases the gas yield¹⁶. However, gasification of biomass using supercritical water (SCW) has the potential to overcome these barriers. SCW offers an attractive alternative to avoid the energy intensive drying process, particularly when the water content is above 30%⁶. Above 31% moisture content, the energy conversion efficiency of SCW gasification is always higher than thermal gasification, pyrolysis, liquefaction, or anaerobic digestion⁵. The lower dielectric constant and weaker hydrogen bonding of water in the supercritical state compared to water under ambient conditions makes SCW similar to organic solvents. Therefore, organic compounds that are present in the biomass have enhanced solubility in SCW, with the various reactions taking place in a single fluid phase. The high diffusivity of SCW is also favorable for enhanced mass transfer during the gasification process⁹¹. The high effective diffusion coefficient of SCW (about 100 times higher than that of ambient water) diminishes the chance of any mass-transfer gradient in the catalyst internal surface area⁹. Using the SCW process also provides high pressure product that eliminates further compression steps, contributing to its energy efficiency.

The advantage of using glucose as the model compound of biomass is that it is soluble in water and represents a wide fraction of biomass compounds present in both agricultural waste and sewage sludge². In this study, glucose was used for the biomass analog for the activity tests. During glucose gasification in SCW, a group of competing reactions occur as follows¹:



As the objective of biomass gasification in supercritical water is generally hydrogen production, reactions (4.3) and (4.4) must be restrained as CO reacting with water to form CO₂ and H₂ is desired in reaction (4.2). Other than the gaseous products mentioned above, some intermediate products (char and tar) are also formed during SCW gasification which can be minimized by partial oxidation to enhance the gasification process and the resulting yield of hydrogen^{11, 75}. By employing a suitable catalyst, the H₂ production can be enhanced, approximated by the following general reactions:



In the last chapter we showed the non-catalytic effects of temperature and oxygen to carbon molar ratio (MR) on hydrogen yield from glucose and on the chemical oxygen demand (COD) destruction. Within the reactor limitations, 500 °C and 0.8 MR were found optimized for the production of hydrogen. 500 °C is considered as a moderate

temperature for SWG producing methane rich gases even using a catalyst¹². However, a proper design of catalyst may produce hydrogen rich gas instead of methane rich gas at moderate temperatures.

To reduce the temperatures (i.e. activation energy) required for the total conversion of biomass, the use of catalysts is still in its infancy. Homogeneous materials like alkali catalysts are readily miscible with water and found very effective for biomass gasification. Lu et al.⁷ used K_2CO_3 for biomass gasification in SCW and found that the H_2 yield was two times higher than that without catalyst at the same conditions. Watanabe et al.¹⁵ studied the effect of both base (NaOH) and metal (ZrO_2) catalysts on the gasification of lignin in SCW. NaOH proved 2-5 times more effective than ZrO_2 for hydrogen production. However, alkali catalyst recovery, re-use and reactor corrosion problems are significant concerns with these types of catalysts¹⁶.

Using a supported solid catalyst can avoid these separation and reactor corrosion problems. As well, heterogeneous metal catalysts are also relatively easy to recover, helping reduce the cost of the catalyst. However, chromium, tungsten, platinum, and palladium have shown very low activity⁶⁹. A wide range of heterogeneous catalysts for SCWG was investigated by Sato et al.⁷³. They found that the activity order is $Ru/\gamma-Al_2O_3 > Ru/C > Rh/C > Pt/\gamma-Al_2O_3, Pd/C$ and $Pd/\gamma-Al_2O_3$. Although Ru showed very good activity, even a trace amount of S can cause Ru catalyst poisoning²⁰. In addition, Pt group noble metals are prone to methanation of carbon oxides in the presence of hydrogen, which increases with an increase of temperature²¹. Furthermore, the relatively high price of noble metals makes these catalysts less attractive if suitable low cost heterogeneous catalysts can be formed.

Using nickel, a relatively inexpensive metal, Furusawa et al.²³ found that carbon and hydrogen yields increased from 8.3% and 14.1% to 22.7% and 46.2% respectively when 0.05 g of 20 wt% Ni/MgO catalyst was added at 400 °C. A nickel catalyst was also found to be favorable for cracking tar molecules and promoting the WGS reaction²⁴. When compared to the available alternative catalysts, nickel displays several favorable attributes including high activity and low cost. Nickel also has a high melting point (1453°C) which is very important for a biomass gasification catalyst.

However, the amount of nickel loading on the support is a key factor for a successful catalyst synthesis. Sato et al.⁸⁶ reported that a maximum hydrogen yield was obtained with 10wt% Ni/MgO during the gasification of lignin in SCW. Beyond 10wt% nickel loading, the hydrogen production decreased and the amount of methane formation increased. In the last chapter, it was found that the maximum yield of hydrogen was obtained with 11wt% Ni on θ -alumina and hydrogen production decreasing and the methane increasing above this loading. At 18wt% Ni loading on θ -Al₂O₃, a reduction of carbon dioxide was observed with an equivalent amount of methane formation indicating enhanced methanation of CO₂. The CO product remained nearly constant using 7.5 to 18wt% Ni loading on θ -Al₂O₃,⁷⁵ indicating that CO did not participate significantly in the methanation reaction. Methane is very stable in SCW, and does not convert into any smaller molecules¹³.

Conventional catalysts have low surface area per unit volume which limits the contact area between the reactants and the metallic surface of the catalysts. Nano catalysts with high surface areas and aspect ratios can help eliminating the challenge. It is also evident

that high surface area catalysts increase the activity and selectivity by increasing the active catalyst sites for the reactants.

Production of hydrogen rich gases, and inhibition of the methanation reaction of CO₂ motivated the present study. In this study we wanted to synthesize low cost catalyst with favorable selectivity to produce hydrogen while destroying any organic matter completely so that no other processing is necessary for further treatment of liquid effluent from the reactor. In this regard, Ni on La impregnated Al₂O₃ catalysts were investigated for SCW gasification of glucose for the first time. Kim previously found that Cerium acts as a promoter of the WGS reaction when performing auto exhaust emission control²⁶. La and Ce have very similar chemical properties with respect to cation charge, ionic radii, and stability of organic and inorganic complexes²⁷. Therefore La may act as promoter for water gas shift reaction in SCW and thus increase hydrogen yield. In addition, it is hypothesized that the La₂O₃ acted as an adsorbent which selectively adsorbs carbon dioxide^{29,92}; as a result methanation of CO₂ may be reduced.

Other than impregnation on alumina nanofibers to synthesize nano-catalysts, ultrafine NiO-La₂O₃-Al₂O₃ aerogel catalyst was also prepared by combination of a sol-gel method and a supercritical drying technique. Aerogels show promise in catalytic applications due to their unique morphological and chemical properties. An aerogel is a solid-state substance similar to a gel where the liquid component is replaced with gas. Aerogels made with aluminum oxide are known as alumina aerogels. These aerogels, especially when "metal-doped" with another metal, are used as catalysts. The main advantages of sol-gel techniques for the preparation of materials are low temperature of processing, versatility, flexible rheology allowing easy shaping and embedding.

4.2 Experimental

The model compound glucose, metallic precursors nickel nitrate hexahydrate [Ni(NO₃)₆·6H₂O], lanthanum nitrate hexahydrate [La(NO₃)₃·6H₂O], reagent grade 98% Al(III) isopropoxide, 99.5% isopropanol, 99.7% acetic acid were obtained from Sigma-Aldrich (Mississauga, Ontario, Canada), and used as received. Hydrogen peroxide (H₂O₂) was added as an oxidant for partial oxidation of intermediate products using a 50% H₂O₂ in water solution as received from EMD Chemicals Inc. De-ionized water, was obtained from an ultrapure water system (EASY pure LF, Mandel Scientific co, model BDI-D7381) to prepare the solutions. For catalyst preparation, γ -Al₂O₃ pellets with 3 mm average particle diameter, 198 m²/gm BET surface area and pore volume of 0.421 cm³/gm received from Aldrich (Mississauga, Canada). The BET (Brunauer-Emmett-Teller) surface area, pore size and distribution, and pore volume were determined from nitrogen adsorption and desorption isotherm data obtained at 77 K with a constant-volume adsorption apparatus (Micromeritics ASAP 2010) using N₂ as the probe gas. The prepared samples were degassed at 150°C for 5 hour before the nitrogen adsorption experiments.

4.2.1 Catalysts Synthesis

4.2.1.1 Incipient impregnation

The La₂O₃ doped 18wt% Ni/ θ -Al₂O₃ catalysts were prepared via incipient wetness technique, as described previously²². The alumina nanofibers were synthesized in supercritical carbon dioxide (scCO₂) as a green solvent using alumina isopropoxide and acetic acid³¹ and described in chapter 7. The as received γ -Al₂O₃ and alumina nanofibers

were transformed to θ -Al₂O₃ which has better high temperature properties by calcining at 1050 °C¹². θ -Al₂O₃ was found to be stable in SCW. On the other hand γ -Al₂O₃ was found to be dissolved in SCW. It may be due the defects in crystalline structure of γ -Al₂O₃⁸². θ -Al₂O₃ has monoclinic symmetry in catalyst structure⁸². In addition, converting γ -Al₂O₃ to θ -Al₂O₃ pore size increased which allows better impregnation of active metals, and penetration of bulky intermediate products formed by SCWG. The synthesis process includes two steps: (i) modification of the support θ -Al₂O₃ with La₂O₃ followed by (ii) nickel loading, or reversed when studying order of addition. The solutions were prepared by dissolving (Ni(NO₃)₂·6 H₂O or La(NO₃)₃·6 H₂O) salts in de-ionized water. 130 vol% of pore volume of support θ -Al₂O₃ was used to prepare the nitrate solutions. During the impregnation step, the nitrate solutions were introduced to the θ -Al₂O₃ with continuous mixing. After impregnation, the resultant samples were dried slowly (0.5 °C/min) and then treated with NH₃-H₂O vapor as described previously^{22, 93} to convert the metal salt anion to ammonium salt. The NH₃-H₂O vapor treated sample was dried to 120 °C at a rate 1°C/min and then to 250 °C at a rate 1.5 °C/min for one hour. This thermal treatment also helped to remove ammonium salts by sublimation. Finally, the catalysts were reduced using hydrogen (5% by volume) in nitrogen. A block diagram showing the sequence of catalyst synthesis steps is given below:

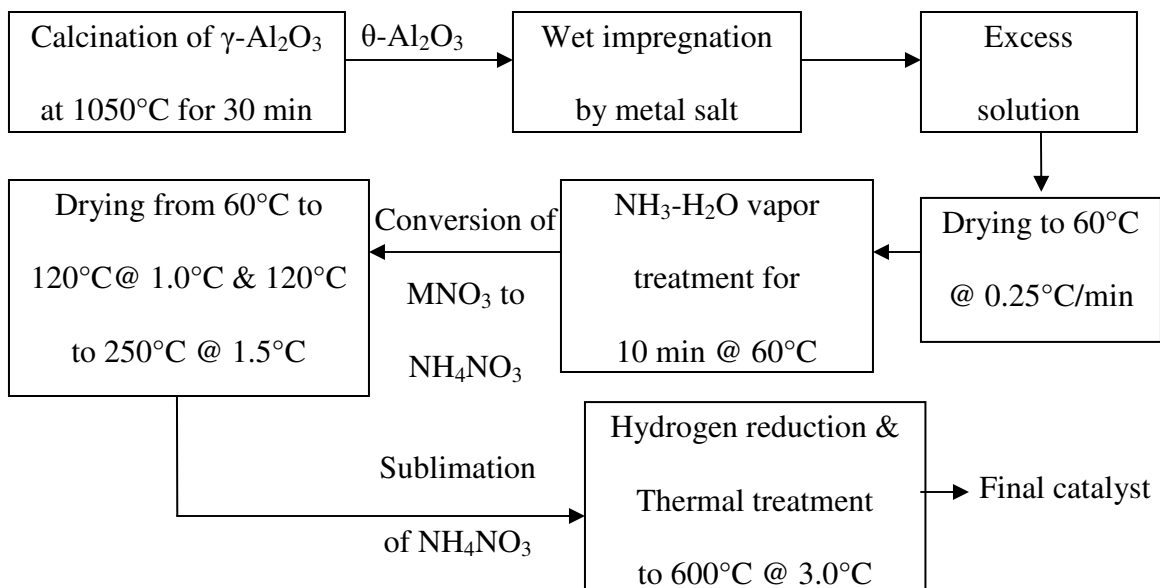


Figure 4.1: Block diagram of catalyst synthesis.

4.2.1.2 Sol-gel technique

In the second approach for catalyst synthesis, the required amount of aluminum isopropoxide (i.e. 20 gm for synthesizing 5 gm of catalyst) dispersed in isopropanol (80 ml) was placed in a 250 ml flask and the resultant mixture was kept under vigorous stirring at 75°C for one hour. To the cloudy sol, 0.3 ml of 1M nitric acid was added for peptization (the process responsible for the formation of stable dispersion of colloidal particles) and the sol was refluxed with stirring at 75°C for 1 h to obtain clear sol. Here acetic acid was used as the polycondensation agent for slow hydrolysis of aluminum isopropoxide. An appropriate amount of lanthanum nitrate and nickel nitrate were dissolved in isopropanol and the individual solutions were then added to the clear boehmite sol at 15 minutes intervals, with the resultant mixture refluxed at 75°C for 1 h with vigorous stirring. The transparent sol turned to olive green upon addition of the

nickel solution and sudden gelation was observed. The sol was kept for three days at room temperature in a sealed flask for aging. After aging, the resultant gel was washed with acetone to remove any traces of water, nitric acid, etc. This washed gel was dried in scCO₂ at 4000 psi and 60 °C to remove unreacted acid, alcohol and ester from the gel formation. The rate of venting CO₂ was approximately 0.2ml/min to prevent collapse of nano-structured morphology. At the end of drying, a porous aerogel was obtained which was calcined to 200 °C in air at a rate of 1.5°C/min to prevent the collapse of porous structure keeping the high surface area. The catalysts were then reduced using hydrogen (5% by volume) in nitrogen at 600 °C.

4.2.2 Catalyst Activity Tests in Supercritical Water

The activity of the synthesized catalysts was established using a 600 ml batch autoclave reactor constructed from Hastelloy C-276, equipped with 1.5 kW electric furnace for heating (Autoclave Engineers, Erie, Penn., USA) as described in the last chapter. Briefly, in a typical experiment the required amount of catalyst was loaded along with 70 ml of deionized water which were injected into the reactor, which was finally purged with He for 10 minutes. The reactor was then pressurized to 0.7MPa with helium in order to prevent water evaporation and then heated to 500 °C. With the increase of temperature the reactor pressure increased to about 28 MPa at 500 °C. The required amount of glucose solution was then pumped into the reactor using a syringe pump (Isco Model 100 DX, Lincoln NE, USA). The initial reaction time (t_0) was started upon injection of the feed into the reactor. The oxidation agent H₂O₂ was injected after 15 minutes of reaction time with the syringe pump to facilitate partial oxidation of the reaction intermediates. After 30 min reaction time, the products were cooled down to ambient temperature using

a double pipe heat exchanger and separated by a gas-liquid separator operating by sudden expansion (from 0.635 inner diameter of stainless tube to 3 liter volume vessel). The product gas was then passed through a 2 micron filter to remove any remaining moisture and passed through an OMEGA mass flow meter (FMA 1700/1800 series 0-2 L/min, Laval, Quebec, Canada). The product gases were then collected in a 3L volume Tedlar gas sampling bag for subsequent analysis.

4.2.3 Products Analysis

To determine the percent of gasification and hydrogen yield, the product gases were analyzed by gas chromatography (Shimadzu, GC-2014) using a 120/80 D Hayesep stainless steel Nickel packed column (Grace Davidson) with dimensions of 6.2 m x 3.18 mm, a thermal conductivity detector (TCD) and helium as the carrier gas. The gas yield, and carbon gasification efficiency (CGE), were calculated as shown in equations 4.7 and 4.8, as reported by Yu et al⁶¹.

$$yield = \frac{mol\ of\ gas\ produced}{mol\ of\ glu\ cosine\ in\ feed} \quad (4.7)$$

$$CGE = \frac{mol\ carbon\ in\ produced}{mol\ carbon\ in\ feed} \times 100\% \quad (4.8)$$

The liquid effluents from the SCWG experiments were analyzed to measure the Total Organic Carbon (TOC) content using a TOC-VCPH (Shimadzu Instruments). The TOC decomposition X, was used to evaluate the extent of decomposition, as defined by:

$$TOC\ decomposition,\ X = 1 - \frac{[TOC]_e}{[TOC]_0} \quad (4.9)$$

where $[TOC]_0$ is the initial TOC and $[TOC]_e$ is the residual TOC after reaction.

4.3 Results and Discussion

In this study the synthesis and comparative performance of Ni/ θ -Al₂O₃ and Ni-La/ θ -Al₂O₃ catalysts were investigated for the production of hydrogen from glucose using supercritical water gasification (SCWG). The effect of La₂O₃ for promoting hydrogen yield and reducing the methanation activity was studied. The reaction mechanism is described.

4.3.1 BET Surface area, Pore size, Pore volume

The surface area, average pore diameter and pore volume of the prepared catalysts are summarized in Table 4.1 using BET method.

Table 4.1. Physical properties of the synthesized catalysts.

	Catalysts	S _{BET} (m ² /g)	D _{pore} (nm)	V _{pore} (cm ³ /gm)
A	θ -alumina pellets (commercial)	57	17.4	0.248
B	7.5wt%Ni/ θ -alumina	51	14.0	0.179
C	11wt%Ni/ θ -alumina	49	13.8	0.154
D	18wt% Ni/ θ -alumina	46	10.2	0.118
E	3.5wt% La ₂ O ₃ / θ -alumina	60	15.9	0.237
F	7wt% La ₂ O ₃ / θ -alumina	50	11.4	0.143
G	3.5wt% La ₂ O ₃ -18wt% Ni/ θ -alumina	48	12.9	0.154
H	3.5wt% La ₂ O ₃ -18wt% Ni/ θ -alumina*	46	6.8	0.078
I	3.5wt% La ₂ O ₃ -18wt% Ni/ θ -alumina (crushed)	44	17.8	0.202
J	3.5wt% La ₂ O ₃ -18wt% Ni/ θ -alumina nanofiber	101	15.0	0.373
K	Nano structured 3.5wt% La ₂ O ₃ -18wt% Ni- alumina (sol-gel)	339	4.2	0.381

S_{BET} = BET surface area; D_{pore}= Adsorption average pore diameter (4V/A); V_{pore}= Single-point adsorption total pore volume per gram. * La₂O₃ impregnated after Ni loading. All catalysts were reduced at 600 °C.

After nickel loading the surface area (S_{BET}), average pore diameter (D_{pore}), and pore volume (V_{pore}) of the catalysts decreased (Catalyst A to D). Pore blocking by the nickel species is believed to be mainly responsible for the reduced surface area and pore volume.

Contrary to Ni loading, it is interesting to see that after La_2O_3 loading on alumina the surface area was slightly increased (catalyst E compared to unloaded alumina A) indicating that La_2O_3 was primarily deposited on the outer surface of the alumina support. The large diameter of the La^{3+} ions hinders diffusion into the alumina pores and is subsequently dispersed as a monolayer on the top of the θ -alumina surface⁹⁴. However, increasing the amount of lanthanum to 7wt% onto Al_2O_3 (catalyst F) also decreased the surface area and pore volume attributed to blockage of inter-crystalline pores.

When depositing the same amount (3.5 wt%) of La on alumina before Ni loading (catalyst G) a higher surface area, pore diameter and pore volume were found compared to La loaded after Ni loading (catalyst H). This can be attributed to La being deposited on active nickel on top of the catalyst surface.

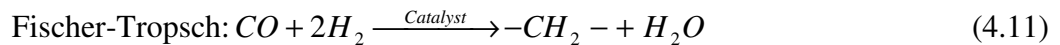
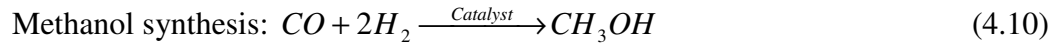
The Nano catalysts showed significantly higher surface areas. Sol-gel derived catalysts showed the highest surface area with smallest average pore size (micro pores) among the catalysts evaluated. Formation of microporous network may be the reason for the high surface area. Another reason is that the sol-gel derived catalyst support was not converted to θ - Al_2O_3 like the other catalyst supports, as all the metals and support were mixed together during synthesis. The nanofiber catalysts at θ phase of the support showed much higher surface areas than the commercial catalysts of the same phase.

4.3.2 Catalysts evaluation

In the last chapter, gasification followed by partial oxidation at 15 minutes reaction time was found beneficial for the higher hydrogen production and organic carbon destruction. Within the reactor limitation at a reaction time of 30 minutes and temperature of 500 °C, oxygen to carbon molar ratios (MR) 0.8 was found optimum towards hydrogen production. In this investigation, the catalytic activity of both plain Ni and La modified Ni on θ -Al₂O₃ catalysts was analyzed with and without oxidant in a batch autoclave reactor using glucose as the biomass model compound. When oxidant was applied, MR(carbon to oxygen molar ratio) 0.8 at 15 minutes reaction time was used for partial oxidation of unconverted organic compounds.

4.3.2.1 Effects of types of catalysts

Figure 4.2 displays the product gas yield data for the three different Ni loadings on θ -Al₂O₃ catalysts used in the gasification of glucose in SCW. One can see from Figure 4.2 that with the variation of nickel loading from 7.5 to 18wt%, the hydrogen and carbon monoxide yields were not affected significantly. The hydrogen to carbon monoxide ratio is around 1:2, which can be considered a poor syngas ratio. For production of methanol or diesel (Fischer-Tropsch), the syngas ratio (hydrogen:carbon monoxide) should be higher than 2:1 (equations 4.10 and 4.11).



As also shown in Figure 4.2, the CO yield remains almost constant while the formation of methane increased and the formation of carbon dioxide decreased for Ni loading 11 to 18wt%. Enhancement of the methanation reaction of CO₂ with an increased amount of nickel has been considered to be responsible for this increased methane and decreased CO₂ formation. This observation is consistent with the results reported by Youssef et al⁹³ using 7 to 18wt% Ni on alumina catalysts under similar reaction conditions. Loosely bonded nickel on the alumina support deposited by excess nickel loading may be responsible for this methanation reaction. As the methanation reaction consumes hydrogen produced from the gasification reaction, the hydrogen yield would be higher with increased Ni loading if this methanation reaction could be restrained.

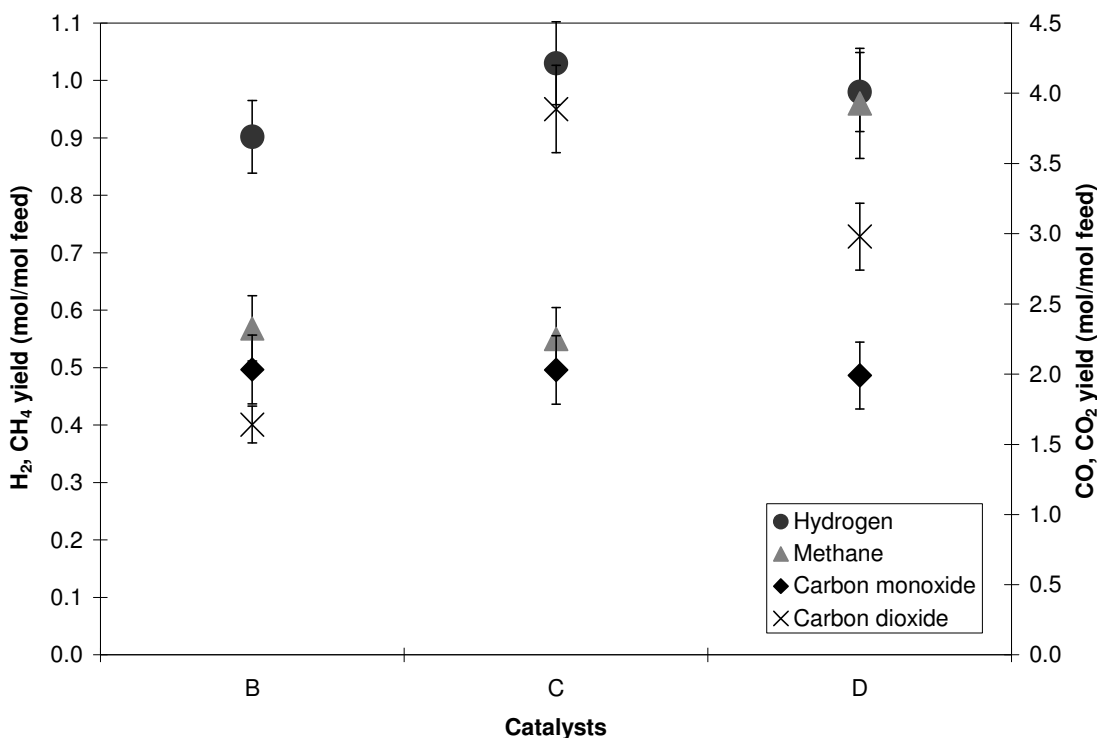


Figure 4.2: Effect of Ni loading on theta alumina pellets on gaseous product where, B) 7.5wt% Ni/ θ Al₂O₃, C) 11wt% Ni/ θ Al₂O₃, D) 18wt% Ni/ θ Al₂O₃ T= 500 °C, MR=0.8, t=30 min, P=28MPa, Feed= 0.25M Glucose.

To further examine the role of lanthanum on the gaseous products, La_2O_3 on alumina catalysts were also evaluated under the same reaction conditions. From Figure 4.3, it is observed that lanthanum on alumina (cat. E and cat. F) increased the hydrogen and carbon dioxide yield and decreased the carbon monoxide and methane formation significantly compared to nickel on alumina (cat. D). This result confirms that lanthanum oxide acts as co-catalyst rather than promoter in SCWG.

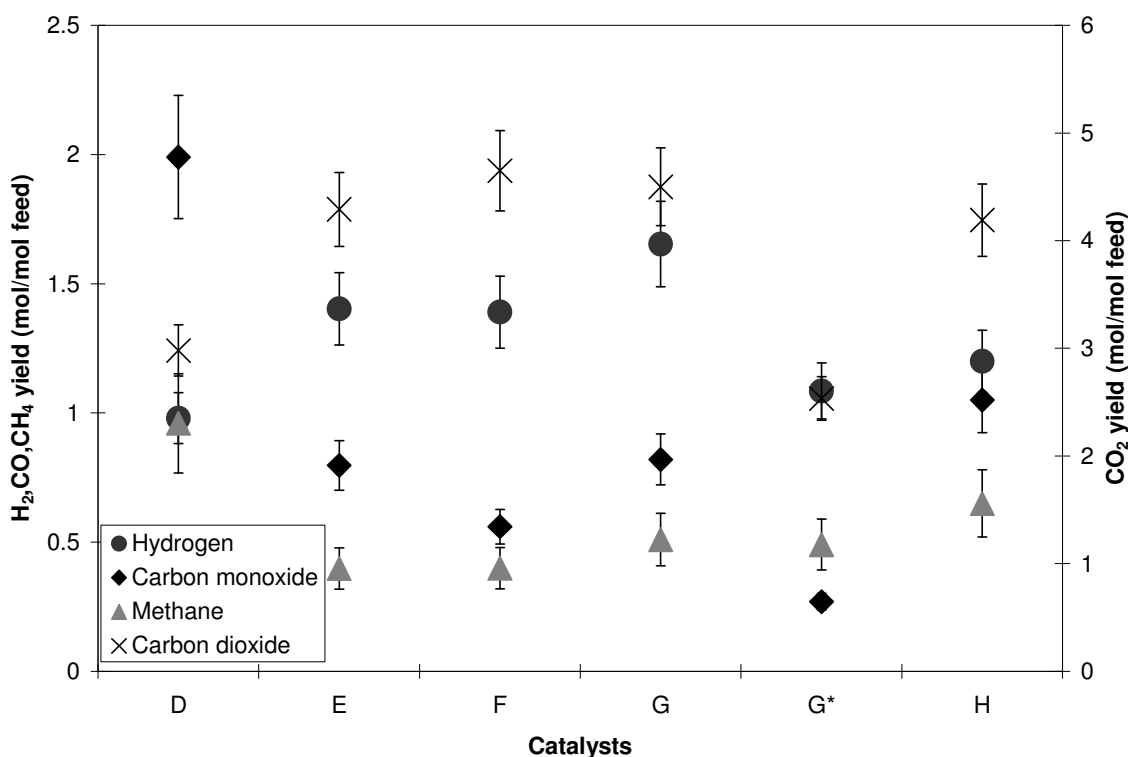


Figure 4.3: Effect of Ni, La_2O_3 and Ni- La_2O_3 on theta alumina pellets on gaseous product where, D) 18wt%Ni/ θ Al_2O_3 , E) 3.5wt% La_2O_3 / θ Al_2O_3 , F) 7 wt% La_2O_3 / θ Al_2O_3 , G) 18wt% Ni -3.5wt% La_2O_3 / θ Al_2O_3 (La_2O_3 impregnated before Ni loading), G*) 18wt%NiO -3.5wt% La_2O_3 / θ Al_2O_3 (oxidized at 500 °C before reaction), H) 18wt% Ni -3.5wt% La_2O_3 / θ Al_2O_3 (La_2O_3 impregnated after Ni loading); T= 500 °C, MR=0.8, t=30 min, P=28MPa, Feed= 0.25M Glucose, Catalyst= 1.0gm.

With an increased loading of lanthanum oxide (cat. F), the hydrogen yield was not affected compared to catalyst E (lower La loading), while the carbon monoxide formation decreases and the carbon dioxide formation increases. This observation can be attributed to oxidation of CO, whose concentration was slightly decreased with an excess loading of lanthanum. Comparing catalyst D with catalysts E and F, a higher hydrogen yield with corresponding lower carbon monoxide formation is observed and attributed to lanthanum as a co-catalyst of the WGS reaction, which consumes carbon monoxide. The observed lower yield of methane and higher yield of CO₂ with La on alumina can be attributed to the inhibition of the methanation reaction and promotion of the WGS reaction by La.

The loading of 18wt% nickel on La modified alumina catalyst (cat. G) increased the hydrogen yield 25 mol% compared to catalyst E and F and 65mol% compared to catalyst D (Figure 4.3). Comparing catalyst D (18wt%Ni/Al₂O₃) with catalyst G (18wt%Ni-3.5wt% La₂O₃/Al₂O₃), the methane formation decreased approximately 50mol% with La adsorption (Figure 4.3). The formation of methane was approximately similar to that found by La/Al₂O₃ catalysts. From the reported results⁹², it is hypothesized that the La₂O₃ acted as an adsorbent which selectively adsorbs carbon dioxide²⁹. As a result, the methanation reaction (Equation 5) was significantly minimized, hence the lower methane formation. Like catalysts E and F, lanthanum modified alumina even after loading 18wt% nickel (cat. G) reduces the formation of carbon monoxide (Figure 4.3) while increasing CO₂ and H₂ indicating the promotion of the WGS reaction (equation 4.2). Therefore, using the La with 18wt% nickel loaded catalyst (cat. G), the hydrogen production was considerably enhanced. At the investigated reaction temperature (500 °C), the hydrogen yield with 18wt% Ni on lanthanum modified alumina support (cat. G) is significantly

higher than that reported previously for glucose gasification in SCW with or without catalysts^{13, 74, 75, 95}.

It is seen that methanation of carbon dioxide is restrained even in the presence of higher amounts of nickel on the catalyst (Cat. G). Lanthanum impregnation before and after nickel loading also significantly affected the gaseous product yields. When comparing the effects of the sequence of La₂O₃ loading, lanthanum oxide loading before (cat. G) and after (cat. H) Ni loading, from Figure 4.3 it is seen that lanthanum loading before nickel loading enhances the hydrogen yield, while the carbon monoxide is lowered by about 60mol%. Even the methane formation in catalyst G (La is loaded before Ni loading) is lower compared to catalyst H (La is loaded after Ni loading). The results indicate that La₂O₃ blocked some active nickel species when lanthanum was loaded after nickel on the alumina support. La molecule has much larger radii than Ni molecule; therefore if Ni is loaded after La, free space of La still remains to act as catalyst active sites for SCWG.

The oxidized catalyst (by oxidation of catalyst G to G*) shows about 50% less hydrogen production with a reduction of carbon oxides indicating less gasification. This result indicates that the reduced catalysts are more active than the oxidized catalysts.

From the above discussion, catalyst G (18wt%Ni-3.5wt%La₂O₃/θ-Al₂O₃) shows the best performance among the evaluated catalysts for hydrogen production with a very good syngas (hydrogen to carbon monoxide) ratio slightly higher than 2, which can be used as a low emission fuel source and is suitable for synthetic diesel and methanol production. Catalyst G is used for further study to investigate the effect of size, oxidant, reaction time, temperature, and feed concentration.

The liquid effluents from the SCWG experiments that did not gasify were measured by TOC analysis. Figure 4.4 shows the carbon gasification efficiency (CGE), and TOC destruction of the evaluated catalysts.

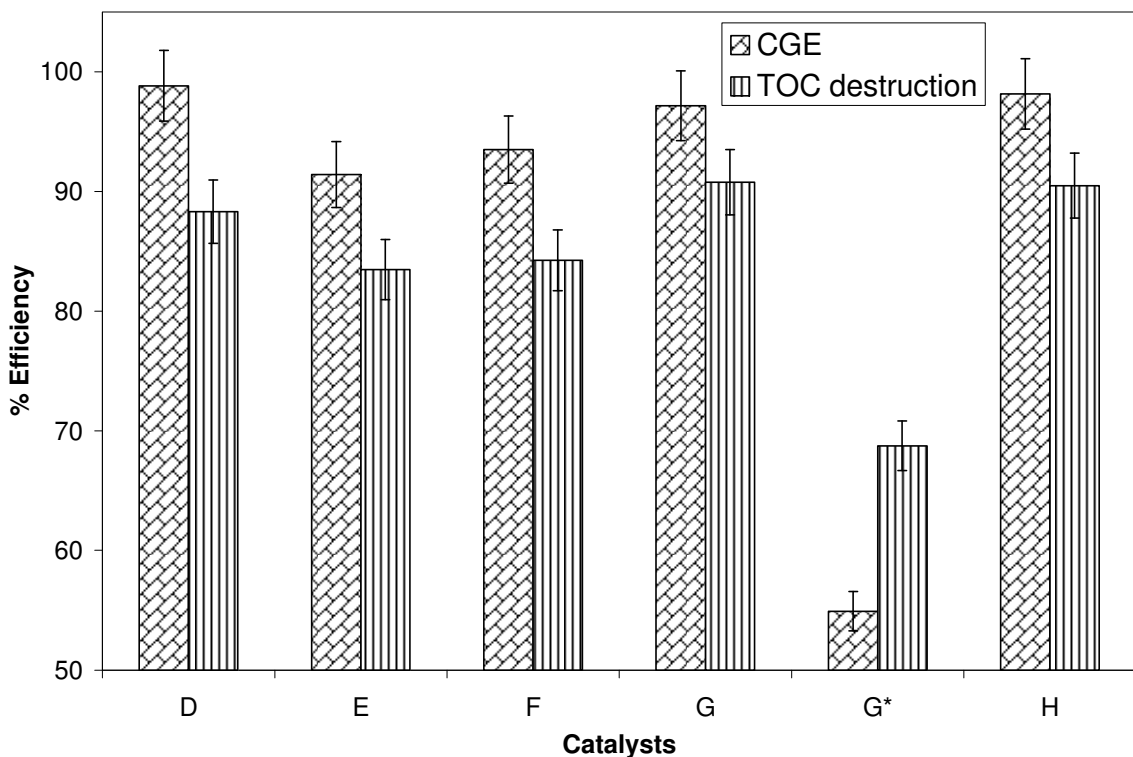


Figure 4.4: Effect of Ni, La₂O₃ and Ni-La₂O₃ on carbon gasification efficiency and TOC destruction where, D) 18wt% Ni/ θ Al₂O₃, E) 3.5wt% La₂O₃/ θ Al₂O₃, F) 7 wt% La₂O₃/ θ Al₂O₃, G) 18wt% Ni -3.5wt% La₂O₃/ θ Al₂O₃ (La₂O₃ impregnated before Ni loading), G*) 18wt% NiO -3.5wt% La₂O₃/ θ Al₂O₃ (oxidized at 500 °C before reaction), H) 18wt% Ni -3.5wt% La₂O₃/ θ Al₂O₃ (La₂O₃ impregnated after Ni loading); T= 500 °C, MR=0.8, t=30 min, P=28MPa, Catalysts=1.0gm, Feed= 0.25M Glucose.

It is seen that up to 91% of TOC decomposition was obtained using the studied catalysts. High CGE and TOC conversion are due to further oxidation of intermediate products by hydrogen peroxide after 15 minutes SCWG reaction of glucose. 97to 98% carbon gasification efficiency is achievable with Ni and Ni loaded catalysts (cat. D, G, H) while lanthanum shows comparatively lower carbon gasification efficiency (cat. E and F) and

TOC conversion. The highest TOC decomposition was observed with 18wt%Ni loaded on 3.5wt% lanthanum modified alumina (cat. G) (Figure 4.4).

4.3.2.2 Effects of catalyst size

To evaluate the catalyst particle size on gas yield, experiments with catalyst G (average size 3 mm), grinded powder of catalyst G (average size 0.1-0.3 mm), and nano catalysts (Ni-La impregnated on nano alumina fibers, average catalyst support size 0.5-1.0 μm^{31}) at 500 °C and 28MPa for 30 minutes were conducted without using oxident. For comparison, direct sol-gel prepared nano aerogel catalyst was also investigated. All of the catalysts evaluated were La modified Ni/Al₂O₃.

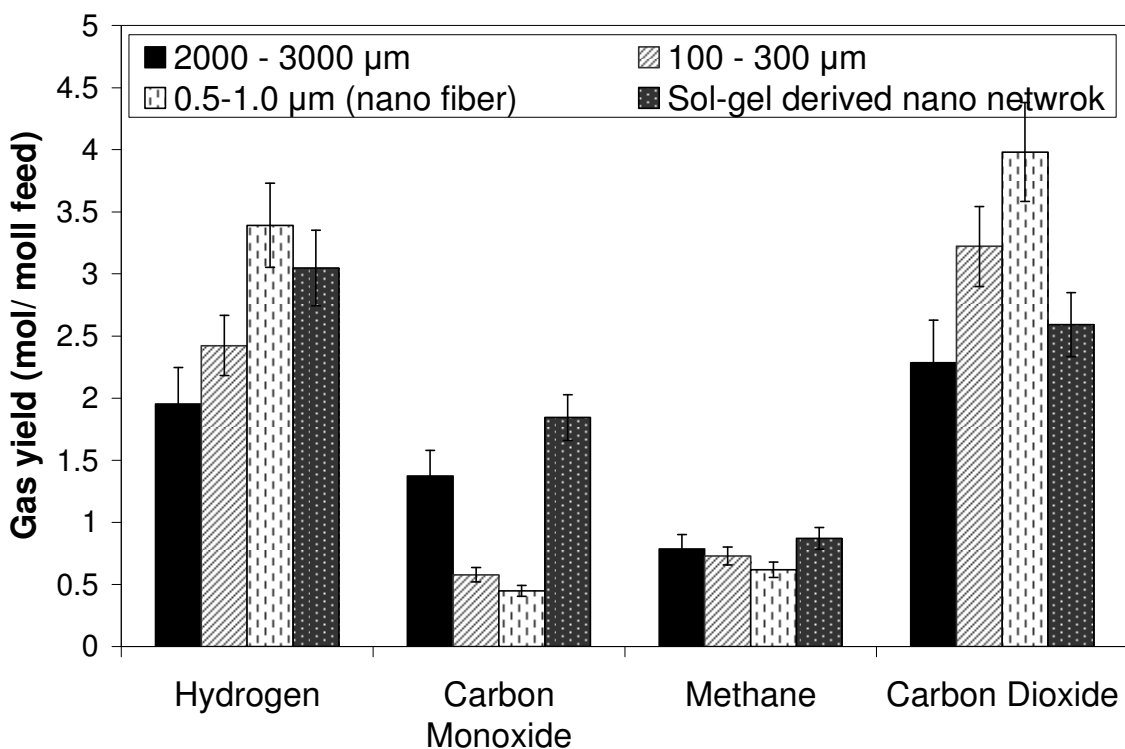


Figure 4.5: Effect of catalysts (Ni-La₂O₃/Al₂O₃) size on gaseous products. T= 500 °C, t=30 min, P=28MPa, MR=0.0, Feed= 0.25M Glucose, Catalyst 1.0 gm.

From Figure 4.5 it is seen that the hydrogen yield increased with decreasing catalyst size. The nano catalyst showed the highest yield while the pellet size (approx. 3 mm) showed the lowest activity. Carbon monoxide and methane also decreased with decreasing catalysts size. This phenomenon can be explained by an increased number of active sites available by exposing blocked pores (created by metal impregnation) for reactions with the smaller particles compared to larger particles. Another reason may be due to coarse catalysts may poses some mass transfer limitation. During the study of catalytic phenol oxidation in supercritical water, Oshima et al.⁹⁶ showed that external mass transfer resistance was negligible for small size catalysts (size 0.18-0.25 mm), however larger size catalysts posed some mass transfer resistance. Some bulky intermediate products of SCWG may not be able to use micropores of coarser size catalysts. One dimensional nanofibers can overcome these problems by exposing a higher surface area and higher dispersion of active metals on the surface. It was previously discussed that lanthanum increased the water gas shift reaction and retarded the methanation reaction. Nano aerogel catalysts using direct metals loading through the sol-gel technique showed a comparatively higher hydrogen yield compared to coarser heterogeneous catalysts but lower hydrogen production compared to the fibrous nano catalysts. Sol-gel derived catalysts showed a higher CO and CH₄ production compared to other catalysts. Low CO₂ with high CO production by the sol-gel derived catalyst is attributed to lowering the water gas shift (WGS) reaction, i.e. La might not contributes to enhance the WGS reaction like impregnated catalysts and thus reducing hydrogen production. This phenomenon can be attributed to the formation of Ni-La-Al-O network by direct addition of metal salt during synthesis of the sol-gel reaction. Unlike the impregnation method,

where metals are deposited on the support, in the sol-gel process, metals are incorporated with the supports. Kaddouri et al. found Ni-La-Si-O system during synthesizing Ni-La on silica by a sol-gel process via propionates⁹⁷. It was previously shown that oxidized catalyst has a lower activity towards hydrogen production (Figure 4.3; cat G*). However, the nano catalysts showed a much higher performance towards hydrogen selectivity (Fig. 4.3) compared to the conventional impregnated catalysts.

The effect of the particle size on total organic carbon (TOC) conversion and carbon gasification efficiency (CGE) are shown in Figure 4.6.

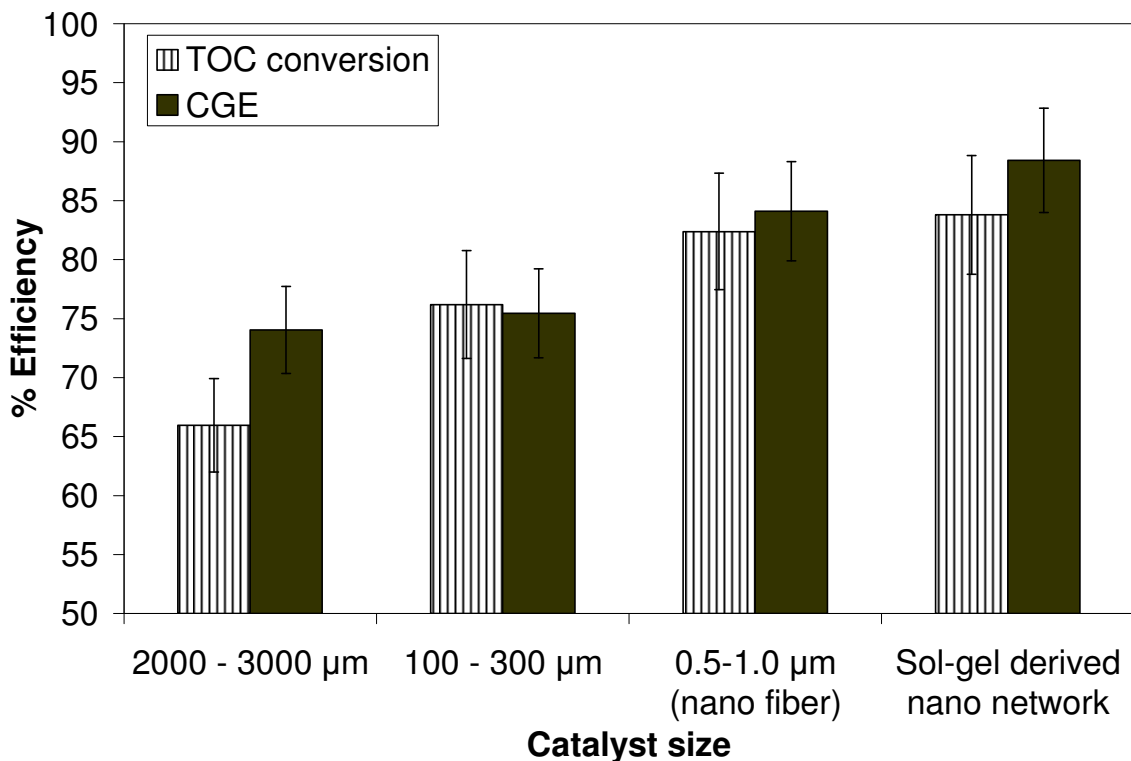


Figure 4.6: Effect of catalysts (Ni-La₂O₃/Al₂O₃) size on TOC conversion and CGE; T= 500 °C, t=30 min, P=28MPa, MR=0.0, Feed= 0.25M Glucose, Catalyst 1.0 gm

TOC conversion and carbon gasification efficiency increased with decreased catalyst size i.e. increased surface area. TOC conversion and carbon gasification efficiency over 80% was achieved using the nano catalysts. The Sol-gel prepared catalysts showed the best performance in terms of TOC conversion and CGE. But from Figure 4.5 it is seen that hydrogen production is less using the sol-gel prepared catalyst than that using the nanofiber catalysts. This can be explained that although carbon gasification was higher (high yield of CO and CH₄) using the sol-gel derived catalysts, the WGS reaction was not enhanced by La in comparison to nanofiber catalysts. This phenomenon can be attributed to incorporation of metals (especially La) with the support during synthesis using the sol-gel process.

4.3.2.3 Effects of Oxidant

For comparison purposes, gasification and partial oxidation (oxidant introduced at 15 minutes reaction time) of glucose in SCW was conducted with crushed catalyst G (18wt%Ni-3.5wt%La₂O₃/θAl₂O₃). Figure 4.7 shows the effect on the gaseous product yields.

Interestingly it is seen that both H₂ and CH₄ production are higher in the gasification process than that with partial oxidation. However production of CO₂ is much higher in the partial oxidation process. This may be explained as the direct oxidation of some carbonaceous products to CO₂ occurs instead of producing CO which could undergo the WGS reaction producing H₂ and CO₂. Oxidation of carbonaceous products also limits conversion to methane by decomposition of any intermediate products. Some direct conversion of CO to CO₂ by oxidation may also happen that reduces the WGS (equation

4.2) and the methanation reaction (equation 4.3) of CO. On the other hand in gasification both the WGS and methanation of CO took place. These are the possible reasons for lower production of H₂ and CH₄ and higher production of CO₂ by oxidation compared to gasification.

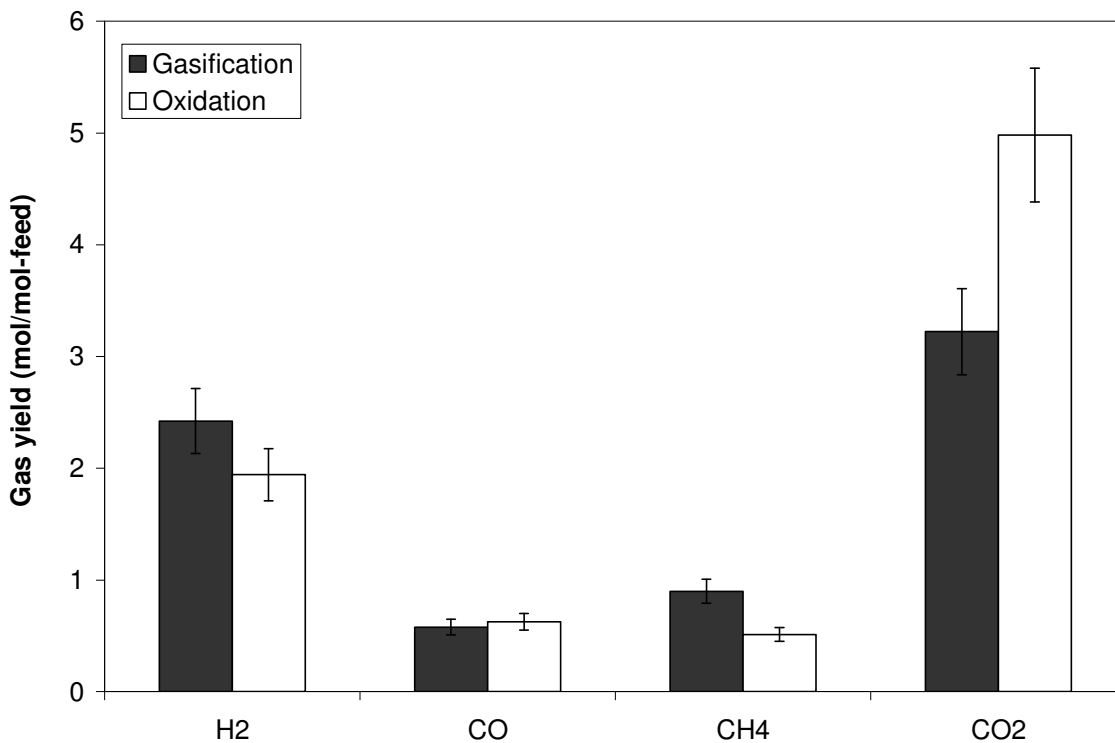


Figure 4.7: Effect of oxidant on gaseous products. Catalyst 18wt% Ni-3.5wt% La₂O₃/θAl₂O₃, size: 0.1-0.3 mm, amount =1.0 gm, T=500 °C, P=28MPa, Feed= 0.25M glucose.

Figure 4.8 provides a comparison of TOC conversion and CGE for gasification and partial oxidation. It is seen that both TOC destruction and CGE increased slightly by using oxidant. The oxidant helps to gasify carboneous products to carbon oxides mostly to CO₂ as confirmed by gaseous yields (Figure 4.7). From the gaseous products it is seen that using oxidant production of H₂ and CH₄ decreased although here we observed both

TOC destruction efficiency and CGE increased significantly. This raises the question of where the excess hydrogen goes to. One possible explanation is that some water is formed through oxidation instead of steam reforming, WGS and methanation reactions (equations 4.1 to 4.4) which could be responsible for reduction of H₂ and CH₄ as follows:

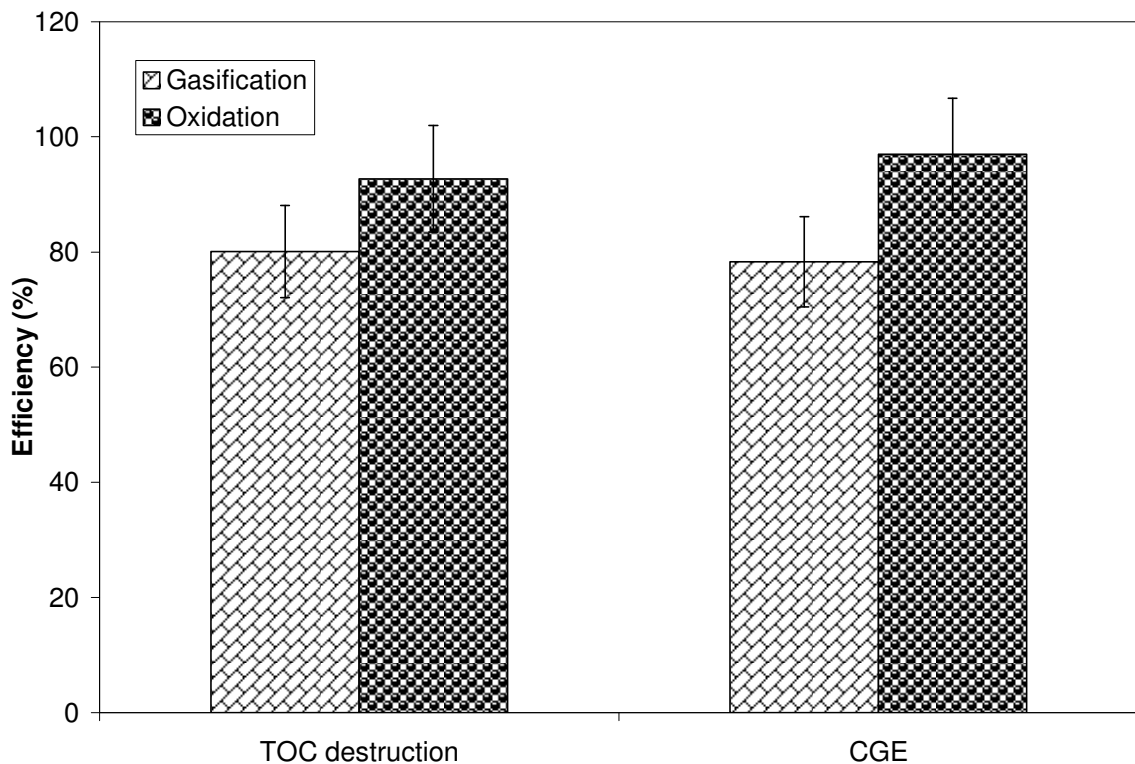


Figure 4.8: Effect of oxidant on TOC conversion and CGE. Catalyst 18wt% Ni-3.5wt% La₂O₃/θAl₂O₃, size: 0.1-0.3 mm, amount =1.0 gm, T=500 °C, P=28MPa, Feed= 0.25M glucose.

4.3.2.4 Effect of Residence Time and Temperature

As seen from the previous section using catalyst G (crushed 18wt% Ni-3.5wt% La₂O₃/θAl₂O₃), partial oxidation produced less hydrogen; here using the same catalyst, we examine the effect of reaction time and temperature on the gaseous and

liquid products without using oxidant. Figure 4.9 shows the time and temperature effects on the gaseous products formed during SCWG of glucose. Increasing reaction time increases the hydrogen production (Figure 4.9 A), while carbon monoxide decreases with time (Figure 4.9 B).

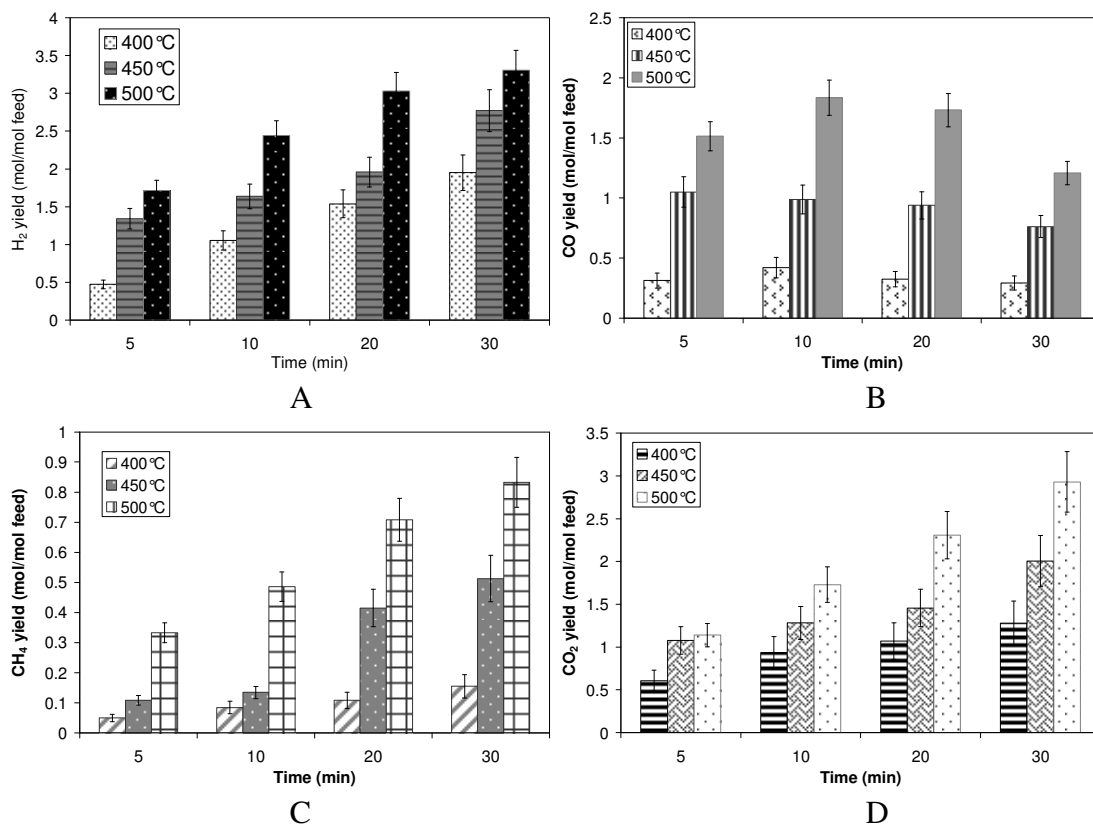


Figure 4.9: Effect of time and temperature on gaseous products. Catalyst size: 0.1-0.3 mm, amount =1 gm, P=28MPa, Feed= 0.25M Glucose.

Reduction of carbon monoxide yield with increasing hydrogen can be attributed to the water gas shift reaction, shown by equation 4.2. From this observation, it can be hypothesized that at the initial stage of the reaction (up to 10 minutes) intermediate tar decomposition to CO dominates the WGS reaction of CO. Methane and carbon dioxides also increase with time and temperature. There may be some methanation reaction of

carbon oxides and some methane coming from the dissociation of intermediate liquid products with increasing time and temperature.

Figure 4.10 shows that increasing reaction time and temperature leads to the TOC conversion and CGE increasing i.e. the gaseous products increased due to a higher conversion of the liquid intermediates.

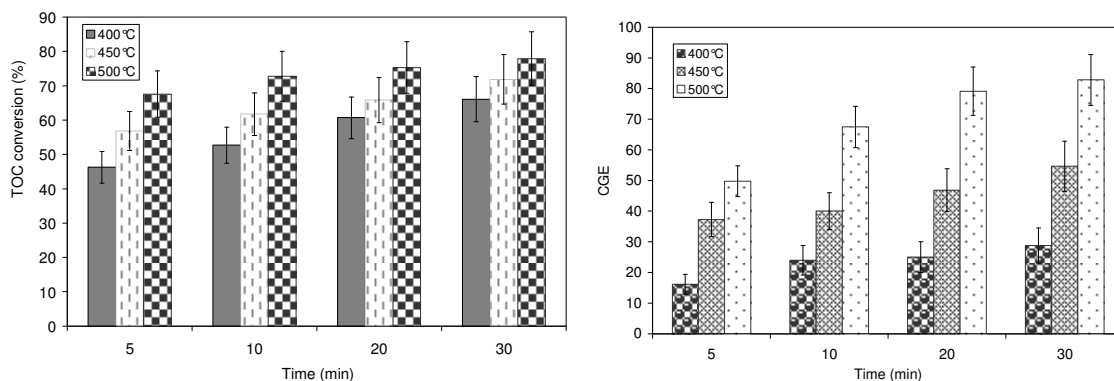


Figure 4.10: Effect of time and temperature on TOC conversion and CGE. a) TOC conversion, b) CGE. Catalyst size: 0.1-0.3 mm, amount =1 gm, P=28MPa, Feed= 0.25M Glucose.

To further study the effect of reaction time, the temperature was fixed at 500 °C, and the reaction time was increased to 60 and 120 minutes. The hydrogen yield starts decreasing at 60 minutes and 120 minutes (Figure 4.11). It is interesting that both hydrogen and carbon monoxide decreased at higher reaction times while methane and carbon dioxides increased. This observation may be explained as both the water gas shift and methanation reactions of carbon monoxide (reaction 4.2 and 4.3) happened at higher reaction times.

Combination of equations 4.2 and 4.3 gives (WGS and methanation reactions)



Equation 4.13 can explain the reason for reduction of CO and H₂ with an increase of CO₂ and CH₄.

From Figure 4.11 it is also seen that both the TOC conversion and CGE increases with reaction time. TOC conversion reached almost 90% while CGE reached over 96% due to increased gasification.

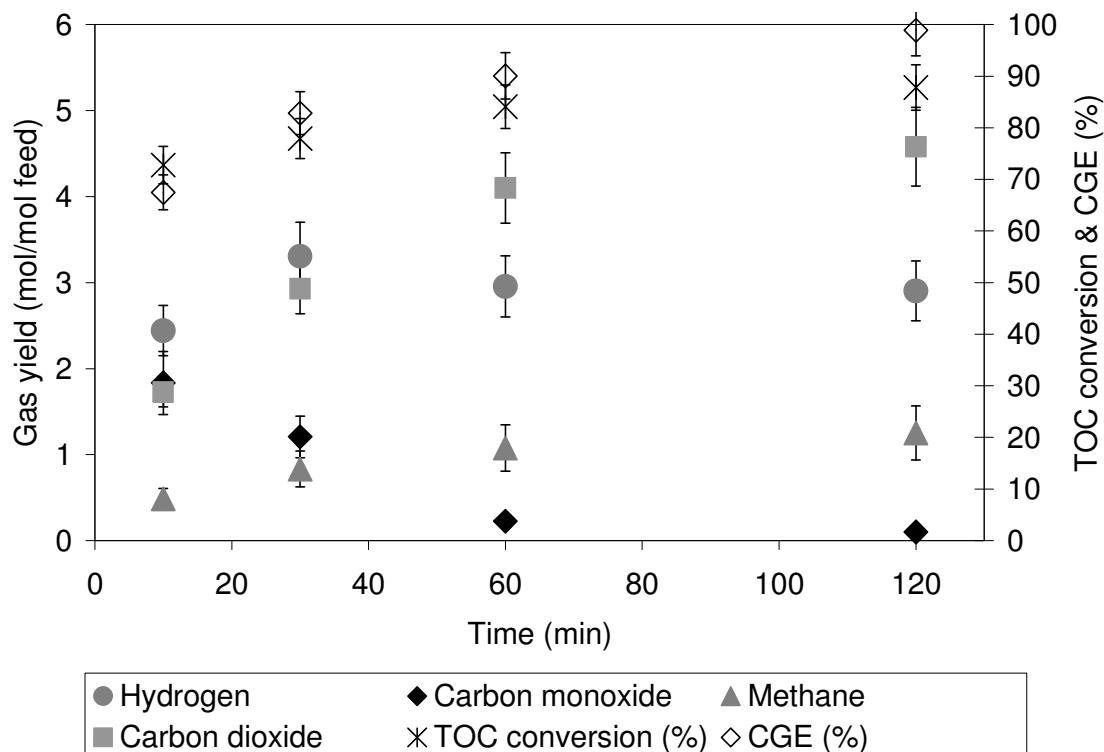


Figure 4.11: Effect of time and temperature on gaseous products and TOC conversion and CGE. Catalyst size: 0.1-0.3 mm, amount =1 gm, MR=0.0, T=500 °C, P=28MPa, Feed= 0.25M Glucose.

4.3.2.5 Effect of Feed Concentration

Figure 4.12 shows the effect of feed concentration on the gaseous products and TOC conversion and carbon gasification efficiency using crushed catalyst G (crushed 18wt%Ni-3.5wt%La₂O₃/θAl₂O₃) without oxidant. It is seen that higher concentrations

lower the hydrogen and carbon dioxide yield, while only a slight increase of carbon monoxide and methane production is observed. Similar results were found by Kirsten et al.⁶³. A thermodynamic analysis by Yan et al.⁴⁹ also showed a similar tendency. The TOC conversion and carbon gasification efficiency being reduced with increased concentration is attributed to a lower gasification of organic compounds occurring. From the above observations it is clear that low concentration with increased time and temperature is favorable for the production of hydrogen and higher gasification yields.

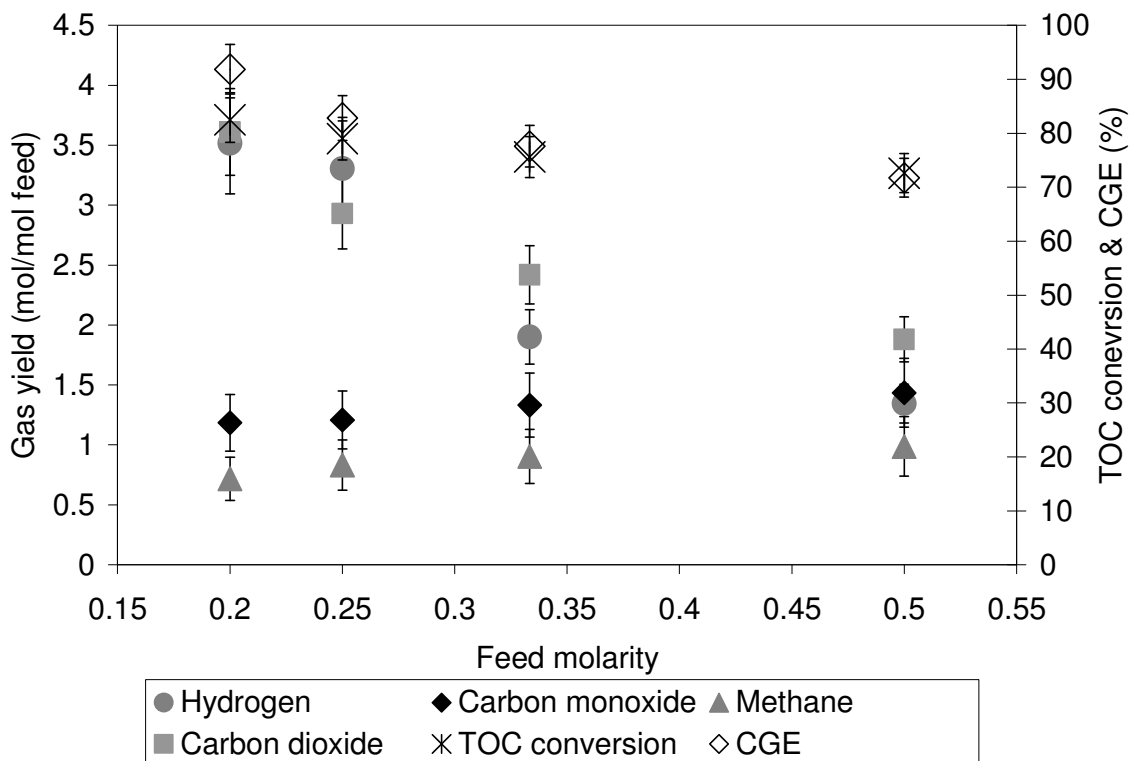


Figure 4.12: Effect of feed concentration on gaseous products and TOC conversion and CGE. Catalyst size: 0.1-0.3 mm, amount =1 gm, MR=0.0, T=500 °C, P=28MPa.

4.3.2.6 Effects of TOC destruction on gaseous yield

Destruction of TOC affects the yield of gaseous products. For a better understanding of the performance of catalysts, high concentrated glucose corresponding to low TOC conversion was studied. The TOC conversion was varied for the different catalysts with the same feed concentration. Figure 4.13 shows that the gas yields with 18wt%Ni/ θ - Al_2O_3 (cat. D), 3.5wt% La_2O_3 / θ - Al_2O_3 (cat. E) and 18wt%Ni-3.5wt% La_2O_3 / θ - Al_2O_3 (cat. G).

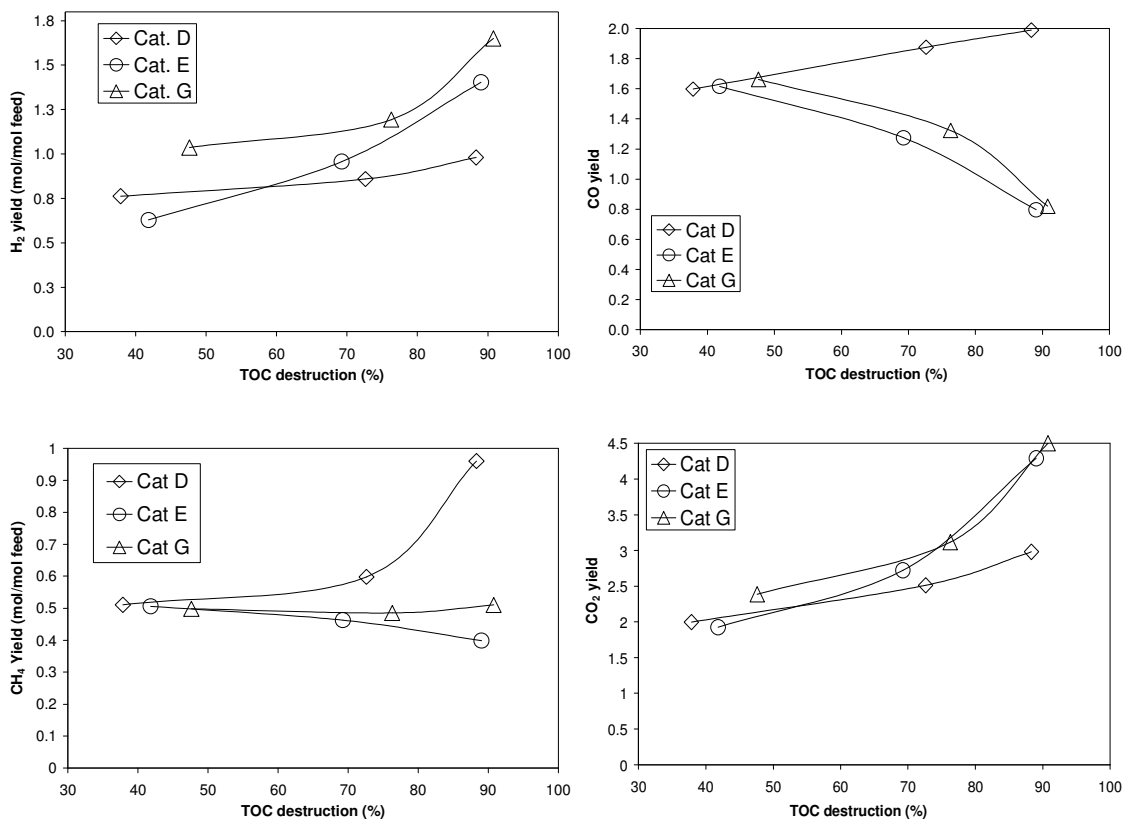


Figure 4.13: Effect of TOC destruction on gaseous products. D) 18wt%Ni/ θ Al_2O_3 , E) 3.5wt% La_2O_3 / θ Al_2O_3 G) 18wt%Ni -3.5wt% La_2O_3 / θ Al_2O_3 ; T= 500 °C, MR=0.8, t=30 min, P=28MPa, Feed= 0.25M Glucose.

In all cases the 18wt%Ni-3.5wt%La₂O₃/ θ -Al₂O₃ (cat. G) shows the best performance in terms of hydrogen yield. CO increases with TOC destruction using Ni/Al₂O₃ catalyst (cat. D) whereas with the lanthanum and lanthanum modified catalysts (Cat. E and G), the CO yield decreased. This phenomenon is described by the water gas shift reaction being boosted by lanthanum.

Using La₂O₃/ Al₂O₃ (cat. E), and Ni-La₂O₃/ Al₂O₃ (cat. G), CH₄ formation was barely affected; while using Ni/ Al₂O₃ catalyst (cat. D), the CH₄ formation was increased significantly with increased TOC conversion. Lower hydrogen and carbon dioxide were formed using catalyst D compared to catalysts E and G. This observation confirms that the carbon dioxide methanation reaction was enhanced using the plain Ni catalyst and resisting this reaction by adsorption with lanthanum.

4.3.3 Mechanistic Elucidation and Reaction Mechanism

The reaction pathways for dissociation of glucose in supercritical water have been described in detail elsewhere^{52, 62}. In the supercritical region, the ion product is higher than that in ambient water, providing hydroxyl or hydronium ions to catalyze reactions such as hydrolysis and water eliminations as well as rearrangements⁵². Water elimination may also occur via a free-radical reaction pathway. The carbon-carbon scission is a typical free-radical reaction. Cortright et al.⁸⁴ reported the mechanism of C-C, C-O cleavage and dehydration, dehydrogenation and hydrogenation of biomass reforming in the presence of metal catalyst in liquid water. More than thirty intermediate products in liquid were reported through glucose gasification in supercritical water^{53, 54}. From our evaluation results, it is seen that TOC reduces while CGE increases with time. Therefore

it can be hypothesized that glucose is first broken down into several water-soluble intermediates, which later undergo steam-reforming reactions to produce gaseous products.

Glucose \rightarrow water-soluble intermediate \rightarrow gases

Let us consider the ideal case, glucose gasification in supercritical water should follow equation 4.14.



However, if SCWG of glucose solely followed reaction 4.19, the molar ratio of CH_4/CO_2 and H_2/CO_2 would become 0:6 and 2:1 respectively. Moreover, the presence of methane is significant, between 7 to 14 mol%, increasing with time suggesting decomposition of glucose to methane via intermediate products. Another possibility is methanation of carbon oxides (equation 4.3 and 4.4). If methane is formed only by the methanation, the reaction tendency of carbon oxides and hydrogen would be decreased. From our evaluation and reported results, CH_4 is observed even at the lowest reaction time. Therefore methane may form via thermal decomposition of glucose and intermediate products. In addition, a high concentration of water helps drive the methanation reactions (equation 4.3 and 4.4) in the reverse direction. Moreover, it is seen that the lanthanum modified catalyst retarded the methanation reaction (section 4.3.2.1).

Therefore, the thermal decomposition of glucose can be written as follows:



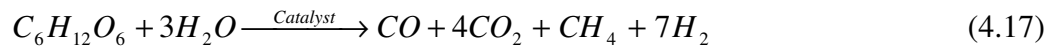
CO further undergoes the WGS reaction to produce additional H_2 and CO_2 .



The high excess of water may help drive the WGS shift reaction in the forward direction i.e. not limited by chemical equilibrium. In addition, La enhances the WGS reaction. The resultant stoichiometric equation from combining (4.15) and (4.2) should be:



If all glucose molecules fed were converted by this reaction, the molar ratio of CO₂/H₂ and CH₄/H₂ would be 0.625:1 and 0.125: 1 respectively. From the experimental results at 500 °C (Figure 4.9) it is seen that CO₂/H₂ varied with time from 0.65:1 to 1.5:1, attributing that H₂ is formed less than the assumed reaction (equation 4.16). If the WGS reaction is the main source of CO₂; the molar ratio of CO₂/H₂ would be the same (equation 4.2). However, a significant reduction of CO/H₂ ratio with time from 0.88:1 to 0.03:1(Figure 4.9) confirms the major role of WGS for H₂ production. The presence of CO also helps prove that the entire CO did not go to the WGS reaction. Therefore the equation 4.16 can be rewritten as follows:



From equation 4.17, the molar ratio of CO₂/H₂ and CH₄/H₂ are 0.57:1 and 0.14: 1 respectively. The experimental results of the CO₂/H₂ and CH₄/H₂ ratios are only a little higher than the proposed reaction (equation 4.17) at the beginning while increasing with time. On the other hand, the experimental CH₄/H₂ molar ratio at 500 °C varied with time from 0.2:1 to 0.4:1, attributing formation of CH₄ is higher than the proposed reaction (equation 4.16). Increasing the ratio of methane to hydrogen indicates that some methane is also coming from the methanation reactions (equations 4.3 and 4.4). Therefore it can be hypothesized that the initial gasification reaction of glucose followed equation 4.17.

However decomposition of intermediate products (equation 4.6), WGS (equation 4.2), and methanation reactions (equations 4.3 and 4.4) are competitively taking place in the reaction system at the conditions investigated in the current system.

4.4 Conclusions

The hydrogen yield during supercritical water gasification of glucose was found to increase with lanthanum modified nickel on alumina heterogeneous catalyst. This was attributed to retardation of the methanation reaction of carbon dioxide and by promoting the water gas shift reaction. Adsorption of carbon dioxide, one of the main products of SCWG/SCWO reaction, by lanthanum oxide is ascribed for the shift of the reaction equilibrium, thus enhancing hydrogen production. Adsorption of lanthanum before nickel loading on the support was found more active towards hydrogen production. Gasification of glucose was found to produce more hydrogen than partial oxidation using the lanthanum modified catalysts. However, the total organic carbon conversion and carbon gasification efficiency increased significantly with addition of oxidant. The reason for the lower hydrogen production is explained as a direct oxidation of carbon monoxide to carbon dioxide which otherwise can participate in the water gas shift reaction for further hydrogen yield.

Decomposition of TOC can be increased by nickel loading on lanthanum modified alumina. However, excess lanthanum did not increase the hydrogen yield and TOC decomposition. Increasing the reaction time increases the hydrogen yield and TOC destruction. One important finding is that use of 18wt%Ni/ θ -Al₂O₃ produces methane rich gas whereas after adsorption, La produces hydrogen rich gaseous products.

Additionally, syngas ratio ($H_2:CO$) of 18wt%Ni/ $\theta-Al_2O_3$ is 1:2 whereas addition of La changes the ratio ($H_2:CO$) to 2:1; an ideal ratio for production of methanol ($CO + 2H_2 \rightarrow CH_3OH$), and synthetic fuel.

Another finding is that the smaller the catalyst size, the higher the hydrogen production, carbon gasification efficiency and TOC destruction. Nano catalysts showed higher activity compared to coarser heterogeneous catalysts. Increased active sites, i.e. active metal dispersion were attributed to these increased activities. Sol-gel derived aerogel catalyst where metals were loaded directly was found very active towards hydrogen production and TOC destruction. However, hydrogen production with sol-gel derived catalyst was comparatively less than metals loaded on nanofiber catalysts. This phenomenon was attributed to incorporation of active metals with alumina main structure forming Ni-La-Al-O network by the sol-gel derived process. Although integration of Ni with main Al-structure by this method showed very good activity towards gasification, unlike impregnated catalysts the desired WGS reaction was not enhanced by incorporated La.

Chapter 5

Characterization of fresh and spent Ni based catalysts used for supercritical water gasification.

In this chapter synthesized fresh and spent Ni-based catalysts were characterized in order to gain a better understanding of the catalyst's role in supercritical water gasification. The evaluation results found in chapter 3 and 4 motivated us to characterize catalysts in detail for future commercial SCWG use. Part of this chapter is reproduced from the submitted article by the author: Characterization of nickel based catalysts used in supercritical water gasification of glucose with permission from Applied Catalysis A: General; Elsevier Ltd.

5.1 Introduction

Energy shortages and environmental pollution are two major concerns for a sustainable future. Among many options, gasification of waste biomass for the production of hydrogen, as a renewable and green alternative energy source has received significant attention recently. Gasification of biomass in supercritical water (SCW) offers an attractive alternative to avoid the energy intensive drying process. In this approach, biomass is hydrolyzed by water into smaller molecules in the presence of a suitable catalyst. SCW exists at temperatures and pressures above the critical point of water and is an innovative solvent to dissolve organic materials. Many applications of this new solvent such as oxidation of organic wastes, gasification of biomass and separation of metals has been researched with and without catalysts; however the role of the catalyst

has not been sufficiently addressed. Catalysts can play a major role in supercritical water gasification for the desired yield. A useful catalyst is normally characterized by a balance of its activity and stability. However the properties of SCW are completely different from ambient water which makes the catalyst behave differently. In SCW, maintaining catalyst activity is critical which may become deactivated from catalyst structure changes, loaded metals may be agglomerated or transformed, and different types of coke may be formed on the catalyst surface. A metal oxide may retain its active crystalline phase, but the crystal may coarsen or grow larger under hydrothermal environments. Because crystal growth normally results in a loss of surface area and activity, it becomes an important selection criterion for use in SCWG.

One important property of SCW is that there exists almost no mass transfer limitation. Generally, catalytic reactions are mass-transfer limited due to the high reaction rates, low diffusion rates, and poor fluid flow characteristics. The high effective diffusion coefficient of SCW (about 100 times higher than that of ambient water) diminishes the chance of any mass-transfer gradient in the catalyst internal surface area⁹. The Thiele modulus, which represents the degree of internal or pore diffusion limitation, was shown to be less than unity for SCW, indicating that pore-diffusion limitations do not exist in the catalyst⁹. Although SCW has very good characteristics, high pressure and temperature and corrosive nature of SCW rigorously affects the catalyst's properties.

Homogeneous materials like alkali catalysts are readily miscible with water and found very effective for biomass gasification^{7, 15}. However, alkali catalysts recovery, re-use and reactor corrosion problems are significant concerns with these types of catalysts¹⁶.

Water-insoluble (heterogeneous) catalysts have been preferred by researchers to minimize unwanted contamination of liquid effluents. In this regard, heterogeneous catalysts based on noble metals for SCWG has been reported by Sato et al.⁷³. They found that the activity order is $\text{Ru}/\gamma\text{-Al}_2\text{O}_3 > \text{Ru}/\text{C} > \text{Rh}/\text{C} > \text{Pt}/\gamma\text{-Al}_2\text{O}_3, \text{Pd}/\text{C}$ and $\text{Pd}/\gamma\text{-Al}_2\text{O}_3$. However, when one considers the high cost and limited availability of noble metals, it is more practical, from the industrial standpoint to develop low cost transition metal-based catalyst with high stability and activity. Moreover, although Ru showed very good activity, even a trace amount of S can cause Ru catalyst poisoning²⁰. In addition, Pt group noble metals are prone to methanation of carbon oxides in the presence of hydrogen, which increases with an increase of temperature²¹.

Using nickel, a relatively inexpensive metal, Furusawa et al.²³ found that carbon and hydrogen yields increased from 8.3% and 14.1% to 22.7% and 46.2% respectively when 0.05 g of 20 wt% Ni/MgO catalyst was added at 400 °C. A nickel catalyst was also found to be favorable for cracking tar molecules and promoting the WGS reaction²⁴. When compared to the available alternative catalysts, nickel displays several favorable attributes including high activity and low cost. Nickel also has a high melting point (1453°C) which is very important for a biomass gasification catalyst.

La_2O_3 is known to be able to stabilize alumina and can avoid metal agglomeration⁹⁸. Moreover, La doped Ni/ Al_2O_3 catalysts were found to be very active for increasing hydrogen production through retarding the methanation and promoting the water gas shift reaction in our previous study (chapter 4).

Recent reviews on previous studies of catalytic SCWG demonstrated the feasibility of catalytic SCWG and focused on the activity of different catalysts, the reaction pathways, and the probable reaction kinetics mainly based on the product distribution^{4, 30}. However, none of these studies focused on the physical or chemical changes of catalysts, interaction with support, coke deposition on the catalyst surface, or adsorption of any product by the metals during SCWG and how these changes in the catalysts might correlate with their activities. Such information would improve our current understanding of catalyst behavior and catalyst deactivation during SCWG processing. Therefore, characterization of the fresh and spent catalysts is critical for a better understanding of the catalyst role in SCW and the reaction mechanism.

5.2 Experimental

The synthesized fresh and spent catalysts used in SCWG were investigated using various physiochemical instruments. The characterization techniques involved were to determine if the catalyst experiences any physical or chemical change, interaction with support, types of coke formation, adsorption of any main product to shift the equilibrium conditions during gasification in supercritical water. The synthesis procedures of catalysts were described in detail in chapter 4.

5.2.1 Characterization Techniques

The BET (Brunauer-Emmett-Teller) surface area, pore size and distribution, and pore volume were determined from nitrogen adsorption and desorption isotherm data obtained at 77 K with a constant-volume adsorption apparatus (Micromeritics ASAP 2010) using

N₂ as the probe gas. The prepared samples were degassed at 150°C for 5h before the nitrogen adsorption experiments.

The catalyst reduction temperature, the available amount of reduced metal species, and metal support interaction were assessed using the temperature programmed reduction (TPR) method. The temperature programmed oxidation (TPO) method was applied to determine the coke deposited on the spent catalyst while CO₂-temperature programmed desorption (TPD) was carried out to determine the CO₂ adsorption properties of the synthesized catalysts. All the TPR, TPO, and TPD experiments were carried out using a Micromeritics Autochem 2920. Before TPR measurements, 100-150 mg of the fresh catalyst was completely oxidized at 750 °C by flowing a stream of gas containing 5% O₂ in He. For the spent catalysts no pretreatment i.e oxidation was carried out in order to determine if any carbeneous deposition or oxidation of catalysts happened during SCWG. The TPR analysis was performed by circulating a stream of gas containing 10 % H₂ and balanced Ar at a rate of 50 mL/min. The temperature was raised from ambient to 750°C at a rate of 10°C/min. A thermal conductivity detector (TCD) was used to record the change of hydrogen concentration of the gas stream passing through the catalyst sample for calculating the amount of hydrogen consumed during the reduction process.

The amount of reducible species was calculated from the amount of hydrogen consumed during TPR analysis using the following equation:

$$W_{Ni} = \frac{MW_{Ni} V_{H_2} \rho_g}{\nu} \quad (5.1)$$

where, W_{Ni} represents the weight of reducible species, MW_{Ni} the molecular weight of nickel, V_{H_2} the volume of hydrogen consumed, ρ_g the gas molar density at STP and v is stoichiometric number based on the reaction. The reaction involved can be written as:



where one mole of hydrogen is required to reduce one mole of nickel. The % of reduction was thus calculated according to the following equation:

$$\% \text{ Reduction} = \frac{W_{Ni}}{W} \times 100\% \quad (5.3)$$

where, W_{Ni} represents the weight of reducible species, and W is the actual metal amount in the catalyst.

TPO was carried out subsequent to the TPR experiments by flowing a stream of 5% O_2 and balanced He gas through the bed of reduced catalyst at a rate of 50 mL/min. The bed temperature was increased from ambient to 750°C at a rate of 10°C/min and the TCD detector analyzed the gas in the exit stream. For CO_2 -TPD analysis, 10% CO_2 and balance He gas was flowed through the bed of reduced catalyst at a rate of 50mL/min; the temperature was raised at 10°C/min to 500°C and kept for 30 min, i.e. the typical reaction temperature and time of supercritical water gasification. The CO_2 adsorbed catalysts were then cooled to 60 °C and raised to 900 °C at 10°C/min with helium flow to determine adsorbed CO_2 from the desorption peaks with respect to temperature; TCD analyzed the exit gas stream.

H_2 pulse chemisorptions experiments were also conducted using a Micromeritics Autochem 2920 to determine the active metal surface area, the percent dispersion and the active particle size of the nickel crystallites on the alumina support. A stream of Ar gas

was flowed through a bed of pre-reduced catalyst at a rate of 50 mL/min. When the argon flow was stable, a series of hydrogen pulses (1.0 mL) were injected into the system at 40°C with the gas leaving the system being analyzed by a TCD detector. As hydrogen gas was adsorbed on the active nickel sites, peaks were created in the TCD reading of the outlet stream. The hydrogen pulse was discontinued when two consecutive peaks showed the same area.

The amount of hydrogen chemically adsorbed on the active sites of the catalyst was used to calculate the percent dispersion according to:

$$\%D = \frac{AX}{Wf} \quad (5.4)$$

where A is a constant, X is the total hydrogen chemisorbed, W is the percentage of weight metal and f is the fraction of reduced metal. The average crystal size (d_v) can be calculated from the following equation:

$$d_v = \frac{\phi V_m}{S_m} \times \frac{1}{\%D} \quad (5.5)$$

where ϕ represents the particle shape constant, S_m represents the average surface area of metal surface exposed per surface metal atom, and V_m represents the volume of metal atoms.

Thermogravimetric analysis (TGA) was performed to measure the weight gain due to oxidation of reduced catalysts, and the weight loss due to oxidation of adsorbed species (carbon) on the spent catalysts. The analysis was performed using a TGA/SDT A851 instrument at a heating rate of 10°C/min in air.

Powder X-ray diffraction (XRD) patterns of crushed catalysts were collected to estimate crystallinities of fresh and used catalysts. A Rigaku rotating-anode XRD was used employing CuK α radiation, with monochromation achieved using a curved crystal, diffracted beam, graphite monochromator. The instrument was operated at 45kV and 160mA, using the normal scan rate of 10° per minute (equivalent to 0.5° two-theta on conventional diffractometers) in the 2 θ range from 2° to 82°. X-rays were collimated using 1° divergent and scatter slits, and a 0.15mm receiving slit.

The crystalline sizes can be calculated using the Scherrer equation⁹⁹:

$$d_{XRD} = \frac{0.9\lambda}{(\beta - \beta_0) \cos \theta} \quad (5.6)$$

where d_{XRD} is the volume average diameter of the crystallite, λ is the Cu-K α radiation (1.79 radian), and $(\beta - \beta_0)$ is the full width at half maxima of the peak.

The coke deposition on the catalyst surface was characterized by Raman spectroscopy using a Kaiser Optical Systems RXNI-785 with an excitation wavelength of 785 nm.

The nanostructured morphologies of the sample were obtained from Transmission Electron Microscopy (TEM) images (Model JEOL 2010F). Before TEM analysis, the powdered samples were dispersed in methanol by sonication and then placed and dried by normal evaporation on a copper grid covered with holey carbon film.

5.3 Results and Discussion

5.3.1 BET Surface area, Pore size, Pore volume

The surface area, average pore diameter and pore volume of the prepared fresh and spent catalysts are summarized in Table 5.1.

Table 5.1: Physiochemical properties of catalysts:

Catalysts		S_{BET} (m^2/g)	D_{pore} (nm)	V_{pore} (cm^3/gm)	
A	θ -alumina	57	17.4	0.248	
B	7.5wt%Ni/ θ -alumina*	51	14.0	0.179	
C	11wt%Ni/ θ -alumina*	49	13.8	0.154	
D	18wt% Ni/ θ -alumina*	Fresh	46	10.2	0.118
		Spent	31	9.6	0.076
E	3.5wt% $\text{La}_2\text{O}_3/\theta$ -alumina	Fresh	60	15.9	0.237
		Spent	50	9.9	0.125
F	7wt% $\text{La}_2\text{O}_3/\theta$ -alumina	Fresh	50	11.4	0.143
		Spent	45	11.0	0.124
G	3.5wt% La_2O_3 -18wt% Ni/ θ -alumina	Fresh	48	12.9	0.154
		Spent	40	9.5	0.091
H	3.5wt% La_2O_3 -18wt% Ni/ θ -alumina**	Fresh	46	6.8	0.078
		Spent	36	10.1	0.091
J	3.5wt% La_2O_3 -18wt% Ni/ θ -alumina nanofiber	Fresh	101	15.0	0.373
		Spent	12	11.9	0.024
K	Nano structured 3.5wt% La_2O_3 -18wt% Ni-alumina (sol-gel)	Fresh	339	4.2	0.381
		Spent	25	7.6	0.051

S_{BET} = BET surface area; D_{pore} = Adsorption average pore diameter (4V/A); V_{pore} = Single-point adsorption total pore volume per gram. ** La_2O_3 impregnated after Ni loading. * Reference catalysts⁷⁵

After nickel loading the surface area, average pore diameter, and pore volume of the catalysts were decreased (Catalyst A to D). Pore blocking by the nickel species is believed to be mainly responsible for the reduced surface area and pore volume. All the spent catalysts (after SCWG for 30 mins at 500 °C and 28 MPa) also showed lower surface area, pore volume, and pore diameter than the fresh catalysts. Increasing the metallic crystallize size by agglomeration during SCWG is mainly responsible for decreased surface area of the spent catalysts, as further analyzed later. Deposition of intermediate products (mainly carbon) during the gasification reaction on the catalyst pores is another reason for the reduced pore volume and surface area of the spent catalysts, (further analyzed later).

Contrary to Ni loading, it is interesting to see that after La_2O_3 loading on alumina the surface area was slightly increased (catalyst E compared unloaded alumina A) indicating that La_2O_3 was primarily deposited on the outer surface of the alumina support. The large diameter of the La^{3+} ions hinders diffusion into the alumina pores and is subsequently dispersed as a monolayer on the top of the θ -alumina surface⁹⁴. However, increasing the amount of lanthanum to 7wt% onto Al_2O_3 (catalyst F) also decreased the surface area and pore volume attributed to blockage of inter-crystalline pores.

When depositing the same amount (3.5 wt%) of La on alumina before Ni loading (catalyst G), a higher surface area, pore diameter and pore volume were found compared to La loaded after Ni loading (catalyst H). This can be attributed to La being deposited on Ni (catalyst H) hides some active nickel i.e. decreases some available Ni on top of the catalyst surface, as further confirmed by subsequent temperature programmed analysis.

Exposing nano catalysts to SCW reduced the surface areas and pore volumes drastically. This may be due to agglomeration, collapse of the nano porous structures, as further confirmed later.

5.3.2 Temperature Programmed Reduction

In a supported nickel catalyst, the nickel sites are active in their metallic form. Hence, for optimum catalyst performance, the catalyst must be reduced, i.e. activated before exposing to the actual reaction conditions. Therefore, the most important characteristic of a nickel catalyst that should be first investigated is its reducibility. In this study, TPR analysis was carried out in order to determine the reduction temperature, and the amount of reducible species for the prepared catalysts. TPR characterization also provides information to help understand the metal-support interactions and the different species present on the surface of the support. Figure 5.1 displays the TPR profiles of the investigated catalysts and for the La-Al₂O₃ reference material synthesized in this study. Although the synthesized catalysts were oxidized to 750°C, they were found to be reduced completely below 675 °C. It has been previously reported that high temperature calcination increases resistance to nickel reduction, and calcination of Ni on Al₂O₃ in air at 750 °C requires above 800 °C for reduction¹⁰⁰. These excellent reduction characteristics of our catalysts are attributed to the procedure which includes ammoniacal treatment, being different from the reported synthesis¹⁰⁰.

The reduction profile (Figure 5.1) of both the La modified and plain nickel on alumina catalysts show two overlapping peaks between 350 °C and 700 °C. For all the catalysts, the maxima of the first peak appeared between 450 °C and 500 °C while the second

maxima occurred between 600 °C and 650 °C, suggesting that two major species of Ni oxide exist. In the case of a supported nickel catalyst, the species reduced above 600 °C is attributed to NiAl_2O_4 ¹⁰¹. Therefore, the peaks below 600 °C are ascribed to NiO, whereas the peaks 600 °C to 650 °C are due to NiO incorporated with NiAl_2O_4 .

High temperature oxidation/reduction reinforces any chemical interactions with the support, changes the NiO crystallite size, and incorporates mobile Al^{3+} into the NiO crystallites, resulting in the formation of nickel aluminate¹⁰⁰.

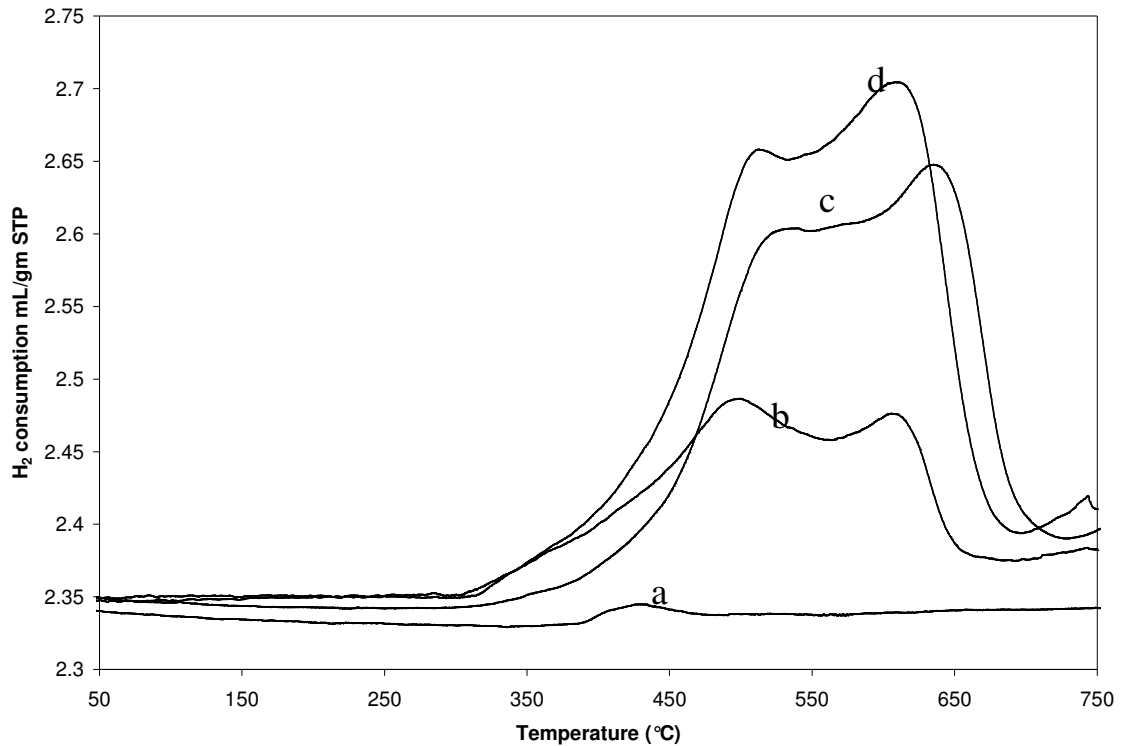


Figure 5.1: TPR profile of a) 3.5wt% $\text{La}_2\text{O}_3/\theta\text{-Al}_2\text{O}_3$ b) 3.5wt% La_2O_3 -18% Ni/ $\theta\text{-Al}_2\text{O}_3$ (La loaded after Ni loading) c) 3.5wt% La_2O_3 -18% Ni/ $\theta\text{-Al}_2\text{O}_3$ (La loaded before Ni loading), d) 18wt% Ni/ $\theta\text{-Al}_2\text{O}_3$.

It was previously suggested that small NiO crystallites with high dispersion on the support are reduced at comparatively high temperatures indicating that most of the nickel species are NiO¹⁰⁰. Therefore, reduction of the 650 °C species may be NiO strongly attached to the support with formation of some NiAl₂O₄.

The TPR profile clearly shows that lanthanum has negligible reducibility even when the catalysts reached 750 °C under hydrogen flow (Figure 5.1a). When comparing the effects of the sequence of La₂O₃ loading, the results indicate that La₂O₃ blocked some nickel species when lanthanum was loaded after nickel on the alumina support. As a result, the amount of reducible nickel species significantly decreased (Figure 5.1b). On the other hand, when La₂O₃ was loaded before Ni, hydrogen consumption for reduction of Ni was affected significantly less compared to 18wt%Ni loading on alumina (Figure 5.1d). Another important aspect of La₂O₃ adsorption is shifting the reduction temperature, as La₂O₃ helps reduce the nickel species by shifting the peak to higher temperatures by lowering the hydrogen consumption. This phenomenon can be attributed to better dispersion of Ni and enhanced interactions between Ni and La₂O₃ to form La₂NiO₄ that may not be fully reduced. It was previously shown that nickel reacts with lanthanum at high temperature (>700 °C) to form La₂NiO₄¹⁰².

Figure 5.2 shows the TPR spectra of spent catalysts after SCWG which shows two distinct peaks. It should be noted that spent catalysts were not oxidized before TPR analysis. As the TPR peaks appear, it can be concluded that the catalysts were oxidized during SCWG. The low temperature peak is assigned to NiO phase reduction while the high temperature peak is due to NiAl₂O₄ reduction. When comparing between Figures 5.1 and 5.2, it is noticed that complete reduction shifts from 675 °C (Figure 5.1) to above 800

°C (Figure 5.2) and the size of the low temperature peak was significantly decreased after exposing the catalyst to the SCW reaction environment. This observation indicates that a significant amount of nickel reacted with the alumina support during SCW conditions forming nickel aluminates¹⁰¹. The La doped Ni/Al₂O₃ catalyst (Fig 5.2c) consumed a higher amount of hydrogen for reduction and the low peak of aluminate indicates that a higher amount of nickel oxide remains on the catalyst which in turn shows better stability. Low hydrogen consumption can also be attributed to some dissolution or erosion of metal in the harsh SCW environment¹⁰³.

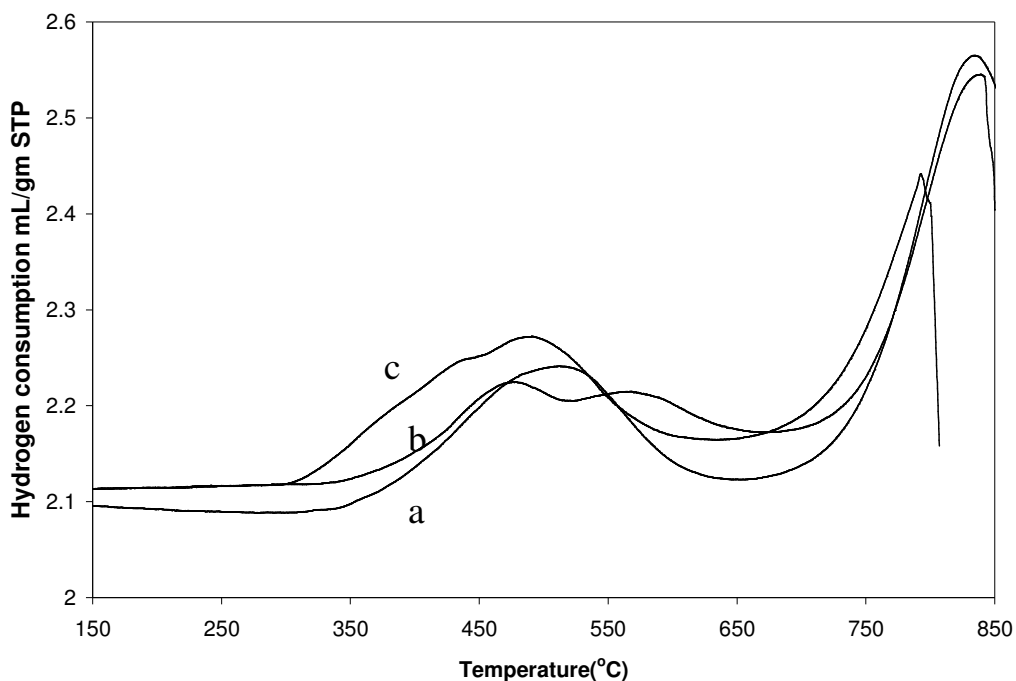


Figure 5.2: TPR profile of spent catalysts: a) 18wt% Ni b) 3.5wt% La₂O₃-18wt% Ni (La loaded after Ni loading) c) 18wt% Ni -3.5wt% La₂O₃ (La loaded before Ni loading).

Figure 5.3 shows the TPR spectra of fresh nano catalysts. Contrary to the pelletized catalysts, metals impregnated on nanofibers (Figure 5.3 a) showed peaks at 480 °C and

595°C (below 600 °C) ascribed to deposited NiO (as discussed earlier). The shoulder at 595°C is attributed to NiO strongly attached to the support alumina. On the other hand sol-gel derived nano catalyst (Figure 5.3 b) showed one small peak at 428°C ascribed to bulk NiO on the catalyst surface. The small peak attributed to most of the metals doped by the direct sol-gel method could not be reduced ascribed to formation of Ni-La-Al-O alloy structure. In impregnation method, metals were deposited on catalyst support which could be reduced easily by using temperature program method.

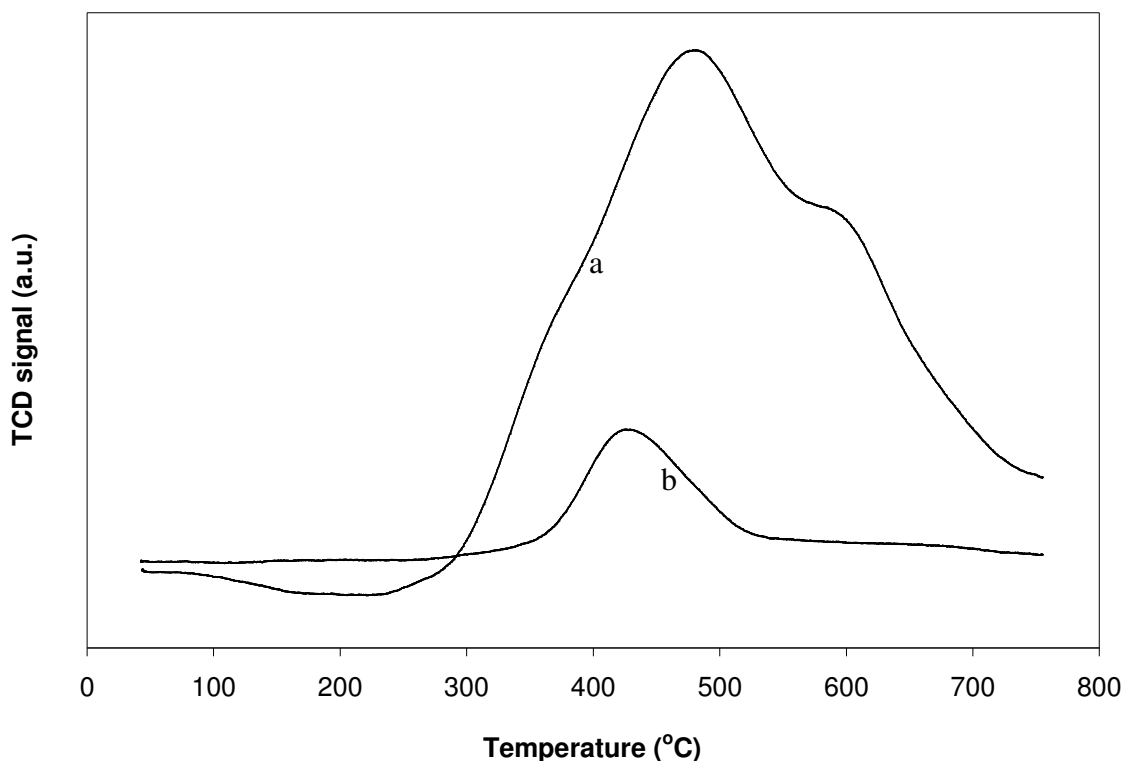


Figure 5.3: TPR profile of fresh nano catalysts: a) 18wt% Ni-3.5wt% La₂O₃/ ̸-Al₂O₃ nanofiber b) Sol-gel derived Ni-La-Al-O catalyst.

Figure 5.4 shows the TPR spectra of the spent nano catalysts without pre-treatment by oxygen flow. Like impregnated catalysts, nano catalysts were also oxidized during

SCWG. It should be noted that no oxidant was used during SCWG with these nano catalysts. It is seen that use in SCW shifted the reduction temperatures towards higher temperatures. For the nanofiber catalysts (Figure 5.4 a), the first broader peak at 567°C is attributed to a major portion of deposited nickel remained as NiO even after SCW exposure, however the peak at 773°C is ascribed to a significant amount of nickel interacted with the support alumina forming NiAl₂O₄. On the other hand a small peak at 500 °C with the sol-gel derived catalyst indicates that some impurities from SCWG or metallic NiO may be present on the catalyst surface that are not bonded with the catalysts main structure.

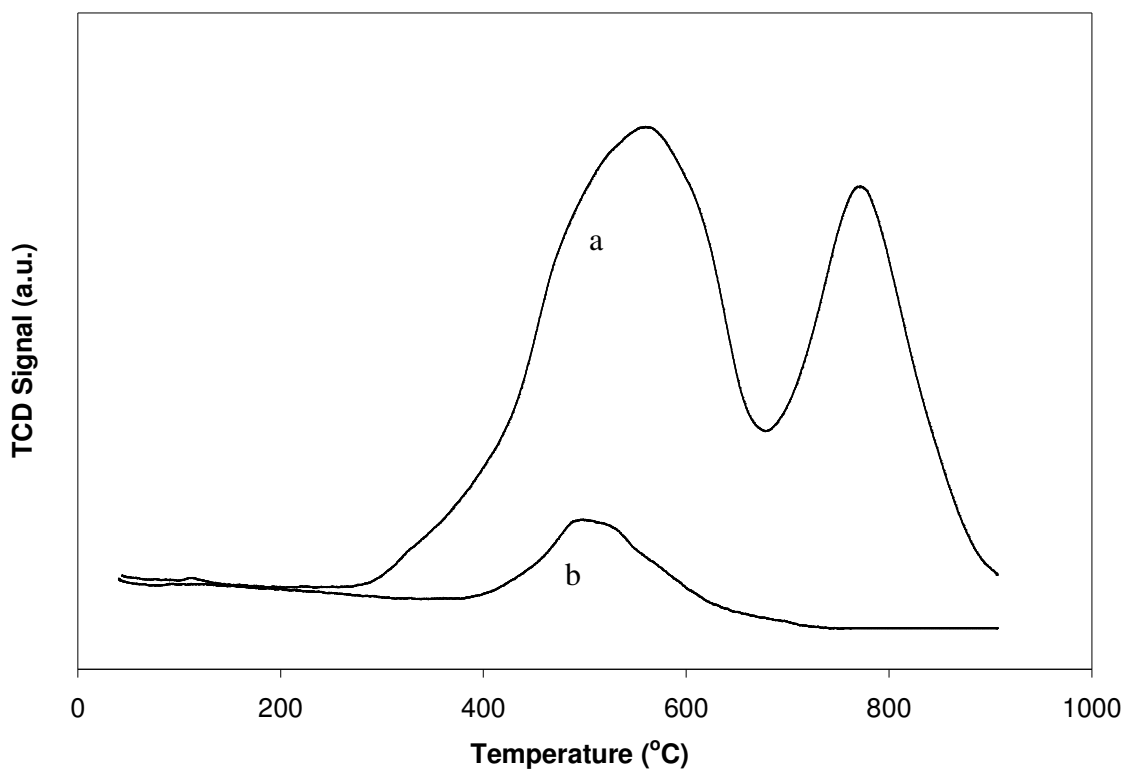


Figure 5.4: TPR profile of spent nano catalysts: a) 18wt% Ni-3.5wt% La₂O₃/θ-Al₂O₃ nanofiber b) Sol-gel derived Ni-La-Al-O catalyst.

Using Equations (5.2 and 5.3); Figure 5.5 displays the percent of nickel reduction of fresh and spent catalyst during TPR analysis. It is clear from this figure that except for the sol-gel derived catalysts, the reducibility of both the fresh and spent catalyst is very high (above 90 %). It can be concluded that nickel present in the catalyst, can be regenerated by simple reduction. Very low reducibility of sol-gel derived catalyst further confirms that most of the metals loaded during synthesis formed Ni-La-Al-O structural bonds, which are relatively stable.

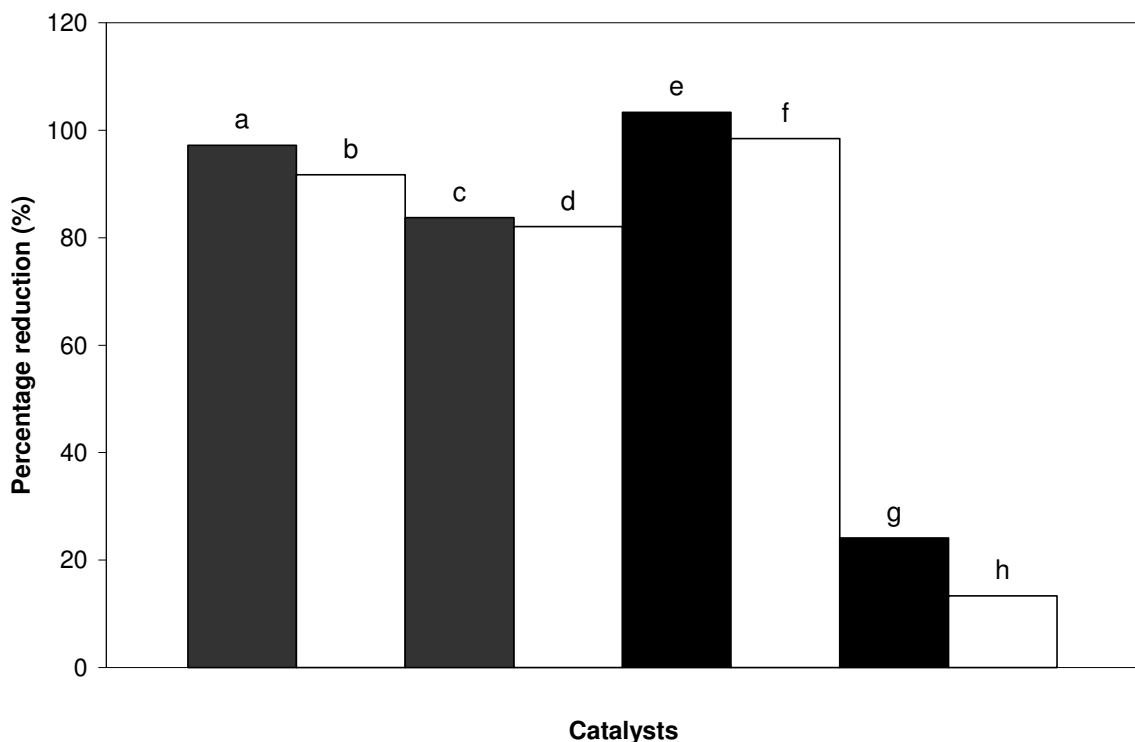


Figure 5.5: Metal percent reduction: a-b) 18wt% Ni / θ - Al_2O_3 , c-d) 3.5wt% La_2O_3 -18wt% Ni/ θ - Al_2O_3 , e-f) 3.5wt% La_2O_3 -18wt% Ni / θ - Al_2O_3 fibers, g-h) Direct sol-gel derived Ni-La-Al-O; a-c-e-g) Fresh catalysts, b-d-f-h) Spent catalysts.

Interestingly, the % reduction was found greater than 100% when La_2O_3 was loaded after Ni. This can be explained by the formation of NiAl_2O_4 and the partial reduction of La_2O_3 ¹⁰⁴. If non-stoichiometric reduction occurs due to the presence of NiAl_2O_4 , the amount of

hydrogen needed may be greater than the amount of hydrogen required for the available NiO, which has been shown to over estimate the % reduction ¹⁰⁴.

5.3.3 H₂ Pulse Chemisorption

Pulse chemisorption experiments were performed in order to determine the active metal surface area, the % metal dispersion and the active particle size of the nickel crystals on the alumina support. No peak was found for lanthanum on alumina as lanthanum has negligible reducibility. A decrease in the active surface area and the number of active sites is also an indication of agglomeration.

Table 5.2 shows the pulse chemisorption results obtained for the nickel based catalysts synthesized in this investigation.

Table 5.2: Hydrogen chemisorption results for reduced catalysts.

Catalysts	Metal dispersion (%)	Active metal surface area		Active particle diameter (nm)	
		(m ² /gm sample)	(m ² /gm metal)		
B	2.86	1.62	19.05	35.4	
C	2.49	1.82	16.55	40.73	
D	Fresh	2.27	2.72	15.13	44.55
	Spent	0.53	0.63	3.50	192.65
G	Fresh	1.31	1.39	8.71	77.37
	Spent	0.62	0.66	4.10	164.32
H	Fresh	1.50	1.80	10.02	67.28
	Spent	0.84	1.00	5.57	120.95
J	Fresh	5.28	3.87	35.16	19.17
	Spent	1.23	0.90	8.15	82.62
K	Fresh	0.13	0.093	0.85	793.60
	Spent	0.10	0.073	0.66	1020.68

It is important to mention that no hydrogen chemisorption was detected when only La_2O_3 was loaded on the alumina support. This confirms that for the La_2O_3 doped nickel catalyst samples, hydrogen chemisorption occurred on the nickel sites.

As can be seen in Table 5.2, with an increased metal loading (catalysts B to C to D), the metal dispersion decreased, and the active particle diameter increased due to the formation of larger metal crystallites. The surface area of nickel sites gives information on the active metal area measured by chemisorption. An increase in the active metal (nickel) surface area per gram of catalyst and a decrease in the active metal surface area per gram metal are other indications of the formation of larger crystallites. Although it has been reported that lanthanum oxide helps to disperse metallic crystallites¹⁰⁵, the metal dispersion and surface area were significantly decreased when 18wt%Ni was loaded on 3.5wt% La_2O_3 modified alumina support (catalyst G) or 3.5wt% La_2O_3 on the 18wt% Ni/ Al_2O_3 . This may be due to the formation of La_2NiO_4 in the catalyst preparation stage. During the calcination step, at elevated temperature (750 °C in this case) in the presence of oxygen, La reacts with Ni to form La_2NiO_4 ¹⁰² that causes blocking of nickel crystallites¹⁰⁶. Strong metal–support interactions may also have influenced the amount of H_2 adsorbed¹⁰⁶. Another possibility that can cause the same effect is the presence of strongly chemisorbed hydrogen on the metal particles, formed during the reduction step, which inhibits any further hydrogen chemisorption¹⁰⁶.

Nanofiber catalysts (Cat. J) showed the best metal dispersion, and active metal surface areas among the catalysts evaluated. This finding is ascribed to the formation of small metallic crystals (smallest among catalysts evaluated) on the support. Like the other catalysts, agglomeration of active metal on the spent nanofiber catalyst resulted in the

formation larger metallic crystallites on the surface. On the contrary, the direct sol gel derived catalyst showed extremely low metal dispersion, active metal surface area with very large metallic crystal diameter. This result further confirms that a small amount of bulk metal remained on the catalyst surface while most of the active metals were integrated within the main Ni-La-Al-O structure.

A decrease in metal dispersion and an increase in the active particle diameter of spent catalysts from SCWG indicate that some agglomeration of metals occurred. As well, a decrease in the surface area may also be due to dissolution or erosion of metal occurring under SCW conditions¹⁰³.

5.3.4 Temperature Programmed Desorption

Since CO₂ is one of the major products of supercritical water biomass gasification, the CO₂ adsorption properties of the experimental catalysts was studied by TPD in which the amount of CO₂ adsorbed on the catalyst surface at 500 °C for 30 min is measured by desorption analysis. Figure 5.6 shows the TPD profile of CO₂ by the catalysts in which two major peaks are observed. This result can be attributed to the different bonding modes of CO₂ with the active sites during adsorption on the surface. Cox¹⁰⁷ showed that coordination of CO₂ onto metal oxides has different energies which leads to different desorption profiles. The lower temperature peak (180 to 250 °C) is due to desorption of CO₂ with the weakest bonding mode on the catalyst active sites. On the other hand, strong bonds of CO₂ with catalyst require higher temperatures to produce more energy for desorption of CO₂.

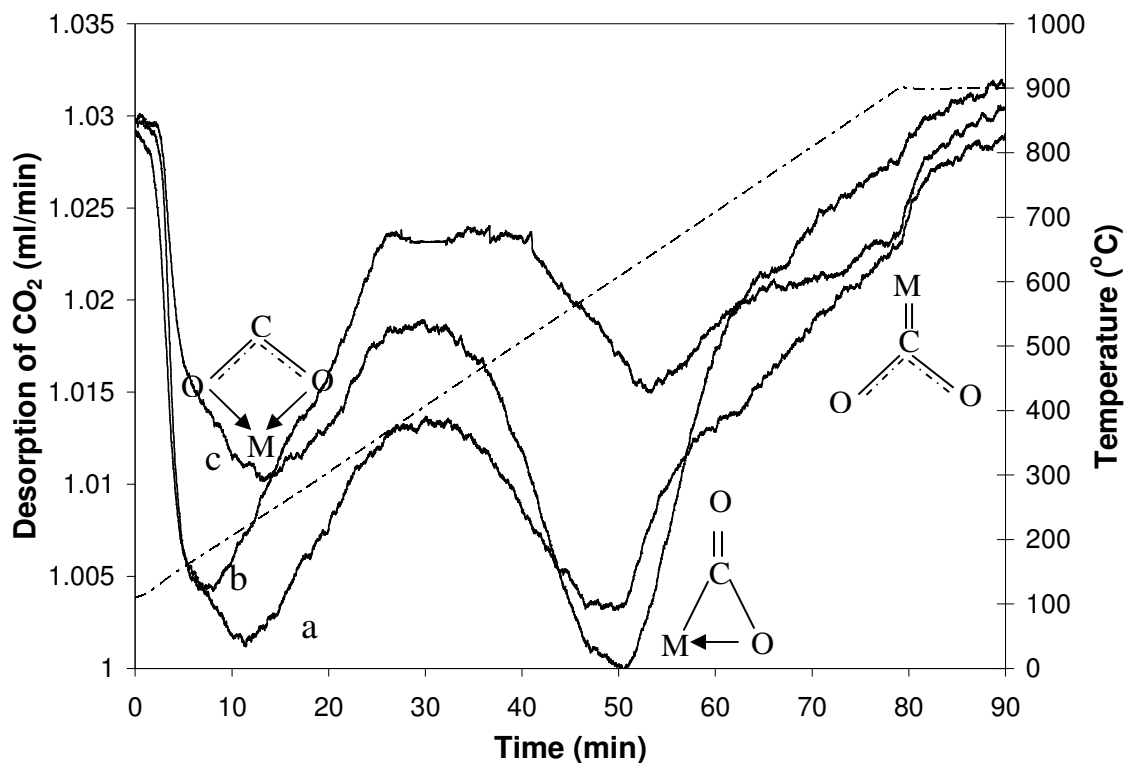


Figure 5.6: Temperature programmed desorption. (a) 3.5wt% La₂O₃, (b) 18wt% Ni, (c) 3.5wt% La₂O₃-18wt% Ni.

From Figure 5.6 it is seen that most CO₂ on the Ni surface is adsorbed weakly and desorbed at 185°C. Both weak and strong bonding of CO₂ on La₂O₃ is observed which desorb at 225°C and 600 °C, respectively. Interestingly on the Ni-La₂O₃ catalyst surface, mostly strong bonding of CO₂ was observed that needed 600 °C to be desorbed. As our reaction temperature is 500 °C, the strong bonding portion of CO₂ coordination remains adsorbed on the Ni-La₂O₃ surface.

5.3.5 TGA Analysis

Following the SCWG reaction, the spent catalyst samples were collected and further analyzed using TGA to characterize the effect of the SCW environment on the catalyst

structure and stability. TGA is also of interest as it is useful in determining possible carbon deposition on the solid catalyst during the reaction. Figure 5.7 shows the weight loss curves of the different catalysts as a function of temperature in air. Figure 5.7a is the TGA curve of fresh 18wt% Ni/ θ -Al₂O₃ catalyst, where 1.5% weight reduction before 200 °C is observed due to loss of adsorbed water during reduction or gases adsorbed from the environment. The weight gain after 200 °C exceeds 100% due to the oxidation of Ni to NiO. After 600 °C, non-stoichiometry formation of nickel aluminate forms active metal¹⁰¹. The weight gain of lanthanum modified reduced nickel on alumina (Figure 5.7b) is comparatively low, indicating that a stronger interaction of nickel with lanthanum prohibits oxidation of nickel. The weight loss of spent catalyst (Figure 5.7c-f) is due to the removal of adsorbed water, gases and deposited carbonaceous species. No net weight gain of the spent catalysts was observed, indicating that reduced catalysts were already oxidized during SCWG process (confirmed by TPR analysis). The initial weight loss up to 200 °C is ascribed to adsorbed water during the reaction and any easily oxidizable carbonaceous species¹⁰⁸. The oxidation of coke (carbon deposit) to CO and CO₂ mainly occurred at 360 °C, consistent with the results of others.¹⁰⁹. The weight loss was least for the spent 18wt%Ni on alumina (Fig 5.7c) compared to the other La₂O₃ modified catalysts (Figure 5.7d-f). This may be due to formation of graphitic carbon on the nickel catalysts. Pinherio et al.¹¹⁰ found that the larger the amount of graphite like carbon deposition on a catalyst surface, the lower the weight loss. They reported that for Ni catalysts, graphite like carbon forms in higher amounts than with Pt catalysts¹¹⁰. The formation of graphite like carbon on Ni and inhibition of this type of coke formation by La modified catalysts was further confirmed by XRD, and Raman analysis as discussed below. In addition, the

amorphous carbon encapsulating the agglomerated Ni particles of spent catalysts was found difficult to gasify, similar to that found by Matsukata et al.¹¹¹. The other reason for high weight loss by spent La_2O_3 is that strongly bonded CO_2 on La_2O_3 requires higher temperatures to desorb than used in the reaction as shown by CO_2 -TPD analysis.

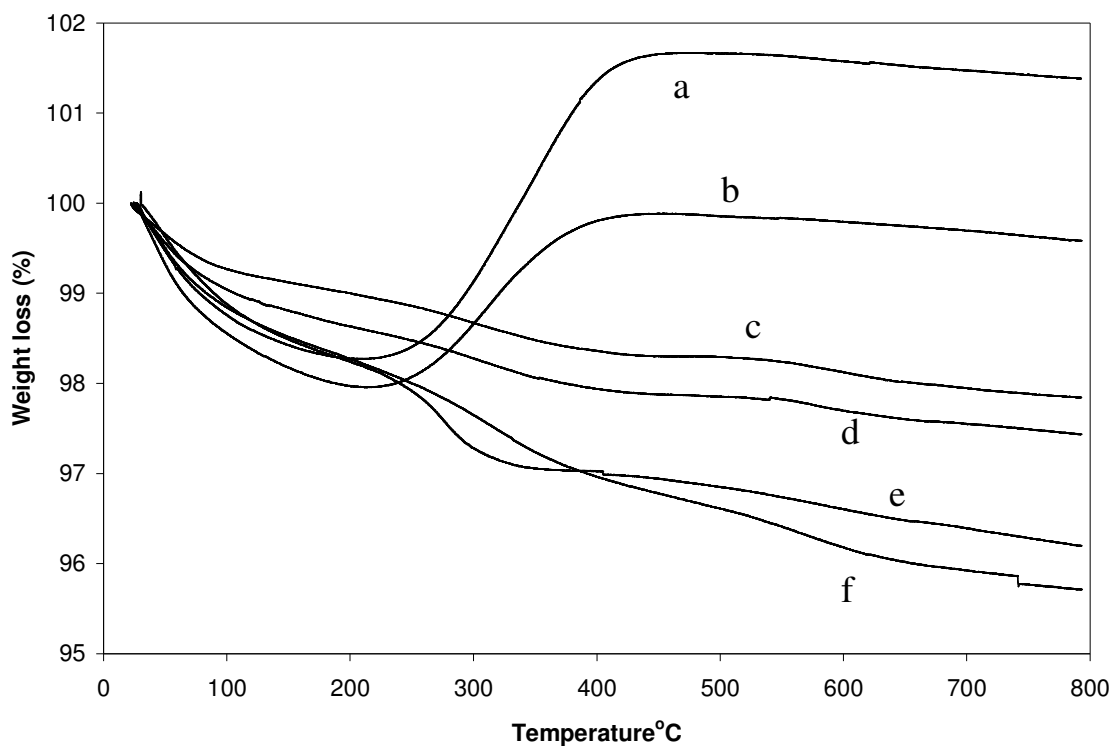


Figure 5.7: TGA Analysis a) 18wt% Ni/ θ - Al_2O_3 (Fresh) , b) 18wt% Ni-3.5wt% La_2O_3 / θ - Al_2O_3 (Fresh, La_2O_3 loaded before Ni loading), c) 18wt% Ni/ θ - Al_2O_3 (Spent), d) 18wt% Ni-3.5wt% La_2O_3 / θ - Al_2O_3 (Spent, La_2O_3 loaded before Ni loading), e) 18wt% Ni-3.5wt% La_2O_3 / θ - Al_2O_3 (Spent, La_2O_3 loaded after Ni loading), f) 3.5wt% La_2O_3 / θ - Al_2O_3 (Spent).

Adsorbed CO_2 by lanthanum modified spent catalysts lost weight in two ways: i) dissociation of lanthanum oxycarbonate formed during reaction (confirmed by XRD analysis) and ii) reaction of oxycarbonate with surface carbon to produce carbon oxides. Impregnation of lanthanum before and after nickel impregnation also affects the weight

loss significantly. As discussed earlier, if lanthanum is impregnated after nickel (Fig 5.7e), there is a layer of lanthanum oxide over nickel which helps to form extra carbeneous complex. On the other hand, if lanthanum oxide is loaded before nickel (Fig 5.7d), the weight loss is due to coke formation and some carbonated lanthanum complex. Lanthanum oxide is known to have a high ability to adsorb water and carbon dioxide⁹² (as shown in Figure 5.6) that results in a higher weight loss.

5.3.6 Raman Spectroscopy Analysis

To probe the structure and crystallite size of coke on spent reforming catalysts, Raman spectroscopy has been extensively used. Figure 5.8 shows a typical Raman spectrum of spent catalysts without any sample pre-treatment. The peak around 1581cm^{-1} , which is more prominent on the Ni/Al₂O₃ catalyst, confirms the presence of graphitic coke¹¹². However on the La modified catalyst, this peak is less intense showing the inhibition of graphitic coke. The peaks around 1300cm^{-1} are due to carbon nano particles, amorphous carbon, or defective filamentous carbon¹¹², which also shows that the La modified catalyst helps to inhibit formation of carbon. Further characterization of the coke on spent catalysts was performed using XRD and temperature programmed oxidation analysis.

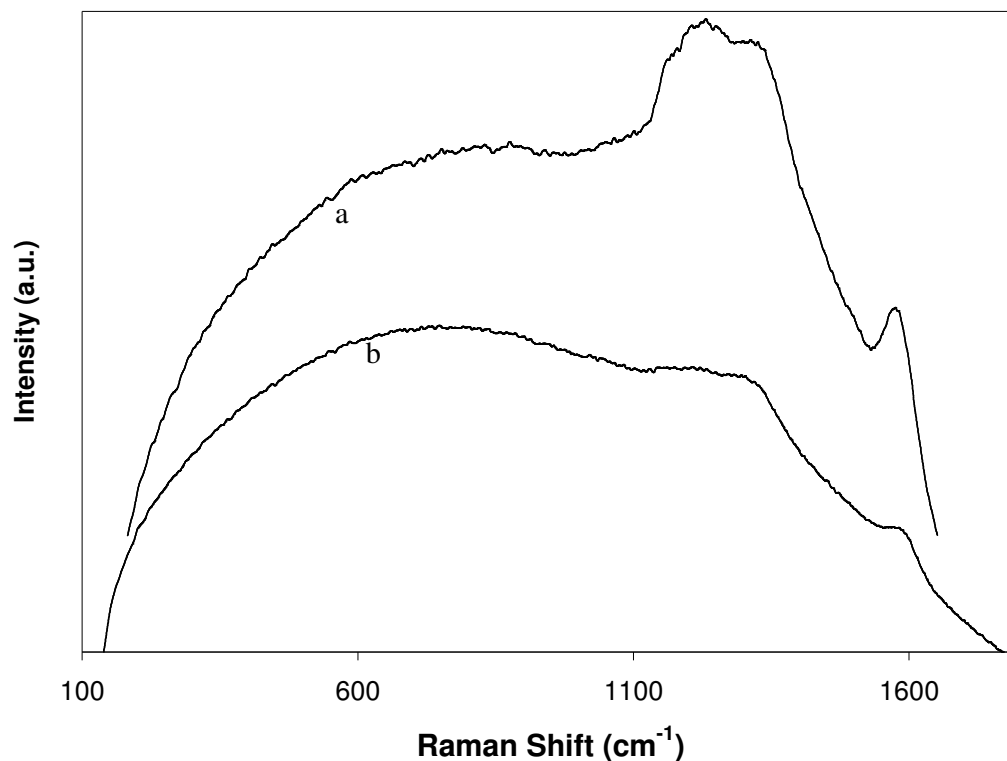


Figure 5.8: Raman spectra of the coke of spent catalysts. (a) 18wt% Ni/ θ -Al₂O₃ (b) 18wt% Ni- 3.5wt% La₂O₃/ θ -Al₂O₃

5.3.7 XRD Analysis

XRD measurements were conducted for the investigated catalysts before and after SCWG to investigate any changes, as shown in Figure 5.9.

The peaks at 52.26° and 61.3° on the fresh reduced Ni catalysts (Fig 5.9 a,e) are due to metallic nickel¹¹³, which subsequently disappears on the spent catalysts. Nickel oxides (50.86°) and nickel aluminates (78.26°) appear on the spent catalyst. The peaks at 43.52° and 67.94° of nickel loaded spent catalyst (Figure 5.9 b,f) intensified due to the formation of nickel aluminate^{113, 114} and at 41.06° from the formation of NiO¹¹⁴. The peak at 73.2°

appears only on the nickel-lanthanum-alumina spent catalyst (Figure 5.9f) and can be attributed to the formation of La_2NiO_4 ¹⁰².

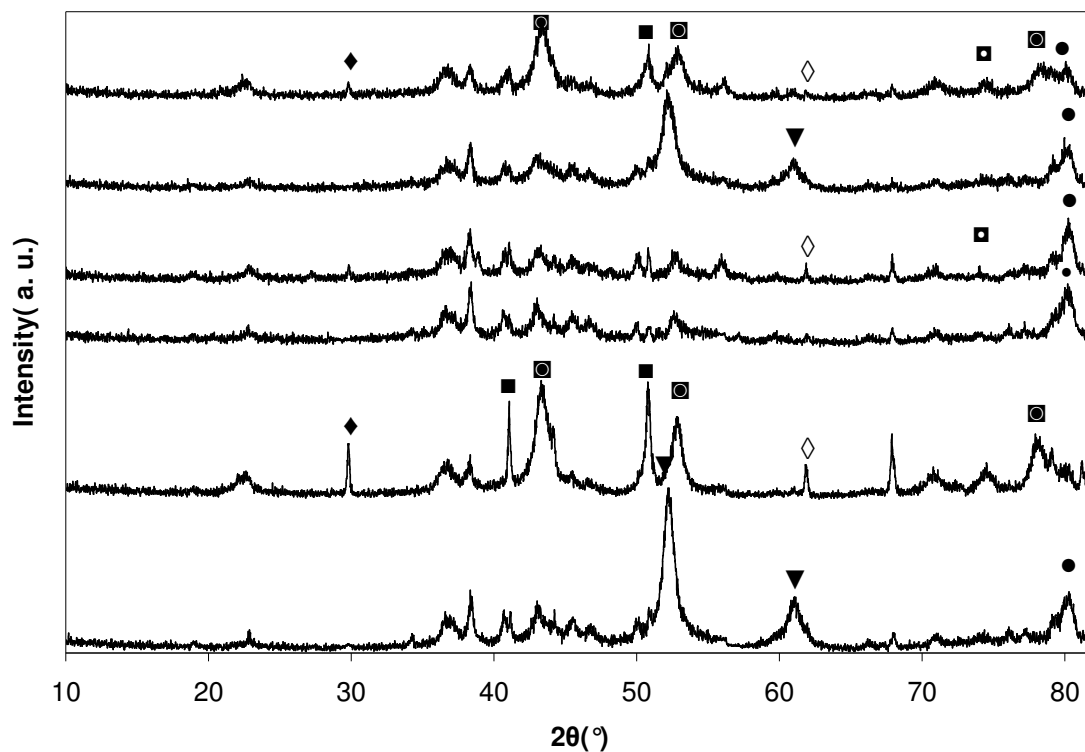


Figure 5.9: XRD patterns of a-c-e) Fresh Catalysts, b-d-f)Spent catalysts; a-b) 18wt% Ni/ θ - Al_2O_3 , c-d) 3.5wt% La_2O_3 / θ - Al_2O_3 , e-f) 18wt% Ni-3.5wt% La_2O_3 / θ - Al_2O_3 . \blacklozenge - Graphite; \bullet - Al_2O_3 ; \blacktriangledown -Ni; \blacksquare - NiAlO_4 ; \blacksquare -NiO; \blacksquare - $\text{La}_2\text{O}_2\text{CO}_3$; \blacklozenge - coke; \circ - La_2NiO_4 ; \square - La_2O_3

The peaks at 29.84° and 61.92° on the spent catalyst can be attributed to different types of coke that formed on the catalyst surface. The peak at 61.92° , only on the spent catalysts, can be attributed to the formation of carbonaceous products or coke during SCWG while the peak at 29.84° appears on spent Ni/ Al_2O_3 (Fig 5.9b), indicating the formation of graphite type coke¹¹³. A very tiny peak forms on lanthanum-loaded spent

catalysts at 56.24° and 74.04° which can be ascribed to the formation of lanthanum oxycarbonate¹¹⁵.

Figure 5.10 shows the XRD peaks of fresh and spent catalysts at different reaction time. It is seen that conversion of Ni to NiO and NiAlO₄ happened mainly in the first five minutes.

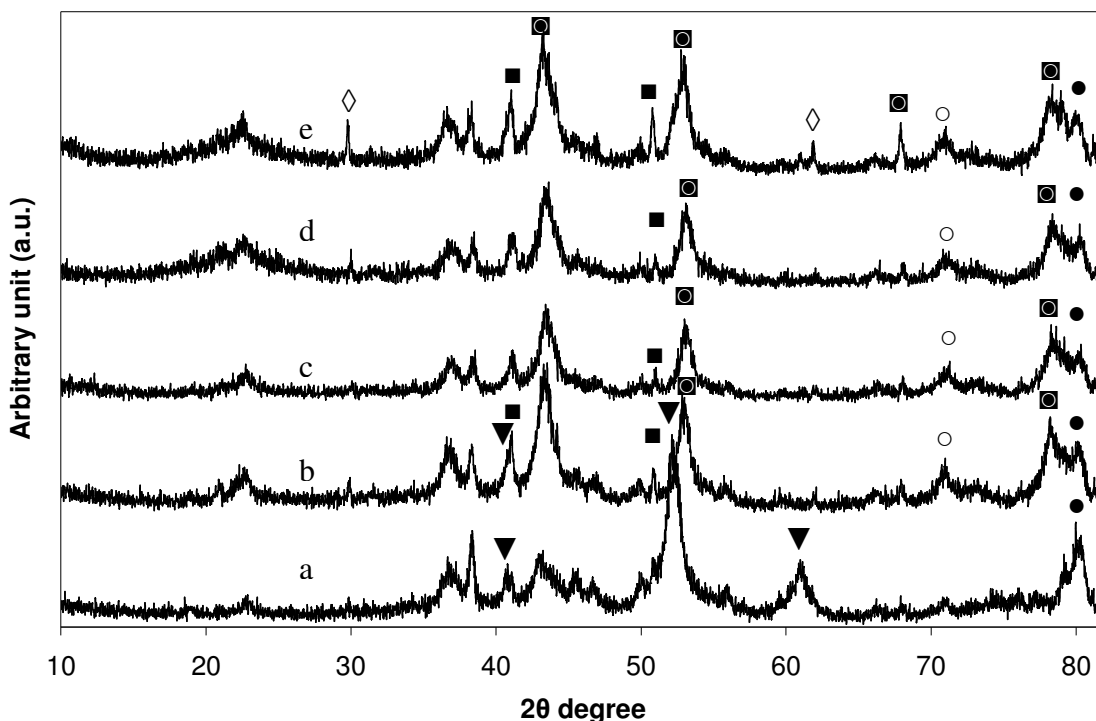


Figure 5.10: Reaction time effect on XRD patterns of Ni-La₂O₃/Al₂O₃ a) Fresh catalyst, Spent catalysts at: b) 5 min c) 20 min, d) 30 , e) 60 min ; ▼-Ni; □-NiAlO₄; ■-NiO; ●-Al₂O₃; ○-La₂NiO₄; ◇- coke.

The size of Ni (d_{xrd}) was found to be approximately 86 nm while the size of NiO was a little larger and ranged from 92 nm to 93.5 nm. A similar effect is seen for the other crystallites. Therefore the effect of catalysts' surface change after initial conversion (5 minutes in batch reactor) can be considered negligible.

Figure 5.11 shows the XRD peaks of fresh and spent nano catalysts to verify the crystallinity change in nano structure.

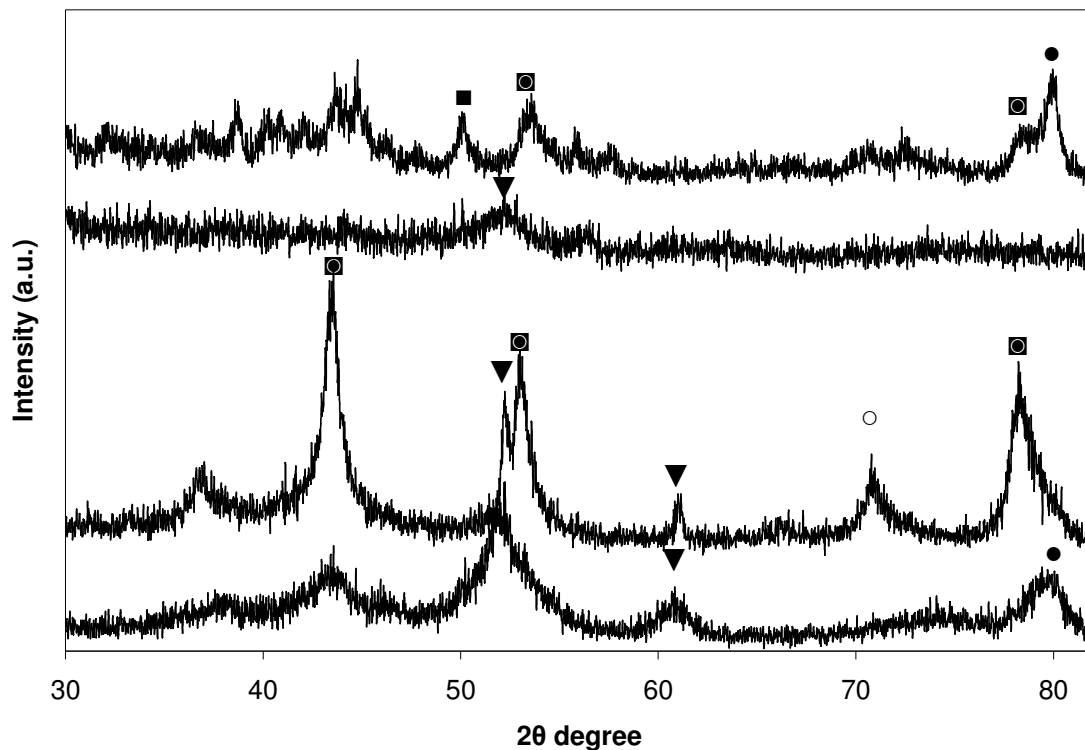


Figure 5.11: XRD patterns of a-b) 18wt% Ni/ θ - Al_2O_3 (nanofiber), c-d) Ni La-Al sol-gel derived; a-c) Fresh Catalysts, b-d) Spent catalysts; ●- Al_2O_3 ; ▼-Ni; ◻- NiAlO_4 ; ■-NiO

The nanofiber catalyst showed similar characteristics as shown with pellet size catalysts due to the same impregnation procedure (Figure 5.11 a-b). However, the direct metals loading by sol-gel method showed that fresh catalyst was mostly amorphous (Figure 5.11c). A tiny peak for Ni at 52.26° further confirmed that a small amount of bulk Ni was attached on the surface while most of the metals were integrated with the support. Exposure to SCW transformed the catalysts to formation of NiAlO_4 .

5.3.8 Temperature Programmed Oxidation of Spent Catalysts

Temperature programmed oxidation (TPO) of the spent catalysts was performed to further examine the characteristics of deposited carbonaceous products on the catalysts during reaction, as shown in Figure 5.12. There are three types of coke or carbonaceous products present as indicated from the figure. The low temperature peak is more reactive to oxygen, and has been assigned to coke deposited on metallic centers¹¹⁶. The second peak type is attributed to coke deposited near the metal-support interphase,¹¹⁷ while the third type is less reactive, appearing at higher temperature, and corresponds to coke deposition on the support¹¹⁶. This coke type is far from the active metallic centers, which catalyze the carbon gasification¹¹⁷.

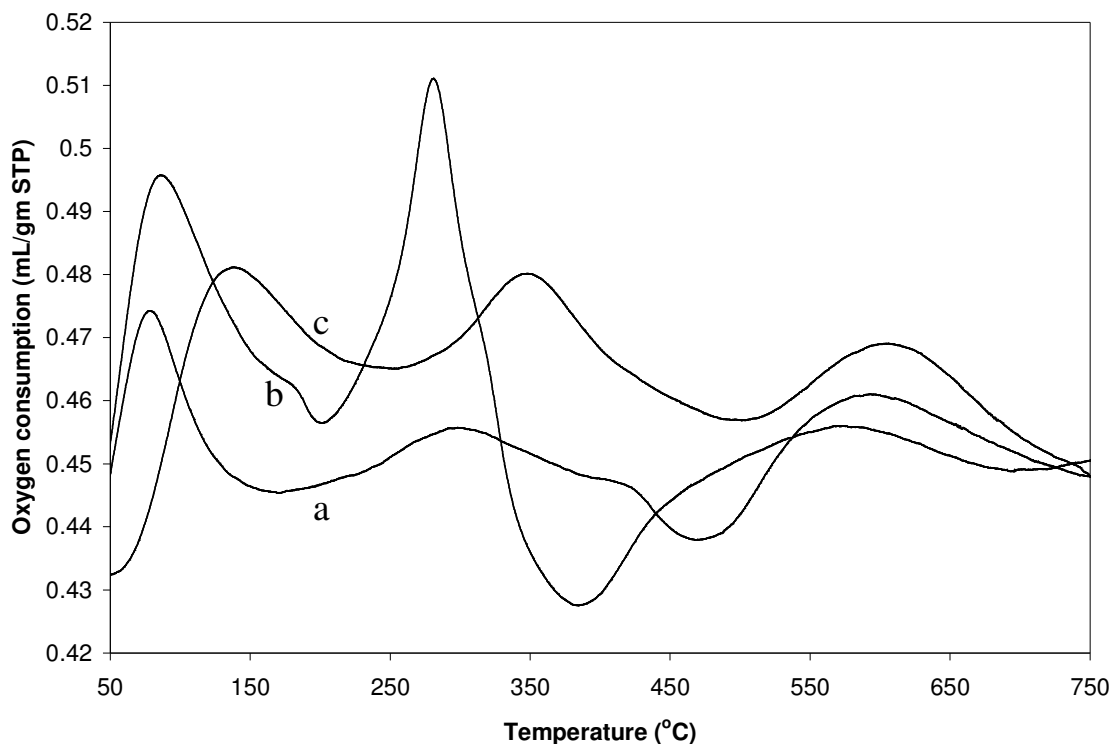


Figure 5.12: Temperature programmed oxidation profile of a) 18wt% Ni/ θ - Al_2O_3 (Spent) b) 18wt% Ni-3.5wt% La_2O_3 / θ - Al_2O_3 (Spent), c) 3.5wt% La_2O_3 / θ - Al_2O_3 (Spent)

The oxidation of coke (carbon deposit) to CO and CO₂ mainly occurred at 360 °C¹⁰⁹. The oxygen consumption is low on the spent 18wt%Ni/θ-Al₂O₃ (Figure 5.12a) compared to lanthanum and lanthanum modified catalysts. The literature shows that coke formation is higher on Ni/La₂O₃ than Ni/Al₂O₃¹¹⁸. Lanthanum oxide not only adsorbs carbon dioxides easily but also may form lanthanum oxycarbonate (La₂O₂CO₃), similar to reforming type reactions^{29,92}. As discussed earlier, this oxycarbonate reacts with deposited coke and acts as a self cleaner by producing carbon monoxide which later reacts with oxygen or water to form carbon dioxide.

5.3.9 TEM analysis

To observe any structural change in the catalysts, TEM analysis was performed. Figure 5.13 shows the TEM images of fresh and spent catalysts. It is clearly seen that structural changes occurred after using in SCWG. Comparing Figure 5.13a with 5.13b it is further confirmed that metals impregnated on the supports agglomerated when exposed to SCW.

The fibrous structure of the nanofiber catalysts was distorted by reaction in the SCW environment (Figure 5.13 c-d). The severe transformation occurred with the sol-gel derived catalysts. The porous aerogel structure of direct sol-gel derived catalysts transformed to non-uniform nano structures (such as nano sheet, rod, sphere, cube etc.).

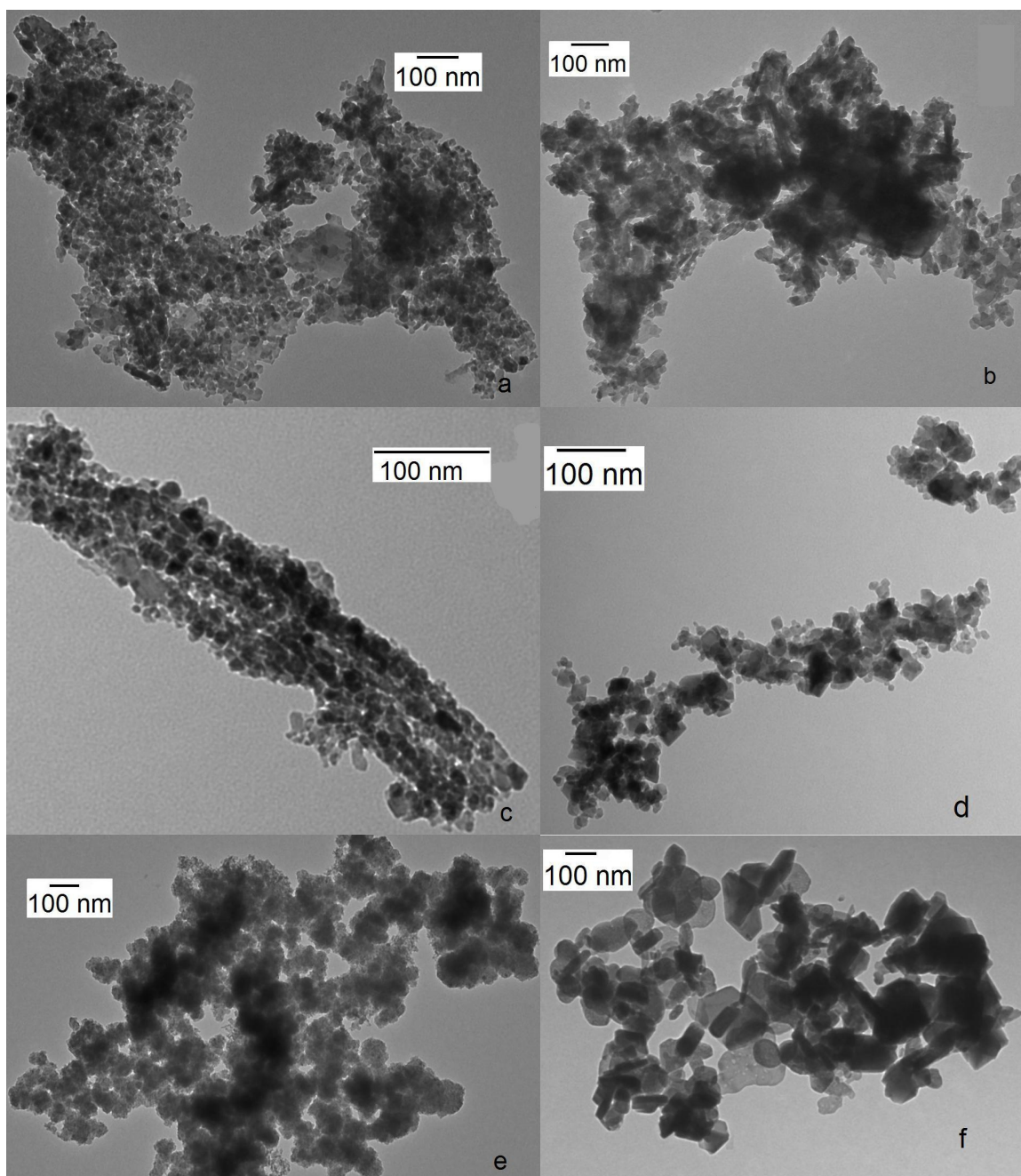


Figure 5.13: TEM images of a-b) 18wt% Ni-3.5wt% La₂O₃/θ-Al₂O₃(pellet), c-d) 18wt% Ni-3.5wt% La₂O₃/θ-Al₂O₃ (fiber), e-f) Ni-La-Al-O (direct sol gel derived); a-c-e) Fresh catalysts, b-d-f) Spent catalysts

5.3.10 Reaction mechanism

Carbon dioxide adsorption, comparatively low coke formation and the formation of lanthanum oxycarbonate using the La modified catalysts can be described as follows:

Formation of lanthanum oxycarbonate by adsorbing carbon dioxide



Lanthanum oxycarbonate species reacts with surface carbon (scavenging coke) formed by glucose or intermediate product decomposition (confirmed by XRD and Raman analysis) at the periphery to form carbon monoxide and lanthanum oxide



By adsorbing carbon dioxide and releasing carbon monoxide, lanthanum helps to resist the methanation reaction of CO₂ and further enhances the water gas shift (WGS) reaction.



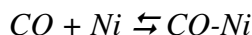
From our previous study (chapter 4) it is seen that although La adsorbs CO₂; production of CO₂ increased with time. From equations 5.7 and 5.8, one can see that two mol of CO is released if one mol of CO₂ is adsorbed scavenging one mol of coke by La. From the WGS reaction, these two mol of CO produce two mol of CO₂. Therefore, the net CO₂ production is positive.

This mechanism can help to explain the higher yield of hydrogen, lower yield of methane and high yield of carbon dioxide by lanthanum and lanthanum modified catalysts compared to plain nickel catalyst.

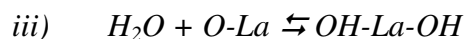
The water gas shift reaction and carbon dioxide methanation reaction on the catalyst surface can be described as follows:

Water gas shift reaction:

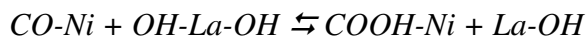
- i) Carbon monoxide adsorbs reversibly on nickel



- ii) Water adsorbs dissociatively on lanthanum oxide



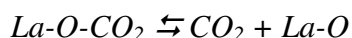
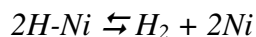
- iv) Carboxyl formation takes place via the reaction of adsorbed CO with hydroxyl group on the lanthanum



- v) The carboxyl species and second hydroxyl group on lanthanum react to form adsorbed hydrogen and carbon dioxide

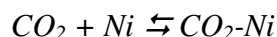
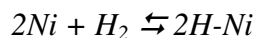


- vi) Once an adjacent nickel site becomes free this carboxyl complex decomposes into the reaction products. Hydrogen competes with carbon monoxide for nickel adsorption sites. Similarly carbon dioxide is adsorbed strongly on lanthanum

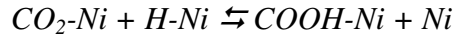


Methanation reaction of carbon dioxide over Ni:

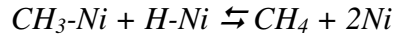
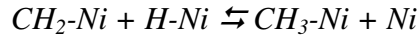
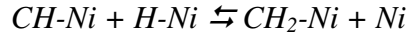
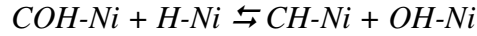
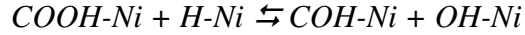
- vii) Adsorption of hydrogen and carbon dioxides



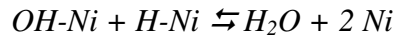
viii) Formation of carboxyl



ix) Reaction with adsorbed hydrogen



x) Releasing the adsorbed hydroxyl group



As mentioned in chapter 4, lanthanum and cerium have similar chemical properties. Germani and Schuurman reported a similar mechanism for water gas shift reaction over Pt/CeO₂/Al₂O₃.¹¹⁹ The reaction mechanism for the methanation of carbon dioxide is similar to that reported by Vandervella and Bowkera.¹²⁰ As carbon dioxide is produced from the WGS reaction, the total production of carbon dioxide remained high. As a result of the WGS reaction, carbon monoxide is consumed while increasing the hydrogen yield. This also helps to reduce the catalyst deactivation by coke formation. Reduction of methane formation is attributed to the produced carbon dioxide or carbon monoxide which did not undergo the methanation reaction even in the presence of a high amount of nickel doped with La.

5.4 Conclusions

Synthesized catalysts by impregnation method were found to have excellent reduction characteristics and can be regenerated by simple reduction. However, agglomeration of impregnated metals by exposure in SCW was found to reduce the active metal surface area. Lanthanum modified catalysts was found to reduce graphitic coke formation and adsorption of carbon dioxide that can contribute to retard methanation of carbon dioxide in the presence of hydrogen. Adsorption of carbon dioxide, one of the main gaseous product, can shift equilibrium to the product direction and thus increase desired product, hydrogen. Formation of lanthanum oxycarbonate by adsorbing carbon dioxide to lanthanum also scavenges deposited carbon and thus helps to minimize catalyst deactivation. Reacting with carbon, lanthanum oxycarbonate produces more carbon monoxide which in turn may enhance the water gas shift reaction and thus increase the hydrogen yield. The reaction mechanism of adsorption of carbon dioxide, WGS reaction, and methanation reaction on nickel sites were discussed.

Nanofiber catalysts were found to have high dispersion of active metals due to the high aspect ratio compared to the other synthesized catalysts. High dispersion of active metal can increase the catalyst activity. Sol-gel derived catalysts were found to have high surface area with mainly amorphous nano network structure of Ni-La-Al-O. However, the high surface areas of nano catalysts were abruptly reduced after SCWG due to structural changes.

Although lanthanum modified catalysts were found to be very active in SCWG (chapter 4), exposure of catalysts in SCW severely affects their physical and chemical structure.

Metal-support interaction of all catalysts was found to be prominent in SCW. Nano network of sol-gel derived catalysts was transformed to non uniform nano particles.

Chapter 6

Development of kinetic model for TOC destruction from supercritical water gasification of glucose

In this chapter, a global kinetic model of supercritical water gasification of glucose was developed for the utilized batch reactor. To reduce the complexity of the model, no oxidant was used for TOC destruction. Crushed La modified Ni/Al₂O₃ catalysts were used for evaluation. A MATLAB program was developed to solve the non-linear regression analysis of differential model equation. This chapter is mostly a reproduction from the article by the author submitted to Industrial Engineering and Chemistry Research¹²¹: Development of kinetic model for TOC destruction from supercritical water gasification of glucose.

6.1 Introduction

Supercritical water gasification is an economically viable and ecologically safe destruction technology for treating wet biomass waste from agricultural or industrial residues into combustible gases without requiring a feedstock drying procedure. Under supercritical conditions, water exhibits gas-like diffusion rates along with high liquid like collision rates, with the reaction taking place in the homogeneous phase. On the other hand, the solubility of inorganic compounds decreases dramatically in supercritical water, facilitating separation of valuable products such as phosphates. Moreover, supercritical

water is not only a solvent for organic materials but also a reactant which can help to produce fuel gas from organic resources. One important property of SCW is that there exists almost no mass transfer limitation. Generally catalytic reactions are mass-transfer limited due to the high reaction rates, low diffusion rates, and poor fluid flow characteristics. A high effective diffusion coefficient for supercritical water (about 100 times higher than ambient water) diminishes the chance of mass-transfer gradients developing in the catalyst internal surface area⁹. The Thiele modulus, which represents the degree of internal or pore diffusion limitation, is much less than unity for supercritical water, which indicates that pore-diffusion limitations do not exist in the catalyst⁹.

Because of the high moisture content, conventional gasification processes for gasification of sewage sludge, agricultural wastes, and food processing wastes are not considered promising. The conversion efficiency of supercritical water gasification is always higher than for other conventional processes when the moisture content is above 31%⁵. Cellulose is known as one of the most difficult components for dissolving in hot water³⁵. The complete conversion of cellulose to glucose and its oligomers can be achieved at temperatures as high as 400 °C in supercritical water conditions³⁶. Therefore gasification of glucose in supercritical water can be considered as a good model for gasification of more complex cellulosic biomasses.

Heterogeneous catalysts are preferable over homogeneous alkali catalysts to avoid reactor corrosion problems while being relatively easy to recover^{122, 123}. During the study of catalytic phenol oxidation in supercritical water, Oshima et al.⁹⁶ showed that external mass transfer resistance was negligible for small size catalysts (size 0.18-0.25 mm),

however larger size catalysts posed some mass transfer resistance. In this respect we have introduced crushed (0.1-0.3 mm) catalysts to observe the effect on the products.

Total organic carbon (TOC) is the amount of carbon bound in an organic compound and is often used as a non-specific indicator of water quality. TOC detection is an important measurement because of the effects it may have on the environment, human health, and manufacturing processes. TOC is a highly sensitive, non-specific measurement of all organics present in a sample. It can be used to regulate the organic chemical discharge to the environment in an agriculture or manufacturing plant. In addition, low TOC can confirm the absence of potentially harmful organic chemicals in water used to manufacture pharmaceutical products. In this respect, for this study we investigated the destruction and rate of TOC during SCWG.

A kinetic analysis of the decomposition rate in SCWG is important to design the required reactor system. However, kinetic information describing SCWG is limited especially for longer residence times. Depending on the feed type, gasification increases with increased residence time^{14, 124}. Jesus et al.⁶⁰ correlated results of gasification of corn silage at 700 °C and 25 MPa in SCW with time and developed a linear relationship between carbon conversion (Y_C) and residence time(τ):

$$Y_C = K\tau = 0.11\tau \quad (R^2=1) \quad (6.1)$$

They also proposed a model for corn silage using mathematical approximation based on zero-order kinetics as follows:

$$Y = 10^2 \exp\left(\frac{47.9[KJ]}{RT[K]}\right)\tau(\text{min}^{-1}) + 10^{-2.8} \exp(6.1 \times 10^{-3} T[K]) \quad (6.2)$$

Lee et al.¹²⁵ also found that below 600 °C, the hydrogen yield increases with increased residence time when gasifying glucose in supercritical water. They conducted a kinetic analysis assuming pseudo first order reaction during the gasification of glucose in supercritical water. Their kinetic investigation leads to the following first order reaction rate for COD (chemical oxygen demand) degradation as a function of the corresponding concentration C_c :

$$-r_c = 10^{2.95 \pm 0.23} \exp\left(-71.0 \pm \frac{3.9}{RT}\right) C_c \quad (6.3)$$

Although they assumed zero order for water, they agreed that non-first order kinetics would have given a better correlation of the experimental data.

For higher destruction of TOC or COD, some researchers have introduced oxidant and studied the kinetics for supercritical water oxidation assuming zero order for oxidant and water. Jin et al.⁵⁶ studied the TOC kinetics for oxidation of food wastes. They found the reaction to be fast at the early stage of reaction (within 50 seconds) and slow afterwards. They assumed the oxidation reaction as first order and simplified the TOC conversion as:

$$\ln(1-X) = -kt \quad (6.4)$$

where X is the conversion of TOC, t is time, and k is reaction rate constant (function of temperature). To determine the value of k from the slope they plotted $\ln(1-X)$ vs t . As the straight line did not go the origin as required by equation 6.4, the reaction kinetics were not entirely first order.

Due to the complex reaction mechanism of SCWG that involves multi-component reactants (feed and other reactants formed as intermediate products) and products, Goto et al.⁷⁶ performed a kinetic analysis of TOC for the destruction of municipal sewage

sludge and alcohol distillery wastewater. They simplified the kinetic study by assuming zero order for oxygen and unity for the reaction order. Portela et al.¹²⁶ performed a generalized kinetic model based on acetic acid and carbon monoxide as the main refractory intermediates for supercritical water oxidation of cutting oil wastes.

Oshima et al.⁹⁶ oxidized phenol in supercritical water using manganese oxide as the catalyst. They showed that the mass transfer limitation for small size catalysts is negligible. Assuming first order reaction for phenol oxidation they proposed two models which could not be discriminated due to a lack of data.

Kinetic studies on supercritical water gasification have been much less studied than supercritical water oxidation. One major shortcoming of these studies is the assumption of a first order reaction rate. The assumption of zero order for other reactants, such as oxygen and water may also be misleading for a proper understanding of reaction behavior. Using excess oxygen Hernandez et al.¹²⁷ and Lee et al.¹²⁸ found that the order of oxygen concentration was not zero. However, they simplified their model applying an initial rate method. All of the researchers assumed no effect of water concentration i.e. zero order on TOC destruction since it is used in excess over the stoichiometric requirement. However our previous study (chapter 4) showed that the lower the feed concentration (i.e. higher water: feed ratio) the higher is the TOC conversion.

Most of the lab based SCWG reactors use a volume of only a few milliliters while no kinetic data available in the literature at longer residence times, which may be required for industrial implementation in a tubular reactor. More than thirty intermediate products were detected by Hologate et al.⁵³ (425-600 C and 246 bar) and by Williams and

Onwudili⁵⁴, development of a rigorous kinetic model is difficult and has less practical importance. For engineering purposes, it often is sufficient to develop a global rate model to express the reduction of components in SCWG of organic wastes. Decomposition of carbon containing components expressed as total organic carbon (TOC) by SCWG increases the gaseous yields. In our previous study (chapter 4), we showed that the higher the TOC destruction, the higher the hydrogen and other gaseous product yields.

Therefore, in this study a global kinetic model for TOC destruction without using oxidant has been developed with time and temperature dependency. The pressure effect was not studied due to reactor limitations; moreover, conducting over 200 experiments Kersten et al.⁶³ found the pressure dependence range of 13.8 to 41.8 MPa on reaction products to be insignificant. Hao et al.¹⁴ also observed no great effect on gasification efficiency and the fraction of gas product from 25MPa to 30 MPa at 500 °C and 650 °C.

6.2 Experimental method

In the experiments, the model compound glucose was obtained from Sigma-Aldrich (Mississauga, Ontario) and used as received. De-ionized water, 18.2 M-cm, was obtained from an ultrapure water system (EASY pure LF, Mandel Scientific co, model BDI-D7381) to prepare the solutions.

Supercritical water gasification experiments were conducted using a 600 ml autoclave batch reactor made of Hastelloy C-276 equipped with 1.5 kW electric furnace for heating (Autoclave Engineers, Erie, Penn., USA). The schematic diagram and experimental procedure was described in detail elsewhere⁹³. Briefly, in a typical experiment 70 ml of deionized water with 1 gram of catalyst was loaded into the reactor, then evacuated

followed by purging with He gas for 10 minutes. The reactor was then pressurized to 2.5 MPa with helium in order to prevent water evaporation and pressurized to 24 MPa by heating to 400 °C. The concentrated glucose solution (0.25 M) was then pumped into the pressurized reactor using a syringe pump (Isco Model 100 DX, Lincoln NE, USA); providing a final reactor pressure of 28MPa. The initial reaction time (t) was started as soon as the feed was injected into the reactor. After the required reaction time, the products were cooled to ambient temperature using a double pipe heat exchanger and separated by a sudden expansion gas-liquid separator (both heat exchangers and gas-liquid separator are designed by the author and manufactured at the UWO machine shop). The product gas was then passed through a 2 micron filter to remove any remaining moisture and passed through an OMEGA mass flow meter (FMA 1700/1800 series 0-2 L/min, Laval, Quebec, Canada). The product gases were then collected in a 3L volume Tedlar gas sampling bag for subsequent GC analysis.

To analyze the percent of gasification and hydrogen yield, the product gases were analyzed by gas chromatography (Shimadzu, GC-2014) using 120/80 D Hayesep stainless steel Nickel packed column (Grace Davidson) with dimensions of 6.2 m x 3.18 mm, a thermal conductivity detector (TCD) and helium as the carrier gas. To measure the total carbon content in the liquid effluent that did not gasify, Total Organic Carbon (TOC) was analyzed with a TOC-VCPH (Shimadzu Instruments). This is an analytical method that determines the amount of organics through measurement of content generated during organic matter oxidation. The TOC decomposition X was used to evaluate the extent of oxidative decomposition, and defined as:

$$\text{TOC decomposition, } X = 1 - \frac{[\text{TOC}]}{[\text{TOC}]_0} \quad (6.5)$$

where $[\text{TOC}]_0$ is the initial TOC and $[\text{TOC}]$ is the residual after reaction.

Gas yield, and carbon gasification efficiency (CGE), were calculated as shown in equation 5.7 and 5.8 as defined by Yu et al⁶¹.

$$\text{yield} = \frac{\text{mol of gas produced}}{\text{mol of glucose in feed}} \quad (6.6)$$

$$\text{CGE} = \frac{\text{mol carbon in produced gas}}{\text{mol carbon in feed}} \quad (6.7)$$

6.3 Results and Discussion

6.3.1 Effect of Reaction Time and Temperature

Here we examine the effect of reaction time and temperature on the TOC destruction with crushed Ni on La-alumina catalysts. Reaction time and temperature have a large effect on the gaseous and liquid products as shown in chapter 4.

Figure 6.1 shows that increasing reaction time and temperature leads to the TOC conversion and CGE increasing i.e. the gaseous products increases due to a higher conversion of the liquid intermediates.

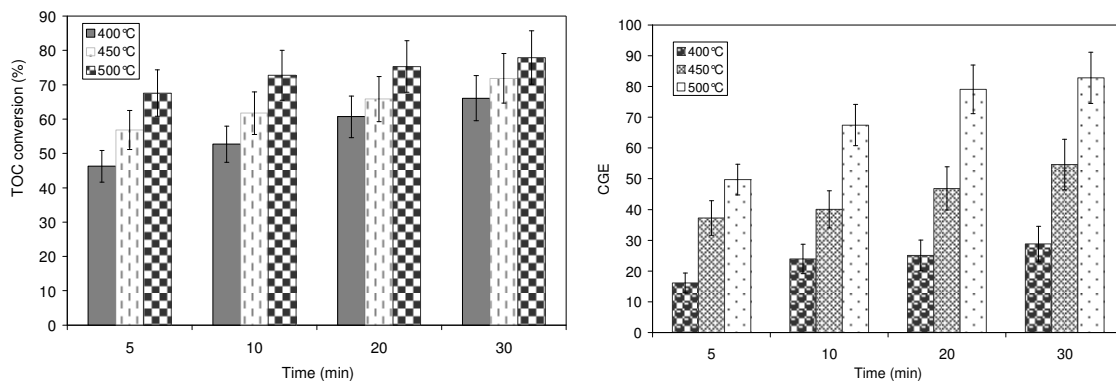


Figure 6.1: Effect of time and temperature on TOC conversion and CGE. a) TOC conversion, b) CGE. Catalyst size: 0.1-0.3 mm, amount =1 gm, P=28MPa, Feed= 0.25M Glucose.

To further study the effect of reaction time, the temperature was fixed at 500 °C, and reaction time was increased to 60 and 120 minutes. From Figure 6.2 it is also seen that both the TOC conversion and CGE increases with reaction time. The TOC conversion reached almost 90% while CGE reached over 96% due to increased gasification.

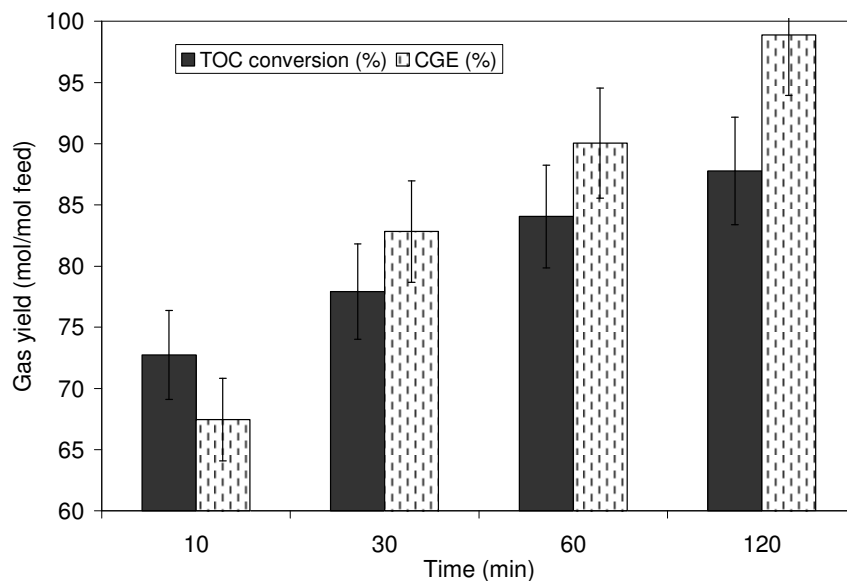


Figure 6.2: Effect of time on TOC conversion and CGE. Catalyst size: 0.1-0.3 mm, amount =1 gm, T=500 °C, P=28MPa, Feed= 0.25M Glucose.

6.3.2 Effect of Concentration

Figure 6.3 shows the effect of feed concentration on the TOC conversion and carbon gasification efficiency. The TOC conversion and carbon gasification efficiency being reduced with increased concentration is attributed to a lower gasification of organic compounds occurring.

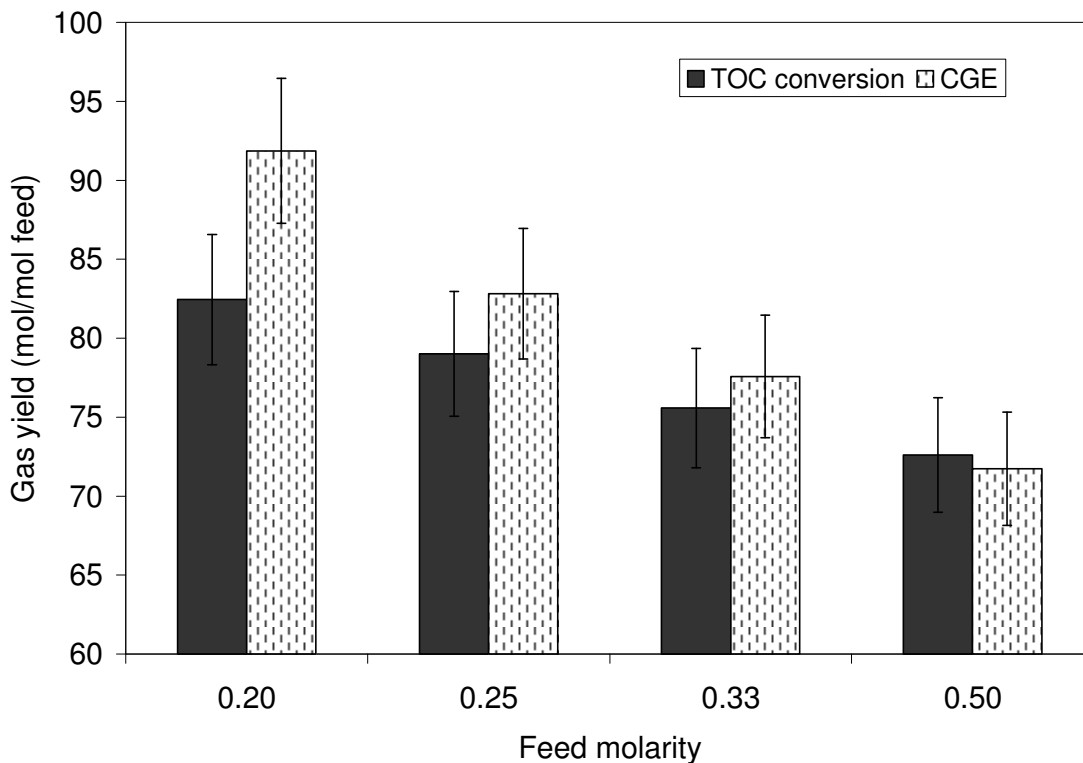


Figure 6.3: Effect of feed concentration on TOC conversion and CGE. Catalyst size: 0.1-0.3 mm, amount =1 gm, reaction time = 30 min, T=500 °C, P=28MPa.

From the above observations it is clear that low concentration with increased time and temperature is favorable for the TOC destruction and higher gasification yields.

6.4 Reaction Kinetics of TOC destruction

The reaction kinetics of glucose decomposition in supercritical water was studied previously in small tubular reactors with residence times shorter than 35 seconds^{125, 129}. As summarized by Lu et al.¹³⁰ under supercritical water conditions the reaction proceeds by a free radical reaction mechanism. Intermediate liquid products need longer residence times for further gasification as shown by the preview experimental results. The gaseous products also undergo internal reactions (e.g. WGS, carbonation etc.) with longer residence times which can also contribute to the observed changes.

From the earlier study of XRD analysis (chapter 4) and literature survey^{9, 96}, we assumed that the catalyst structure change (i.e oxidized crystallites) happened in the beginning of the reaction. Therefore it is assumed that after initial change, the structure and catalytic effect on gasification remains steady with time (from 5 minutes to 120 minutes in our study). The activity of the catalyst for TOC destruction and gasification efficiency was evaluated for the kinetic model development for the time range of 5 minute to 120 minutes. It has also been shown that in supercritical water, mass transfer limitations on the catalyst surface is negligible⁹, especially with particles less than 0.5 mm⁹⁶. In our study we crushed catalysts to a 0.1-0.3 mm size. Therefore the catalyst surface concentration is assumed approximately equal to the bulk concentration. Therefore the global rate equation for the overall hydrolysis reaction may follow a power-law rate expression and can be written as:

$$r = -\frac{d[C_n]}{dt} = k[C_n]^p[H_2O]^q \quad (6.8)$$

where $[C_n]$ and $[H_2O]$ indicate the concentration of reactants and water, respectively. p is the order of the reaction with respect to reactant, and q is the order of the reaction with respect to water.

6.4.1 Model one

As discussed in the introduction, for simplification, most of the researchers have assumed first order reaction during decomposition in supercritical water gasification and ignored the effect of water. Since water is used in excess and exists with reactants in a single homogeneous phase in SCWG, the reaction order can be assumed zero for water. Equation (5.24) then becomes

$$-\frac{d[C_n]}{dt} = k[C_n]^p \quad (6.9)$$

From an environmental point of view, COD or TOC concentration is the common parameter to measure the pollution in waste waters. Substituting C_n with $[TOC]$ the equation (6.9) will become,

$$-\frac{d[TOC]}{dt} = k[TOC]^p \quad (6.10)$$

If the reaction is assumed to be a first order reaction, integration of equation (6.10) will become,

$$-\ln \frac{[TOC]}{[TOC]_0} = kt \quad (6.11)$$

The experimental data of TOC at different temperatures are plotted as $-\ln[TOC]/[TOC]_0$ vs time in Figure 6.4.

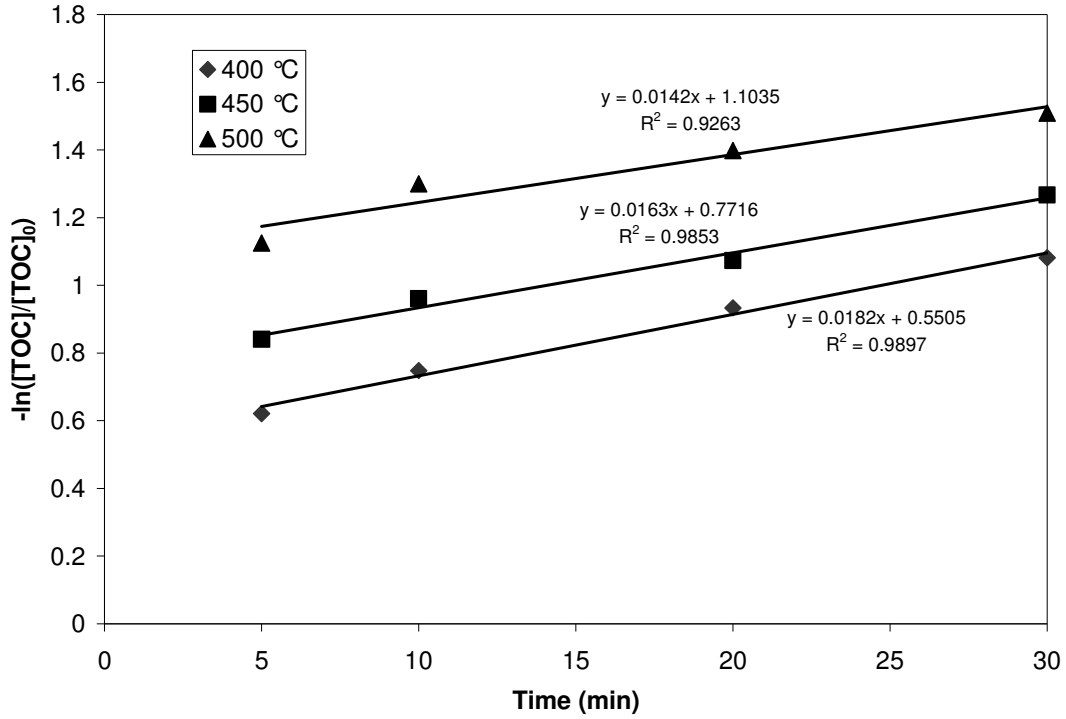


Figure 6.4: Plot $-\ln([TOC]/[TOC]_0)$ against residence time for TOC decomposition in SCWG.

Figure 6.4 clearly shows a linear relationship with a slow reaction and the assumption of pseudo first order being applied. The slope can be attributed to the reaction rate constant k which has a dependency on temperatures, normally expressed using the Arrhenius equation,

$$k = A \exp \frac{(-E)}{(RT)} \quad (6.12)$$

where A is the pre-exponential factor, E the activation energy, R the universal gas constant, and T is the temperature in Kelvin. To calculate the activation energy, equation (6.12) was transformed into the logarithmic form, which is plotted in Figure 6.5.

$$\ln k = \ln A - \frac{E}{RT} \quad (6.13)$$

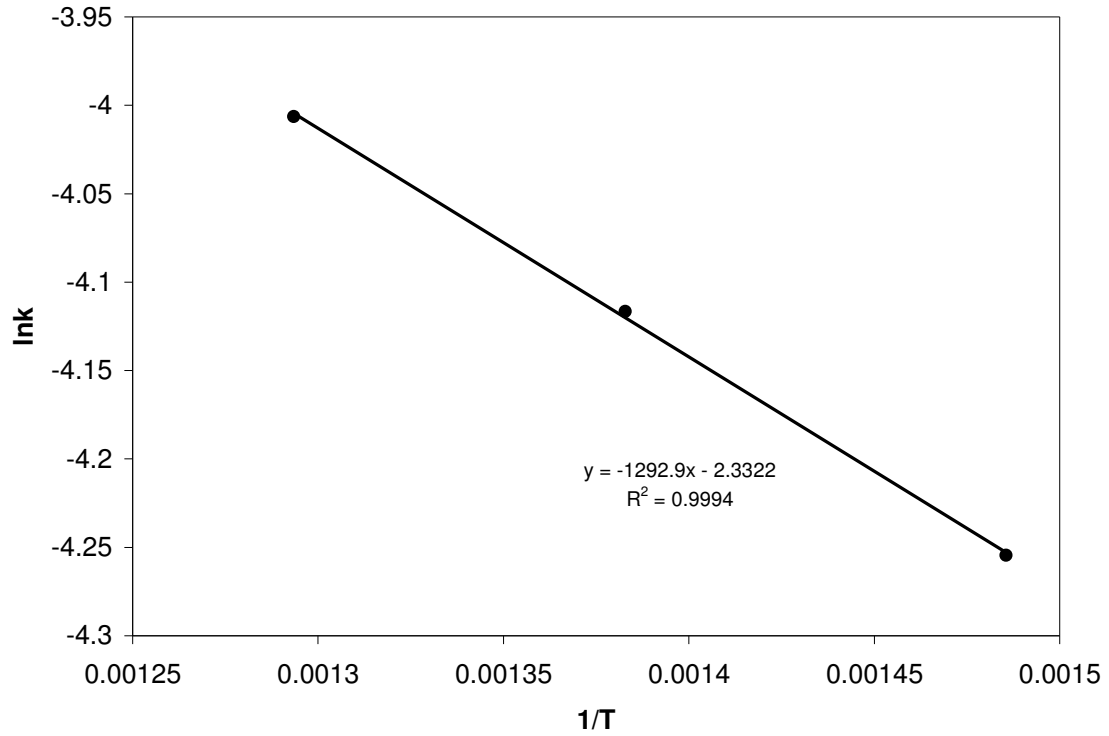


Figure 6.5: Assumed first order Arrhenius plot for TOC decomposition in SCWG

From the intercept of Figure 6.5 the value of the pre-exponential factor is approximately 9.71×10^{-2} and from the slope, the activation energy E is calculated to be 10.75 KJ/mol and corresponding $k_{400 \text{ }^\circ\text{C}} = 1.42 \times 10^{-2} / \text{min}$, $k_{450 \text{ }^\circ\text{C}} = 1.63 \times 10^{-2} / \text{min}$, $k_{500 \text{ }^\circ\text{C}} = 1.82 \times 10^{-2} / \text{min}$.

The model equation can be written as,

$$-\frac{d[TOC]}{dt} = 9.71 \times 10^{-2} \exp\left(\frac{-10750(\text{J/mol})}{RT(\text{K})}\right)[TOC] \quad (6.18)$$

The parity plot of this model is shown in Figure 6.6.

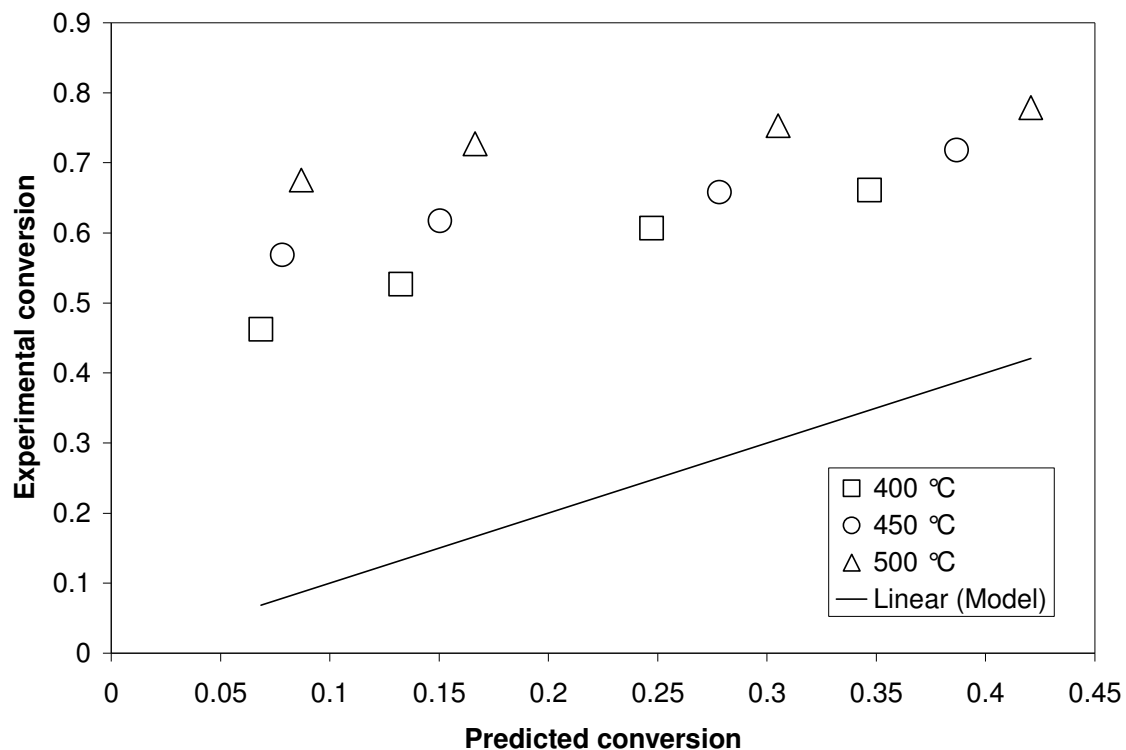


Figure 6.6: Comparison of the TOC conversion between experimental data and predicted values by model one.

From the parity plot (Figure 6.6) a large difference in the experimental and predicted model is observed, which we attribute to invalid assumptions. As shown earlier in Figure 6.4, it is evident that the straight lines drawn for the experimental data do not go through the origin according to equation (6.11). Therefore the experimental reaction does not obey the model predicted, i.e. first order kinetics. Furthermore, as discussed in section 6.3.2, the concentration of feed i.e. feed to water ratio has a large effect on TOC decomposition. Therefore the effect of water cannot be ignored.

6.4.2 Model two

Since supercritical water has negligible mass transfer limitation with small size catalyst particles (0.1-0.3 mm) and water is used in large excess of the stoichiometric requirement, the changes of the concentration due to reaction on the catalyst surface can be considered negligible, i.e. the concentration of water at the catalyst surface can be regarded to be the same as that in the bulk fluid. Therefore, assuming the surface reaction obeys a power rate law model and substituting C_n with $[TOC]$, the equation (6.8) can be re-written as,

$$-\frac{d[TOC]}{dt} = k[TOC]^p [H_2O]^q \quad (6.19)$$

Let's assume at time t ,

$$\text{Total organic carbon concentration, } [TOC] = [TOC]_0 (1-X) \quad (6.20)$$

where $[TOC]_0$ is the initial concentration, X is conversion factor of TOC.

$$\text{Water concentration, } [H_2O] = [H_2O]_0 (1-Y) \quad (6.21)$$

where $[H_2O]_0$ is initial concentration, Y is conversion factor of H_2O .

The relation of Y and X can be written as follows:

$$Y = aX$$

where ' a ' is a constant.

Therefore, the water concentration can be written as,

$$[H_2O] = [H_2O]_0 (1-aX). \quad (6.22)$$

The overall reaction rate can be written as follows:

$$-\frac{d[TOC]_0(1-X)}{dt} = k[TOC]_0^p (1-X)^p (1-aX)^q [H_2O]_0^q \quad (6.23)$$

Partial differentiation of the left hand side and rearranging gives equation 6.24:

$$\frac{d(X)}{dt} = k[TOC]_0^{p-1} (1-X)^p (1-aX)^q [H_2O]_0^q \quad (6.24)$$

The reaction rate constant k has an Arrhenius temperature dependency described by equation 6.12. To minimize cross-correlation between parameters the Arrhenius equation can be rewritten as:

$$k = k_0 \exp\left[\frac{-E_{app}}{R} \left(\frac{1}{T} - \frac{1}{T_m}\right)\right] \quad (6.25)$$

where, E_{app} is the activation energy and k_0 the pre-exponential factor and T_m being the centering temperature to minimize cross-correlation between parameters.

Since the initial concentrations are fixed, therefore,

$$\text{Let } k' = k_0[TOC]_0^{p-1}[H_2O]_0^q \quad (6.26)$$

Differentiating and rearranging with equation 6.25 and 6.26, the rate equation becomes

$$\frac{d(X)}{dt} = k' \exp\left[\frac{-E_{app}}{R} \left(\frac{1}{T} - \frac{1}{T_m}\right)\right] (1-X)^p (1-aX)^q \quad (6.27)$$

This is a differential equation with 5 unknowns: k' , E , p , q , a . As a non-linear regression is required to fit the rate of reaction, a Matlab program was developed to solve this differential equation by estimating the unknown parameter values (see Appendix A3).

Confidence values can be calculated by minimizing the sum of square differences of the experimental and predicted conversions for all data points using the following equation¹³¹:

$$s^2 = \sum_i^{N_{exp}} (X_{exp} - X_{pred})^2 \quad (6.28)$$

The estimated pre-exponential factor k' and the activation energy are $2.7 \pm 0.2 \times 10^{-4}$ and 85.57 ± 7.5 kJ/mol respectively. Putting the value of initial concentration in equation (6.26), the value of k is found to be $1.04 \pm 0.09 \times 10^{-5} \text{ s}^{-1} \text{ ppm}^{-2.75}$. The experimental data led to reaction orders of $p=2.25$ for TOC, $q=1.5$ for water respectively. The value of constant 'a' is found to be 1.25. The uncertainties reported here are 95% confidence intervals. The corresponding co-relation co-efficient (R^2) is 0.96. Finally the values of the established kinetic parameters were introduced into the power rate-law model equation. The differential equation was solved to predict the TOC conversion at different reaction times and temperatures.

Figure 6.7 shows a parity plot of the TOC conversion predicted from the global power rate law using the parameters from experimental data against the rate obtained experimentally.

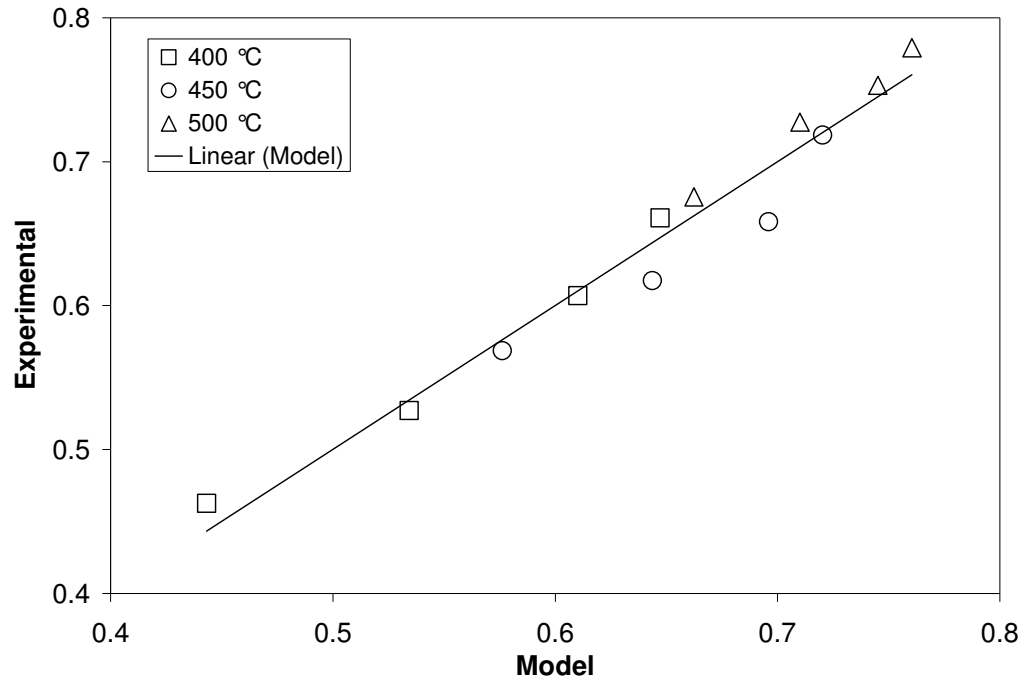


Figure 6.7: Comparison of the TOC conversion between experimental data and predicted values by the power-law rate expression of the surface reaction (model two).

6.5 Conclusions

Temperature and concentration have a large effect on TOC destruction and carbon gasification efficiency. Assumption of a first order reaction for TOC destruction of SCWG of glucose and ignoring water concentration due to the large excess led to an erroneous kinetic model development. A global kinetic model for TOC destruction was developed using non-linear regression, which convincingly fit the experimental results.

Chapter 7

One-pot procedure to synthesis of high surface area alumina nanofibers in supercritical carbon dioxide

This chapter includes the synthesis of high surface area alumina nanofiber as a catalyst support in supercritical carbon dioxide without using any extra water, organic solvent, surfactant, chelating agent, or other additives. Detailed characterization, morphology, and mechanism are described forming the nanostructures. This chapter is mainly reproduced from the article by the author published in Langmuir³¹: One-Pot Procedure to Synthesize High Surface Area Alumina Nanofibers Using Supercritical Carbon Dioxide.

7.1 Introduction

High surface area alumina, i.e. Al₂O₃, has found a diversity of applications due to its high thermal, chemical and mechanical stability.¹³² These applications include catalysis, catalyst supports, and adsorptive materials for various separation processes. In the form of fibers, alumina can be also used for reinforcing plastics as a grinding or polishing material,¹³³ tissue engineering,¹³⁴ or filtration of viral aerosols.¹³⁵

As with many other metal oxide materials, researchers are exploring a variety of techniques on how to prepare nanofibrous alumina materials with high surface areas for the many emerging applications. Successful efforts to obtain nanowires, nanofibers, and nanorods of alumina have been reported over the past decade.¹³⁶⁻¹⁴⁷ The most common

strategy for synthesizing such materials is using surfactant-templates, hydrothermal or the solvothermal process. In the templating approach, the templates play a crucial role in the formation and growth of the fibers, however, must be removed after synthesis.¹⁴⁸ The hydrothermal process requires temperatures above 100 °C and often forms lamellar hydrated hydroxides due to the fast hydrolysis of aluminum precursors in aqueous media, even in the presence of surfactant molecules.¹⁴⁹ Lee et al.¹⁴⁰ reported synthesizing a series of alumina nanotubes, nanofibers, and nanorods by the hydrothermal method by varying the type of ionic or non-ionic surfactant. Zhu et al. obtained 30-60 nm long γ -alumina nanofibers with 3 nm dia. from inorganic aluminum salt aluminum hydrates using poly(ethylene oxide) as the surfactant at 100 °C.¹⁴⁷ Another three step synthesis pathway was reported by Zhang et al to synthesize porous lathlike nanoparticles using non-ionic triblock surfactants.¹³⁹ Although it was proposed that the surfactant directs the fibrils growth by forming rodlike micelles,¹⁵⁰ recently Wang et al.¹⁴¹ reported a non-surfactant route for synthesizing fibrous δ -alumina using hexamethylenetetramine as an additive for homogeneous hydrolysis of inorganic salt aluminum nitrate and ethanol-water as solvent. Using the solvothermal approach, γ -alumina rod was obtained by thermal decomposition of boehmite precursor which was prepared using the solvothermal method with inorganic hydrated alumina salt, sodium hydroxide and sodium dodecyl benzene sulfonate surfactant in a mixed solvent of water and dimethylbenzene.¹³⁸

From the various literature studied, it is noticed that the synthesis of nanostructured materials is generally conducted in aqueous or aqueous-organic solvents to disperse reactants where water is used for hydrolysis. To control the hydrolysis and condensation rates of alumina precursors by direct use of water, complex solvent mixtures or chelating

agents are required. However, using organic solvents and additives are considered as environmentally hazardous. Moreover, the surfactant removal process requires heat treatment, which may lead to collapse of the nanostructure.

Recently, direct sol-gel reactions in supercritical carbon dioxide (scCO₂) have attracted much attention for synthesizing oxide nanomaterials. As examples, SiO₂ monolithic aerogels and nanoparticles have been synthesized by reacting of silicon alkoxides with formic/acetic acid;¹⁵¹⁻¹⁵³ TiO₂ and ZrO₂ nanofibers, nanospheres and mesoporous monoliths have been produced by polycondensation of metal alkoxides with either acetic acid or water droplets with the aid of surfactants.¹⁵⁴⁻¹⁵⁹ Supercritical CO₂ (scCO₂) is an attractive alternative to conventional organic solvents due to its unique features of tunable physical properties and environmental benignness.¹⁶⁰ Carbon dioxide is inexpensive, environmentally benign and non-flammable with low viscosity, “zero” surface tension and high diffusivity in supercritical condition, that is favorable for synthesizing superior ultrafine and uniform nanomaterials.³² Moreover, complete removal of excess acetic acid with scCO₂ by venting is easy, no drying process is required, the porous nanostructure can be maintained, and potentially polymer nanocomposites can be synthesized in the same pot.¹⁶¹ Following a similar procedure in this work, no surfactant or additives were used making this a novel one pot synthesis route to fabricate high surface area alumina nanofibers.

7.2 Experimental

7.2.1 Materials

All the chemicals used in this work were reagent grade. 98% Al(III) isopropoxide, 99.7% acetic acid from Sigma-Aldrich Chemical Co., were used without further purification. Instrument grade carbon dioxide (99.99%) was obtained from Praxair, Canada.

7.2.2 Preparation of Al₂O₃

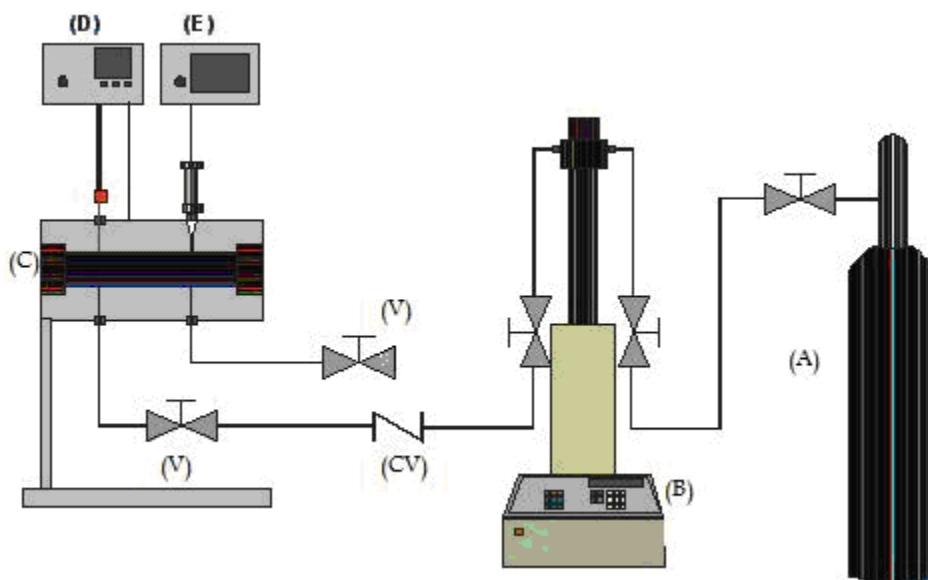


Figure 7.1: Experimental set up; A-CO₂ tank, B- Pump, C- View cell, D- Temperature controller, E- Pressure indicator.

Figure 7.1 provides the experimental setup which is also provided elsewhere.³³ In a typical synthesis, aluminum isopropoxide was mixed with excess acetic acid (1:10 mmol:mmol basis) and then placed in a 10 mL view-cell reactor pre-heated to the desired temperature, followed by stirring and addition of CO₂ to the desired pressure. The concentration of aluminum isopropoxide ranged from 0.2 – 0.5 mmol/ml scCO₂ while the

temperature and pressure were varied from 40 °C to 80 °C, and 4000 psi to 7500 psi respectively. Excess acetic acid was used for complete hydrolysis of alkoxide. For comparison purposes, a lower ratio of alumina isopropoxide to acetic acid (1:5, mmol:mmol basis) was also examined. When solid alumina alkoxide and acetic acid were mixed in the view cell using a magnetic Teflon stir-bar, a non-transparent white phase was formed after several hours stirring under supercritical conditions. After continuous stirring of the mixture for 24 hrs, the view cell was kept at rest for 10 days for aging at synthesis conditions for complete reaction and self-assembly. To ensure complete reaction, no precipitation was observed by venting a few drops of reaction mixture into water ensuring complete condensation of the precursor. To remove unreacted acetic acid and byproduct, i.e. alcohol etc. from the gel formed in the view cell, a supercritical carbon dioxide washing step was conducted under the same synthesis conditions until no smell of acetic acid was detected. To prevent collapse of the nanostructure morphology, CO₂ was used to wash the aerogel at ≈0.25ml/min. The as prepared alumina was then calcined at 1.5°C/min to the desired temperature (600°C /800°C /1050°C) using a Thermolyne 1500 furnace (NY, USA).

7.2.3 Characterization

The BET (Brunauer-Emmett-Teller) surface area, pore size and distribution, and pore volume were determined from nitrogen adsorption and desorption isotherm data obtained at 77 K with a constant-volume adsorption apparatus (Micromeritics ASAP 2010) using N₂ gas (99.995% pure; obtained from Praxair,Canada). The prepared samples were degassed at 150°C for 5h before measurements. The pore size distributions of as-prepared

samples were determined by a BJH (Barett-Joyner-Halenda) model.¹⁶² The nanostructured morphologies of the sample were obtained from Scanning Electron Microscopy (SEM) micrographs (Model LEO 1530) and Transmission Electron Microscopy (TEM) images (Model JEOL 2010F). Before TEM analysis, the powdered samples were dispersed in methanol by sonication and then placed and dried by normal evaporation on a copper grid covered with holey carbon film. Thermogravimetric Analysis (TGA) and Differential Thermal Analysis (DTA) were performed to measure the weight loss, the rate of weight loss, the heat effects associated with drying, decomposition, and phase changes as a function of temperature. TGA/DTA analysis was performed using a TGA/SDT A851 instrument at a heating rate of 10°C/min in air. Fourier transmission infrared (FTIR) was used to identify the chemical groups present in the synthesized samples. For FTIR analysis powdered samples were mixed with potassium bromide (KBr) powder and pressed into disks. The FTIR spectrum was recorded using a Bruker Tensor 27 Spectrometer with a resolution of 4 cm⁻¹ scanning from 4,000 to 400 cm⁻¹ at room temperature. Powder X-ray diffraction (XRD) patterns were collected to estimate crystallinities and the structural changes of the synthesized material. A Rigaku rotating-anode XRD was used employing CuK α radiation, with monochromation achieved using a curved crystal, diffracted beam, graphite monochromator. The instrument was operated at 45kV and 160mA, using the normal scan rate of 10° per minute (equivalent to 0.5° two-theta on conventional diffractometers) in the 2 θ range from 2° to 82°. X-rays were collimated using 1° divergent and scatter slits, and a 0.15mm receiving slit. The surface composition of the nanomaterials was determined by XPS, using a Kratos Axis Ultra spectrometer using a monochromatic Al

K(alpha) source (15mA, 14kV). Survey and high-resolution spectra were obtained using an analysis area of ~300x700 microns and pass energies of 160 eV and 20 eV, respectively. Spectra were charge corrected to the main line of the carbon 1s spectrum (C-C, C-H) set to 285.0 eV.

7.3 Results and discussion

7.3.1 Synthesis of Nanofibers

The experimental conditions utilized for synthesizing fibers, presenting the resulting morphology of the samples synthesized under various concentrations, temperatures, and pressures in scCO₂, are summarized in Table 7.1. The surface area, adsorption average pore diameter, and single-point adsorption total pore volume per gram are presented.

The morphology of the synthesized alumina aerogels using scCO₂ as both the synthesis and drying agent was assessed by electron microscopy (SEM and TEM). Initial experiments utilized a low concentration of AIP (0.2 mmol/ml scCO₂) with excess HAc (AIP to HAc 1:10 in molar ratio) to facilitate complete hydrolysis. Low concentration was also found to facilitate easy dispersion and avoid initial agglomeration of reactants. The effects of the synthesis temperature on the nanostructure were investigated as shown in Figure 7.2.

Table 7.1: Physiochemical properties of the synthesized alumina nanostructures at different conditions.

Experimental Parameters				T _{cal} (°C)	S _{BET} (m ² /gm)	D _{pore} (Å)	V _{pore} (cm ³ /gm)	Nanostructure
AIP:H Ac	AIP conc. (mmol/ml ScCO ₂)	Syn. Temp. (°C)	Syn. Pres. (psi)					
1:10	0.2	40	6000	As- prep.	115	61.2	0.176	Mixture of nano- spheres, pentagons, rods, fibers, etc.
				600	77	69.6	0.134	
		50	6000	As- prep.	481	113.7	1.37	Floppy porous structure
				600	263	122.2	0.804	
		60	6000	As- prep.	579	70.6	1.021	Very porous structure with some nanofibers
				600	272	136.2	0.927	
		80	6000	As- prep.	436	104.9	1.142	Nano fibrous network
				600	263	160.2	1.053	
1:10	0.3	80	6000	As- prep.	355	106.8	0.949	Nanofibers ranging from 500 nm to over 1000 nm.
				600	268	138.2	0.924	
				800	242	124.4	0.752	
				1050	108	145.8	0.395	
1:10	0.5	80	6000	As- prep.	330	141.5	1.171	Fibers less than 50 nm.
				600	279	181.5	1.267	
1:10	0.3	80	4000	As- prep.	382	70.3	0.672	Nanofibers connected with trunks
				600	297	99.1	0.736	
			7500	As- prep.	403	71.7	0.723	Nanofibers connected with trunks
				600	287	102.5	0.735	
1:5	0.3	80	6000	600	31	36.2	0.278	Micro and nano bars

Other synthesis parameters: Degassing temperature is 150 °C, AIP:HAc= Aluminum Isopropoxide:Acetic acid mmol ratio; AIP Conc.= Aluminum isopropoxide concentration; Syn Temp.= Synthesis temperature; Syn Pres.= Synthesis pressure; T_{cal}= Calcination temperature; As-prep= As prepared; S_{BET}= BET surface area; D_{pore}= Adsorption average pore diameter (4V/A); V_{pore}= Single-point adsorption total pore volume per gram.

At a synthesis temperature of 40 °C and 6000 psi, mixed nanostructures (rod, sphere, fibers, pentagon etc.) were formed with a very low BET surface area (115m²/gm)

as shown in Figure 7.2-a,b. This low surface area is attributed to agglomeration of these irregular shaped alumina nanostructures. When the synthesis temperature was increased to 60 °C, a porous structure with some nanofiber formation developed, as shown by the SEM and TEM micrographs in Figure 7.2-c and d, respectively. The surface area increased significantly to 579m²/gm, along with an observed morphology change from irregular shaped nanostructures to floppy porous structure. This morphology change is attributed to the higher synthesis temperature providing more thermal energy favoring the formation of an expanded structure of unfolded bohemite particles.¹⁶³

The surface area of the fibers synthesized in scCO₂ is much higher than conventional alumina and reported alumina fibers of 376m²/gm prepared using a PEO surfactant.¹⁴⁷ A further increase of synthesis temperature to 80 °C resulted in a more fibrous nanostructure being formed (Figure 7.2-e,f). The surface area of these samples decreased slightly from 579cm²/gm to 496cm²/gm. The morphology changes may also be due to the decreased density of scCO₂ with temperature i.e. 0.96 gm/ml at 40 °C/6000 psi decreasing to 0.83 gm/ml at 80 °C /6000 psi.

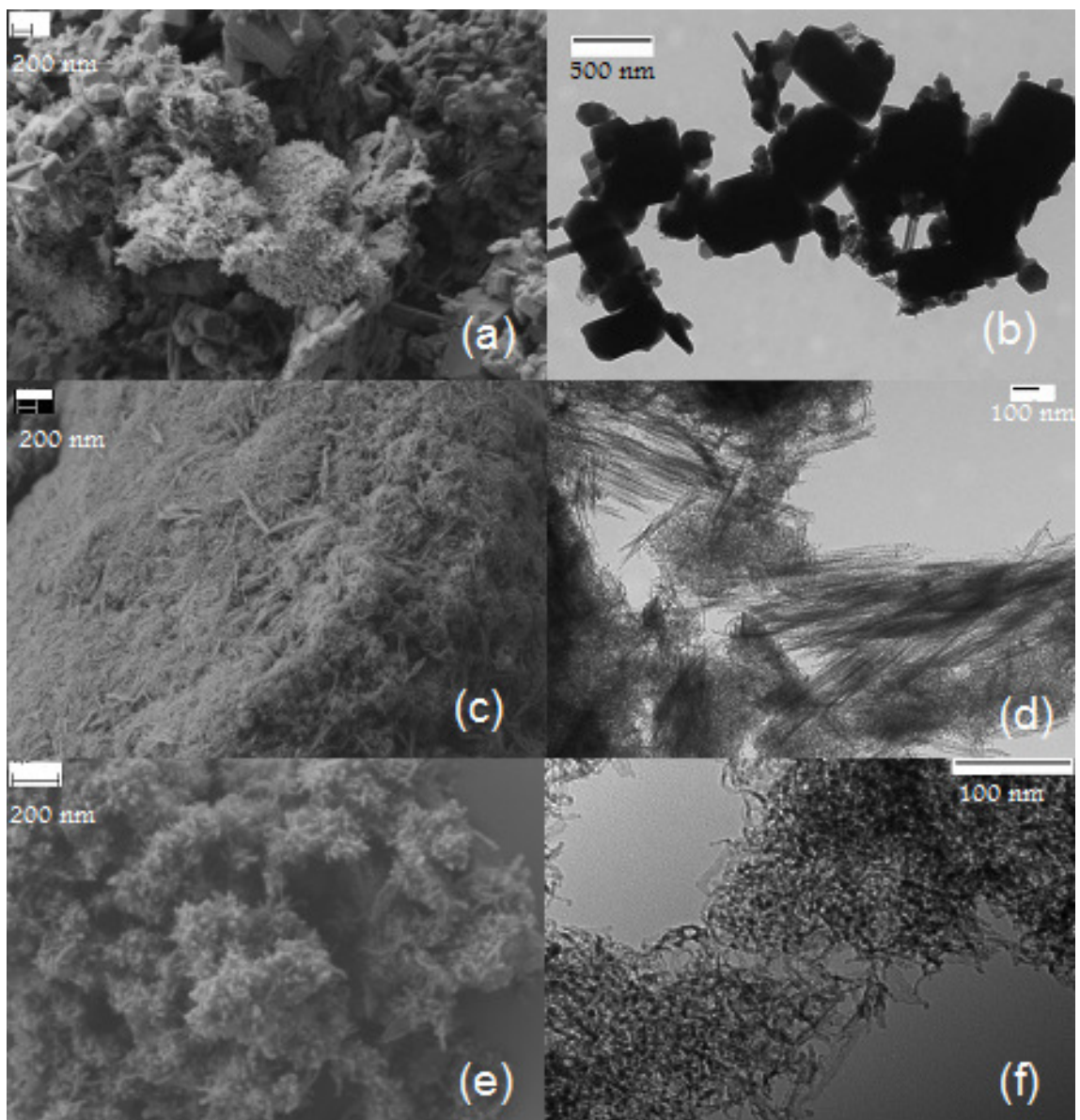


Figure 7.2: SEM (a,c,e) and TEM (b,d,f) images of nanoscale alumina particles with varying synthesis temperatures: a-b) 40 °C; c-d) 60 °C, e-f) 80 °C. Concentration of AIP to ScCO₂ 0.2mmol/ml, synthesis pressure 6000 psi, calcination temperature 600 °C, AIP:HAc 1:10 mmol ratio.

Figure 7.3 provides the N₂ adsorption/desorption isotherms and pore-size distributions for the nanostructured alumina obtained using synthesis temperatures from 40 to 80 °C in scCO₂. As shown in Figure 7.3a, the shapes of the nitrogen adsorption–desorption

isotherms and their hysteresis loops are those of typical “type IV” isotherms with H3 and H4 loops¹⁶⁴. The sample synthesized at 40 °C shows H4 loops¹⁶⁴ due to the irregular shapes and broad size distribution, supporting the SEM images, which showed irregular shape nanoparticles. For the samples prepared at 60 and 80 °C, type IV, H3 loops were formed, confirming mesopores with platelike materials with slitlike pores¹⁶⁴.

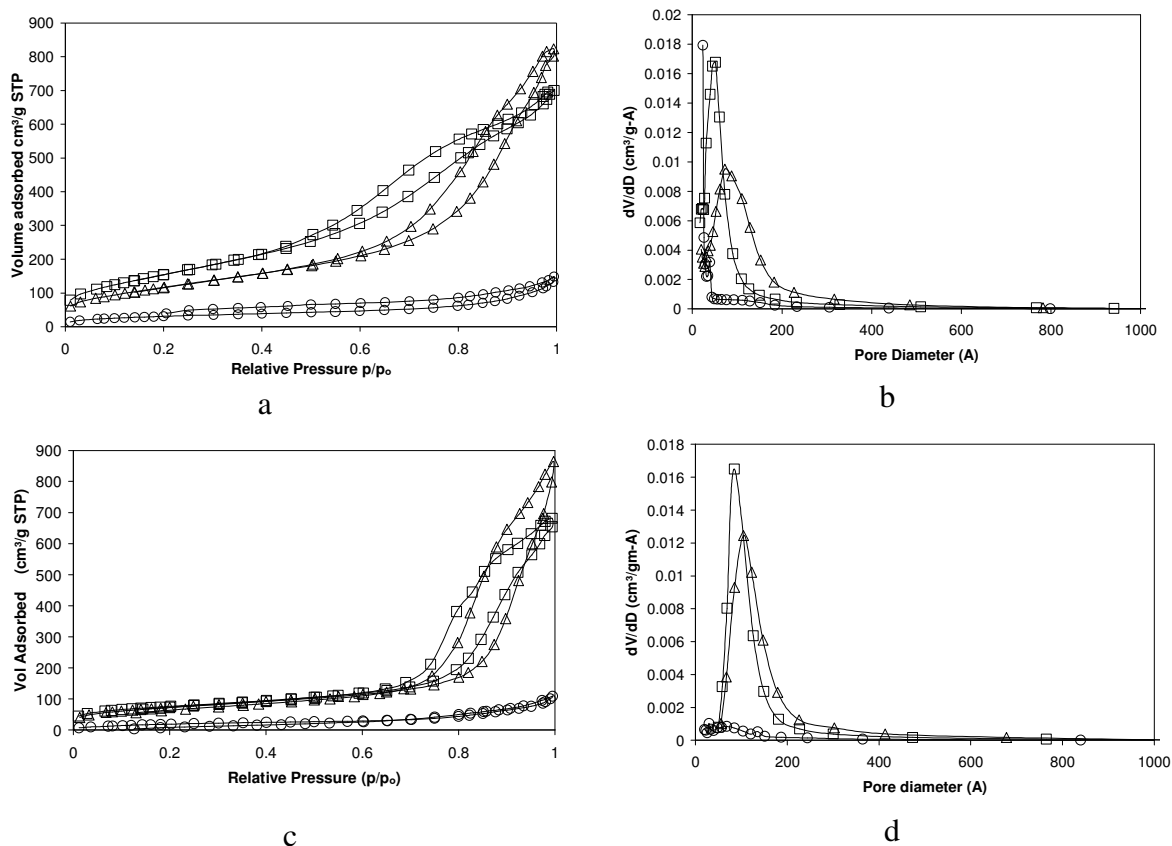


Figure 7.3: N₂ adsorption/desorption isotherms (a,c) and pore-size distributions (b,d) of nanostructured alumina: a, b- as prepared; c,d Calcined at 600 °C: ○- 40 °C, □- 60 °C, △- 80 °C.

The pore size distributions calculated from the isotherms are presented in Figure 7.3b, which shows that unimodal mesopores are formed at each temperature. The sample prepared at 60 °C shows a narrow distribution with high peak intensity. In contrast, the

pore size distribution is relatively broader in the sample synthesized at 80 °C. The broader distribution of pore sizes is attributed to the interparticle spaces of stacked nanofibers. Figure 7.3-c and d shows similar behavior when the alumina samples were calcined at 600 °C, with the effect of calcination described in detail later.

After observing nanofiber formation, the effects of concentration, pressure and alkoxide to acid ratio were investigated maintaining the reaction temperature at 80 °C. Figure 7.4 a shows from the SEM micrograph that longer fibers were formed when the concentration was increased to 0.3 mmol alumina isopropoxide/ml ScCO₂ maintaining the pressure at 6000 psi and alkoxide to acid ratio at 1:10. Further increasing of concentration (0.5 mmol alumina isopropoxide/ml scCO₂) resulted in agglomeration with some short nanofibers being formed (Figure 7.4b). When decreasing the alkoxide to acid ratio from 1:10 to 1:5 at 80 °C and 6000 psi, much larger structures were formed with some fiber-like sheets as shown in Figure 7.4c. These gave a low surface area of 31m²/gm.

The pressure effect (4000 psi and 7500 psi) on alumina nanostructures was examined keeping the synthesis temperature (80 °C) and alkoxide to acid ratio (1:10) at the optimized conditions. At 7500 psi (scCO₂ density 0.88gm/ml) nanofibers connected with a porous trunk structure was formed (Figure 7.4d) with lower BET surface area (287 m²/g).

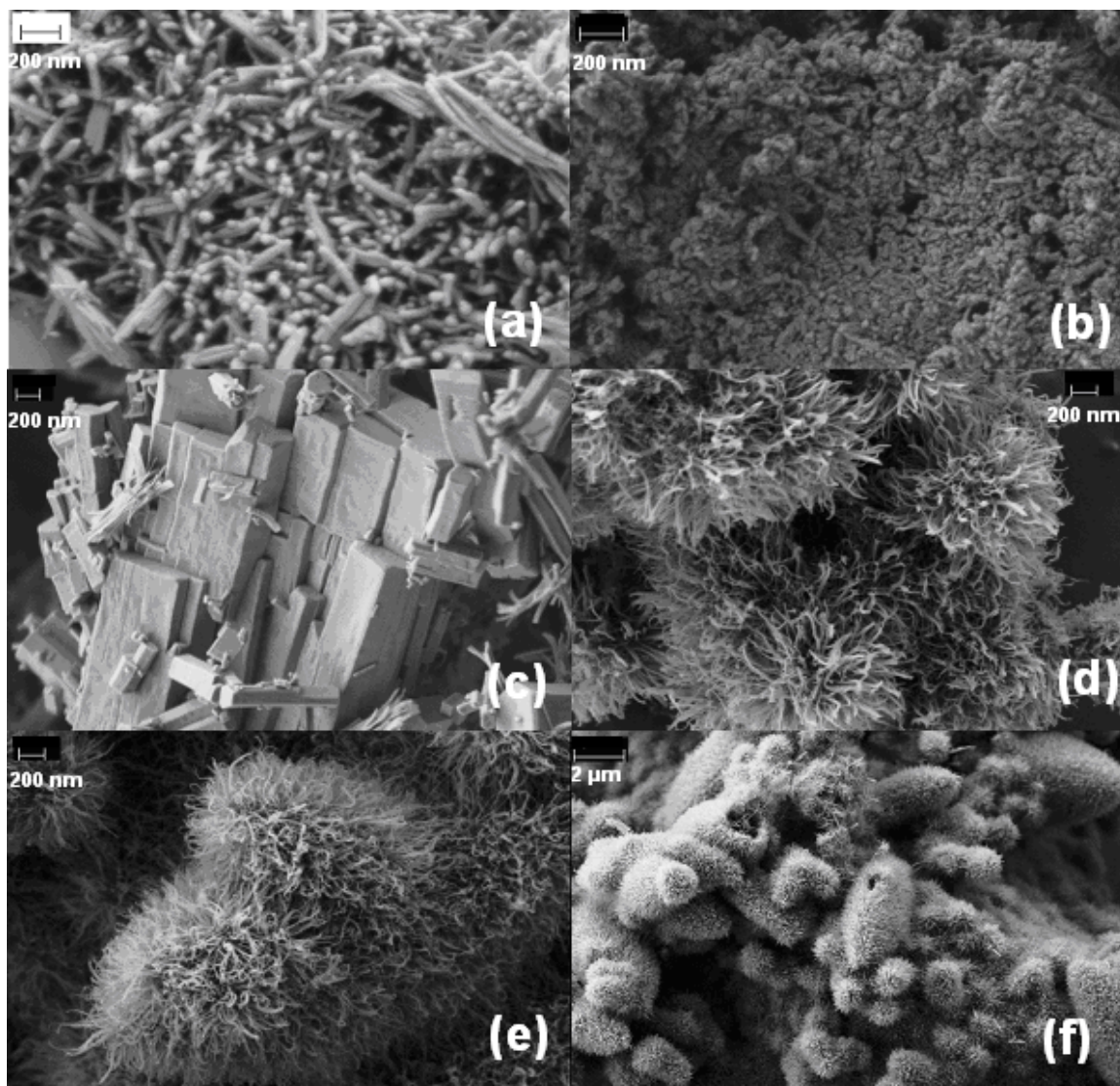


Figure 7.4: SEM images of nanoscale alumina particles at varying synthesis conditions in scCO₂ at 80 °C a) AIP 0.3mmol/ml, AIP: HAc 1:10, 6000 psig b) AIP 0.5mmol/ml, AIP: HAc 1:10, 6000 psig, c) AIP 0.3mmol/ml, AIP: HAc 1:5, 6000 psig, d) AIP 0.3mmol/ml, AIP: HAc 1:10, 7500 psig, e-f) AIP 0.3mmol/ml, AIP: HAc 1:10, 4000 psig.

Interestingly, a similar structure was also observed at lower pressure of 4000 psi with BET surface area 297 m²/g.(Figure 7.4-e,f). The lower pressure likely provides less penetration of CO₂ in the drying state leading to the observed microstructure of these

nanofibers as shown in Figure 7.4f. The low resolution SEM pictures of Figure 7.4a-d are provided in Figure 7.5.

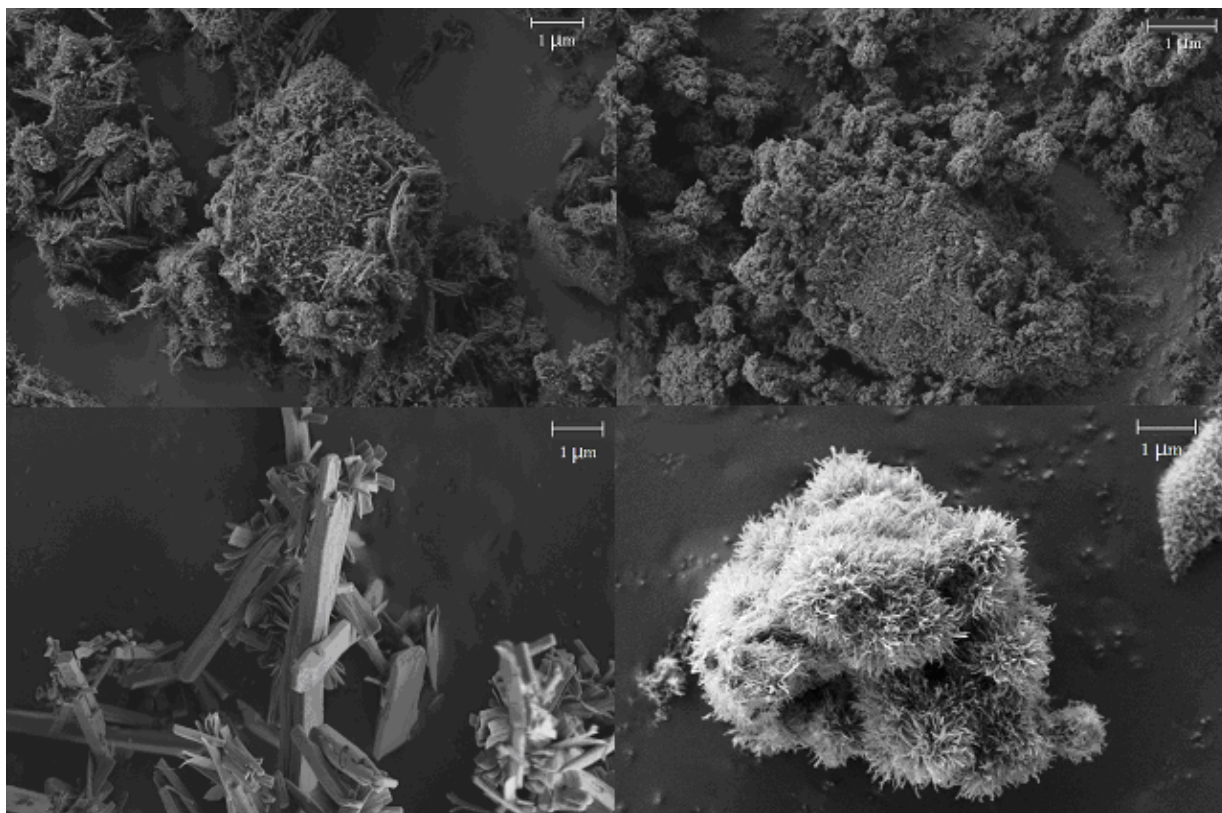


Figure 7.5: SEM images of calcined (600 °C) nanoscale alumina particles at varying synthesis conditions in scCO₂ at 80 °C a) AIP:scCO₂ 0.3 mmol/ml, AIP: HAc 1:10, 6000 psi; b) AIP:scCO₂ 0.5 mmol/ml, AIP: HAc 1:10, 6000 psi; c) AIP:scCO₂ 0.3 mmol/ml, AIP: HAc 1:5, 6000 psig; d) AIP:scCO₂ 0.3 mmol/ml, AIP: HAc 1:10, 7500 psi.

7.3.1.1 Effects of Calcination on Nanostructure

To examine the thermal stability of the synthesized long fibers (synthesized at 80 °C with concentration of AIP in scCO₂ = 0.3 mmol/mL, AIP to HAc = 1:10, pressure = 6000 psi), the samples were calcined at varying temperatures up to 1050 °C and then examined by electron microscopy as shown in Figure 7.6. The nanofibers shown in Figure 7.4a (calcined at 600 °C) were further calcined to 800 and 1050 °C and examined by SEM, as

shown in Figure 7.6-a and b. Maintaining the fibrous structure at these high temperature conditions illustrates the thermal stability of the nanofibers.

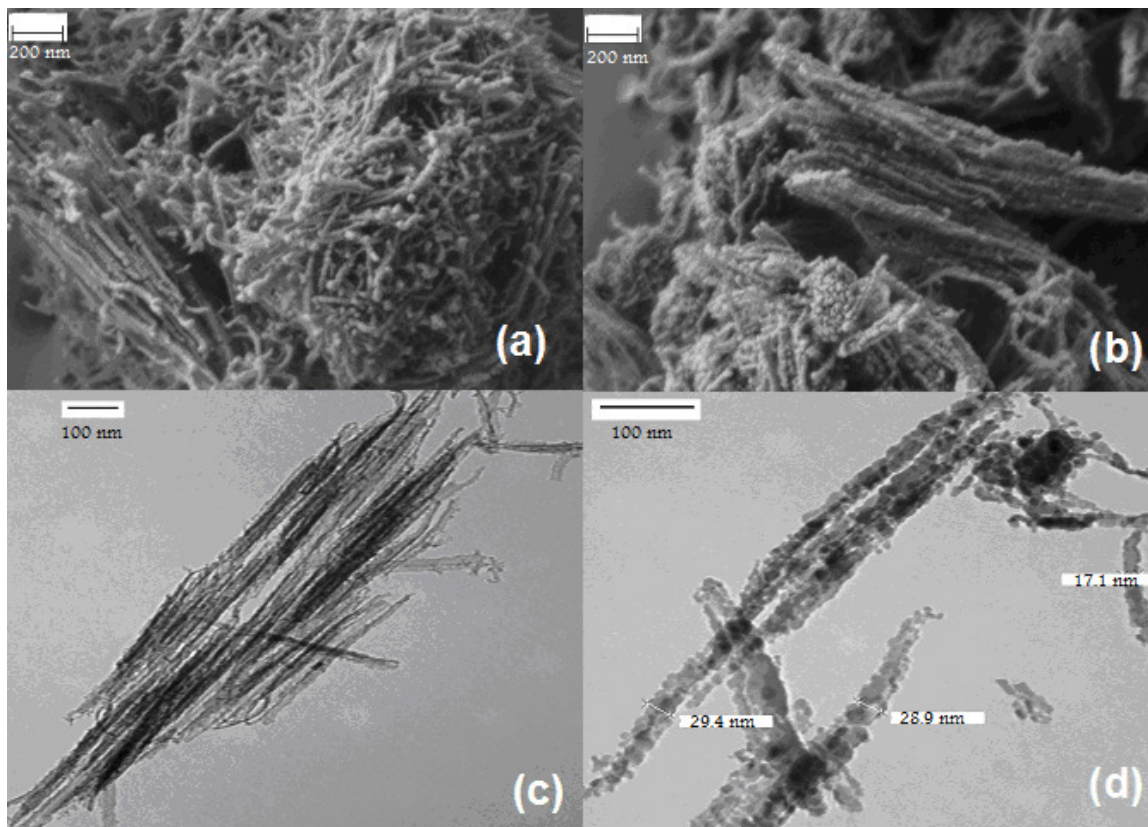


Figure 7.6: SEM (a,b) and TEM (c,d) images of alumina nanofibers calcined at varying temperatures a) 800 °C, b) 1050 °C, c) 600 °C, d) 1050 °C. AIP concentration 0.06gm/ml ScCO₂; AIP:HAc 1:10; 6000 psig.

From the TEM images of the samples calcined at 600 and 1050 °C (Figure 7.6c, d), it is seen that at 600 °C the nanofibers are uniform while at 1050 °C nanocrystallites are formed that are linearly attached to one another forming fibers. The crystallinity is further confirmed by XRD analysis in subsequent characterization. Heat stable high aspect ratio nanofibers were formed with diameters 11–29 nm and 500–1000 nm length. The fibers are stable and crystalline at 1050 °C (Figure 7.6d). The formation of –Al–O–Al– bridges

(further corroborated by FTIR analysis) may be the reason for the heat stabilization effect because their formation allows the disappearance of the cationic vacancies from the surface. Beguin et al. stabilized alumina toward thermal sintering by making $-Al-O-Si-$ bridges which resulted in the disappearance of cationic vacancies¹⁶⁵.

The effect of calcination on N_2 adsorption/desorption isotherms and pore-size distributions of alumina nanofibers are provided in the (Figure 7.7). These show that a lower volume of N_2 gas adsorption per relative pressure, compared to the as-prepared sample, attributed to the lower surface area. Type IV, H3 loops confirm mesopores with platelike materials with slitlike pores even after being calcined at 1050 °C.

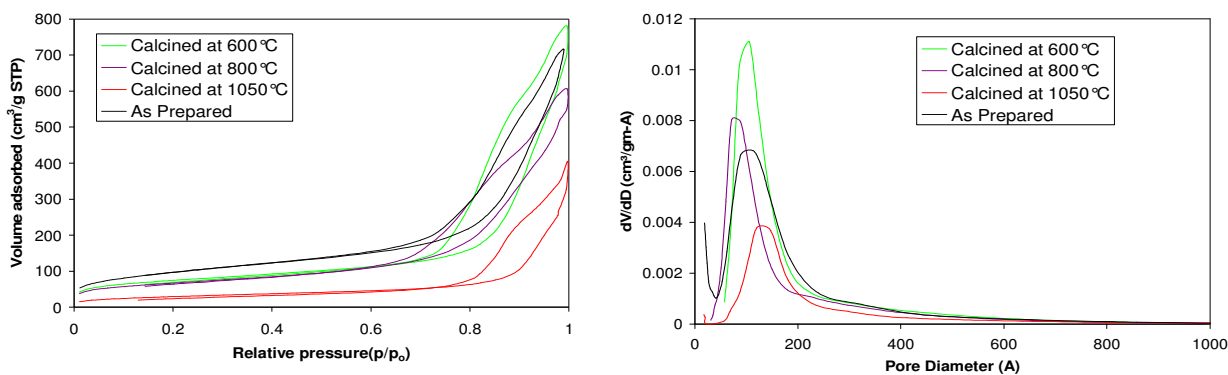


Figure 7.7: Calcination effect on N_2 adsorption/desorption isotherms (left) and pore-size distributions (right) of alumina nanofibers. Synthesis condition is AIP:scCO₂ 0.3 mmol/ml; AIP:HAc 1:10; 6000 psi, 80 °C.

The reason for the increment of average pore sizes after calcination of the as-prepared sample (synthesized at 80 °C with concentration of AIP in scCO₂ 0.3 mmol/mL, AIP to HAc 1:10, pressure 6000 psi) to 600 °C (Table 7.1) is due to the evolution of gas (CO₂ and water vapor) during heat treatment¹⁶⁶. At the same time, pore volumes were decreased due to the formation of denser materials. However, after 600 °C, when the

same sample was further heated to 800 °C, the BET surface area, pore size, and pore volume all decreased (Table 7.1) due to collapse of some micropores, intercrystalline spaces of stacked nanofibers, and agglomeration.

The TGA/DTA curves were measured for the as-prepared alumina fibers (synthesized at 80 °C with concentration of AIP in scCO₂ = 0.3 mmol/mL, AIP to HAc = 1:10, pressure = 6000 psi) as shown in Figure 6.8. The TGA curve in Figure 6.8a shows 4% weight loss in the range of 25–215 °C, attributed to physically bound adsorbed organic molecules and water produced during synthesis¹⁴². A 63% weight loss in the region of 215–600 °C is attributed to the removal of organic groups (the bridging acetate coordinated to Al atoms) which agrees with the IR and XPS analysis results as described later. About 2.5% weight loss is due to formation of other phases at higher temperatures¹⁶⁷.

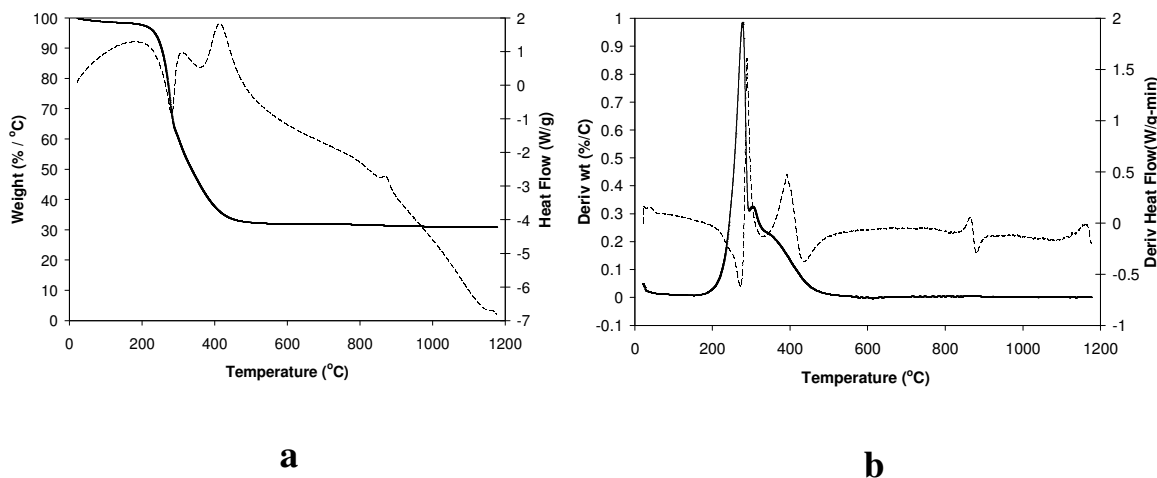


Figure 7.8: TGA-DTA analysis of alumina nanofibers. a) TGA-DTA, b) Derivative of TGA-DTA; Solid line: Weight change (TGA); Broken line: Heat Flow (DTA).

The exothermic peak at 875 °C in Figure 8a from the DTA heat flow trace is attributed to the phase change to δ -alumina, while the very small exothermic peak at 1172 °C is attributed to transformation to α -alumina¹⁶⁸. Figure 6.8b shows a plot of the derivative of the TGA and DTA heat flows, which more clearly shows removal of loosely bound and coordinated bidendate materials, and the phase transformations to δ - and α -alumina.

Although increasing calcination temperatures did not destroy the nanostructure, the BET surface area and pore volume were decreased gradually, as described in Table 6.1. A decrease of surface area from 355 m²/g (as-prepared) to 268 m²/g calcined at 600 °C is due to the removal of adsorbed species and dehydration of the alumina. A further reduction in surface area to 242 m²/g and pore volume at 800 °C is attributed to pore collapse and phase changes, as further confirmed by TGA/DTA analysis. The BET surface area of 108 m²/g after calcining at 1050 °C is still higher than that found by Ji et al. (55.4 m²/g at 1000 °C)¹⁶⁸. This result shows promise for high surface area application at elevated temperatures, such as catalyst supports for emerging high temperature processes such as H₂ generation from biomass gasification. The sintering propensity of the alumina nanofibers is low due to very large porosity and small contact area between fibers¹⁴⁷, which accounts for the high surface area of the synthesized alumina at high temperature¹⁴¹.

Figure 7.9 provides the FTIR traces of both the as-prepared and calcined alumina nanofibers. For the as-prepared aerogel in Figure 7.9a, the peaks at 1580 cm⁻¹ and from 1400 to 1470 cm⁻¹ are assigned to the asymmetric and symmetric stretching of bridging bidendate acetate groups, respectively, indicating that HAc formed bridging complexes with the alumina nanostructures¹⁶⁹. This is an important observation, which provides us

with direct evidence for the reaction mechanism and self-assembly steps in $scCO_2$, as described further below. The peaks below 1053 cm^{-1} are attributed to the Al–OH–Al group¹⁴², which disappears after calcination. A small peak is observed at 1710 cm^{-1} from C=O bond stretching, while the small peaks about 3000 cm^{-1} are due to C–H stretching. The sharp peak at $\sim 3700\text{ cm}^{-1}$ and the broad peak at $\sim 3500\text{ cm}^{-1}$ are attributed to the isolated and hydrogen-bonded Al–OH, respectively (Figure 7.9a). With elevated calcination temperatures, the disappearance of peaks from 1400 to 1580 cm^{-1} indicates the removal of the bidentate acetate group upon calcination (Figure 7.9b–d).

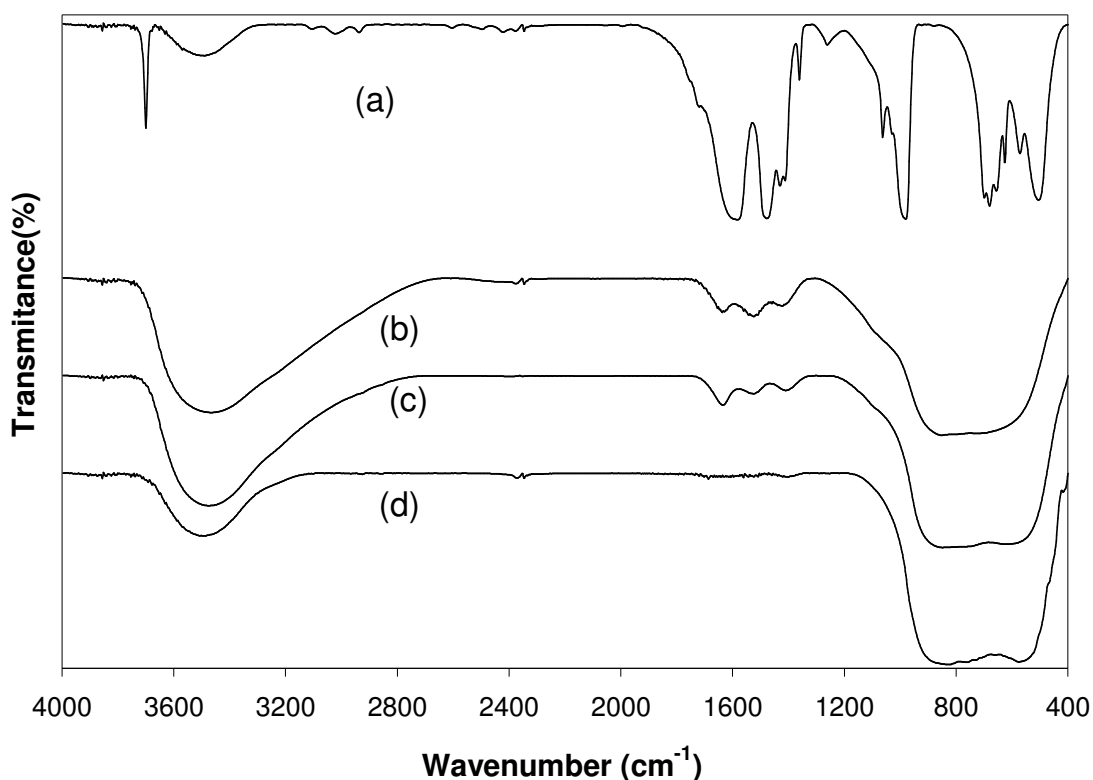


Figure 7.9: FTIR analysis: a) As prepared, Sample calcined at b) 600 °C, c) 800 °C, d) 1050 °C.

There are more –OH groups after calcination which can be explained by the bidentate acetates being replaced by –OH groups. For alumina, to remove water completely generally requires heating to over 1100 °C to produce α -Al₂O₃. In addition, from the peak changes in the regions of 3400–3700 cm⁻¹ and below 1000 cm⁻¹, it can be observed the gradual formation of oxo bonds.

The crystalline phase of the as-prepared alumina nanofibers was further identified by X-ray powder diffraction, as shown in Figure 7.10. Here we see that many broad peaks are evident of as prepared sample, which are different from the known alumina materials, and are assigned to a material with a formula Al(OH)(COOCH₃)₂ as described later.

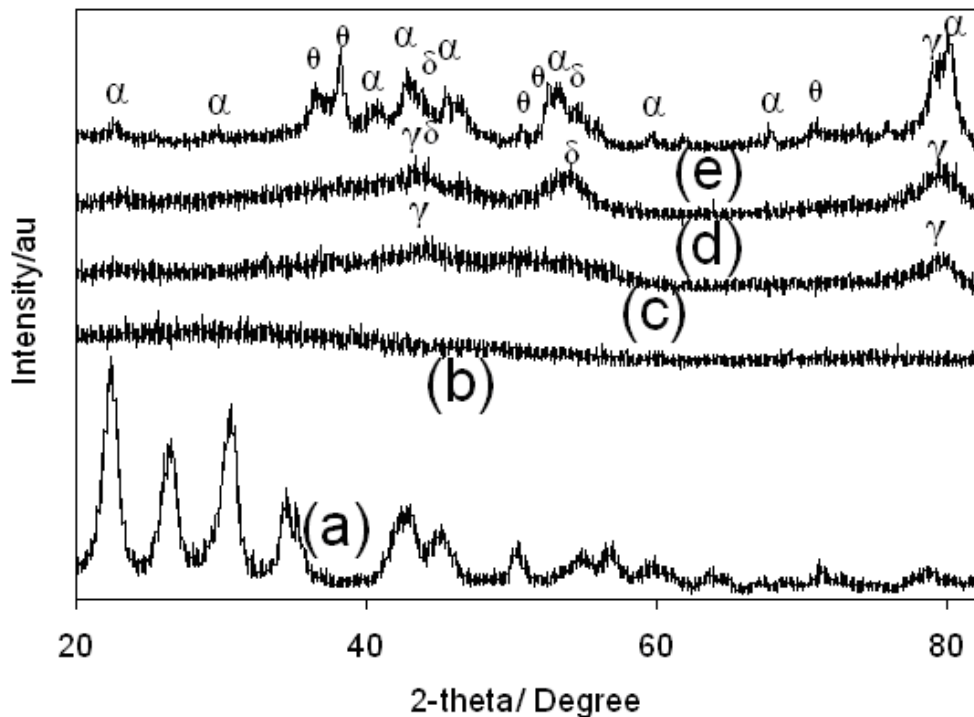


Figure 7.10: XRD analysis: a) As prepared, b) Sample calcined at 600 °C, c) Commercial gamma alumina, d) Calcined sample at 800 °C, e) Sample calcined at 1050 °C.

With elevated calcination temperatures, the aerogel peaks disappear at 600 °C, Figure 10b, indicating the destruction of the crystalline structure due to removal of bridging acetate groups; γ -Al₂O₃ appears at 800 °C (Figure 7.10d), while θ and α -Al₂O₃ appear at 1050 °C (Figure 7.10e). This crystallization trend after calcination agrees with the observations by others.^{140, 142, 167, 170} For comparison purposes, Figure 7.10c shows the commercial gamma alumina. The broad and weak XRD peaks can be explained by a retarded phase transformation of the nanostructured aerogel.¹⁷¹

7.3.1.2 Mechanism of Nanofiber Formation

Our IR, TGA, and XRD analysis results show that a significant amount of bidentate acetate groups as well as OH groups were present in the as-prepared nanofibers. In order to study the surface functionality and elemental composition, the as-prepared aerogel was further examined by XPS analysis (Figure 7.11). The elemental analysis results show that the molar ratio of Al/C/O is ca. 1:4:5. In Figure 11b, there is a small O(1s) signal at 532.99 eV and a large O(1s) signal at 531.85 eV. The small signal is assigned to the oxygen in adsorbed water or HAc, which has a higher energy level than the oxygen bond to aluminum atoms due to the higher electronegativity of hydrogen than aluminum. In Figure 7.11c, two types of carbon are dominant and their atomic ratio is about 1. The C(1s) signal at 288.92 eV is contributed by the carbon from -O-C-O- group, and the C(1s) signal at 284.80 eV is contributed by the carbon in the CH₃- group. Based on the information provided by the IR and XPS analysis, the formula of the as-prepared aerogel is consistent with [Al(OH)(CH₃CO₂)₂]_n. According to this formula, the weight loss of Al(OH)(CH₃CO₂)₂ upon calcinations is 63% if the formed calcination product is AlO(OH), which is supported by our TGA and XRD results (vide supra).

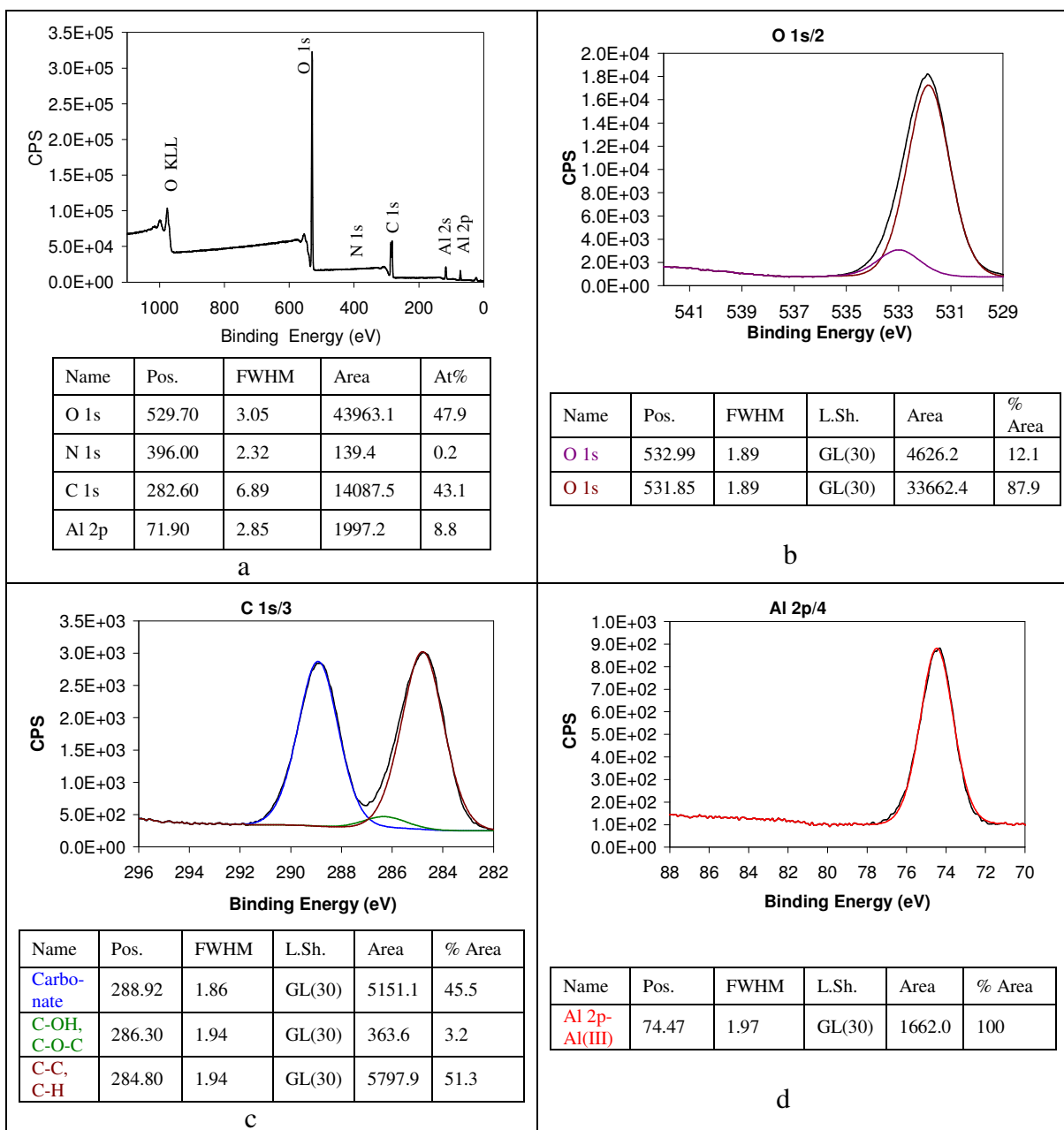


Figure 7.11: XPS Analysis of as prepared alumina nanofiber.

Based on our experimental evidence, Figure 7.12 shows the proposed structure of the as-prepared linear alumina polycondensate aerogel formed during the sol-gel chemistry in $scCO_2$. This $[Al(OH)(CH_3CO_2)_2]_n$ structure has the acetate group as a bidentate that

bridges two aluminum atoms. The linear macromolecules will form linear colloidal particles when the molecular weight is high enough and eventually form nanofibers, similar to the formation of TiO_2 nanofibers that we observed previously in scCO_2 ³⁴.

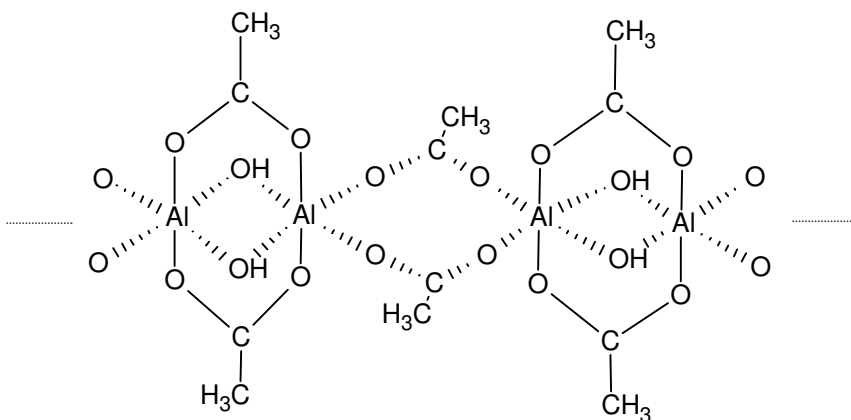


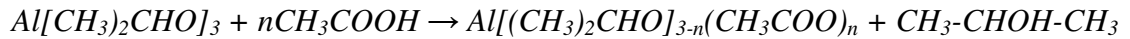
Figure 7.12: Schemetic diagram of the structure of the linear macromolecule with a repeating unit of $\text{Al}(\text{OH})(\text{CH}_3\text{CO}_2)_2$.

The evolution of the polycondensates into nanofibers or nanospheres can be explained by aggregation of rigid colloidal particles as described by Brinker and Scherer¹⁷². When the straight polycondensates grow long enough, the solubility decreases and small spherical concentrated regions called *coacervates* are formed, decreasing the interfacial energy. The arrangement of the polycondensates in the *coacervates* results in elliptical *tactoids*, in which the straight chains are organized due to intermolecular interactions. The polycondensates end up with a rigid nanofiber structure (*crystalloid*) as observed by electron microscopy³⁴.

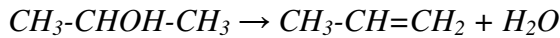
According to previous studies by others, during the sol–gel process, HAc reacted rapidly with aluminum alkoxide, generating alcohol and Al-carboxylate^{173, 174}. Production of

water occurs via either esterification or alcohol dehydration steps. As the esterification reaction is very slow relative to the dehydration reaction, and alumina can catalyze the dehydration reaction, it has been suggested that water is produced mainly by the dehydration of alcohol¹⁷³. As soon as water is produced, the hydrolysis reaction occurs instantly, which is followed by condensation reactions^{168, 173, 175, 176}. These basic steps are outlined as follows:

i) Substitution

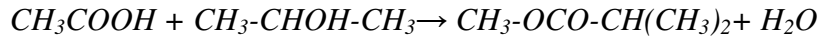


ii) Dehydration



OR

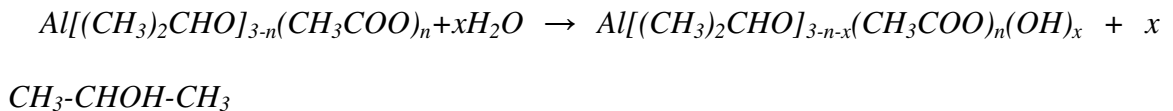
Esterification



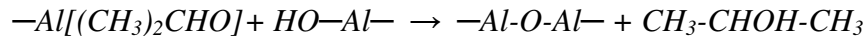
iii) Hydrolysis



or



iv) Condensation polymerization



These sol-gel chemical reactions continue during aging after gelation, producing strengthening, stiffening, and shrinkage of the alumina network. This results in the observed changes in the structural and textural properties of the final aerogel product¹⁷⁷.

If the gel is aged in the original reaction medium, small clusters continue to diffuse and attach to the main network, making the network both stiffer and stronger¹⁷⁷. Ten days of static aging resulted in high surface areas of alumina as shown by Ji et al¹⁶⁸.

As aluminum alkoxide is very reactive to water and precipitates quickly, a controlled hydrolysis for alumina nanostructure formation is crucial for a well-defined nanostructure formation. As water was not added to this one-pot reaction process in scCO₂, the in situ generated water (through the dehydration step) likely fuels the sol-gel reactions. The controlled hydrolysis in scCO₂ is further enhanced by the low solubility of water in scCO₂ (~0.1 wt%), which would decrease the sol-gel reaction rate and facilitate the formation of well-defined nanostructure instead of precipitate.¹⁷⁵

In addition, acetic acid is known to slow down the hydrolysis rate of metal alkoxides in water. The acetate group coordinates to the metal ions, preventing precipitate formation.¹⁷⁸ A significant amount of hydrogen bonding between acetic acid molecules has been observed in scCO₂ that would similarly slow down the sol-gel process.¹⁷⁹ These effects facilitate the formation of uniform nanostructures. Hence, our results in this work show that acetic acid was an excellent reaction agent in scCO₂ for producing alumina nanofibers without adding water for hydrolysis or any other additives for nanostructure formation.

7.4 Conclusions

A novel method for synthesizing alumina nanofibers is reported for the first time using a one-pot sol-gel route in scCO₂ with acetic acid as the polycondensation agent. This process uses no extra water, organic solvent, surfactant, chelating agent or other

additives. The synthesis temperature, pressure, concentration and alkoxide to acid ratio were found to play a key role in nanofiber formation. The acetate bidentate helps to form linear macromolecules, facilitating fiber formation. A high acid ratio, high temperature and sufficient pressure >4000 psig, facilitated fiber formation. Also, high acid ratio helps to increase the solubility in CO₂. Although the BET surface area of mesoporous floppy chunk was found as high as 579gm/cm³ at 60 °C and 6000 psi with aluminum isopropoxide concentration 0.2mmol/ml scCO₂, the best result with respect to long nanofibers and high aspect ratio were found at 80 °C and 6000 psi with aluminum isopropoxide concentration 0.3mmol/ml scCO₂. Thermal treatment of these fibers at up to 1050 °C did not change the nanostructure morphology. The BET surface area of these fibers remains over 100gm/cm³ even at 1050 °C. This synthesized mesoporous nanofibers with high surface area and porosity, high aspect ratio, and thermal stability make the fibers attractive for nanocatalysts or catalyst supports.

Chapter 8

Conclusions and Recommendations

8.1 Conclusions

Gasification and destruction of total organic compounds (TOC) of a model waste biomass compound (glucose) was studied in detail using a 600ml batch reactor in supercritical water. The supercritical water gasification technique presented in this thesis can be applied to environment friendly waste treatment, production of hydrogen or syn gas from the waste. The success of the gasification and TOC destruction depends on temperature, types of catalysts, reaction time, concentration of feed, oxidant etc. High temperature, low feed concentration, longer reaction times are favorable to the selectivity of hydrogen production as well as TOC destruction. Oxidant is favorable to total gasification and TOC destruction. However, the selectivity for hydrogen depends on the catalyst rather than the oxidant. The reactor temperature restriction limits the experiments to be investigated up to 500 °C. This moderate temperature limits gasification and TOC destruction, and the gaseous products are mostly methane rich. In an attempt to address this limitation, non-noble metallic catalysts were synthesized, characterized and evaluated for gasification in supercritical water. Use of catalysts only can increase the gasification, TOC destruction and yield of hydrogen. The homogeneous and noble metal catalysts were avoided due to some limitations discussed in chapter 2, 3, 4, and 5. The major outcomes from this study include: (1) hydrogen rich gaseous products is achievable at moderate temperatures (T_c to 500 °C) using non-noble metal catalysts like Ni-La/Al₂O₃; (2) the production of H₂ was found to be significantly higher than the reported H₂ by SCWG; (3) TOC destruction upto

98% is achievable using oxidant; (4) higher hydrogen yield was achieved by supercritical water gasification than supercritical water oxidation using Ni-La/Al₂O₃ catalyst (5) nickel was found to crack tar and char and increase gasification; (6) reduced nickel was found to have a higher efficiency than oxidized nickel; but (7) metallic nickel oxidized in supercritical water even without using oxidant and may produce hydrogen; (8) beyond a certain amount of nickel loading, the methanation reaction was increased; (9) graphitic type coke was found to be formed on nickel catalyst; (10) lanthanum modified catalyst was found to inhibit the methanation reaction, along with graphitic coke formation and enhance the water gas shift reaction; (11) lanthanum adsorbs CO₂ that in turn increases hydrogen selectivity (12) the smaller the size of catalysts, the higher is the selectivity, (13) nano catalysts showed the best performance towards hydrogen yield and TOC destruction among all catalysts examined; (14) synthesis of high surface area alumina nanofibers in supercritical carbon dioxide was found to be thermally stable at atmospheric pressure and could be promising as a nano catalyst support.

The physical and chemical properties of catalysts influence the selectivity, reaction mechanism, length of use, regeneration etc. Hence, detailed characterization of fresh and spent catalysts was conducted to determine the effect of supercritical water gasification on catalysts and possible future usage and catalyst design. The synthesized catalysts were found to have excellent reduction characteristics. Although the non-noble metals Ni, La are found to be promising in SCWG, agglomeration of metallic sites by exposing in SCW was found to be a major drawback.

Loading of metals (Ni, La on alumina) by direct so-gel method resulted in integration of metals forming a Ni-La-Al-O nanostructure. Incorporation of metals with the main

support loaded by this method showed high activity towards hydrogen production or TOC destruction compared to conventionally metal impregnation on commercial alumina support. However, integration of lanthanum leads not to promoting the water gas shift reaction resulting less hydrogen production compared to nanofiber catalysts. Exposure of the sol-gel derived catalysts to SCW transformed to non uniform nano particles.

The novel method for synthesizing alumina nanofibers for the first time using a one-pot sol-gel route in $scCO_2$ with acetic acid as the polycondensation agent can be promising due to environment friendliness. This process uses no extra water, organic solvent, surfactant, chelating agent or other additives. The backbone of nano catalyst (alumina nanofibers) could sustain high temperature (1050 °C) at atmospheric pressure; however, the fibrous structure morphology was distorted when exposed to supercritical water.

The kinetics of SCWG is important for feasibility test and to design the catalysts as well as reactors. The detailed reaction mechanism of SCWG was discussed and explained. The assumption of first order and ignoring water concentration due to high excess was found erroneous. A global kinetic model for destruction of TOC was developed using MATLAB by non-linear regression analysis. This model convincingly satisfied the experimental results.

8.2 Recommendations

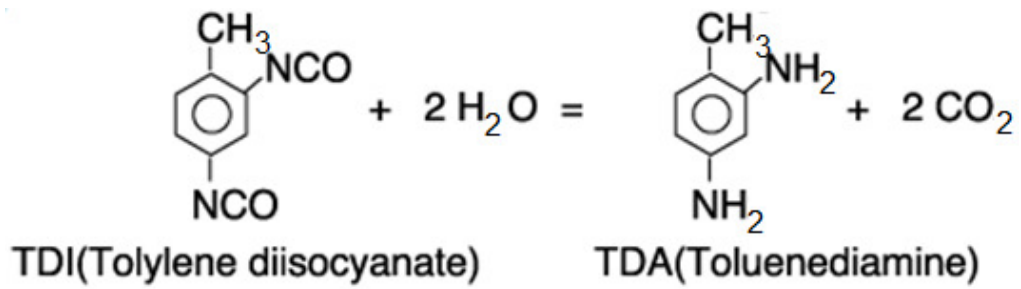
SCWG of glucose using non noble catalysts can lead to the potential viability of industrial application for biomass waste treatment and production of hydrogen. The following recommendation should be considered:

- i) Catalysts should be further improved for total removal of Tar, CO and CH₄ at lower temperatures.
 - a) Trace amounts of noble metals with Ni-La/Al₂O₃ could be applied for higher hydrogen selectivity.
 - b) As metals form complex with structure and the alloys were found to act like catalysts; high surface area Ni-Al, Ni-Ru-Al network synthesis by sol-gel method can be applied as catalysts.
 - c) Rutile titania as catalyst support can be applied as it is corrosion resistant and could be stable in SCW.
- ii) Other model compounds (cellulose, lignin, hemicellulose etc.) and real life agricultural/industrial wastes, sewage sludge should be investigated at lower temperatures using catalysts.
- iii) Detailed kinetic model for dissociation of liquid intermediate products should be developed.
- iv) A continuous process should be developed with a few seconds residence time for evaluation of real life industrial viability.

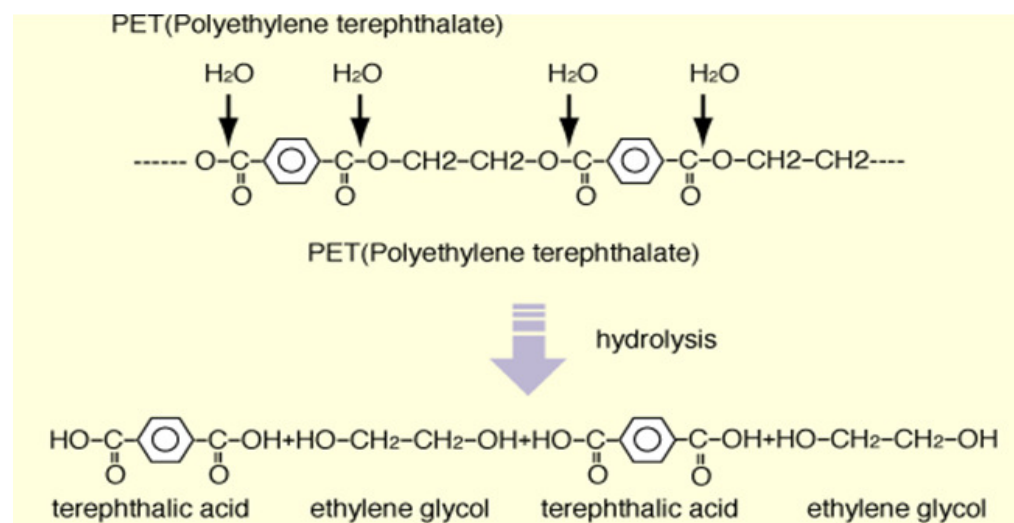
Other than biomass waste, plastic waste can be recycled using SCW due to its environment friendliness compared to conventional processes. The reactions can be written as follows:

1. Recovering Toluene diamine (TDA) from Toluene di-isocyanate (TDI) residue

for making polyurethane plastic.



2. Hydrolysis of PET to PTA and ethylene glycol.



Development of catalysts can improve the plastic waste recycling.

Bibliography

1. Guo, L. J.; Lu, Y. J.; Zhang, X. M.; Ji, C. M.; Guan, Y.; Pei, A. X., Hydrogen production by biomass gasification in supercritical water: A systematic experimental and analytical study. *Catal. Today* **2007**, 129, 275.
2. Gasafi, E.; Meyer, L.; Schebek, L., Energetic efficiency and options for improving sewage sludge gasification in supercritical water. *Int. J. Energy Res.* **2007**, 31, 346.
3. Xu, X.; Matsumura, Y.; Stenberg, J.; Antal, M. J., Carbon catalyzed Gasification of Organic Feedstocks in Supercritical Water. *Ind. Eng. Chem. Res.* **1996**, 35, 2522.
4. Basu, P.; Mettanan, V., Biomass Gasification in Supercritical Water – A Review. *Int. J. Chem. Reactor Eng.* **2009**, 7, R3.
5. Yoshida, Y.; Dowaki, K.; Matsumura, Y.; Matsuhashi, R.; Li, D.; Ishitani, H.; Komiyama, H., Comprehensive comparison of efficiency and CO₂ emissions between biomass energy conversion technologies—position of supercritical water gasification in biomass technologies. *Biomass Bioenergy* **2003**, 25, 257.
6. Savage, E. P., A perspective on catalysis in sub- and supercritical water. *J. of Supercritical Fluids* **2009**, 47, 407.
7. Lu, Y. J.; Guo, L. J.; Ji, C. M.; Zhang, X. M.; Hao, X. H.; Yan, Q. H., Hydrogen production by biomass Gasification in Supercritical water: A parametric study. *Int. J. Hydrogen Energy* **2006**, 31, 822.
8. Archer, D.; Wang, P., The dielectric constant of water and Debye–Hückel limiting law slopes *J. Phys. Chem. Ref. Data* **1990**, 19, (2), 371.

9. Ding, Z. Y.; Frisch, M. A.; Li, L.; Gloyna, E. F., Catalytic Oxidation in Supercritical Water. *Ind. Eng. Chem. Res.* **1996**, 35, 3257.
10. Williams, P. T.; Onwudili, J., Subcritical and Supercritical Water Gasification of Cellulose, Starch, Glucose, and Biomass Waste. *Energy Fuels* **2006**, 20, 1259.
11. Yoshida, T.; Oshima, Y., Partial Oxidative and Catalytic Biomass Gasification in Supercritical Water: A Promising Flow Reactor System. *Ind. Eng. Chem. Res.* **2004**, 43, 4097.
12. Peterson, A. A.; Vogel, F.; Lachance, R. P.; Froling, M.; Antal, M. J.; Tester, J. J. W., Thermochemical biofuel production in hydrothermal media: A review of sub- and supercritical water technologies *Energy Environ. Sci.* **2008**, 1, 32.
13. Lee, I. G.; Kim, M. S.; Ihm, S. K., Gasification of Glucose in Supercritical Water. *Ind. Eng. Chem. Res.* **2002**, 41, (5), 1182.
14. Hao, X. H.; Guo, L. J.; Mao, X.; Zhang, X. M.; Chen, X. J., Hydrogen production from glucose used as a model compound of biomass gasified in supercritical water. *Int. J. Hydrogen Energy* **2003**, 28, 55.
15. Watanabe, M.; Inmomata, H.; Osada, M.; Sato, T.; Adschiri, T.; Arai, K., Catalytic Effects of NaOH and ZrO₂ for partial oxidative gasification of n-hexadecane and lignin in Supercritical Water in Supercritical Water. *Fuel* **2003**, 82, 545.
16. Antal, M. J. J.; Allen, S. G.; Schulman, D.; Xu, X., Biomass Gasification in Supercritical water. *Ind. Eng. Chem. Res.* **2000**, 39, 4040.
17. Hao, X.; Guo, L.; Zhang, X.; Guan, Y., Hydrogen production from catalytic gasification of cellulose in supercritical water. *Chem. Eng. J.* **2005**, 110, 57.

18. Byrd, A. J.; Pant, K. K.; Gupta, R. B., Hydrogen production from glucose using Ru/Al₂O₃ catalysts in supercritical water. *Ind. Eng. Chem. Res.* **2007**, 46, 3574.
19. Osada, M.; Sato, T.; Watanabe, M.; Adschiri, T.; Arai, K., Low-temperature catalytic gasification of lignin and cellulose with a ruthenium catalyst in supercritical water. *Energy Fuels* **2004**, 18, (2), 327.
20. Osada, M.; Hiyoshi, N.; Sato, O.; Arai, K.; Shirai, M., Reaction pathway for catalytic gasification of lignin in presence of sulfur in supercritical water. *Energy Fuels* **2007**, 21, (4), 1854.
21. Panagiotopoulou, P.; Kondarides, D. I.; Verykios, X. E., Selective methanation of CO over supported noble metal catalysts: Effects of the nature of the metallic phase on catalytic performance. *Appl. Catal. A:General* **2008**, 344, 45.
22. Choudhury, M. B. I.; Ahmed, S.; Shalabi, M. A.; Inui, T., Preferential methanation of CO in a syngas involving CO₂ at lower temperature range. *Appl. Catal. A:General* **2006**, 314, 47.
23. Furusawa, T.; Sato, T.; Sugito, H.; Miura, Y.; Sato, M.; Itoh, N., Hydrogen production from the Gasification of Lignin with Nickel Catalysts in Supercritical water. *Int. J. Hydrogen Energy* **2007**, 32, 699.
24. Courson, C.; Makaga, E.; Petit, C.; Kiennemann, A., Development of Ni Catalysts of Gas Production from Biomass Gasification: Reactivity in Steam-and dry-Reforming. *Catal. Today* **2000**, 63, 427.
25. Resende, F. L. P.; Savage, P. E., Effect of Metals on Supercritical Water Gasification of Cellulose and Lignin. *Ind. Eng. Chem. Res.* **2010**, 49, (6), 2694.

26. Kim, G., Ceria-promoted three-way catalysts for auto exhaust emission control. *Ind. Eng. Chem. Prod. Res. Dev.* **1982**, 21, (2), 267.
27. Evans, C. H., *Biochemistry of the lanthanides*. Plenum Press: New York, 1990.
28. Zhang, Z. L.; Verykos, X. E., A stable and active nickel-based catalyst for carbon dioxide reforming of methane to synthesis gas. *J. Chem. Soc., Chem. Commun.* **1995**, 71.
29. Fatsikostas, A. N.; Kondarides, D. I.; Verykios, X. E., Production of hydrogen for fuel cells by reformation of biomass-derived ethanol. *Catal. Today* **2002**, 75, 145.
30. Guo, Y.; Wang, S. Z.; Xu, D. H.; Gong, Y. M.; Ma, H. H.; Tang, X. Y., Review of catalytic supercritical water gasification for hydrogen production from biomass *Renew. Sust. Energ. Rev.* **2010**, 14, (1), 334.
31. Chowdhury, M. B. I.; Sui, R.; Lucky, R. A.; Charpentier, P. A., One-Pot Procedure to Synthesize High Surface Area Alumina Nanofibers Using Supercritical Carbon Dioxide. *Langmuir* **2010**, 26, (4), 2707.
32. Lucky, R. A.; Charpentier, P. A., A One-Step Approach to the Synthesis of ZrO₂-Modified TiO₂ Nanotubes in Supercritical Carbon Dioxide. *Advanced Materials* **2008**, 20, 1755.
33. Sui, R., Rizkalla, A.S., Charpentier, P.A., Formation of Titania Nanofibers: A Direct Sol–Gel Route in Supercritical CO₂. *Langmuir* **2005**, 21, (14), 6150.
34. Sui, R., Rizkalla, A.S., and Charpentier, P.A., FTIR Study on the Formation of TiO₂ Nanostructures in Supercritical CO₂. *The Journal of Physical Chemistry B* **2006**, 110, 16212.
35. Allen, S. G.; Kan, L. C.; Zemann, A. J.; Antal, M. J. J., Fractionation of Sugar Cane with Hot Compressed Liquid Water. *Ind. Eng. Chem. Res.* **1996**, 35, 2709.

36. Sasaki, M.; Kabyemela, B.; Adschiri, T.; Malaluan, R.; Hirose, S.; Takeda, N.; Arai, K. In *Cellulose Hydrolysis in Supercritical Water*, The 4th International Symposium on Supercritical Fluids, Sendai, Japan, 1997; Sendai, Japan, 1997; p 583.
37. Yesodharan, S., Supercritical water oxidation: and environmentally safe method for the disposal of organic wastes *Current Science* **2002**, 82, 1112.
38. Wagner, W.; Prass, A., The IAPWS formulation 1995 for the thermodynamic properties of ordinary water substance for general and scientific use. *Journal of Phys. Chem. Ref. Data* **2002**, 31, (2), 387.
39. Töhheide, K., Water at high temperatures and pressures. In *Water: A Comprehensive Treatise*, Franks, F., Ed. Platinium Press, Inc: New York, 1972; p 463.
40. Bandura, A.; Lvov, S., The ionization constant of water over wide ranges of temperature and density *J. Phys. Chem. Ref. Data* **2006**, 35, (1), 15.
41. Dautzenberg, F. M., Ten Guidelines for Catalyst Testing. In *Characterization and Catalyst Development: An Interactive Approach In ACS Symposium Series 411*, Bradley, S. A., Gattuso, M. J., Bertolacini, R. J., Ed. American Chemical Society: Washington, DC, 1989; p 99.
42. Matsumura, Y., Evaluation of Supercritical water gasification and Biomethanation for Wet Biomass Utilization in Japan. *Energy Convers. Manage* **2002**, 43, 1301.
43. Gasafi, E.; Reinecke, M. Y.; Kruse, A.; Schebek, L., Economic Analysis of Sewage Sludge Gasification in Supercritical Water for Hydrogen Production. *Biomass Bioenergy* **2008**, 32, 1085.

44. Boukis, N.; Galla, U.; Müller, H.; Dinjus, E., Biomass Gasification in Supercritical Water, Experimental Progress Achieved with the VERENA Pilot Plant. In *15th European Biomass Conference & Exhibition*, Berlin, Germany, 2007; p 1013.
45. Lu, Y.; Guo, L.; Zhang, X.; Yan, Q., Thermodynamic modeling and analysis of biomass gasification for hydrogen production in supercritical water *Chem. Eng. J.* **2007**, 131, (1-3), 233.
46. Li, X. T.; Grace, J. R.; Lim, C. J.; Watkinson, A. P.; Chen, H. P.; Kim, J. R., Biomass gasification in a circulating fluidized bed. *Biomass Bioenergy* **2004**, 26, 171.
47. Li, X.; Grace, J. R.; Watkinson, A. P.; Lim, C. J.; Ergudenler, A., Equilibrium modeling of gasification: a free energy minimization approach and its application to a circulating fluidized bed coal gasifier. *Fuel* **2001**, 80, 195.
48. Tang, H.; Kitagawa, K., Supercritical water gasification of biomass: thermodynamic analysis with direct Gibbs free energy minimization *Chem. Eng. J.* **2005**, 106, (3), 261.
49. Yan, Q.; Guo, L.; Lu, Y., Thermodynamic analysis of hydrogen production from biomass gasification in supercritical water *Energy Convers. Manage* **2006**, 47, (11-12), 1515.
50. Antal, M. J., Synthesis gas production from organic wastes by pyrolysis/steam reforming. In *Energy from Biomass and Wastes* Klass, D. L., Ed. Washington, DC; Institute of Gas Technology, Chicago, 1978; p 495.
51. Voll, F. A. P.; Rossi, C. C. R. S.; Silva, C.; Guirardello, R.; Souza, R. O. M. A.; Cabrala, V. F.; Cardozo-Filho, L., Thermodynamic analysis of supercritical water

gasification of methanol, ethanol, glycerol, glucose and cellulose. *Int. J. Hydrogen Energy* 34, (24), 9737.

52. Kruse, A.; Gawlik, A., Biomass Conversion in Water at 330–410 °C and 30–50 MPa. Identification of Key Compounds for Indicating Different Chemical Reaction Pathways. *Industrial & engineering chemistry research* **2003**, 42, (2), 267.

53. Hologate, H. R.; Meyer, J. C.; Tester, W. J., Glucose Hydrolysis and Oxidation in Supercritical water. *AIChE J.* **1995**, 41, 637.

54. Williams, P. T.; Onwudili, J., Composition of Products from the Supercritical Water Gasification of Glucose: A Model Biomass Compound. *Ind. Eng. Chem. Res.* **2005**, 44, 8739.

55. Jesus, P.; Boukis, N.; K., C. B.; E, D., Influence of process variables on gasification of corn silage in supercritical water, *Industrial Engineering Chemistry research. Ind. Eng. Chem. Res.* **2006**, 45, 1622.

56. Jin, F.; Kishita, A.; Moriya, T.; Enomoto, H., Kinetics of oxidation of food wastes with H₂O₂ in supercritical water. *J. Supercrit. Fluids* **2001**, 19, 251.

57. Delgado, J.; Aznar, M.; Corella, J., Biomass gasification with steam in fluidized bed: effectiveness of CaO, MgO for hot raw gas cleaning. *Ind. Eng. Chem. Res.* **1997**, 36, 1535.

58. Matsumura, Y.; Minowa, T.; Xu, X.; Nuessle, F.; Adschiri, T.; Antal, J. M., High pressure carbon dioxide removal in supercritical water gasification of biomass. *Ind. Eng. Chem. Res.* **1996**, 864.

59. Matsumura, Y.; Minowa, T.; Potic, B.; Kersten, S. R. A.; Prins, W.; Swaaij, W. P. M. V.; Beld, B. V. D.; Elliott, D. C.; Neuenschwander, G. G.; Kruse, A.; Antal, M. J.,

Biomass gasification in near- and super-critical water: status and prospects *Biomass Bioenergy* **2005**, 29, 269.

60. Jesus, P.; Boukis, N.; Czarnetzki, B. K.; Dinjus, E., Gasification of Corn and Clover Grass in Supercritical Water. *Fuel* **2006**, 85, 1032.

61. Yu, D.; Aihara, M.; Antal Jr., M. J., Hydrogen production by steam reforming glucose in supercritical water. *Energy Fuels* **1993**, 7, 574.

62. Kabyemela, B. M.; Adschiri, T.; Malaluan, R. M.; Arai, K., Glucose and Fructose Decomposition in Subcritical and Supercritical Water: Detailed Reaction Pathway, Mechanisms, and Kinetics. *Ind. Eng. Chem. Res.* **1999**, 38, 2888.

63. Kersten, S. R. A.; Potic, B.; Prins, W.; Swaaij, W. P. M. V., Gasification of Model Compounds and Wood in Hot Compressed Water. *Ind. Eng. Chem. Res.* **2006**, 45, (12), 4169.

64. Minowa, T.; Ogi, T., Hydrogen Production from Cellulose using Reduced Nickel Catalyst. *Catal. Today* **1998**, 45, (1-4), 411.

65. Kruse, A.; Meier, D.; Rimbrecht, P.; Schacht, M., Gasification of pyrocatechol in supercritical water in the presence of potassium hydroxide. *Ind. Eng. Chem. Res.* **2000**, 39, 4842.

66. García Jarana, M. B.; Sánchez-Oneto, J.; Portela, J. R.; Nebot Sanz, E.; Martínez de la Ossa, E. J., Supercritical Water Gasification of Industrial Organic wastes. *J. Supercrit. Fluids* **2008**, 46, 329.

67. Yanik, J.; Ebale, S.; Kruse, A.; Saglam, M.; Yuksel, M., Biomass gasification in supercritical water. II. Effect of catalyst *Int. J. Hydrogen Energy* **2008**, 33, (17), 4520.

68. Sinag, A.; Kruse, A.; Rathert, J., Influence of the heating rate and the type of catalyst of the formation of key intermediates and on the generation of gases during hydrolysis of glucose in supercritical water in a batch reactor. *Ind. Eng. Chem. Res.* **2004**, 43, 502.
69. Elliott, D. C., Catalytic hydrothermal gasification of biomass Biofuels. *Biofuels, Bioprod. Bioref.* **2008**, 2, 254.
70. Yoshida, T., Oshima, Y., Matsumura, Y., Gasification of Biomass Model Compounds and Real Biomass in Supercritical Water. *Biomass Bioenergy* **2004**, 26, 71.
71. Minowa, T.; Zhen, F.; Ogi, T., Cellulose decomposition in hot-compressed water with alkali or nickel catalyst. *Journal of Supercritical Fluids* **1998**, 13, 253.
72. Byrd, A. J.; Pant, K. K.; Gupt, R. B., Hydrogen production from glycerol by reforming in supercritical water over Ru/Al₂O₃ catalyst. *Fuel* **2008**, 87, 2956.
73. Sato, T.; Osada, M.; Watanabe, M.; Shirai, M.; Arai, K., Gasification of alkylphenols with supported noble metal catalysts in supercritical water. *Ind. Eng. Chem. Res.* **2003**, 42, 4277.
74. Watanabe, M.; Inmomata, H.; Arai, K., Catalytic hydrogen generation from biomass (glucose and cellulose) with ZrO₂ in supercritical water. *Biomass Bioenergy* **2002**, 22, 405.
75. Youssef, E. A.; Chowdhury, M. B. I.; Nakhla, G.; Charpentier, P., Effect on nickel loading on hydrogen production and chemical oxygen demand (COD) destruction from glucose oxidation and gasification in supercritical water. *Int. J. Hydrogen Energy* **2009**, 35, 5034.

76. Goto, M.; Nada, T.; Kodama, A.; Hirose, T., Kinetic Analysis for Destruction of Municipal Sewage Sludge and Alcohol Distillery Wastewater by Supercritical Water Oxidation. *Ind. Eng. Chem. Res.* **1999**, 38, 1863.
77. Blasi, C. D.; Branca, C.; Galgano, A.; Meier, D.; Brodzinski, I.; Malmros, O., Supercritical Gasification of Wastewater from Updraft Wood Gasifiers. *Biomass Bioenergy* **2007**, 31, 802.
78. Yan, B.; Wei, C. H.; Hu, C. S.; Xie, C.; Wu, J. Z., Hydrogen Generation from Polyvinyl Alcohol-Contaminated Wastewater by a Process of Supercritical Water Gasification. *J. Environ. Sci.* **2007**, 19, 1424.
79. Calvo, L.; Vallejo, D., Formation of organic acids during the hydrolysis and oxidation of several wastes in sub- and supercritical water. *Ind. Eng. Chem. Res.* **2002**, 41, 6503.
80. Adschiri, T.; Shibata, R.; Sato, R.; Watanabe, M.; Arai, K., Catalytic Hydrodesulfurization of Dibenzothiophen through Partial Oxidation and Water-Gas Shift reaction in Supercritical Water. *Ind. Eng. Chem. Res.* **1998**, 37, 2634.
81. Wang, W.; Padban, N.; Ye, Z.; Olefsson, G.; Andersson, A.; Bjerle, I., Catalytic Hot Gas Cleaning of Fuel Gas from an Air-blown Pressurized Fluidized-bed Gasifier. *Ind. Eng. Chem. Res.* **2000**, 39, 4075.
82. Cai, S. H.; Rashkeev, S. N.; Pantelides, S. T.; Sohlberg, K., Atomic scale mechanism of the transformation of γ -alumina to α -alumina. *Physical review letters* **2002**, 89, (23), 235501.

83. Inui, T.; Suehiro, M.; Saita, Y.; Miyake, T.; Takegami, Y., Enhancement of Methanation Activity by Ammonia-water Vapor Treatment at the Stage of Catalyst-metal Salt Supported on a Carrier *Appl. Catal.* **1982**, 2, 389.
84. Cortright, R. D.; Davda, R. R.; Dumesic, J. A., Hydrogen from catalytic reforming of biomass-derived hydrocarbons in liquid water. *Nature* **2002**, 418, 964.
85. Gupta, J. B. G. a. R. B., Hydrogen productin by methanol reforming in supercritical water: catalysis by in-situ-generated copper nanoparticles. *Int. J. Hydrogen Energy* **2007**, 32, 2374.
86. Sato, T.; Furusawa, T.; Ishiyama, Y.; Sugito, H.; Miura, Y.; Sato, M.; Suzuki, N.; Itoh, N., Effect of Water density on the Gasification of Lignin with Magnesium Oxide Supported Nickel Catalysts in Supercritical Water. *Ind. Eng. Chem. Res.* **2006**, 45, 615.
87. Chowdhury, M. B. I.; Hossain, M. M.; Charpentier, P. A., Production of hydrogen-rich gas in Supercritical Water from Glucose using La-promoted Ni/Al₂O₃ catalysts *Ind. Eng. Chem. Res.* **2010**, Submitted.
88. Solar and Hydrogen: Energy Economics, http://greenecon.net/solar-and-hydrogen-energy-economics/energy_economics.html#more-45.
89. Schmieder, H.; Abeln, J.; Boukis, N.; Dinjus, E.; Kruse, A.; Kluth, M.; Petrich, G.; Sadri, E.; Schacht, M., Hydrothermal gasification of biomass and organic wastes *J. of Supercritical Fluids* **2000**, 17, (2), 145.
90. Boehman, A. L.; Corre, O. L., Combustion of Syngas in Internal Combustion Engines. *Combust. Sci. and Tech* **2008**, 180, 1193.
91. Kritzer, P., Corrosion in high-temperature and supercritical water and aqueous solutions: a review. *J. Supercrit. Fluids* **2003**, 29, 1.

92. Rodulfo-Baechler, S. M. A.; Permi'a, W.; Aray, I.; Figueroa, H.; Gonza'lez-Corte's, S. L., Influence of lanthanum carbonate phases of Ni/La_{0.98}Sr_{0.02}O_x catalyst over the oxidative transformation of methane. *Catal. Lett.* **2006**, 112, 231.
93. Youssef, E. A.; Chowdhury, M. B. I.; Nakhla, G.; Charpentier, P., Effect on nickel loading on hydrogen production and chemical oxygen demand (COD) destruction from glucose oxidation and gasification in supercritical water. *Int. J. Hydrogen Energy* **2010**, 35, 5034.
94. Oudet, F.; Courtine, P.; Vejux, A., *J. Catal.* **1988**, 114, 112.
95. Hao, X.; Guo, L. J.; Mao, X.; Zhang, X. M.; Chen, X. J., Hydrogen production from glucose used as a model compound of biomass gasification in supercritical water. *Int. J. Hydrogen Energy* **2003**, 28, 55.
96. Oshima, Y.; Tomita, K.; Koda, S., Kinetics of the Catalytic Oxidation of Phenol over Manganese Oxide in Supercritical water. *Ind. Eng. Chem. Res.* **1999**, 38, 4183.
97. Kaddouri, A.; Gronchi, P.; Centola, P.; Rosso, R. D., On the Preparation of Ni-La Supported on Silica by Sol-gel Process via Propionates *J. Therm. Anal. Calorim.* **2000**, 62, 609.
98. Zhang, X.; Walters, A. B.; Vannice, M. A., NO Adsorption, Decomposition, and Reduction by Methane over Rare Earth Oxides. *J. Catal.* **1995**, 155, 290.
99. Lemaitre, J. L.; Menon, P. G.; Delannay, F., *The measurement of catalyst dispersion*. Dekker: New York, 1984; Vol. 15.
100. Molina, R.; Poncelet, G., α -Alumina-Supported Nickel Catalysts Prepared from Nickel Acetylacetonate: A TPR Study. *J. Catal.* **1998**, 173, 257.

101. Richardson, J. T.; Lei, M.; Turk, B.; Forster, K.; Twigg, M. V., Reduction of model steam reforming catalysts : NiO/ α -Al₂O₃. *Appl. Catal. A:General* **1994**, 110, 217.
102. Dupeyrat, C. B.; Valderrama, G.; Meneses, A.; Martinez, F.; Barrault, J.; Tatibouët, J. M., Pulse study of CO₂ reforming of methane over LaNiO₃ *Appl. Catal. A:General* **2003**, 248, 143.
103. Yu, J.; Savage, P. E., Phenol oxidation over CuO/Al₂O₃ in supercritical water *Appl. Catal. B.:Environmental* **2000**, 28, 275.
104. Sedor, K. E.; Hossain, M. M.; De Lasa, H. I., Reactivity and stability of Ni/Al₂O₃ oxygen carrier for chemical-looping combustion (CLC) *Chem. Eng. Sci.* **2008**, 63, (11), 2994.
105. Wang, S.; Lu, G. Q. M., *Energy Fuels* **1996**, 10, 896.
106. Gallego, G. S.; Mondragón, F.; Tatibouët, J. M.; Barrault, J.; Dupeyrat, C. B., Carbon dioxide reforming of methane over La₂NiO₄ as catalyst precursor— Characterization of carbon deposition. *Catal. Today* **2008**, 133-135, 200.
107. Cox, P. A., *The Element on Earth-Inorganic Chemistry in the Environment*. Oxford University Press: Oxford, 1995.
108. Jianjun, G.; Lou, H.; Zhao, H.; Chai, D.; Zheng, X., *Appl. Catal. A:General* **2004**, 273, 2004.
109. Akande, A. J.; Idem, R. O.; Dalai, A. K., Synthesis, characterization and performance evaluation of Ni/Al₂O₃ catalysts for reforming of crude ethanol for hydrogen production. *Appl. Catal. A:General* **2005**, 287, 159.

110. Pinheiro, A. N.; Valentini, A.; Sasaki, J. M.; Oliveira, A. C., Highly stable dealuminated zeolite support for the production of hydrogen by dry reforming of methane. *Appl. Catal. A:General* **2009**, 355, 156.
111. Matsukata, M.; Matsushita, T.; Ueyama, K., A novel hydrogen/syngas production process: Catalytic activity and stability of Ni/SiO₂ *Chem. Eng. Sci.* **1996**, 51, 2769.
112. Guo, J.; Lou, H.; Zheng, X., The deposition of coke from methane on a Ni/MgAl₂O₄ catalyst. *Carbon* **2007**, 45, 1314.
113. Wang, S.; Lu, G. Q., Reforming of methane with carbon dioxide over Ni/Al₂O₃ catalysts: Effect of nickel precursor. *Appl. Catal. A:General* **1998**, 169, (2), 271.
114. Han, Y. S.; Li, J. B.; Ning, X. S.; Yang, X. Z.; Chi, B., Study on NiO excess in preparing NiAl₂O₄ *Mater. Sci. Eng., A* **2004**, 369, 241.
115. Taylor, R. P.; Schrader, G. L., Lanthanum catalysts for methane oxidative coupling: a comparison of the reactivity of phases. *Ind. Eng. Chem. Res.* **1991**, 30, (5), 1016.
116. Barbier, J.; Marecot, P.; Martín, N.; Elassal, A.; Maurel, R., *Stud. Surf. Sci.* **1980**, 40, 53.
117. Parera, J. M.; Fígoli, N. S.; Traffano, E. M., *J. Catal.* **1983**, 79, 481.
118. Wang, S.; Lu, G. C., Catalytic Activities and Coking Characteristics of Oxides-Supported Ni Catalysts for CH₄ Reforming with carbon dioxide. *Energy Fuels* **1998**, 12, 248.
119. Germani, G.; Schuurman, Y., Water-Gas Shift Reaction Kinetics Over μ -structured Pt/CeO₂/Al₂O₃ Catalysts. *AIChE J.* **2006**, 52, 1806.

120. Vandervella, H. D.; Bowkera, M., The methanation reaction on a nickel catalyst: CO, H₂ competition for dissociated oxygen. *Appl. Catal.* **1987**, 30, 151.
121. Chowdhury, M. B. I.; Hossain, M. M.; Charpentier, P. A., Catalytic hydrogen production through supercritical water gasification of Glucose: Kinetic analysis. *Ind. Eng. Chem. Res.* **2010**, Submitted.
122. Chowdhury, M. B. I.; Hossain, M. M.; Charpentier, P. A., Study of La promoted Ni/Al₂O₃ catalysts in Supercritical Water for H₂ Production from Glucose. *Appl. Catal. B. : Environmental* **2010**, APCATB-D-10-00023.
123. Lee, I. G.; Ihm, S. K., Catalytic Gasification of Glucose over Ni/Activated Charcoal in Supercritical Water. *Ind. Eng. Chem. Res.* **2009**, 48, 1435.
124. Williams, P. T.; Onwudili, J., Composition of Products from the Supercritical Water Gasification of Glucose: A Model Biomass Compound. *Ind. Eng. Chem. Res.* **2005**, 44, 8739.
125. Lee, I. G.; Kim, M. S.; Ihm, S. K., Gasification of Glucose in Supercritical Water. *Ind. Eng. Chem. Res.* **2002**, 41, 1182.
126. Portela, J. R.; Nebot, E.; Ossa, E. M., Generalized kinetic models for supercritical water oxidation of cutting oil wastes. *J. of Supercritical Fluids* **2001**, 21, 135.
127. Hernandez, M. J. A.; Leeke, G. A.; Santos, R. C. D., Catalytic Supercritical water Oxidation for the Destruction of Quinoline over MnO₂/CuO mixed Catalyst. *Ind. Eng. Chem. Res.* **2009**, 48, 1208.
128. Lee, B. M.; Veriansyah, B.; Kim, S. H.; Kim, J. D.; Lee, Y. W., Total Organic Carbon Disappearance Kinetics for Supercritical Water Oxidation of Dimethyl

- Methylphosphate Used as a Chemical Agent Simulant. *Korean J. Chem. Eng.* **2005**, *22*, 579.
129. Kabyemela, B. M.; Adschiri, T.; Malaluan, R. M.; Arai, K., Kinetics of Glucose Epimerization and Decomposition in Subcritical and Supercritical Water. *Ind. Eng. Chem. Res.* **1997**, *36*, 1552.
130. Lu, Y. J., Guo, L. J., Ji, C. M., Zhang, X. M., Hao, X. H., Yan, Q. H., Hydrogen production by biomass Gasification in Supercritical water: A parametric study. *Int. J. Hydrogen Energy* **2006**, *31*, 1597.
131. Fogler, H. S., *Elements of Chemical Reactor Engineering*. Prentice Hall International (UK) Limited: London, 2000.
132. Euzen, P.; Raybaud, P.; Krokidis, X.; Toulhoat, H.; Le Loarer, J. L.; Jolivet, J. P.; Froidefond, C., *Handbook of Porous Solids*. Wiley-VCH: Weinheim, 2002.
133. Ishii, S.; Inami, Y.; Akasawa, T., Application of alumina fiber reinforced plastics as a grinding material. *Journal of Materials Shaping Technology* **1991**, *9*, (4), 207.
134. Vasita, R.; Katti, D. S., Nanofibers and their applications in tissue engineering. *International journal of Nanomedicine* **2006**, *1*, (1), 15.
135. Li, H. W.; Wu, C. Y.; Tepper, F.; Lee, J. H.; Lee, C. N., Removal and retention of viral aerosols by a novel alumina nanofiber filter *Journal of Aerosol Science* **2009**, *40*, (1), 65.
136. Shen, S. C.; Ng, W. K.; Chen, Q.; Zeng, X. T.; Tan, R. B. H., Novel synthesis of lace-like nanoribbons of bohemite and γ -alumina by dry gel conversion method. *Materials Letters* **2007**, *61*, (21), 4280.

137. González-Peña, V.; Díaz, I.; Márquez-Alvarez, C.; Sastre, E.; Pérez-Pariente, J., Thermally stable mesoporous alumina synthesized with non-ionic surfactant in the presence of amines. *Microporous and Mesoporous materials* **2001**, 44-45, 203.
138. Ma, M. G.; Zhu, Y. J.; Xu, Z. L., A new route to synthesis of γ -alumina nanorods. *Materials Letters* **2007**, 61, (8-9), 1812.
139. Zhang, Z., Pinnavaia, T. J., Mesostructured γ -alumina with a Lathlike Framework Morphology. *Journal of the American Chemical Society* **2002**, 124, (41), 12294.
140. Lee, H. C.; Kim, H. J.; Chung, S. H.; Lee, K. H.; C., L.; Lee, J. S., Synthesis of Unidirectional Alumina Nanostructures without Added Organic Solvents. *Journal of the American Chemical Society* **2003**, 125, (10), 2882.
141. Wang, J.; Wang, Y.; Qiao, M.; Xie, S.; Fan, K., A novel sol-gel synthesis route to alumina nanofibers via aluminum nitrate and hexamethylenetetramine. *Materials Letters* **2007**, 61, 5074.
142. Teoh, G. L.; Liew, K. Y.; Mahmood, A. K. W., Synthesis and Characterization of Sol-Gel Alumina Nanofibers. *Journal of Sol-Gel Technology* **2007**, 44, 177.
143. Liu, Y.; Ma, D.; Han, X.; Bao, X.; Frandsen, W.; Wang, D.; Su, D., Hydrothermal synthesis of microscale bohemite and gamma nanoleaves alumina. *Materials Letters* **2008**, 62, (8-9), 1297.
144. Jin, Y. Z.; Zhu, Y. Q.; Brigatti, K.; Kroto, H. W.; Walton, D. R. M., Catalysed growth of novel aluminium oxide nanorods. *Applied Physics A* **2003**, 77, (1), 113.
145. Zhang, Z.; Hicks, R. W.; R., P. T.; Pinnavaia, T. J., Mesostructure Forms of γ -alumina. *Journal of the American Chemical Society* **2002**, 124, (8), 1592.

146. Santosa, H. d. S., Santosb, P. de S., Pseudomorphic formation of aluminas from fibrillar pseudoboehmite *Materials Letters* **1992**, 13, 175.
147. Zhu, H. C.; Riches, J. D.; Barry, J. C., γ -Alumina Nanofibers Prepared from Aluminum Hydrate with Poly(ethylene oxide) Surfactant. *Chemistry of Materials* **2002**, 14, 2086.
148. Zhu, H. Y.; Gao, X. P.; Song, D. Y.; Bai, Y. Q.; Ringer, S. P.; Gao, Z.; Xi, Y. X.; Martens, W.; Riches, J. D.; Frost, R. L., Growth of Boehmite Nanofibers by Assembling Nanoparticles with Surfactant Micelles. *Journal of Physical Chemistry B* **2004**, 108, (14), 4245.
149. Bagshaw, S. A.; Pinnavaia, T. J., Mesoporous Alumina Molecular Sieves. *Angewandte Chemie, International Edition in English* **1996**, 35, (10), 1102.
150. Cummins, P. G.; Staples, E.; Penfold, J.; Heenan, R. K., The geometry of micelles of the poly(oxyethylene) nonionic surfactants C16E6 and C16E8 in the presence of electrolyte. *Langmuir* **1989**, 5, (5), 1195.
151. Loy, D. A.; Russick, E. M.; Yamanaka, S. A.; Baugher, B. M., Direct Formation of Aerogels by Sol-gel Polymerizations of Alkoxides in Supercritical Carbon Dioxide. *Chem Mater* **1997**, 9, 2264-2268.
152. Moner-Girona, M.; Roig, A.; Molins, E., Sol-gel Route to Direct Formation of Silica Aerogel Microparticles Using Supercritical Solvents. *J Sol-Gel Sci Techn* **2003**, 26, 645-649.
153. Sui, R.; Rizkalla, A. S.; Charpentier, P. A., Synthesis and Formation of Silica Aerogel Particles By a Novel Sol-Gel Route in Supercritical Carbon Dioxide. *J. Phys. Chem. B* **2004**, 108, (32), 11886-11892.

154. Sui, R.; Rizkalla, A. S.; Charpentier, P. A., Formation of Titania Nanofibers: A Direct Sol-Gel Route in Supercritical CO₂. *Langmuir* **2005**, 21, (14), 6150-6153.
155. Sui, R.; Rizkalla, A. S.; Charpentier, P. A., Direct Synthesis of Zirconia Aerogel Nanoarchitecture in Supercritical CO₂. *Langmuir* **2006**, 22, (9), 4390-4396.
156. Lim, K. T.; Hwang, H. S.; Ryoo, W.; Johnston, K. P., Synthesis of TiO₂ Nanoparticles Utilizing Hydrated Reverse Micelles in CO₂. *Langmuir* **2004**, 20, 2466-2471.
157. Tadros, M. E. A., Carol L. J.; Russick, Edward M.; Youngman, Michael P., Synthesis of titanium dioxide particle in supercritical CO₂. *J Supercrit Fluids* **1996**, 9, (3), 172-176.
158. Stallings, W. E.; Lamb, H. H., Synthesis of Nanostructured Titania Powders via Hydrolysis of Titanium Isopropoxide in Supercritical Carbon Dioxide. *Langmuir* **2003**, 19, 2989-2994.
159. Hong, S.-S.; Lee, M. S.; Lee, G.-D.; Lim, K. T.; Ha, B.-J., Synthesis of titanium dioxides in water-in-carbon dioxide microemulsion and their photocatalytic activity. *Mater Lett* **2003**, 57, (19), 2975.
160. Johnston, K. P.; Shah, P. S., Making Nanoscale Materials with Supercritical Fluids. *Science* **2004**, 303, 482-483.
161. Charpentier, P. A.; Xu, W. Z.; Li, X., A novel approach to the synthesis of SiO₂-PVAc nanocomposites using a one-pot synthesis in supercritical CO₂. *Green Chemistry* **2007**, 9, (7), 768-776.

162. Barrett, E. P.; Joyner, L. G.; Halenda, P. P., The Determination of Pore Volume and Area Distributions in Porous Substances. I. Computations from Nitrogen Isotherms. *Journal of the American Chemical Society* **1951**, 73, 373.
163. Kaneko, E. Y.; Pulcinelli, S. H.; Silva, V. T.; Santilli, C. V., Sol-gel Synthesis of Titania-Alumina Catalyst Support. *Applied Catalysis A:General* **2002**, 235, 71.
164. Kruk, M.; Jaroneic, M., Gas Adsorption Characterization of Ordered Organic-Inorganic Nanocomposite Materials. *Chemistry of materials* **2001**, 13, (10), 3169.
165. Beguin, B.; Garbowski, E.; Primet, M., Stabilization of Alumina toward Thermal Sintering by Silicon Addition. *Journal of Catalysis* **1991**, 127, 595.
166. Phalippou, J.; Woignier, T.; Zarzycki, J., *Ultrastructure Processing of Ceramics, Glasses, and Composites*. Wiley: New York, 1984.
167. Diniz, C. F.; Balzuweit, K.; Mohallem, N. D. S., Alumina nanotubes: preparation and textural, structural and morphological characterization. *Journal of Nanoparticle Research* **2007**, 9, 293.
168. Ji, L.; Lin, J.; Tan, K. L.; Zeng, H. C., Synthesis of High-Surface-Area Alumina Using Aluminum Tri-sec-butoxide-2,4-Pentanedione-2-Propanol-Nitric Acid precursors. *Chemistry of Materials* **2000**, 12, 931.
169. Nakamoto, K., *Infrared and Raman Spectra of Inorganic and Coordination Compounds*. Wiley & Sons: New York, 1997.
170. Shek, C. H.; Lai, J. K. L., Transformation Evolution and Infrared Absorption Spectra of Amorphous and Crystalline Nano-Al₂O₃ Powders. *NanoStructured Materials* **1997**, 8, (5), 605.

171. Suh, D. J.; Park, T. J., Fast Sol-Gel Synthetic Route to High-Surface -Area Aerogels. *Chemistry of Materials* **1997**, 9, 1903.
172. Brinker, C. J.; Scherer, G. W., *The Physics and Chemistry of Sol-Gel Processing*. Academic Press: New York, 1990.
173. Rezugui, S.; Gates, B. C., Chemistry of Sol-Gel Synthesis of Aluminum oxides with in Situ Water Formation: Control of the Morphology and Texture. *Chemistry of Materials* **1994**, 6, 2390.
174. Ogata, Y.; Kawasaki, A., The Promoting Effect of Carboxylic and Anhydrides on the Tishchenko Reaction of Benzaldehyde. *Tetrahedron* **1969**, 25, 2845.
175. Sui, R., Rizkalla, A.S., Charpentier, P. A., Direct Synthesis of Zirconia Aerogel Nanoarchitecture in Supercritical CO₂. *Langmuir* **2006**, 22, 4390.
176. Saha, S., Preparation of Alumina by Sol-Gel Process, Its Structure and Properties. *Journal of Sol-Gel Science and Technology* **1994**, 3, 117.
177. Rahman, M. N., *Ceramic Processing*. CRC Press, Taylor & Francis Group: New York, 2007; p 1473.
178. Yi, G.; Sayer, M., An acetic acid/water based sol-gel PZT process II: Formation of a water based solution *Journal of Sol-Gel Science and Technology* **1996**, 6, 75.
179. Yamamoto, M.; Iwai, Y.; Nakajima, T.; Y., A., Fourier Transform Infrared Study on Hydrogen Bonding Species of Carboxylic Acids in Supercritical Carbon Dioxide with Ethanol. *The Journal of Physical Chemistry A* **1999**, 103, 3525.

Appendices

Appendix A1: American Chemical Society's Policy on reprinting published material in Theses and Dissertations

If your university requires a signed copy of this letter see contact information below:

Thank you for your request for permission to include your paper(s) or portions of text from your paper(s) in your thesis. Permission is now automatically granted; please pay special attention to the implications paragraph below. The Copyright Subcommittee of the Joint Board/Council Committees on Publications approved the following:

Copyright permission for published and submitted material from theses and dissertations ACS extends blanket permission to students to include in their theses and dissertations their own articles, or portions thereof, that have been published in ACS journals or submitted to ACS journals for publication, provided that the ACS copyright credit line is noted on the appropriate page(s).

Publishing implications of electronic publication of theses and dissertation material:

Students and their mentors should be aware that posting of theses and dissertation material on the Web prior to submission of material from that thesis or dissertation to an ACS journal may affect publication in that journal. Whether Web posting is considered prior publication may be evaluated on a case-by-case basis by the journal's editor. If an ACS journal editor considers Web posting to be "prior publication", the paper will not be accepted for publication in that journal. If you intend to submit your unpublished paper to

ACS for publication, check with the appropriate editor prior to posting your manuscript electronically.

If your paper has not yet been published by ACS, we have no objection to your including the text or portions of the text in your thesis/dissertation in print and microfilm formats; please note, however, that electronic distribution or Web posting of the unpublished paper as part of your thesis in electronic formats might jeopardize publication of your paper by ACS. Please print the following credit line on the first page of your article: "Reproduced (or 'Reproduced in part') with permission from [JOURNAL NAME], in press (or 'submitted for publication'). Unpublished work copyright [CURRENT YEAR] American Chemical Society." Include appropriate information.

If your paper has already been published by ACS and you want to include the text or portions of the text in your thesis/dissertation in print or microfilm formats, please print the ACS copyright credit line on the first page of your article: "Reproduced (or 'Reproduced in part') with permission from [FULL REFERENCE CITATION.] Copyright [YEAR] American Chemical Society." Include appropriate information.

Submission to a Dissertation Distributor: If you plan to submit your thesis to UMI or to another dissertation distributor, you should not include the unpublished ACS paper in your thesis if the thesis will be disseminated electronically, until ACS has published your paper. After publication of the paper by ACS, you may release the entire thesis (not the individual ACS article by itself) for electronic dissemination through the distributor; ACS's copyright credit line should be printed on the first page of the ACS paper.

Use on an Intranet: The inclusion of your ACS unpublished or published manuscript is permitted in your thesis in print and microfilm formats. If ACS has

published your paper you may include the manuscript in your thesis on an intranet that is not publicly available. Your ACS article cannot be posted electronically on a publicly available medium (i.e. one that is not password protected), such as but not limited to, electronic archives, Internet, library server, etc. The only material from your paper that can be posted on a public electronic medium is the article abstract, figures, and tables, and you may link to the article's DOI or post the article's author-directed URL link provided by ACS. This paragraph does not pertain to the dissertation distributor paragraph above.

Questions? Call +1 202/872-4368/4367. Send e-mail to copyright@acs.org or fax to +1 202-776-8112. 10/10/03, 01/15/04, 06/07/06

Appendix A2: Elsevier Policy on reprinting published material.

Authors publishing in Elsevier journals retain wide rights to continue to use their works to support scientific advancement, teaching and scholarly communication. An author can, without asking permission, do the following after publication of the author's article in an Elsevier-published journal:

- Make copies (print or electronic) of the author's article for personal use or the author's own classroom teaching.
- Make copies of the article and distribute them (including via email) to known research colleagues for their personal use but not for commercial purposes as described below.
- Present the article at a meeting or conference and distribute copies of the article to attendees.
- Allow the author's employer to use the article in full or in part.
- Retain patent and trademark rights and rights to any process or procedure described in the article.
- **Include the article in full or in part in a thesis or dissertation.**
- Use the article in full or in part in a printed compilation of the author's, such as collected writings and lecture notes.
- Use the article in full or in part to prepare other derivative works, including expanding the article to book-length form, with each such work to include full acknowledgment of the article's original publication in the Elsevier journal.

Appendix A3: Matlab Program for non-linear regression of global kinetic model for TOC destruction

```
%% Main File%%
% Calculate and Plot regression statistics from lsqcurvefit.m
% std -standard error of each parameter
% varresid- Variance of residuals
% r2 - R^2 Correlation coefficient
% cor - Correlation matrix for Parameters
% vcv - Variance Covariance Matrix for Parameters
% varinf- Variance inflation factors >10 implies Multicollinearity in x's
% param -Least squares parameter values
% yfit -Response fit using param to get yfit from lsqcurvefit use yfit=residual+ydata
% where residual is the error matrix from lsqcurvefit
% ydata -Response data
% jac -Jacobian value at Least squares parameter values

clear all
clc
global A; global cpred;
%global cinit; global cfinal; global tspan; global T ;
load bdata.txt; % loading experimental data
A=bdata;
TT=[A(:,1)];
temp=[A(:,2)]+273.15;
time=[A(:,3)];
Xpi=[A(:,4)];
Xpf=[A(:,5)];
xdata=[time temp Xpi];

%
Options=optimset('Display','iter','TolFun', 1e-8);
%'MaxFunEvals',4000,'MaxIter',2000);
%
ko=[0.005 4000];
scale=[1];
%
lb=[0 0];
ub=[];
[kn,resnorm,err1,exitflag,output,lambda,jac1]=lsqcurvefit('clcf2',ko,xdata,Xpf,lb,ub,Options)

err2=reshape(err1,length(time),1);
```

```

cmodel=Xpf+err2
Ym=reshape(cmodel,1*length(time),1);
Yd=reshape(Xpf,1*length(time),1)
[std,varresid,r2,cor,vcv,varinf]=arif(kn,Ym,Yd,jac1)
lowerlimit=kn'-std;

```

```

ko=kn(1)
limitko=ko-lowerlimit(1)
E=8.314*kn(2)/1000
limitE=E-lowerlimit(2)*8.314/1000

```

%Function%

```

function [std,varresid,r2,cor,vcv,varinf]=regdata(param,yfit,ydata,jac)

```

```

e=yfit(:)-ydata(:); %error vectorize the Y matrix for multiple outputs
ss=e'*e % best sum of squares
m=length(yfit);n=length(param);
if (m~=n),varresid=ss./(m-n);else, var=NaN;
end % variance of Residuals

```

% CALC VARIANCE COV MATRIX AND CORRELATION MATRIX OF PARAMETERS

%convert jac to full matrix for ver

```

jac=full(jac);
xtx=jac'*jac;
xtxinv=inv(xtx);

```

```

%calc correlation matrix cor and variance inflation varinf
varinf = diag(xtxinv);
cor = xtxinv./sqrt(varinf*varinf');

```

% Plot the fit vs data

```

t=1:m;
plot(t,ydata,'o',t,yfit,'g-')
title(' ydata and ymodel versus observation number')
xlabel(' observation number');
ylabel(' ydata o and ymodel-')
grid;

```

```

disp(' Least Squares Estimates of Parameters')
disp(param')
disp(' correlation matrix for parameters ')
disp(cor)
vcv=xtxinv.*varresid; % mult by var of residuals~=pure error

```

```

disp('Variance inflation Factors >10 ==> Multicollinearity in x"s')
disp(varinf')

std=sqrt(diag(vcv)) % calc std error for each param
disp(' 95%Confidence Interval for each parameter ')
lowerlimit=param'-std;
upperlimit=param'+std;
disp(' Lower Limit CI ')
disp(lowerlimit)
disp(' Upper Limit CI ')
disp(upperlimit)

%Calculate R^2 (Ref Draper & Smith p.46)
r=corrcoef(ydata(:),yfit(:));
r2=r(1,2).^2;
disp('Variance of Residuals ')
disp( varresid )
disp('Correlation Coefficient R^2')
disp(r2)

```

```
% Class 1%
```

```

function dC = clcf1(t,X,flag,temp,param)
global A; global num;
T=temp;
Xp=X(1);

a1=param(1);
e1=param(2);
T0=420+273.15;

k1=a1.*exp(-e1*((1/T)-(1/T0)));

dC(1)=k1.*((1-Xp)^2.4).*(1-1.3*Xp); % Power rate law model
dC = dC(:);

```

```
% Class 2%
```

```

function cpred = clcf2(param,xdata)
global A; global cpred;
time=xdata(:,1);
temp=xdata(:,2);

```



```
Xpi=xdata(:,3);
num=length(time);
to=0.0;
for i=1:num
    T=temp(i);
    tf=time(i);
    tspan=[to tf];
    Xp0=Xpi(i);
    [t,Xp]=ode45('clcf1',tspan,Xp0,[],T,param);
    for j=1
        cpred(i,j)=Xp(length(Xp),j);
    end
end
end
```

Curriculum Vitae

Muhammad B. I. Chowdhury

EDUCATION:

PhD in Chemical Engineering (December, 2010)

Department of Chemical and Biochemical Engineering, University of Western Ontario, Canada.

Master of Science in chemical Engineering (January, 2005)

Department of Chemical Engineering, King Fahd University of Petroleum & Minerals, Saudi Arabia.

Bachelor of Science in Chemical Engineering (September, 1999)

Department of Chemical Engineering, Bangladesh University of Engineering and Technology, Bangladesh.

RESEARCH EXPERIENCE:

May 2006 to August 2010: Research Assistant

Department of Chemical and Biochemical Engineering, University of Western Ontario, Canada.

August 2005 to April 2006: Research Chemical Engineer (Engineer-II)

Research Institute (RI), King Fahd University of Petroleum & Minerals, Saudi Arabia.

September 2002 to August 2005: Research Assistant

Department of Chemical Engineering, King Fahd University of Petroleum & Minerals, Saudi Arabia.

SCHOLARSHIPS:

- (1) Western Engineering Scholarship (2006-2010), University of Western Ontario, Canada.
- (2) Graduate Scholarship (2002-2005), King Fahd Univ. of Petroleum & Minerals, Saudi Arabia.
- (3) Technical Scholarship (1994-1999), Bangladesh Univ. of Engineering & Tech., Bangladesh.
- (4) Board Scholarship (1990-1992), Dhaka Educational Board, Bangladesh.

PUBLICATIONS:

1. **M. B. I. Chowdhury**, R. Sui, R. A. Lucky, P. A. Charpentier, One-Pot Procedure to Synthesize High Surface Area Alumina Nanofibers Using Supercritical Carbon Dioxide, *Langmuir*, 26, 2010.
2. E. A. Youssef, **M. B. I. Chowdhury**, G. Nakhla, P. Charpentier, Effect of nickel loading on hydrogen production and chemical oxygen demand (COD) destruction from glucose oxidation and gasification in supercritical water, *Int. J. Hydrogen Energy*, 35, 2010.
3. **M. B. I. Chowdhury**, S. Ahmed, M. Shalabi, T. Inui, Preferential methanation of CO in a syngas involving CO₂ at lower temperature range, *Appl. Catal. A*, 314, 2006.
4. **M. B. I. Chowdhury** and P. A. Charpentier, Production of Hydrogen-rich gas through supercritical water gasification of glucose using La-modified Ni/Al₂O₃ catalysts, *Ind. Eng. Chem. Res.*, Submitted.
5. **M. B. I. Chowdhury**, M. M. Hossain, P. A. Charpentier, Characterization of nickel based catalysts used in supercritical water gasification of glucose, *Appl. Catal. A*, submitted.
6. **M. B. I. Chowdhury**, M. M. Hossain, P. A. Charpentier, Development of kinetic model for TOC destruction from supercritical water gasification of glucose, *Ind. Eng. Chem. Res.*, Submitted.
7. **M. B. I. Chowdhury**, P. A. Charpentier, Effect of nano catalysts for hydrogen production from biomass gasification in supercritical water, in preparation.